THE FLORIDA STATE UNIVERSITY

COLLEGE OF ARTS AND SCIENCES

MEASUREMENT OF THE POLARIZATION OBSERVABLES I^S AND I^C FOR $\vec{\gamma}\, p \to p\, \pi^+\, \pi^-$ USING THE CLAS SPECTROMETER

By

CHARLES HANRETTY

A Dissertation submitted to the
Department of Physics
in partial fulfillment of the
requirements for the degree of
Doctor of Philosophy in Physics

Degree Awarded:
Spring Semester, 2011

The members of the committee approve the dissertation of Charles Hanretty defended on December 7^{th}, 2010.

Dr. Volker Credé
Professor Directing Dissertation

Dr. Greg Riccardi
University Representative

Dr. Paul Eugenio
Committee Member

Dr. Winston Roberts
Committee Member

Dr. Todd Adams
Committee Member

Approved:

Dr. Mark Riley, Chair, Department of Physics

Dr. Joseph Travis, Dean, College of Arts and Sciences

The Graduate School has verified and approved the above-named committee members.

ACKNOWLEDGMENTS

Even though my name appears on this document, the presented work would have never been completed without the aid of a multitude of people. The following people are not the only ones I have to thank so if your name does not appear, know that I am still thankful for you. Firstly, I would like to thank my advisor, Volker Credé, for his invaluable help and knowledge. From guiding me through the theory, the data analysis and the multitude of coding issues we encountered to dealing with me at stressing times, he stuck with me and pushed me to do better. For this I am very, very grateful.

I would also like to thank FSU's Experimental Hadronic Physics Group and all of its members for their guidance and friendship over the years: Paul Eugenio for his help, guidance, and (even though he may not realize it) for the "tutorial" sessions I sometimes set myself up for. Lukasz Blaszczyk who shared in the early years of my involvement in Hall B and the summer-long stays at Jefferson Lab, who showed me how fun computers and coding can be and who introduced me to the best sporting event in the world (the World Cup). Mukesh Saini who tirelessly (and I mean tirelessly) answered my questions regarding both physics and programming and with whom I had several political as well as pointless discussions. Sungkyun Park for the many discussions he and I had (both about physics and not) and for providing me with a goal of how I want my logbooks to look one day. Craig Bookwalter for his help, the times we had in Peru and our lunches in the various pizza-joints in Cusco (some of the best pizza I've ever had). Alexander Ostrovidov for his computer expertise which keeps our servers alive. Andrew Wilson who helped me understand aspects of physics I had trouble with. And finally Nathan Sparks for his help both in class and with coding. All of the above people deserve additional thanks for the good times we had, the laughs we all shared and the long car rides to Virginia.

I would like to give great thanks to those I have worked with at Jefferson Lab over the years. My first foray into Experimental Nuclear Physics was guided by Doug Higinbotham who showed me just how fun it is. I would like to thank Youri Sharabian for his guidance during my time fabricating the transverse holding coil for FROST. He is a man who has an great amount of knowledge and has some of the most interesting stories. I would like to thank the JLab Target Group for the time I spent with them working on the FROST target: James Brock, Mark Hoegerl, David Meekins, Chris Keith, Chris Carlin, David Griffiths, Paul Hood, and Mike Seely. During my time working on FROST, this group of gentlemen taught me much about machining, cryogenics, how targets are constructed and how they work. I would also like to thank the two other graduate students with whom I worked on the FROST target: Daria Sokhan and Russell Johnstone. Thanks also goes out to the entire g8b run group with a special thanks to Eugene Pasyuk for his uncanny ability

to reply quickly to emails and completely answer any question posed.

My thanks are not relegated to the Jefferson Lab or FSU physics community alone. The relationships I have formed outside of these bounds have been just as invaluable. I would like to thank Mario Encinosa, Heather Encinosa and their family for their support. Specifically I would like to thank Mario Encinosa not only for the physics knowledge he hammered into my brain as an undergrad but also for his attitude regarding learning and physics and for being a second father to me. I would like to thank the life-long friends I made as we were struggling through our undergraduate education. We went through some tough times together (in and out of the classroom) and I don't think I would have made it without them. Thanks also goes to the friends I made outside of physics for they are just as important to me. Many thanks also goes to Veronica Scerra who's love and support kept me from going under during some of my most trying times.

Lastly but most importantly, I would like to thank my parents: Charles Patrick Hanretty and Angela Gaye Davis. Words can never describe the amount of influence they have had on my life nor my profound thanks. It is from these two people that I have learned what hard work and determination are. I offer them my eternal gratefulness for the life they gave me and the things they taught me.

TABLE OF CONTENTS

LIST OF FIGURES

LIST OF TABLES

ABSTRACT

Predictions regarding the excited baryon spectrum provided by symmetric quark models called Constituent Quark Models (CQMs) show good agreement with experimental measurements in the low-energy region (less than ≈ 1.8 GeV). The mass region above ≈ 1.8 GeV, however, contains many resonances which are predicted to exist by these models but have not been experimentally verified [1, 2]. This describes a well known problem in Baryon Spectroscopy, the issue of missing resonances. These resonances are considered missing as the mass measurements made regarding these resonances are either absent or fairly large in their uncertainties [1]. This discrepancy between the theoretical predictions and the experimental measurements can be attributed to several sources. Firstly, the majority of the data regarding the excited baryon spectrum originates from pion-nucleon or kaon-nucleon scattering (which the missing resonances may only weakly couple to). Therefore, as suggested by recent quark model calculations, a study of reactions involving photoproduction (γp) may present a better opportunity for the production of these missing resonances [3]. In addition, previous analyses involved unpolarized data. This absence of polarization leads to ambiguous analysis results, therefore a constraint such as the polarization of the photons can be used in order to further constrain the kinematics of the reaction(s). The analysis of polarized photoproduction data ($\vec{\gamma}p$ or $\vec{\gamma}\vec{p}$) in the low-energy region (< 1.8 GeV) presents the opportunity to further study previously observed resonances, possibly resolving currently unanswered questions about their properties. An analysis of polarized photoproduction data in the high-mass region (> 1.8 GeV) allows for a study of the resonances contributions, providing insight into the issue of the missing resonances.

The study of a photoproduced 3-body final state (such as $\vec{\gamma}p \rightarrow p\ \pi^+\pi^-$) has been indicated as a promising method for detecting the effects of the missing resonances as this final state topology accounts for most of the cross section above ≈ 1 GeV. A study of double-meson final states very well may fill the holes in the experimental data as the majority of analyses regarding this issue have come from the analysis of quasi 2-body final states (such as Nπ, Nη, Nω, KΛ, and KΣ). It is also likely that these missing resonances decay to high mass intermediate states instead of directly into a meson and a ground state nucleon. Therefore the decay of these resonances is more of a chain (resulting in a two-meson-one-ground-state-nucleon state) than a direct decay.

The presence (or absence) of these missing resonances can be determined through quantities sensitive to resonance contributions called polarization observables. A study of a pseudoscalar single-meson final state produced via polarized photoproduction gives access to 7 of these polarization observables. The analysis of a double-meson final state however, allows access to a total of 15 polarization observables. These additional 8 polarization ob-

servables (which are unique to a double-meson final state) arise from the more complicated kinematics needed to describe the reaction. For example, the introduction of a second meson leads gives rise to a second frame in which the two meson are produced back-to-back as well as two additional angles describing the orientation of this plane. By measuring these sensitive quantities, a determination of what resonances contribute, or do not contribute, to the excited baryon spectrum can be determined.

Presented in this work are the first ever measurements of the polarization observable I^s for a final state with two pions and the first ever measurements of I^c for a final state containing charged pions (let alone the first measurements of both observables for the specialized case of $\vec{\gamma}p \rightarrow p\ \pi^+\pi^-$ reactions). The presented measurements were made using the high-statistics data available in the CLAS g8b data set. This data were taken at the Thomas Jefferson National Accelerator Facility (JLab) from July 20^{th} to September 1^{st} of 2005 using linearly polarized photons, an unpolarized liquid hydrogen (LH_2 target), and the CEBAF Large Acceptance Spectrometer (CLAS). The highly-polarized photons were produced via bremsstrahlung using an unpolarized electron beam provided by the Continuous Electron Beam Accelerator Facility (CEBAF) accelerator and a well-oriented diamond radiator. These polarized photons were produced at five different coherent edge energies: 1.3 GeV, 1.5 GeV, 1.7 GeV, 1.9 GeV, and 2.1 GeV. Considering the 200 MeV-wide window of highly polarized photons whose upper limit is the coherent edge energy, and the five different coherent edge energies used, highly polarized photons were produced covering an total energy range of 1 GeV. These data along with the utilized analysis tools have lead to clean, continuous, low-error measurements of I^s and I^c which will aide the hadronic physics community in its search for the complete description of one of the most fundamental systems in nature, the baryon.

CHAPTER 1

INTRODUCTION AND THEORY

Currently one of the areas of curiosity in hadronic physics is the excited baryon spectrum and the resonances contained within. Historically it has been shown that a way to study the underlying physics of composite systems (such as their internal components and structure as well as how its components interact) is to study the excited states of such a system. An example of such a method and its possible results can be seen in the field of Atomic Spectroscopy which has lead to many great and important leaps in physics, namely Quantum Mechanics, the concept of spin (Pauli exclusion principle), and Quantum Electrodynamics (QED). Baryons, particles comprised of more fundamental particles called quarks and gluons, are examples of such composite systems found in nature and therefore can be excited into unstable higher-energy states. This collection of excited states is called the *spectrum* of the baryon. By analyzing this spectrum and its decay products, we as humans can learn more about these sub-atomic particles found in all of nature: how the baryon is formed and behaves when excited, how the quarks and gluons interact and how these interactions affect the system. This learning also aids in the development of theories which can and will extrapolate our present knowledge to the experimental limits and beyond.

1.1 General Motivation

Studying the excited baryon spectrum is not a task easily accomplished. The current theory used to describe the behavior and physics of strong interactions is Quantum Chromodynamics (QCD). However, this advanced theory cannot presently provide a complete description of the interactions involved in the "low energy" regime and in the "high energy" regime presently offer only approximations. In the absence of a fundamental theory derived from first principles, there are phenomenological models which can be used to predict the behavior of these multi-quark particles in the low energy region and thusly their excited spectrum. Such models that treat the baryons as particles composed of three constituent quarks are called Constituent Quark Models (CQMs). Using these models, theorists can predict the spectrum of excited baryons along with the quantum characteristics of the contained resonance states. These models however predict many more states than have been seen experimentally. The states predicted by the CQMs but presently lacking experimental verification are termed *missing resonances*. The pressing issue of missing resonances is not a new source of curiosity and is and has been the focus of many modern day experimental

queries, efforts, and analyses. Measurable quantities called polarization observables, which appear when the kinematics of the reaction are constrained via polarization, are highly sensitive to resonance contributions [4]. Through the analysis of the asymmetries seen in polarized photoproduction data for the reaction $\vec{\gamma}p \to p\ \pi^+\pi^-$, these polarization observables can be extracted, giving insight into the excited baryon spectrum and are sensitive enough to reveal properties (masses and mass-widths) of the resonances themselves.

1.2 From Rutherford to Gell-Mann

The year 1911 marked the emergence of the Rutherford model of the atom into mainstream physics [5]. Although it was already postulated that the atom was comprised of smaller, more fundamental particles (such as the structure proposed by J.J. Thomson's "plum pudding" model), the Rutherford model presented the planetary-like, orderly view of the atom. In 1913, this atomic model was then improved upon by Niels Bohr through the inclusion of Quantum Mechanical principles to make the Rutherford-Bohr model [6]. According to the Rutherford-Bohr model, the system of the atom was described as an electron cloud surrounding a central, positively charged nucleus. Still, the question remained: Was this positively charged nucleus a particle itself or is it also made of something more fundamental? In 1919, this was answered through the discovery of the proton in one of Rutherford's scattering experiments [7] and again by the discovery of the neutron by Chadwick in 1932. The discovery of these two particles (the two nucleons) answered the question regarding whether or not the nucleus was made of more fundamental particles but also brought to light an additional question: If the positively charged proton and electrically neutral neutron are bound together, then what binds them? The Japanese theorist Hideki Yukawa came forth with an answer to this question in 1935. He called this binding force between nucleons the *strong force* and described the interaction between the two nucleons as being the exchange of a particle called a meson (later identified to be a pion, which can be seen in Fig. 1.1).

These initial developments towards the discovery and understanding of subatomic particles, specifically nuclear structure, energized the physics community. Many physicists, spurred on by the idea that there is a slew of particles yet to be seen, soon sought out to discover new sub-atomic particles. Early discoveries of these particles (pions, kaons, and muons) utilized cosmic rays as the source and bubble and streamer chambers as the detector. As technologies developed, tools useful to experimental physicists to both produce and detect new, more short-lived particles emerged in the form of particle accelerators and detector systems. This period (starting in the 1930's) marked an explosion in the number of new particle states detected. Newly seen particles were classified by their quantum numbers with a new quantum number, *strangeness* (S) being introduced to explain the long, "strange" lifetimes of some newly seen particles. This strangeness was later attributed to the presence of the *strange quark* upon its discovery in deep inelastic scattering experiments at the Stanford Linear Accelerator Center. In order to give this ever-growing group of new particles a name, Lev B. Okun introduced the term *hadron* at the 1962 International Conference on High-Energy Physics. This term has become part of the lexicon of particle physics (including its own field) and refers to all particles which are held together and interact via the strong force.

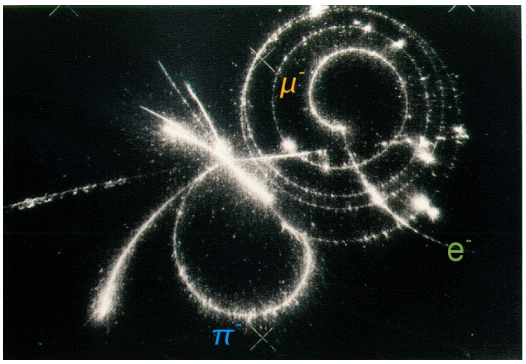

Figure 1.1: A photograph showing the creation and decay of a pion in a streamer chamber. Here, pions originate in a collision in the streamer chamber. One of the pions makes the looping track toward the bottom before it decays into a muon which then curls counterclockwise four times and eventually changes into an electron which moves off towards the lower right [8].

This explosion in the number of new particles seen prompted the theorist Murray Gell-Mann to begin classifying these newly seen particles in terms of their quantum numbers. He began by separating the known particles by baryon number (B) into two groups: B=0 (representing mesons) and B=1 (representing baryons). He then further classified the particles in terms of their total angular momentum (J). The particles contained in these four groups were then arranged on axes corresponding to charge (Q), a quantum number related to the strong force called Isospin (Isospin projection I_z), and strangeness (S). The result of this organization of the known hadrons can be seen in Fig 1.2 for baryons (a three-quark state) and Fig 1.3 for mesons (a quark-antiquark state).

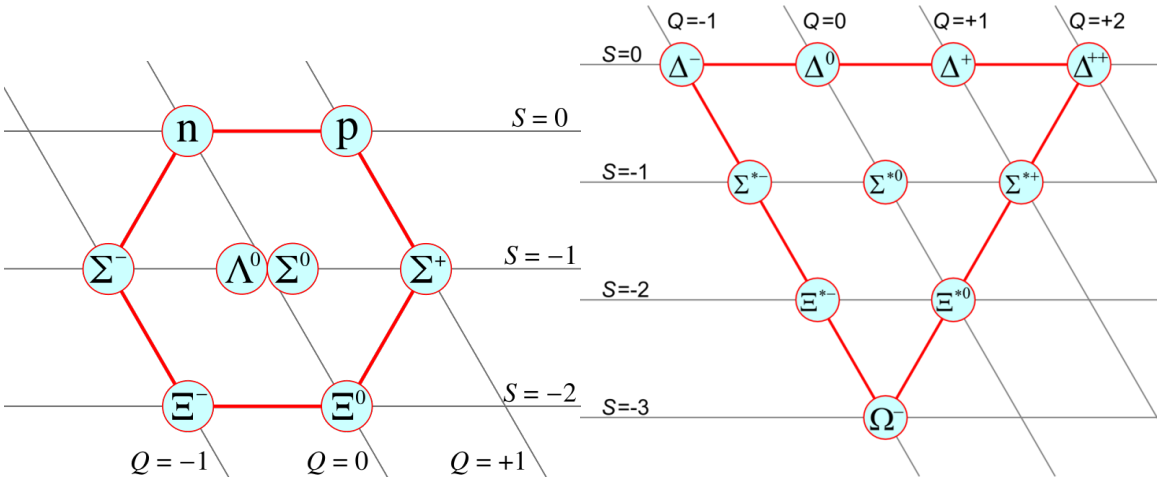

(a) $J^P = \frac{1}{2}^+$ Octet (b) $J^P = \frac{3}{2}^+$ Decuplet

Figure 1.2: The two light baryon (B=1) multiplets. The $J^P = \frac{1}{2}^+$ Octet (named as such as it contains eight particles) to which the nucleon belongs can be seen in (a). The $J^P = \frac{3}{2}^+$ Decuplet (named as such as it contains ten particles) where particles such as the Δ^{++} and Ω^- reside is shown in (b). The Greek letters here indicate the name of the hadron.

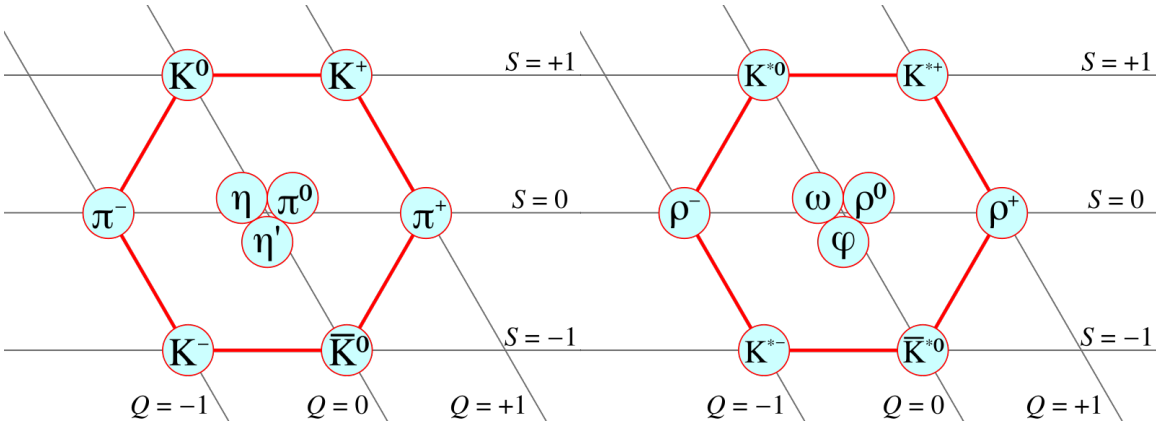

(a) $J^P = 0^-$ Nonet (b) $J^P = 1^-$ Nonet

Figure 1.3: The two light meson (B=0) nonets (named as such as they contain nine particles). The $J^P = 0^-$ Nonet to which the pion belongs is shown in (a) while the $J^P = 1^-$ Nonet is shown in (b). The Greek letters here indicate the name of the hadron.

In making these arrangements of the lightest known hadrons, Gell-Mann was building upon the idea that there exist a symmetry between these particles. His early $J^P = \frac{3}{2}^+$ Decuplet did not contain the Ω^- baryon (as it had not been discovered yet) yet he predicted that there should be a particle at the apex with certain quantum properties. The discovery of the Ω^- in 1964 verified Gell-Mann's predictions regarding its quantum properties and solidified Gell-Mann's scheme.

1.3 The Quark Model

The apparent SU(3) symmetry hinted at by these arrangements of the light hadrons had an interesting implication in the eyes of Gell-Mann and George Zweig. They proposed that this symmetry indicated that the hadron was a bound state of more fundamental particles called *quarks*, a term he derived from Book 2, Episode 4 of James Joyce's *Finnegans Wake* (Zweig preferred the term *aces* but the term *quark* stuck and was eventually adopted by the physics community). These quarks, they proposed, came in three different types or flavors: up (u), down (d), and strange (s). Their emerging model, which later became known as the Quark Model, stated that baryons were particles comprised of three quarks (qqq) and mesons were comprised of a quark-antiquark pair ($q\bar{q}$) (Fig. 1.4) with the quantum properties (such as the quantum numbers) of the baryons and mesons being determined by their quark composition. In addition to the three (baryons) or two (mesons) quarks present in the hadron, there exist many "off-shell" quark-antiquark pairs. These quark-antiquark pairs exist only briefly and do not contribute to the quantum properties of the hadron and form the "sea of quarks" (these quarks are also known as *sea quarks*). The two (in the case of a meson) or three (in the case of a baryon) quarks of the hadron which do contribute the hadron's quantum properties are termed *valence quarks*. It is these quarks that are considered when classifying (and for the most part, modeling) baryons and mesons. The

Quark Model stated that the quark flavors possessed quantum numbers of fractional electric charge of $+2/3$ (for the u quark) or $-1/3$ (for the d and s quarks), a spin of $1/2$ (quarks are fermions), a baryon number of $1/3$, and a quantum number called strangeness (with the strange quark having a strangeness of -1). The arrangement of these three quark (and antiquark) flavors along the same axes of charge, strangeness, and isospin can be seen in Fig. 1.5.

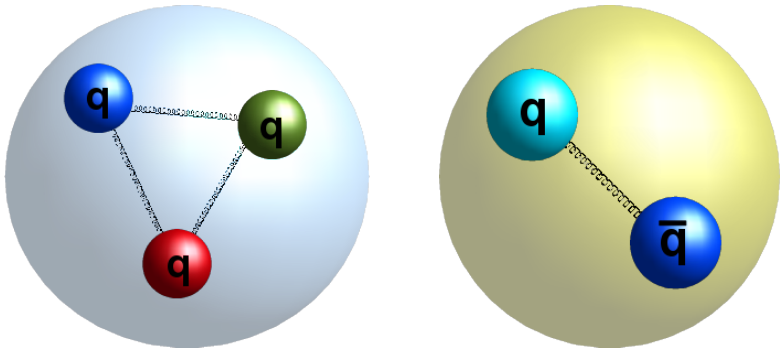

(a) Baryon (b) Meson

Figure 1.4: Diagrams of the quark structure of a baryon (a) and a meson (b).

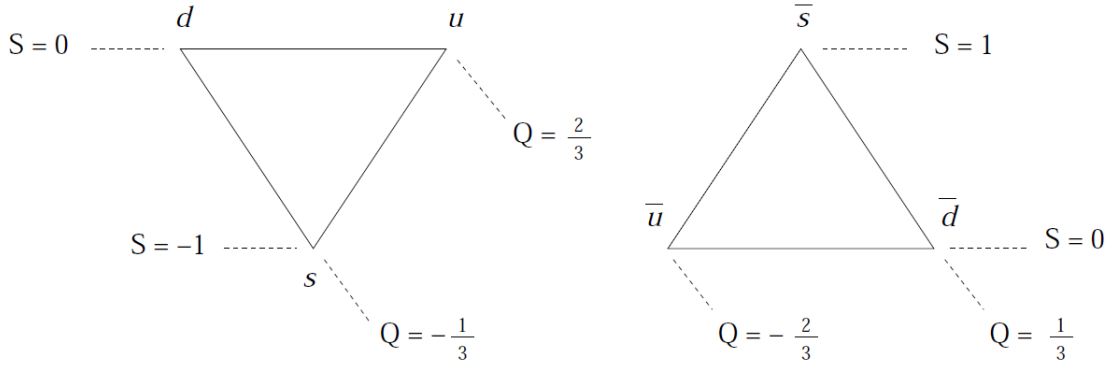

Figure 1.5: Arrangement of the light quarks according to the Quark Model along axes corresponding to the quantum numbers of charge (Q) and strangeness (S) and the unlabeled axis of Isospin (which goes from $-1/2$ to $+1/2$ from left to right in units of $1/2$).

Since the birth of the Quark Model, three additional flavors of quarks have been added to the model and verified via high-energy experiments indicating an SU(6) symmetry. These quarks differ greatly from the three original flavors in their mass and are thusly termed the *heavy quarks* (with the u, d, and s quarks making up the group of *light quarks*). The charm quark (c) was found in the discovery of the J/ψ (a $c\bar{c}$ state) in 1974 [9, 10], the bottom quark (b) with the discovery of the Υ (a $b\bar{b}$ state) in 1977 [11], and the top quark (t) via

its decay in 1995 [12].

The discovery of the Δ^{++}, Δ^{-}, and Ω^{-} puzzled physicists as they were bound states of three identical quarks. If these three quarks possess the same quantum numbers, then this would be a direct violation of the Pauli Exclusion Principle. This prompted Oscar W. Greenberg to propose, in 1964, that the quarks carry one additional quantum number later known as color charge (having the values of red, blue, green, anti-red, anti-blue, and anti-green). He postulated that since color charge cannot be observed experimentally, any particle that exists in nature (and therefore can be detected) must exist as a color singlet, or color neutral state. For example, for a baryon this would mean a combination of red, blue and green and for a meson, a combination of color and anti-color. This quantum property is one that has become accepted by the hadronic physics community, experimentally verified [13] and forms the cornerstone on which Quantum Chromodynamics is founded.

1.4 Taxonomy of the Baryon Spectrum

The naming of the known baryon resonances follows a specific convention. This convention is $X(m)L_{2I2J}$ where X denotes the type of baryon, m the invariant mass of the resonance (in units of MeV/c^2), L is the relative angular momentum between the π (or K) and the nucleon which gave rise to the resonance, I is the isospin of the particle, and J the total angular momentum. Baryons are divided into groups which gives hints to its quark composition as well as isospin. The X denotes these types of baryons. Baryons made of only u and d quarks and having an isospin of 1/2 are termed N and those with isospin 3/2 are called Δ's. Replacing one of the u or d quarks with an s quark (S $= -1$) changes this naming to Λ if it has isospin 0 and Σ if it has isospin 1. Replacing two of the u or d quarks with strange quarks makes the baryon a Ξ resonance with isospin 1/2 (S $= -2$) while replacing all quarks with an s quark (S $= -3$) means the resonance is an Ω. The historical reason for specifying the relative angular momentum of the production particles comes from the fact that the majority of the baryon resonances were discovered using πN or KN scattering. This notation told not only the properties of the baryon resonance but also how it was produced.

1.5 Quantum Chromodynamics (QCD)

It became apparent that a theory was needed to describe this blossoming field of physics. But where and how should this theory start? As defined by our current understanding of physics, there exists in nature four fundamental forces. These forces are: the electromagnetic force, gravity, the weak nuclear force, and the strong nuclear force. The theory of Quantum Chromodynamics (QCD) describes one of these forces, the strong force, and how it governs the interactions of quarks and gluons. Quarks and gluons are two of the most fundamental particles known to modern physics. All hadrons, defined as particles that are held together by and interact via the strong force, are bound states of quarks with baryons being comprised of three quarks and mesons being comprised of a quark-antiquark pair. These quarks occur in nature in six different *flavors*: up, down, charm, strange, top, and bottom and six different *color charges*: red, green, blue, anti-red, anti-blue, and anti-green. It is from

this introduction of color charges that QCD derives its name. In this theory, each quark (regardless of flavor) and gluon carries this color charge and all hadrons that can exist in nature must be a color singlet, or color-neutral, state. Each flavor of quark in QCD has its own anti-particle. A particle's anti-particle possess the same mass but opposite quantum numbers. The properties of the six known flavors of quarks are shown in Table 1.1.

Table 1.1: Table of known quarks and their properties.

Name	**Symbol**	**Mass**	$\mathbf{I_3}$	**J**	**B**	**Q**	**C**	**S**	**T**	**B′**
Up	u	1.5 - 4 MeV/c^2	$+1/2$	$1/2$	$+1/3$	$+2/3$	0	0	0	0
Down	d	4 - 8 MeV/c^2	$-1/2$	$1/2$	$+1/3$	$-1/3$	0	0	0	0
Strange	s	80 - 130 MeV/c^2	0	$1/2$	$+1/3$	$-1/3$	0	-1	0	0
Charm	c	1.15 - 1.35 GeV/c^2	0	$1/2$	$+1/3$	$+2/3$	$+1$	0	0	0
Top	t	174.3 $\pm$ 5.1 GeV/c^2	0	$1/2$	$+1/3$	$+2/3$	0	0	$+1$	0
Bottom	b	4.1 - 4.4 GeV/c^2	0	$1/2$	$+1/3$	$-1/3$	0	0	0	-1

I_3 = Isospin projection; J = total angular momentum; B = baryon number; Q = electric charge; C = charm; S = strangeness; T = topness; B′ = bottomness

In Quantum Electrodynamics (QED), the force carrier and information carrier between particles is the photon, an electrically neutral, massless vector boson. In Quantum Chromodynamics (which deals with hadrons which are bound together by a "glue" known as *gluons*), the gluons serve as the mediators between quarks and possess a color charge of their own. This means that these mediating particles, within their respective theories, contribute very differently to interactions. The electrical neutrality of the photon means that in QED, the photon serves to only mediate interactions and does not participate in them. In contrast, the gluons in QCD (being able to carry both a color and anti-color charge) do not just serve as mediators but also participate in strong interactions. This added source of interaction is one of the reasons for the high level of difficulty that comes with developing, analyzing, and studying QCD.

A well known observation of strong interactions is quark *confinement*. This observation indicates that the attractive force between two quarks does not decrease as the distance between the quarks increases, rather it increases (Fig. 1.6). The consequence of such an observation is that quarks can never exist alone (i.e. it is impossible for there to ever be a free quark) and are therefore bound into hadrons such as baryons and mesons. If one were to pull two quarks apart, the attractive potential between them would increase to the point where there is enough energy to create another pair of quarks and one would now have two quark pairs. This also implies that a measurement of the quark's mass has to be done indirectly as it can never exist by itself and is always part of a system.

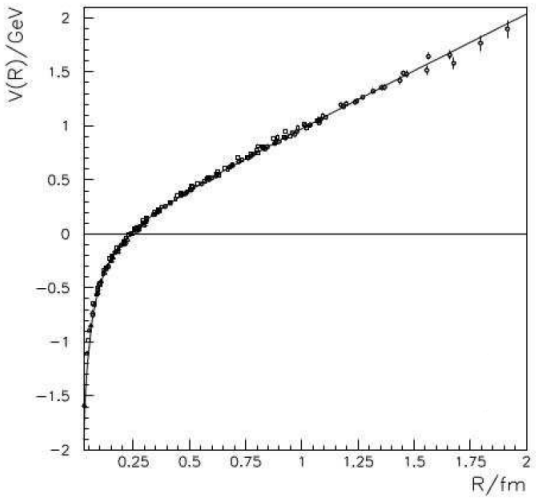

Figure 1.6: The attractive potential between two quarks as a function of the distance between. This ever-increasing potential leads the the property of QCD called quark *confinement*.

Due to the gluons' possession of a color charge, interactions that occur between quarks and gluons can come from a quark emitting (or absorbing) a gluon, a gluon emitting (or absorbing) a gluon, and the direct interaction between two gluons. The last two possibilities (the indirect and direct interactions between gluons) lead QCD down a path that makes it non-linear and difficult to solve analytically. As a result, approaches/theories have to be developed to provide testable approximations for the interactions explained by this theory. One of these approaches, perturbation theory, involves taking the theory to the high-energy limit. As the energy of the system increases (large momentum transfer), the effect of the strong interaction decreases. This phenomenon results from the QCD coupling constant α_s, which describes the strength of these strong interactions, decreasing as the exchange momentum/energy of the system increases (Figure 1.7). This behavior, termed *asymptotic freedom* (a well-known and important property of QCD), occurs when the exchange momentum is large which greatly simplifies the mathematics of the gauge theory and allows for perturbative calculations, the realm of perturbative QCD (pQCD). In this scenario, the quarks contained in the hadron are treated as essentially free-moving, non-interacting quarks. It is then that the well-established procedures of QED for describing photon and electron interactions can be applied to the quarks and gluons. In the lower-energy regime ("medium" energy) the coupling constant, α_s, approaches a value of one. This complicates the theory as it makes it such that the coupling constant cannot be expanded in terms of α_s and QCD becomes non-perturbative. This area, where the theory of QCD cannot presently provide solutions, is the energy regime where the quarks and gluons combine to form hadrons making it a highly important region to study. Thus the strength of the strong coupling constant, α_s, and its effects on the QCD calculations provides for a division the theory into two main areas which attempt to describe the same system (the hadron).

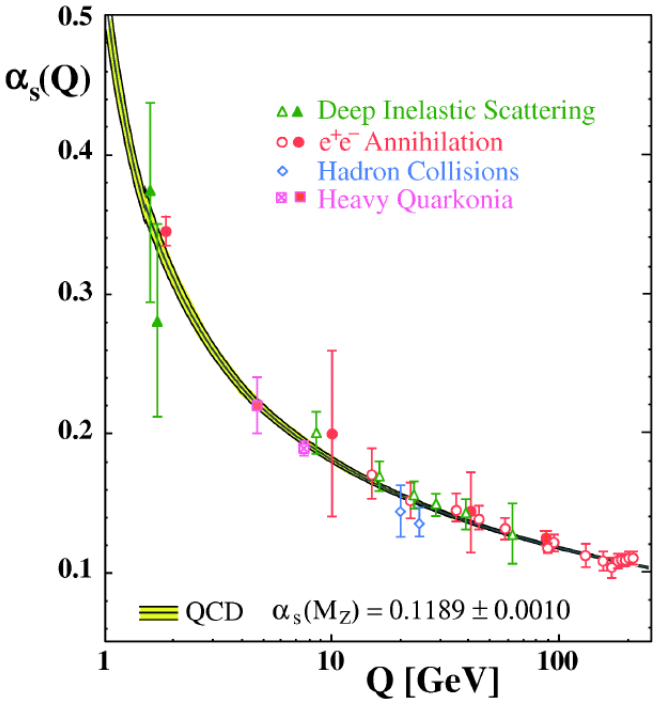

Figure 1.7: The strength of the QCD coupling constant as a function of the exchanged gluon momentum, Q [14].

Attempts to provide theoretical solutions to non-perturbative QCD have mainly been unsuccessful. However, there is one very promising and well-established method called Lattice QCD that has been developed to provide solutions to non-perturbative QCD. This method uses a grid of space-time points to simplify the integral calculations needed for predictions to come out of the theory (QCD). This method has shown some promise. Recent calculations from Lattice QCD in the non-perturbative region of QCD have resulted in the prediction of the masses of the two lowest state octet and decuplet baryons [15]. The main limitation encountered by Lattice QCD comes in the form of the hardware used to carry out the calculations. Extracting testable predictions from the theory requires large amounts of computational power with this requirement greatly increasing when considering light quarks. There have been recent efforts to construct supercomputers at labs such as CERN, JLab, Fermilab, and Brookhaven National Lab for the purpose of carrying out Lattice QCD calculations [17]. Predictions from Lattice QCD have improved over the years with this trend expected to continue as computational technology improves. While this method, and lesser known ones, show much promise for providing approximations and access to areas of the theory previously off limits, the theory in its present form is still a long way from complete. The theory of QCD, the methods for providing analytical solutions to QCD (such as Lattice QCD) as well as the technology to complete and test them continue to evolve. As they do, physics gets closer to predicting and fully describing hadronic interactions, excitations and the excited baryon spectrum.

1.6 Spectroscopy

Spectroscopy is the use of light, sound, or particle emission to gain information about the properties of the matter under investigation. This technique has been utilized to gain knowledge regarding the nature of matter in several scientific disciplines. A good example of this is the field of Atomic Spectroscopy. To gain a deeper understanding of the atom and its structure, atoms were excited via absorption of a photon and then allowed to relax (emission of a photon) and return to their original ground state. When these atoms relaxed, it was seen that they emitted photons at different wavelengths, i.e. the spectrum of that atom. It was seen that this spectrum, instead of exhibiting a continuous distribution, contained discrete lines (Figure 1.8). Already in existence were theories that attempted to explain the structure of an atom (the cubic model, the plum-pudding model, the Saturnian model, and the Rutherford model) yet these theories did not mesh with the experimental evidence. Using the observed spectra to build upon the Rutherford model, Niels Bohr proposed the Bohr Model in 1913. This model described the atom as having a central nucleus surrounded by orbiting electrons which occupy a discrete set of distances corresponding to a discrete set (or *quanta*) of energies. This explained the discrete set of lines seen in the excited spectra of atoms and aided considerably in the development of the theory of Quantum Mechanics. The study of the spectra seen in Atomic Spectroscopy also led to the development of Wolfgang Pauli's *Pauli Exclusion Principle* which led to the discovery of a property of all fermions, an internal angular momentum termed *spin*. The discovery of such a property was also crucial in the development of Quantum Electrodynamics, for which spin plays a major role.

Figure 1.8: The excited spectrum of Hydrogen which exhibits a discrete set of lines as opposed to a continuous distribution.

1.7 Baryon Spectroscopy

The study of the atomic spectra (Atomic Spectroscopy) led to a deeper understanding of the properties and behavior of atoms and atomic processes. Presently, a looming question in Nuclear Physics is in regards to the structure and behavior of the nucleons which make up the nucleus of atoms. These nucleons (protons and neutrons) are baryons which are particles made of three (constituent) quarks. Since these baryons are made of smaller, more fundamental particles, they can be excited not unlike the atom (although the process needed to excite them requires much more energy). In Baryon Spectroscopy however, the decay product is not only a photon but an array of products such as photons, π's, ω's, η's, etc. As there are an array of particles that may be emitted in the de-excitation of a baryon, complicated and highly-developed arrays of particle detectors must be employed in the most

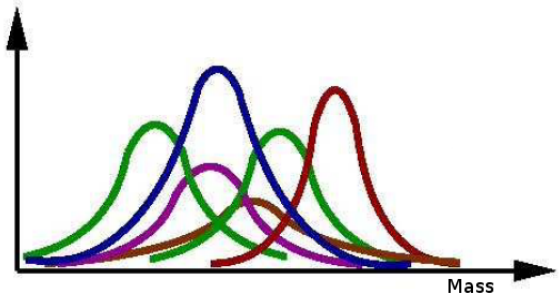

Figure 1.9: A cartoon demonstrating the lineshape of the baryon resonances and how they can interfere with each other.

basic of cases. This is in contrast to the basic techniques for detecting the photons from a de-excited atom used in Atomic Spectroscopy (such as diffraction grating). Still, the basic techniques developed for studying and probing the atom are applicable to the younger field of Baryon Spectroscopy.

In spite of the fact that many principles used in Baryon Spectroscopy are borrowed from Atomic Spectroscopy, resolving the excited baryon spectrum is a much more difficult task. When studying the atomic spectra, the spectral lines are narrow and separate enough for the different spectra to be readily seen. This is a result of their relatively long lifetimes (τ). According to Werner Heisenberg's uncertainty principle:

$$\Delta E \Delta t \approx \hbar. \tag{1.1}$$

Therefore as the lifetime of an excited state increases, the energy width of the state decreases. This can be seen in the excited spectra of atoms as while the visible bands are narrow, they are not infinitely narrow and do have noticeable widths. This width, or *natural linewidth* is inversely proportional to the lifetime of the excited state. The lifetimes of excited baryon are much shorter than that of excited atoms ($\approx 10^{-23}$ s). A result of this short lifetime is a broad width in the mass (or energy) measurement of that (unstable) excited baryon state (also known as a resonance) resembling a Breit-Wigner distribution having a width of at least $\approx$ 100 MeV. This also implies that the individual resonances contained in the excited baryon spectrum, must be not only broad but overlapping (Fig. 1.9). The broad and overlapping characteristics of these states make the determination of which resonances are contained in the excited baryon spectrum a very difficult task: gone are the days when one could look for peaks on an energy scale.

1.8 Modeling the Excited Baryon Spectrum

1.8.1 Constituent Quark Models

In the absence of a fully developed approach which is applicable to the non-perturbative region of QCD, phenomenological models using the confining potential of QCD are used to describe and predict the excited baryon spectrum, namely Constituent Quark Models (CQMs). The modeling of the hadron in this manner began in the 1960's with the baryon

being treated as an object with two independent oscillators, ρ (which links quark #1 and quark #2) and λ (which links the center-of-mass between quark #1 and quark #2 to quark #3) (Fig 1.10). When the behavior of the excited baryon is modeled, both of these oscillators are allowed to become excited and predictions of higher-energy states extracted. As the model evolved, so did its predictions and explanations. For example, in a paper published in 1975, de Rujula, Georgi, and Glashow recalculated the baryon spectrum according to their new model using a one-gluon-exchange (OGE) mediating the interaction between constituent quarks (the DGG model) and were able to extract new mass relations and explain the Δ-N mass splitting [21]. As the CQM Hamiltonian was refined, the model calculations and predictions of the masses of the the low-lying light hadrons more closely resembled that which was seen in experiment. In addition to this however, these new calculations predicted many more baryon resonances than have been observed experimentally. This issue is that which has been termed the *missing resonance problem*.

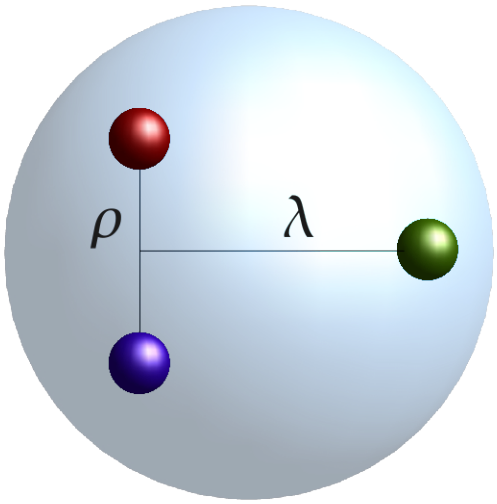

Figure 1.10: A picture of the baryon using the ρ and λ oscillators.

Constituent Quark Models and their predictions are used in the study of the physics that occur in the low/medium-energy regime of QCD where asymptotic freedom does not exist. In this region, the sea quarks and virtual gluons contained in the baryon play an unignorable role and must be accounted for (Figure 1.11). It is known that the baryon is comprised of three quarks called the *valence quarks* from which it derives its quantum numbers. These valence quarks, when possessing only their bare masses, are called *current quarks*. Therefore to account for this sea of quarks and gluons, the current quarks are then "dressed" with the masses/energies of the sea quarks and virtual gluons, making them *constituent quarks*. This is the reason why the constituent quark masses are higher than the masses/energies of the bare quarks (the bare masses of the valence quarks only account for $\approx 1\%$ of the hadron's total mass). By dressing the three current quarks in such a manner, the baryon can be treated as though it is comprised of just three quarks while not negating the effects and presence of the sea particles. While Constituent Quark Models treat the

baryon as a particle comprised of three constituent quarks (thus possessing three degrees of freedom), there are variations in the approaches used for different models. This variation is a result of how the models treat the short-range interactions between the three quarks within the hadron. Three prominent examples of how this short-range interaction is treated involve one-gluon exchange [2], Goldstone boson exchange [22], or instanton exchange [1]. An example of a CQM developed by U. Loring using instantons as the mediator for the short-range interactions can be seen in Figure 1.12 [1].

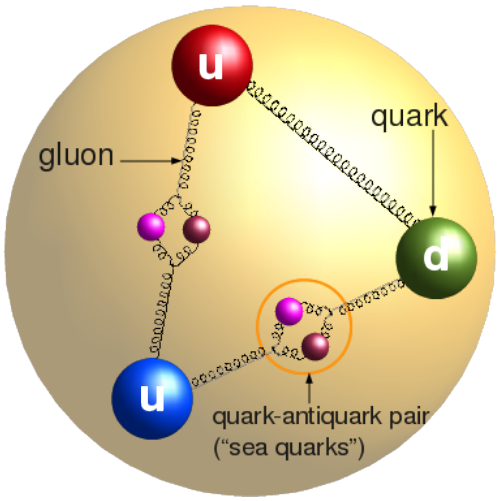

Figure 1.11: A diagram of the three-quark structure of the proton along with the presence of sea quarks and gluons. It is the mass of these sea quarks and gluons with which the current quarks are dressed, becoming constituent quarks.

1.8.2 Missing Resonance Problem

A well-known and long-standing issue in hadronic physics is the issue of missing resonances with much effort invested both from the theoretical and experimental communities. While CQMs treat the short-range interactions between quarks differently when producing their respective predicted spectras, they all share this issue due to their use of a confining potential. Constituent Quark Models have fairly accurately predicted the baryon resonances in the low-energy region (less than ≈ 1.8 GeV). Two good examples of this are the $S_{11}(1650)$ and the $P_{13}(1720)$ (Figure 1.12). However, as one moves to higher masses (> 1.8 GeV) in these models, there are many more states predicted to exist than have been experimentally verified. These states that have been predicted to exist by the models yet lack experimental evidence make up the collection of missing resonances. Some reasons why these states have not been seen experimentally lie in both the theoretical and experimental realms.

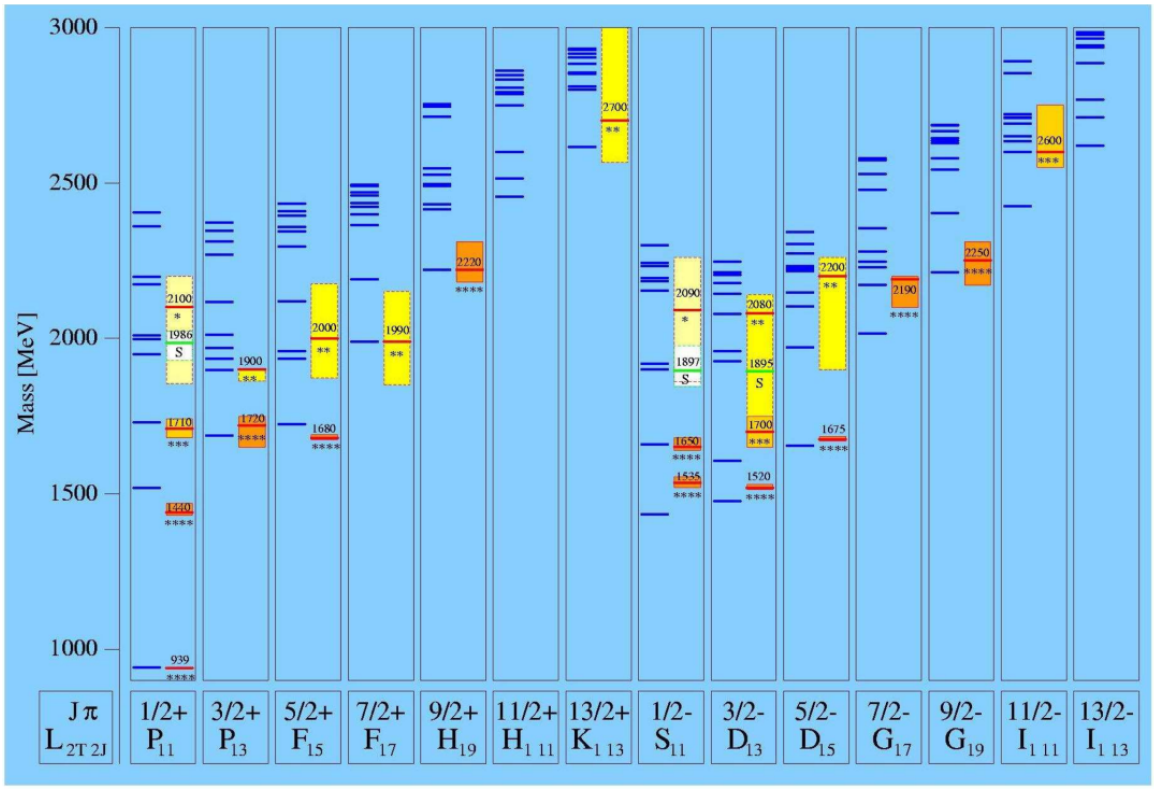

Figure 1.12: A Constituent Quark Model (CQM) developed at Bonn for the N* spectrum using instanton exchange for short-range interactions [1]. The blue lines here represent the resonances predicted to exist by Constituent Quark Model calculations while the blocks represent experimental (mass) measurements (with the height of the block corresponding to the uncertainty in the mass measurement). Many of the predicted resonances have no corresponding experimental measurement, especially in the high-mass region (>1.8 GeV). These resonances form the set of *missing resonances*. The ground state nucleon can be seen as the lowest lying state in the P_{11} column and the first radial excitation of the nucleon, the Roper resonance as the state in the P_{11} column with a mass of 1440 MeV. The number of *'s indicates the ranking of the state set by the PDG [23]. A 4-star state is well-established, a 3-star state has good evidence supporting its existence, 2-star states have some evidence, and a 1-star state has poor/little evidence.

Possible Theoretical Reason: Diquark Structure. As previously stated, the current quark models used to predict the excited baryon spectrum treat the baryons as particles comprised of three constituent quarks. This approach gives the baryon three quark degrees of freedom. This concept however could be flawed, requiring a modification of the models on a fundamental level. A possibility pertaining to the structure of the baryon is that there is not a three-quark structure but a quark-diquark structure. A diagram of the structure of the baryon using each of these two approaches can be seen in Figure 1.13. The hypothesis is that two of the three quarks inside the baryon have colors and spins that are antisymmetric and therefore are attracted to each other and form a bound state thereby "freezing" the ρ oscillator, only allowing excitations of the λ oscillator (Fig. 1.10) [24]. This quark-diquark structure approach simplifies the model calculations from dealing with the excited states of a three-body system to dealing with the excited states of a two-body system. Treating

it in such a fashion decreases the number of degrees of freedom and simplifies many other theoretical calculations and behaviors that must be accounted for (such as spin-orbit mass splitting between baryons) [25]. This quark-diquark structure also means that the excited baryon spectrum can be treated in a manner not unlike the excited meson spectrum. Calculations of the excited baryon spectrum using this approach result in a lower density of baryon states and remove many of the missing resonances from the spectrum. While this concept has not proven to be reality just yet or widely used, there is a possibility that this quark-diquark structure exists and, if it does, would account for the large number of missing resonances.

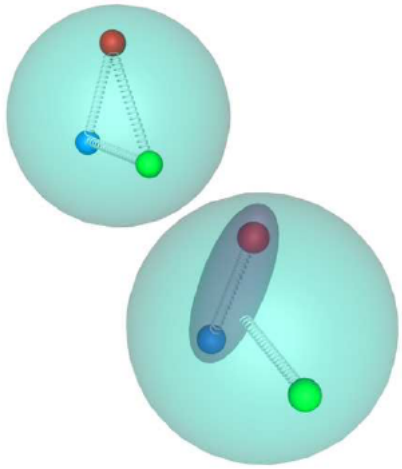

Figure 1.13: A diagram of the internal structure of the baryon using two approaches. The upper-left image demonstrates the internal structure of the baryon as described by using three constituent quarks (three-quark structure). The lower-right image demonstrates the internal structure of the baryon as described by using a quark-diquark structure.

Experimental Reasons. For decades now, almost from the beginning of the theory, experimentalists have performed experiments to study the excited baryon spectrum. While some of the resonances predicted by Constituent Quark Models have been seen experimentally (mass measurements of these resonances are fairly large in their uncertainties), many more of the predicted resonances have still not been seen (Fig 1.12). There exists a few reasons that possibly explain why these missing resonances are still missing in spite of all the efforts to see them [26]. The majority of the data collected (as well as subsequent analyses) regarding baryons overall and specifically, the missing resonance problem, involved pion or kaon production on the nucleon. As suggested by recent quark model calculations, πN scattering may not have led to a discovery of these resonance states as these states may couple strongly to photoproduction (γp) reactions [3]. Therefore the analysis of data from photoproduction experiments may be a better way to reveal these missing resonances.

With the above being said, there have been a collection of experiments and analyses that have utilized photoproduction on the nucleon with the ultimate goal of measuring the baryon spectrum and the resonances contained within (this is also the central motivation

behind the construction of the CLAS detector). So why is this issue still not resolved? The majority of the world photoproduction data involves energies that are fairly low (below $\approx$ 1.8 GeV). As seen in Figure 1.12, the majority of the missing resonances lie in the region above $\approx$ 1.8 GeV. The analysis of data involving these higher energies would reveal more of the baryon spectrum and hopefully, the existence or nonexistence of these missing resonances. Many of these analyses have also involved a channel with one final state meson, a quasi 2-body final state (such as $K^+\Lambda^0$, $K^+\Sigma^0$, Nπ, Nη) [27, 28, 29]. It has recently been indicated, however, that looking at a 3-body final states has great potential for revealing the high-mass missing resonances as they account for most of the cross section above $\approx$ 1 GeV (Fig. 1.14). These missing resonances are also predicted to decay into particles with high masses (excited intermediate states) rather than a final state characterized by a meson and a ground-state nucleon. Therefore the missing resonances may exist as part of a decay chain as an intermediate state leading to a final state with two mesons (for example: $\gamma p \rightarrow N^* \rightarrow \Delta^{++}\pi^- \rightarrow p\ \pi^+\pi^-$). The theoretical widths of these missing states have also been calculated to be at least 150 MeV. Calculations of the decays of these resonances into two-particle channels (like Nπ) result in very narrow particle widths. This indicates that the majority of the decays involve more than just a two-body final state.

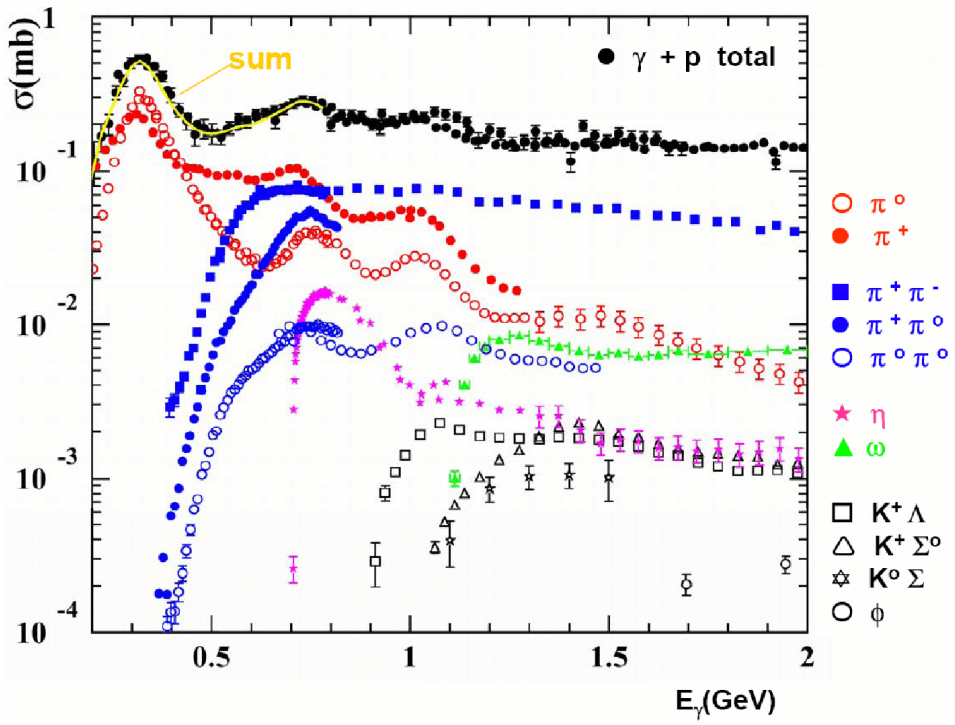

Figure 1.14: A collection of various cross sections for γp reactions. The final state $\pi^+\pi^-$ clearly dominates the total cross section (black line) starting around $E_\gamma \approx 1$ GeV.

1.9 Polarization Observables

Typically one can extract hints (although not trivial as this type of analysis is very difficult) regarding the presence (or absence) of resonance states from an examination of the cross section for a final state. As previously pointed out, the cross section for a $\gamma p \to p\,\pi^+\pi^-$ reaction dominates the collection of cross sections for γp reactions, as is seen in Figure 1.14. The cross section for a $p\ \pi^+\pi^-$ final state is clearly dominant at photons energies (E_γ) greater than ≈ 1 GeV. The shape of the $p\ \pi^+\pi^-$ cross section also demonstrates a difficulty that exists regarding the determination of the resonances contained within. The observed cross section is fairly flat, devoid of obvious structures (peaks) that would indicate the presence of resonance states. The lack of structure is an additional indication of the extent of the overlap of the resonances and rules out "peak hunting" to find resonance states. Therefore another method must be employed in order to unveil what is contained in this cross section.

Measurable quantities called *polarization observables* possess a high degree of sensitivity to the presence (or absence) of baryon resonances especially in the higher mass region (above ≈ 1.8 GeV) where these resonances are most entangled [4]. This makes polarization observables excellent probes for investigating hadronic processes, namely the investigation of the resonances contained (or not contained) in the excited baryon spectrum. It has been established that these resonances are both broad and overlapping and require that they be disentangled through some type of measurement. A measurement of the polarization observables can help to do just this. Model-dependent theoretical values of these polarization observables can be extracted from model calculations and compared to the experimentally measured values. Resonance contributions can then be explored by omitting or including them in model calculations. Figures 1.15 and 1.16 shows such a prediction for several polarization observables, their dependence on the inclusion or exclusion of certain resonances (namely the $P_{31}(1910)$ and $S_{31}(1900)$), and the sensitivity of the observables to particular kinematic variables.

When analyzing a final state containing pseudoscalar one meson and one ground state nucleon, one has access to 7 polarization observables:

$$\begin{aligned}\frac{d\sigma}{d\Omega} = (\frac{d\sigma}{d\Omega})_0 \{\ 1 &- \delta_l\ \mathbf{\Sigma}\ \cos(2\phi) \\ &+ \Lambda_x\ (\ -\delta_l\ \mathbf{H}\ \sin(2\phi)\ +\ \delta_\odot\ \mathbf{F}\ ) \\ &- \Lambda_y\ (\ -\mathbf{T}\ +\ \delta_l\ \mathbf{P}\ \cos(2\phi)\ ) \\ &- \Lambda_z\ (\ -\delta_l\ \mathbf{G}\ \sin(2\phi)\ +\ \delta_\odot\ \mathbf{E}\ )\}.\end{aligned} \tag{1.2}$$

where $\frac{d\sigma}{d\Omega}$ is the differential cross section. The variables δ_l and $\delta_\odot$ are the degree of polarization of the photon beam, be it linearly or circularly, respectively. The degree and direction of target polarization is represented by Λ_x, Λ_y, Λ_z; Λ_x and Λ_y for transverse polarization and Λ_z for longitudinal polarization. The quantities Σ, $\mathbf{H}$, $\mathbf{F}$, $\mathbf{T}$, $\mathbf{P}$, $\mathbf{G}$, $\mathbf{E}$ are the polarization observables obtainable from the analysis of a single-meson final state.

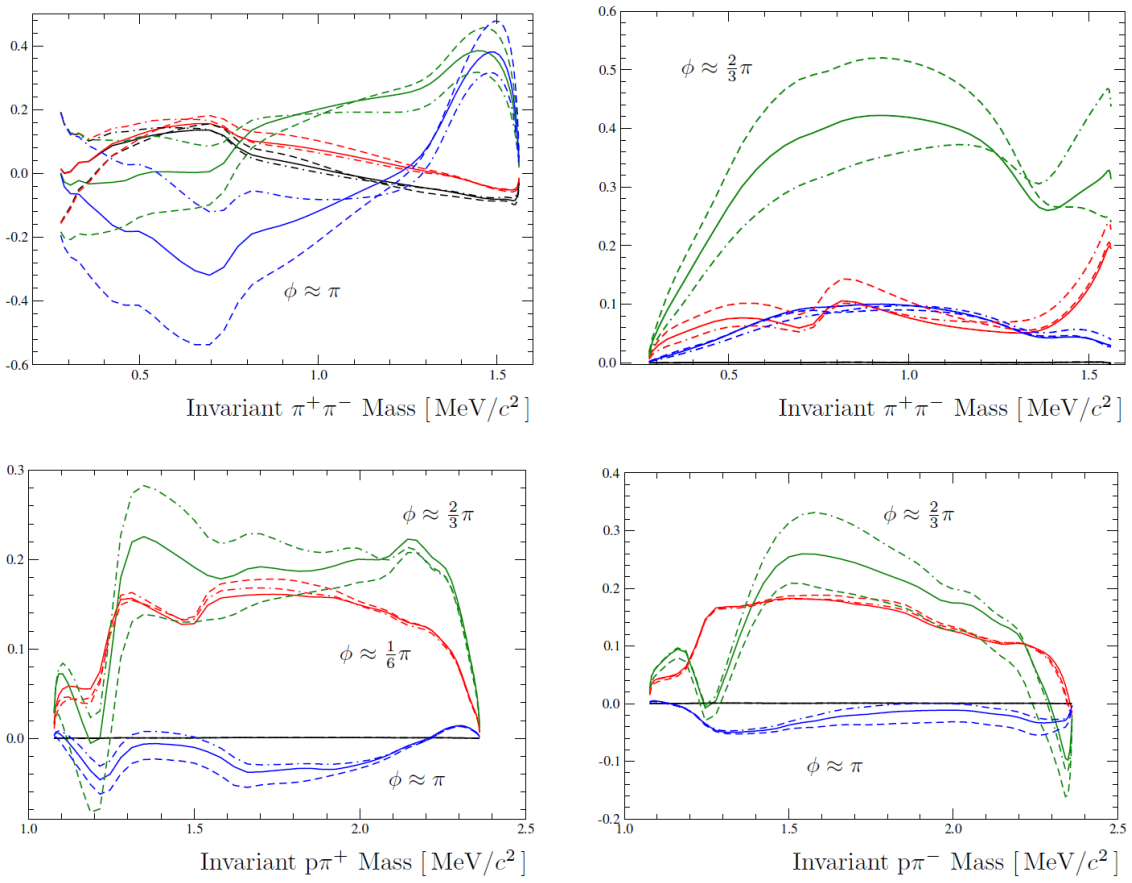

Figure 1.15: Model calculations by W. Roberts [30, 31] showing predicted values of the polarization observables $P_x^{\odot}$ and $P_y^{\odot}$ (two of the polarization observables which exist for a two meson final state for a circularly polarized beam incident on a transversely polarized target) as a function of invariant mass. The top row shows the observable $P_x^{\odot}$ (left) and $P_y^{\odot}$ versus $m_{\pi^+\pi^-}$. The bottom row shows predictions for the observable $P_y^{\odot}$ versus $m_{p\pi^+}$ (left) and $m_{p\pi^-}$ (right). The solid line represents a model calculation containing all resonances (the baryons considered here have a spin of 3/2 or less), the dashed curve represents a model calculation with the $S_{31}(1900)$ omitted and the dot-dash represents a model calculation with the $P_{31}(1910)$ resonance omitted. The black curve represents $\phi^* \approx 0$, red represents $\phi^* \approx \frac{\pi}{6}$, green represents $\phi^* \approx \frac{2\pi}{3}$, and blue represents $\phi^* \approx \pi$. Although these two observables are not measured in this work, the sensitivity of polarization observables is apparent.Here, the angle ϕ^* (for a $p\ \pi^+\pi^-$ final state) is defined as the angle between the decay plane (in which the two pions occur back-to-back) and the reaction plane and is measured with respect to one of the final state pions (see Fig. 1.17).

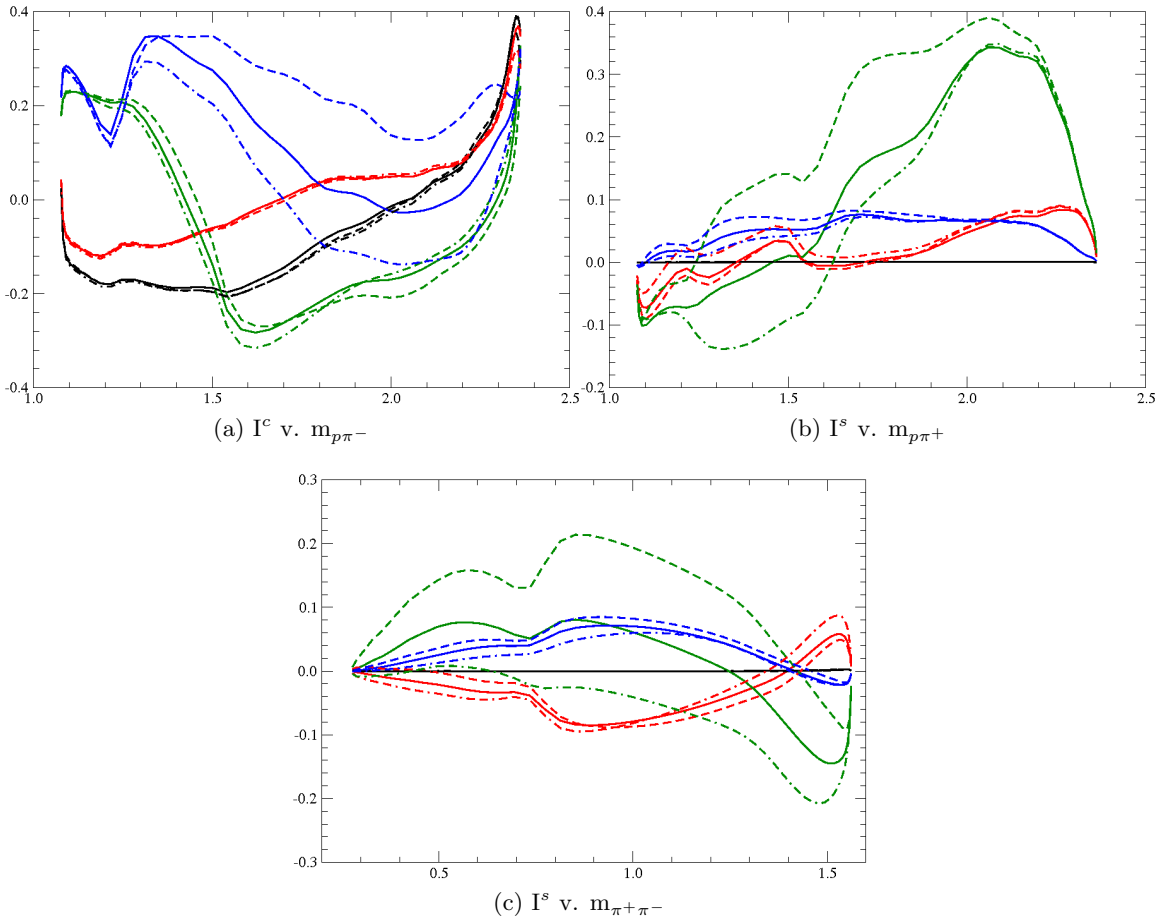

(a) I^c v. $m_{p\pi-}$

(b) I^s v. $m_{p\pi+}$

(c) I^s v. $m_{\pi+\pi-}$

Figure 1.16: Model calculations provided by Winston Roberts [30, 60] which show the predicted values of the polarization observables I^c v. $m_{p\pi-}$ (a), I^s v. $m_{p\pi+}$ (b) and I^s v. $m_{\pi+\pi-}$ (c) for $\gamma p \to p\ \pi^+\pi^-$ reactions. These predictions are shown for various values of ϕ^* with the inclusion or exclusion of certain resonances. The black curve represents $\phi^* \approx 0$, red represents $\phi^* \approx \frac{\pi}{6}$, green represents $\phi^* \approx \frac{2\pi}{3}$, and blue represents $\phi^* \approx \pi$. For each color, the solid line represents a full model calculation including all resonances (the baryons considered here have a spin of 3/2 or less), the dashed lines represent model calculations with the omission of the $S_{31}(1900)$ Δ^* resonance and the dot-dashed lines represent the omission of the $P_{31}(1910)$ Δ^* resonance. Here, the angle ϕ^* (for a $p\ \pi^+\pi^-$ final state) is defined as the angle between the decay plane (in which the two pions occur back-to-back) and the reaction plane and is measured with respect to one of the final state pions (see Fig. 1.17).

When formulated for the analysis of a channel containing two final state mesons, this final state equation picks up three additional terms. These additional terms arise from the increased number of independent kinematic variables needed to properly describe the kinematics of the reaction. These additional kinematic variables are needed not only to describe the orientations of the increased number of particles but also the decay plane which can be formed for every reaction in which the two final state pions occur back-to-back. These additional kinematic variables describe the orientation of the decay frame with respect to the production plane and are measured with respect to one final state pion. A

diagram displaying the kinematics of the $\gamma p \to p\,\pi^+\pi^-$ reactions can be seen in Figure 1.17. An in-depth discussion of these kinematics can be found in Chapter 4.

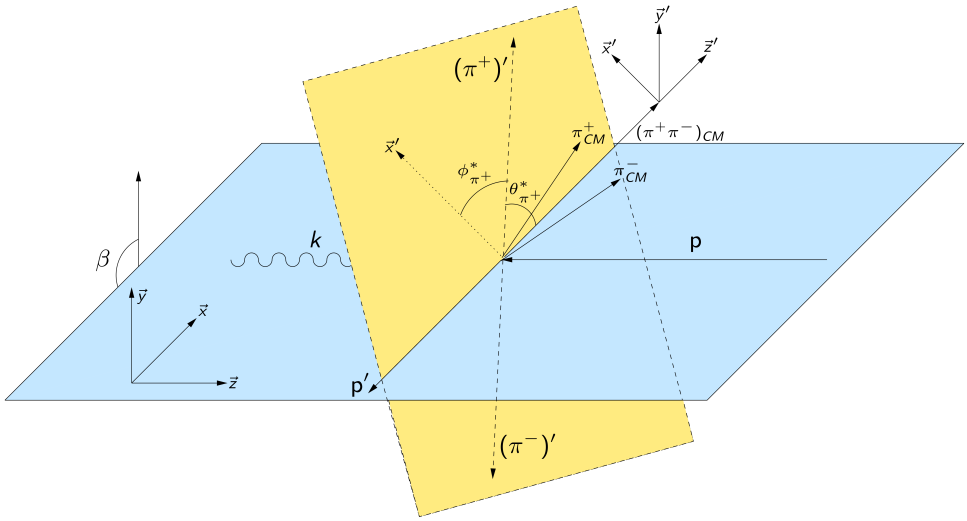

Figure 1.17: A diagram describing (one possible configuration of) the kinematics of $\vec{\gamma}p \to p\,\pi^+\pi^-$ reactions. The blue plane represents the center of mass (CM) production plane while the gold plane represents the decay plane (where the two pions are produced back-to-back). The angle $\phi^*_{\pi^+}$ is the angle between the $(\pi^+)'$ (the 4-vector of π^+ after a boost into the decay frame) and the $\vec{x}\,'$-axis (which lies in the production plane).

For the analysis of a single-meson final state one needs two independent kinematic variables. An analysis of a double-meson final state however, needs five. The reaction rate I for a $\gamma p \to p\,\pi^+\pi^-$ reaction can be written as [4]:

$$\begin{aligned} I = I_0 \{ & (1 + \vec{\Lambda_i} \cdot \vec{\mathbf{P}}) \\ & + \delta_\odot (\mathbf{I}^\odot + \vec{\Lambda_i} \cdot \vec{\mathbf{P}^\odot}) \\ & + \delta_l [\sin(2\beta) (\mathbf{I^s} + \vec{\Lambda_i} \cdot \vec{\mathbf{P^s}}) \\ & + \cos(2\beta) (\mathbf{I^c} + \vec{\Lambda_i} \cdot \vec{\mathbf{P^c}})] \}. \end{aligned} \tag{1.3}$$

Here I_0 is the unpolarized reaction rate. The quantity $\vec{\mathbf{P}}$ is a polarization asymmetry (or a measurable polarization observable) that arises from the polarization of the target material with the degree and direction of target polarization being denoted by $\vec{\Lambda_i}$ (where i denotes the three directions of polarization: x, y, z). The variables δ_l and $\delta_\odot$ again represent the degree of the polarization of the photon beam as well as the type of polarization. The variables $\mathbf{I}^\odot$, $\mathbf{I}^s$, $\mathbf{I}^c$ are also polarization observables with $\mathbf{I}^c$ being equivalent to Σ in the equation for a single-meson final state. The angle used in the arguments of the sine and cosine terms, β, is a combination of the ϕ_{lab} angle and the $\phi_{polarization}$ angle. This takes into account the angle of polarization possessed by the incident photon. In other words:

$$\beta = \phi_{lab} + \phi_{polarization}. \tag{1.4}$$

This two-meson final state equation (equation (1.3)) contains 15 polarization observables as opposed to the 7 seen in the single-meson final state equation (equation (1.2)). This increase in the number of polarization observables means an analysis of a two-meson final state provides inherently more access to the resonances contained in the excited baryon spectrum. This increased access is a combination of the high sensitivity of the polarization observables to resonance contributions/interference effects and the pure number of polarization observables that are at hand and measurable.

In order to reduce equation (1.3) to a form from which we can extract values for particular polarization observables, the conditions under which the data were collected may be applied to the final state equation. In the case of the run conditions under which the analyzed data were taken, the beam of photons was polarized linearly and the target material completely unpolarized. Inserting these run conditions into the two-meson final state equation (1.3) kills all terms with $\vec{\Lambda}_i$ (target polarization) and the term with $\delta_\odot$ (circular polarization of the photon beam). Therefore equation (1.3) reduces to:

$$I = I_0 \{ 1 + \delta_l [\mathbf{I^s} \sin(2\beta) + \mathbf{I^c} \cos(2\beta)] \}. \tag{1.5}$$

Here the number of observables present in equation (1.3) has been reduced from 15 to two. We now have access to the polarization observables $\mathbf{I}^s$ and $\mathbf{I}^c$, making a measurement of these observables possible. These measurements will serve to help shed light on the baryon resonances that contribute to the $p\ \pi^+\pi^-$ cross section in the energy range of this analysis (Figure 1.18).

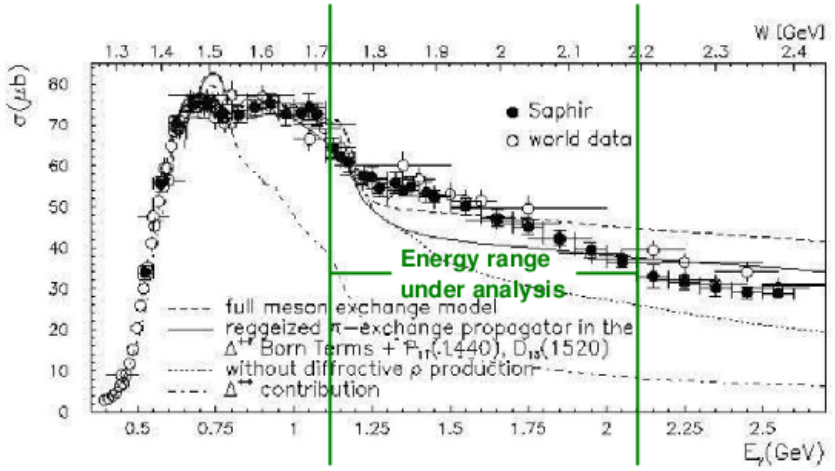

Figure 1.18: The cross section for the reaction $\gamma p \to p\ \pi^+\pi^-$. The photon energy range shown by the green lines corresponds to the (photon) energy range of this analysis.

1.10 Resonances of interest in $\vec{\gamma}p \to p\ \pi^+\pi^-$

The investigation of a double-pion final state in polarized photoproduction data taken on the proton has been predicted to be a promising method for the discovery of high-mass,

missing excited baryon states. Many of these missing states are predicted to decay back down to their ground state through a process involving decays into intermediate states with the emission of a meson. In fact, quark model predictions claim that there is a large coupling of some of these excited states to $\Delta\pi$ and $p\rho$ [3]. The large branching fractions of $\Delta \to p\pi$ (and therefore $\Delta\pi \to p\ \pi^+\pi^-$) as well as $\rho \to \pi^+\pi^-$ (and therefore $p\rho \to p\ \pi^+\pi^-$) [23] make the analysis of a $p\ \pi^+\pi^-$ final state a very viable way of detecting the existence of the missing resonances. This detection of the resonances occurs indirectly as the measured value of the polarization observables are dependent on which resonances were, or were not, produced.

But how can it be known that an analysis looking for the effects of these missing resonances is valid? The decay into a $p\ \pi^+\pi^-$ final state is not relegated to the high-mass, missing states alone. Many known resonances possess a strong coupling to the $p\ \pi^+\pi^-$ final state and an investigation of these states can serve as a check of the analysis (a good example of a known resonance being the $P_{11}(1440)$ Roper Resonance). In addition to this check, unresolved questions and discrepancies regarding these established states can be further investigated or investigated for the first time. A Partial Wave Analysis (PWA) using polarization observable measurements can carry out these investigations into both the known and poorly understood properties of the resonances contained in the excited baryon spectrum as well as which resonances are produced.

1.10.1 $P_{11}(1440)$ Roper Resonance, $D_{13}(1520)$, and $P_{33}(1600)$

The first radial excitation contained in the N* spectrum, the well-known $P_{11}(1440)$ Roper Resonance, is considered a well established state (for instance it is given a 4-star rating by the Particle Data Group). Quark model predictions regarding its mass however, show it having a higher mass than the first negative parity orbital excitation: the $S_{11}(1535)$ (Fig. 1.12). This contradicts experimental measurements which show the mass of the $P_{11}(1440)$ as being ≈ 100 MeV lower than the $S_{11}(1535)$. The answer to why this is can be linked to how the Roper is treated in model calculations. In the majority of the model calculations, the Roper is treated as a bound state with an indefinite lifespan. To account for the discrepancy between model predictions and experimental findings, it has been proposed that the Roper (instead of being a state originating from a direct interaction between an incident pion and the nucleon) is actually a dynamically-generated resonance [32] or perhaps a state with a strong gluonic component [33] (although recent analyses have indicated that the hypothesis of the Roper having a strong gluonic component is incorrect [34]). A further analysis of the measurements of the highly sensitive polarization observables coming from polarized photoproduction data on the proton could serve to clear up some of this controversy as well as reveal aspects regarding the structure of the Roper previously unavailable.

In spite of being considered an established state, the actual contribution of the $D_{13}(1520)$ (Fig. 1.12) to the total cross section for $\gamma p \to p\ \pi^+\pi^-$ is not a resolved issue. The main contributor (resonance) to the cross section for this reaction varies depending on what models are used. In the Valencia model, the decay of the $D_{13}(1520)$ into $\Delta\pi$ dominates the cross section while the Laget model claims that the dominate contribution to the cross section comes from the $P_{11}(1440)$ resonance decaying to a $p\sigma$ final state. Although this issue has

not been completely resolved, the likelihood of the Laget model being correct has been made slim by recent analyses [35, 36]. Since both models lead to reasonable descriptions of the cross section, a clear experimental determination of which model is correct is needed. Past experimental investigations into this matter, however, have failed to reach a clear conclusion as these efforts used unpolarized data. By utilizing the constraint provided by polarization through the analysis of polarized photoproduction data and measuring polarization observables, the contribution of the $P_{11}(1440)$ Roper and the $D_{13}(1520)$ to the cross section for $\gamma p \to p\,\pi^+\pi^-$ can be better understood.

Being the first radial excitation in the Δ spectrum (Fig 1.19), the $P_{33}(1600)$ resonance is often referred to as the *Roper of the* Δ*'s*. Although analogous to the Roper resonance, the $P_{33}(1600)$ differs in the amount and quality of evidence supporting its existence. The Particle Data Group (PDG) [23] has assigned a 3-star classification to this state as opposed to the Roper's 4-star rating. Furthermore, the uncertainty of its mass measurement is much larger than that of the $P_{11}(1440)$. The accruement of more data regarding the mass and properties of the $P_{33}(1600)$ resonance would lead to a better understanding of this Roper of the Δ's.

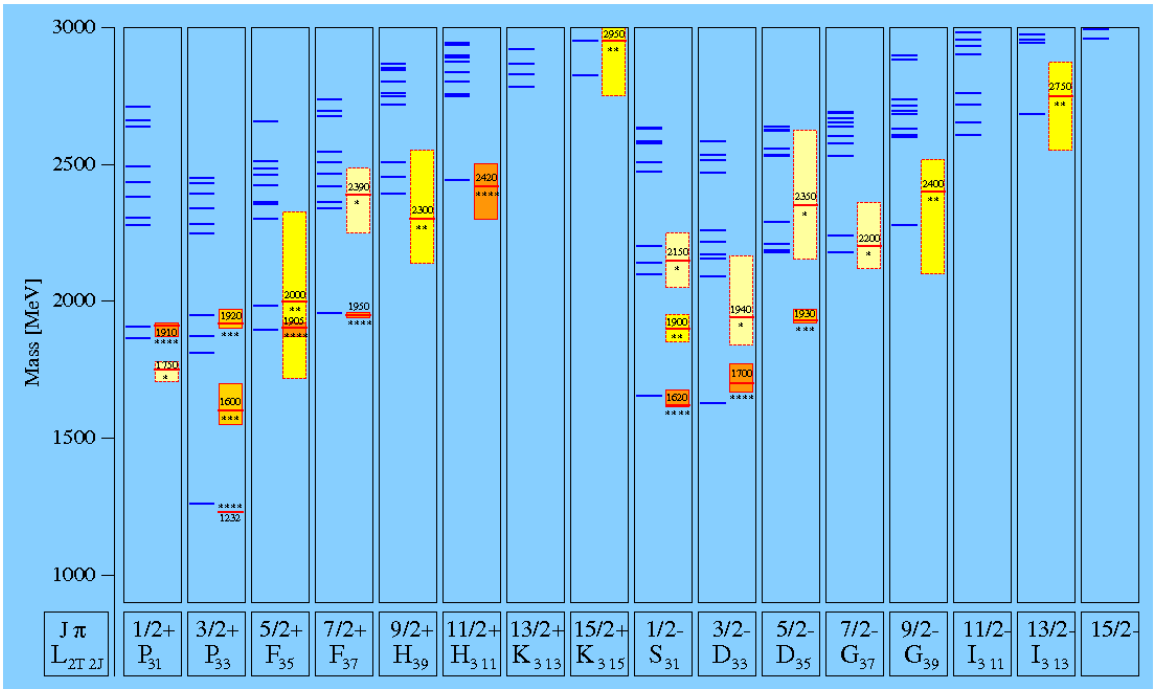

Figure 1.19: A Constituent Quark Model (CQM) developed at Bonn for the Δ^* spectrum using instanton exchange for short-range interactions [1].

1.10.2 $P_{13}(1720)$

The analysis of unpolarized data has revealed the contributions of the $F_{15}(1680)$, $D_{13}(1700)$, $D_{33}(1700)$, and $P_{13}(1720)$ resonances to the total cross section. Specific aspects of their contributions however, such as their isobar contributions, are still not understood (here, isobar

refers to particles belonging to the same isospin multiplet). For example, the properties of the $P_{13}(1720)$, as reported by the CLAS Collaboration, differs from its properties listed by the PDG [37]. Reports from the CLAS Collaboration show the $P_{13}(1720)$ to possess an unusually large width. This large width may be a hint that there is not one but two P_{13} resonance lying close together or a misunderstanding of the $P_{13}(1720)$ as quark models predict only one P_{13} resonance below 1.9 GeV/c^2 (Fig. 1.12). Through an analysis of polarized data, specifically the measurement of polarization observables, these resonances, their properties, and the issue regarding the $P_{13}(1720)$ resonance can be further investigated.

1.10.3 High-mass resonances

The high-mass region (> 1.8 GeV/c^2) of the excited baryon spectrum predicted by CQMs is the realm of the missing resonances. There are several (previously discussed) possible reasons as to why these states have not been seen experimentally. The issue of how the CQMs treat the quark-structure of the baryon (three quark degrees of freedom as opposed to a quark-diquark structure) can be investigated by looking for effects (presence) of the $P_{11}(2100)$, $P_{13}(1900)$, $F_{15}(2000)$, and $F_{17}(1990)$ N* resonances. These four resonances represent part of the second orbital excitation (L=2) of the N* spectrum. More importantly, these resonances form the first set of states that cannot be reproduced using a quark-diquark interpretation of the baryon (where two quarks are frozen together in a ground state diquark) as both oscillators must be excited to produce such resonances (see lower right-hand diagram in Fig 1.13). Therefore if the structure of the baryon is not that of a quark-diquark system then these resonances should not be observed. However, evidence supporting the existence of the $P_{13}(1900)$ has recently been seen in CLAS data [38]. Should the existence of the $P_{13}(1900)$ be verified, the quark-diquark hypothesis would find itself in a quasi-mortally wounded state. Through the measurement of polarization observables, a further investigation into the presence or absence of theses states will serve to further test the quark-diquark hypothesis of the baryon.

In the high-mass region of the Δ^* spectrum predicted by CQMs there lies a group of three negative-parity resonances around 1.9 GeV/c^2 which present a problem not unlike the problem presented by the mass measurements of the $P_{11}(1440)$ Roper and the $P_{33}(1600)$ "Δ Roper". These resonances, $S_{31}(1900)$, $D_{33}(1940)$, and $D_{35}(1930)$, are predicted by quark model calculations to have much higher masses than have been experimentally observed. Furthermore, data regarding these three states is rather sparse as the $S_{31}(1900)$ is a 2-star state, the $D_{33}(1940)$ a 1-star state, and the $D_{35}(1930)$ a 3-star state (as assigned by the PDG). Verifying the existence of these states as well as their previously measured properties is important for refining quark model calculations.

Polarization observables, due to their high degree of sensitivity to resonance contributions, are excellent tools for unambiguously determining what resonances do or do not contribute to both the N* and Δ^* spectrums. A further analysis of the measurements of these quantities allows for a determination of the helicity ratios of the resonances and for the measurement of properties such as masses and widths with a high degree of sensitivity. This makes the measurement of polarization observables a powerful tool for studying the excited spectrum of these fundamental particles.

1.11 Previous Measurements of Polarization Observables

This quest to measure polarization observables with the goal of removing the veil from the excited baryon spectrum is not a new one. In a 2005 paper, S. Strauch *et al.* [CLAS] presented measurements for the polarization observable $I^{\odot}$ for $\vec{\gamma}p \rightarrow p\,\pi^+\pi^-$ reactions using polarized photoproduction data collected at CLAS [39]. In this work, he compared his results to a variety of model predictions and demonstrated the sensitivity of the observables to the presence of resonances. Through the comparison of his measurements with model calculations, it was concluded that further refinement of these symmetric quark models is needed in order to provide an adequate description of his presented measurements of $I^{\odot}$.

In addition to the $I^{\odot}$ measurement at CLAS, the polarization observable I^c (Σ) has been extracted in several analyses by the GRAAL collaboration. These measurements were conducted for double-meson states involving photoproduction on the nucleon resulting in a final state with two neutral pions ($\vec{\gamma}N \rightarrow N\pi^0\pi^0$) [40, 41]. The observable I^s (along with a measurement of I^c) has also been measured at CBELSA/TAPS for $\vec{\gamma}p \rightarrow p\pi^0\eta$ [42]. However, measurements of not only the polarization observable I^c but also I^s for a double-charged-meson final state, namely for $\vec{\gamma}p \rightarrow p\,\pi^+\pi^-$ reactions, is non-existent in the world data set. Therefore this work presents the first measurement of such quantities, making it difficult to determine the manner in which the measurements should be presented. Many of the previous measurements of I^c (Σ) as well as I^s have suffered from the limited amount of statistics available in the data set under analysis. The available amount of statistics is further reduced by the presence of the 5 independent kinematic variables needed to fully describe the kinematics of the reaction(s). In most of the previous analyses, binning in all five of the kinematic variables reduces the statistics of the ϕ-distributions to the point where the fits of the ϕ-distributions cannot be used to make reliable measurements. Therefore many analyses have utilized techniques to reduce the number of kinematic variables, such as reducing a three-body final state to a two-body final state, or simply integrated over them. This analysis, while encountering the same problem to a lesser degree (a reduction of statistics when binning in all kinematic variables), benefited from the high amount of $p\,\pi^+\pi^-$ events contained in the data set under analysis (g8b). The amount of $p\,\pi^+\pi^-$ events contained in the data allow for a high-statistics extraction of the polarization observables even when binning in all five kinematic variables (although in the presented results, two kinematic variables are integrated over). However the combination of there being no established precedent for presenting/displaying I^s and I^c for $p\,\pi^+\pi^-$ final states along with a possible binning in all kinematic variables makes the quest for and the presentation of such measurements a difficult and complicated task.

CHAPTER 2

EXPERIMENTAL APPARATUS AND TECHNIQUES

The facility where the data used for this analysis were collected is the Thomas Jefferson National Accelerator Facility (TJNAF), also known as Jefferson Lab (JLab) in Newport News, Virginia. Jefferson Lab is a National Lab funded by the Department of Energy (DoE) and is currently home to three experimental halls, Hall A, Hall B, and Hall C. The Continuous Electron Beam Accelerator Facility (CEBAF), also located on-site at Jefferson Lab, supplies these three experimental halls with a beam of accelerated electrons. In addition to the experimental halls and the accelerator, Jefferson Lab houses the Free-Electron Laser (FEL) facility, one of the world's most advanced lasers, as well as several research and manufacturing facilities. An aerial view of Jefferson Lab can be seen in Figure 2.1.

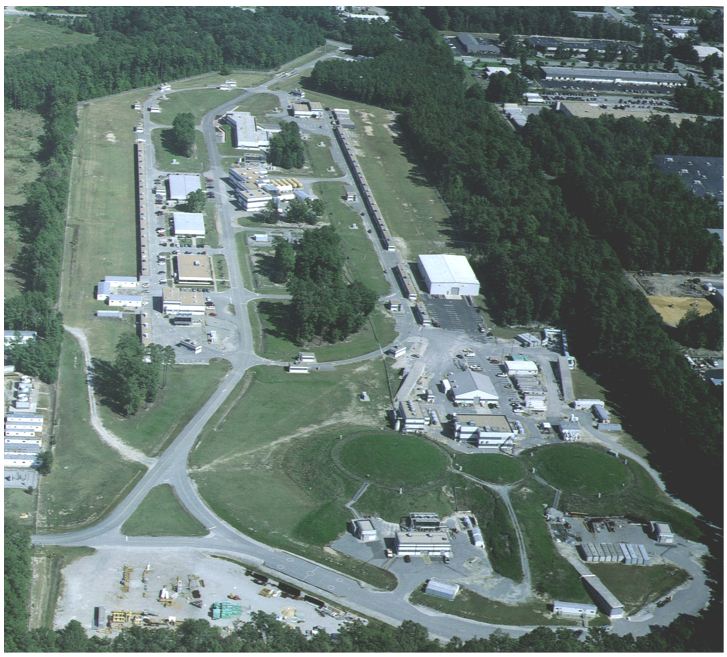

Figure 2.1: An aerial view of the accelerator site at Jefferson Lab. The racetrack shape is the CEBAF accelerator and the three mounds at the bottom of the photograph are the three experimental halls: (left to right) Hall A, Hall B, Hall C.

2.1 The g8b Data Set

The data set used for this analysis was taken between July 20^{th} and September 1^{st}, 2005 as part of the g8b run period in Hall B. The name "g8b" denotes a few properties of the run period. The "g" indicates that it was a photoproduction experiment (photons were incident on the target material), the "8" indicates that it is the eighth approved photoproduction experiment, and the "b" means that it was the second iteration of the "g8" experiment. The main detector used to study the physics events was the CEBAF Large Acceptance Spectrometer (CLAS) [43]. This detector is optimized to study reactions involving multiple charged particles and has nearly a 4π solid angle coverage. The CEBAF accelerator supplied Hall B with unpolarized, accelerated electrons with an energy of 4.551 GeV which were then used to produce a beam of polarized and tagged photons. The photons were linearly polarized via coherent bremsstrahlung radiation through the use of a diamond radiator (goniometer) and tagged using the Hall B Tagger. The g8b run period utilized photoproduction on the proton with the target material being liquid hydrogen (LH_2) cooled using liquid helium (LHe_2). These pieces of hardware along with the Hall B Data Acquisition System (DAQ) led to an impressive data set $\approx$ 30 TB in size and containing 10.7 billion triggers. This chapter will involve the description of the CEBAF accelerator, the CLAS detector, the Hall B Tagger, the goniometer used to produce polarized photons, and other experimental apparatuses used during the g8b run period.

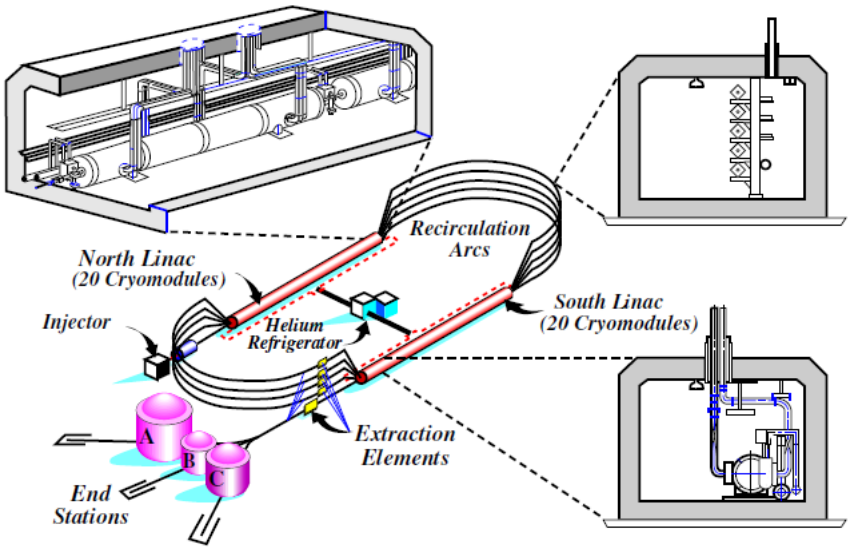

Figure 2.2: A broad-view schematic of the CEBAF accelerator showing the injector, circulating arcs, LINACs, and experimental halls.

2.2 The CEBAF Accelerator

The Continuous Electron Beam Accelerator Facility located at Jefferson Lab is an electron accelerator that is capable of delivering a high-quality beam to all three experimental halls simultaneously, even when the halls have different beam requirements. The accelerator has a racetrack shape, consists of an injector, 9 circulating arcs (4 at one end, 5 at the other), 2 linear accelerators (LINACs), 2,200 magnets of 58 varieties and is 1.4 km in circumference (Figure 2.2). The accelerator's two LINACs run anti-parallel to each other and are able to accelerate the electrons such that they gain ≈ 1.2 GeV for every trip they take around the accelerator. Using these, the CEBAF accelerator is able to deliver a high luminosity, continuous wave beam in ≈ 2 ns bunches. Components that make up this "world's most powerful microscope for studying the nucleus of the atom" [44] will be discussed in the following subsections.

2.2.1 Injector

Electrons accelerated by CEBAF first enter the machine via the Injector. Here, three pulsed lasers illuminate a Gallium Arsenide (GaAs) photocathode. These three lasers, one each for the experimental halls (A, B, and C), are independent diode lasers that are synchronized and combined to strike the GaAs disk at the third subharmonic (499 MHz) of the accelerating cavity frequency (1497 MHz) [45]. By using this three-laser setup, all three halls can be provided with electrons according to their individual requirements (requirements such as beam current and polarization) and all simultaneously receive electrons in 2 ns "buckets". Each one of these beam buckets can have different properties than the one preceding and following it. The electrons produced in the injector also have the potential to be longitudinally polarized with the degree of polarization reaching up to 75%. This is accomplished by circularly polarizing the light from the laser through the use of two Pockel cells (used such that one is a quarter-wave plate and the other a half-wave plate). These electrons are then accelerated by the injector LINAC to ≈ 67 MeV. The injector system then uses an optical chopper to cleanly separate the (2 ns) bunches prior to injecting them into the (North) LINAC.

2.2.2 CEBAF Linear Accelerators (LINACS)

Once the electrons leave the injector, they enter the North LINAC, one of two LINACS used by the CEBAF accelerator. These LINACS each contain 168 Niobium RF cavities which are made superconducting by cooling them to ≈ 2 K and are located at each "straight away" portion of the racetrack-shaped beam line. This cooling occurs via immersion in liquid Helium (LHe). Because the cavities are superconducting at this temperature, there is no heating of the cavities and therefore much less RF power is needed for operation (1/3 of the power required if the cavities were not superconducting) [44]. This also means that the accelerator can operate with a 100% duty cycle (accelerator can operate continuously). A typical cavity can be seen in Figure 2.3.

To accelerate the electrons in the RF cavity, a standing electromagnetic wave is produced in phase with the bundles of electrons. This standing wave produces a charge gradient which serves as the source of the acceleration by maintaining an area of negative field behind

the electrons and a positive field area in front (Figure 2.4). With this method and the current hardware used, each LINAC is able to accelerate the electrons by ≈ 500 MeV per pass with a maximum of 5 passes. This means that the current maximum energy of the electrons coming from CEBAF is ≈ 5.7 GeV with current repairs and tune-ups attempting to increase the maximum energy to its original limit of 6 GeV. In the works for the CEBAF is the near-future upgrade that would increase the maximum energy of the accelerator to ≈ 12 GeV.

Figure 2.3: Two of the superconducting RF cavities used at CEBAF. These cavities are immersed in LHe with the elliptical cavities being perpendicular to the beamline.

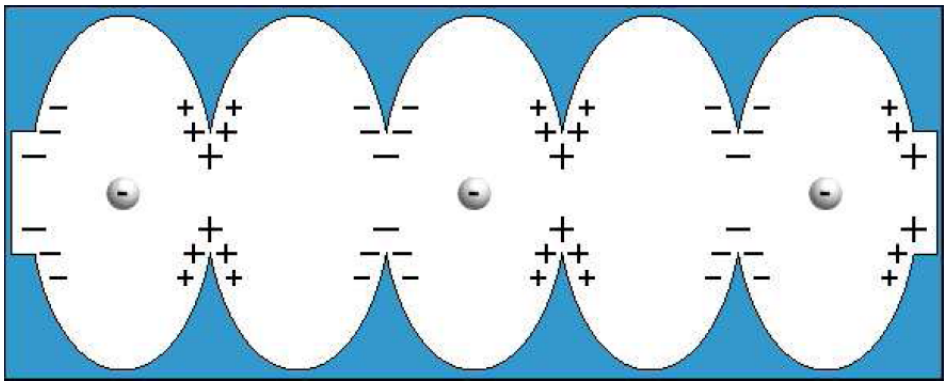

Figure 2.4: A diagram of an RF cavity during operation. The charge gradient produced makes it such that the electrons are always being accelerated.

2.2.3 Recirculation Arcs

In order to accelerate the electrons without the use of a large number of accelerator cavities, recirculation arcs are used so that the electrons can loop around the accelerator, being boosted by the LINACs with every pass. At each end of the accelerator, a series of dipole magnets are arranged in an arc in order to bend the beam 180° up to nine times (the recirculation arcs can be seen in Fig. 2.2). Electrons in the accelerator may differ in their energies (depending on how many passes they have made through the accelerator) but all

must be bent around in an arc of the same radius. To do this, the electron beam is split into a maximum of five different arcs, each one for a different pass number. Each one of these sub-beams uses dipole magnets of different strengths (higher strength for more energetic electrons). The electrons are then bent around the 180° arc before being recombined into a single beam and entering the next LINAC (a picture of these magnets and the different paths of the electrons can be seen in Fig. 2.5). The experimental halls can then choose to extract the beam after any number of passes (≤ 5) with the extraction occurring via a RF separator.

Figure 2.5: A picture of the eastern recirculation arc used at CEBAF. The yellow structures are the electromagnets used to steer the electron beam through the arc. The four different paths the electrons may take in the eastern arc are also visible.

2.3 Experimental Hall B

Of the three experimental halls located at Jefferson Lab, Hall B is the smallest in size. It does, however, house many unique tools along with the largest detector located at JLab. The general pieces of hardware used in Hall B and g8b-specific hardware will be discussed in this section.

2.3.1 Photon Tagger

Experiments in Hall B benefit from having the option of using either the electron beam from the accelerator or a tagged photon beam produced by the Hall B Tagger. This tagger has the capability to tag photons with energies ranging from 20% to 95% of the incident electron beam energy. Once the electrons enter the hall from the CEBAF accelerator, they interact with the radiator and scatter off, producing photons via bremsstrahlung radiation that remain in the beamline. The next major component, moving down the beamline, is the Tagger Magnet which is a C-shaped magnet with an open-yoke design capable of producing a magnetic field up to 1.75 T [46]. The purpose of the Tagger Magnet is to bend all electrons, both the scattered (those that did radiate a photon) and unscattered (those that did not scatter but passed right through the radiator), out of the beamline and

through the E- and T-counter planes which are used to determine the energy and timing of the produced photon. Unscattered electrons are bent out of the beamline and directly into the Tagger's beam dump, bypassing the E- and T-counters. A diagram of the Tagger hodoscope can be seen in Figure 2.6.

E-Counters. The E-counter plane is aligned with the optical focal point of the tagger magnet and is made of 384 plastic scintillators 20 cm long and 4 mm thick with widths varying from 6 to 18 mm (the variance in the widths ensures that the same momentum range is covered by each scintillator) [46]. These scintillators are arranged in an overlapping manner with one scintillator covering 1/3 of its neighbor's width therefore creating 767 separate energy channels (resulting in an energy resolution of 0.001 $\times$ (energy of incident electron)). The scattered electrons are bent through this plane and the position of the corresponding scintillator hit allows for the determination of the scattered electron's momentum/energy. Since the energy of the electron as it left the accelerator is known (E_0) and the energy of the scattered electron is measured (E_e), this leads to a determination of the energy of the radiated photon (E_γ):

$$E_\gamma = E_0 - E_e. \tag{2.1}$$

T-Counters. The determination of the time at which a photon arrived at the target is crucial to any analysis involving photoproduction. A timing resolution of 300 ps or better is needed to associate the measured time of an electron with the corresponding electron bunch and therefore for a determination of the photon time at the target center [46]. This precise time measurement is provided by the T-counter plane with a resolution of $\approx$ 100 ps [43]. This detector plane is positioned parallel to the E-counter plane and consists of 61 scintillator counters, 2 cm thick, which vary in length from 20 cm at the high electron momentum end to 9 cm at the low-momentum end [46].

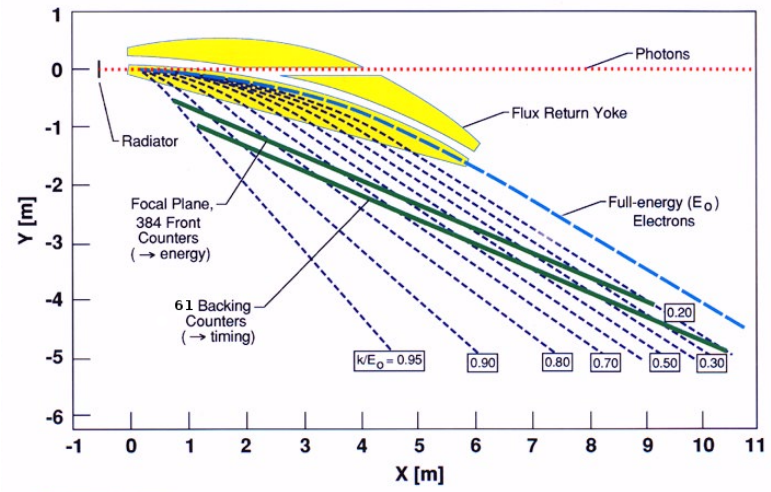

Figure 2.6: A diagram of the Tagger magnet, E- and T-counters used for tagging photons in Hall B with both an energy and times stamp. This drawing also shows the shape of the magnet pole, the photon path through the magnet yoke, and the relative locations of the hodoscope E- and T-planes. The dotted lines traversing the detectors are examples of electron trajectories and are labeled according to the fraction of the incident energy that was transferred to the photon.

2.3.2 Coherent Bremsstrahlung

In addition to being able to produce a beam of tagged photons, the Hall B Tagging Facility can also polarize these photons. Linearly polarized photons are produced via coherent bremsstrahlung with the electrons interacting with a well-oriented diamond radiator. When linearly polarizing these photons, the majority of the highly polarized photons reside in a 200 MeV wide window, the leading edge of which is called the *coherent edge* of the photon spectrum (the portion of the energy spectrum possessing a highly negative slope). The position of this coherent edge is determined by the orientation of the lattice structure of the diamond crystal and can therefore be precisely controlled. This means that linearly polarized photons can be produced at any energy for which the tagger can produce photons. One defining characteristic of the g8b run period is the use of these linearly polarized photons with the degree of polarization of the photons surpassing an impressive 90%. The major parts of the experimental setup used to produce these linearly polarized photons can be seen in Figure 2.7.

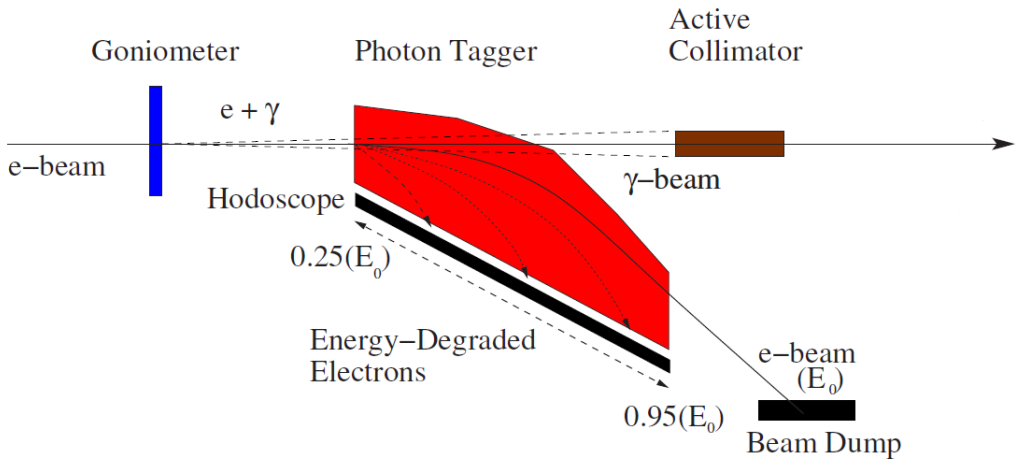

Figure 2.7: Schematic of tagger setup for the production of linearly polarized photons as used during the g8b experiment. The goniometer and active collimator will be discussed in later sections.

Radiators. The process of creating photons via bremsstrahlung radiation in Hall B involves the use of a radiator. In this process, the incoming electrons interact with the electromagnetic field of the nuclei of the radiator material. When the electrons encounter this field, they feel a braking force and radiate a photon with the same trajectory the electron(s) had before they interacted with the radiator (along the beamline). The use of an amorphous radiator such as the Gold/Carbon (Au/C) foil used in Hall B will result in a beam of photons with an energy spectrum which exhibits a smooth distribution with the form of $1/E_\gamma$ and is unpolarized. To both produce linearly polarized photons and produce these photons at certain coherent edge energies, the g8b run period used a well-oriented diamond radiator.

Oriented Diamond Radiator. For certain orientations, the photon beam produced using a diamond radiator shows strong linear polarization [47]. This behavior is a result of the response from the well-ordered structure of the crystal lattice found in diamond as incident electrons scatter off of it. The spectrum produced by such a process contains two main contributions, coherent and incoherent background. The incoherent contribution arises from the constant lattice vibrations occurring in the crystal structure and is a smooth function of E_{gamma} $(\frac{1}{E_\gamma})$ in the high-energy region where

$$E_0 \gg mc^2, \tag{2.2}$$

where E_0 is the energy of the incoming electron and m the electron rest mass. Also in this high-energy region, the energies of the final particles, the electron (E) and photon (k) are assumed to be larger than the rest energy of the electron:

$$E, k > mc^2. \tag{2.3}$$

The coherent contribution is where the highly polarized photons lie. This enhancement over the incoherent background shows a structure that is highly peaked at the lower end of the spectrum but decreases in enhancement towards the higher energies of the emission spectrum (as k approaches E_0). The size and shape of this enhancement peak is affected by the crystal structure while the degree of linear polarization of the photons in the peak is determined by the orientation of the diamond crystal [47]. An enhancement plot showing the energy distribution of polarized photons for two linear polarization settings can be seen in Figure 2.8.

The thickness of the diamond radiator used in g8b was chosen with concern lying in the angle at which the electrons diverge in the crystal structure. This angle needs to be smaller than the *natural emission angle* (θ_γ) [47]:

$$\theta_\gamma = \frac{mc^2}{E_0}. \tag{2.4}$$

This divergence of the electron beam within the crystal arises from and is affected by multiple scattering effects, defects in the crystal lattice, and the divergence of the incident electron beam. The angle with which the electron beam diverges in the crystal is important as it also affects the position of the coherent edge peak and its broadness therefore affecting the degree of polarization of the photons in the peak. From multiple scattering, this spacial divergence can be written as [48]:

$$\theta_{e^-} = \frac{19.2}{E_0}\sqrt{t} \times (1 + 0.038ln(t)), \tag{2.5}$$

where t is the thickness of the radiator material (diamond). To remove the dependence on the incident electron beam, one can then use the relation from equation (2.4), giving

$$\frac{\theta_{e^-}}{\theta_\gamma} = \frac{19.2}{mc^2}\sqrt{t} \ \times \ (1 + 0.038ln(t)). \tag{2.6}$$

From here, the proper radiator thickness can be determined such that the divergence angle is minimized. For the g8b run period it was determined that a diamond radiator

40 μm thick ($\approx 3.6 \times 10^4$ radiation lengths) would be ideal. The diamond radiator used during g8b was 50 μm thick and was a born out of a compromise between what was ideal and what was available.

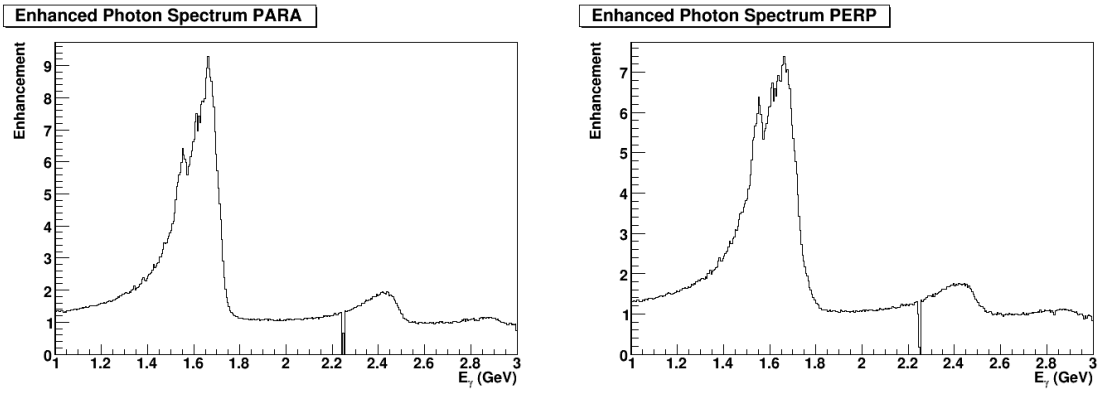

(a) E_γ Enhancement PARA (b) E_γ Enhancement PERP

Figure 2.8: An enhancement plot showing the energy distribution of polarized photons for the two linear polarization settings using g8b data from the 1.7 GeV coherent edge. This enhancement plot was produced by dividing the E_γ distribution for photons produced using a diamond radiator by the E_γ distribution for photons produced using an amorphous radiator (using runs #048544, #048602, and #048641). This division removes the $\frac{1}{E_\gamma}$ behavior which is characteristic to unpolarized photons (photons produced from unpolarized electrons interacting with an amorphous radiator). The small peaks at energies higher than the coherent edge (> 1.7 GeV) represent photon production off of other geometrically equivalent crystal planes in the radiator. The sharp dip seen in both (a) and (b) at $E_\gamma \approx 2.25$ GeV is due to a dead channel in the E-plane of the tagger hodoscope.

Goniometer. As described above, the proper orientation of the diamond radiator is paramount when producing a beam of photons possessing a high degree of linear polarization. To achieve this proper orientation, the g8b goniometer (seen in Fig 2.9) was used throughout the run period to position and hold both the diamond radiator and the amorphous carbon radiator. This goniometer was developed by George Washington University (GWU) and has the ability of orienting the diamond radiator (or another radiator) with an angular precision better than 10 μrad through three axes [49]. The various radiators used were contained in the *target ladder* located in the center of the goniometer. The available degrees of freedom of the goniometer and the target ladder can be seen in Figure 2.10.

Active Collimator. To further improve the polarized photon beam by reducing the contribution from the incoherent background and increasing the overall degree of polarization before it interacts with the target, a collimator can be used [47]. This is due to the coherent photons preferring the forward direction according to the relation seen in equation (2.4) and the incoherent having no angular preference (the incoherent photons have an angular distribution that is nearly independent of the electron energy). The collimator used in g8b was located ≈ 22.9 m downstream of the goniometer and was composed of 13 nickel diskettes, each with an outer diameter of 50 mm and a thickness of 15 mm and each with a 2 mm hole in the middle, all placed in a sheath made of stainless steel. Sandwiched between each disk was 4 mm of plastic scintillator. These pieces of scintillator were used to

measure pair production in real-time (a way to monitor beam position). This real-time use makes this type of collimator an *active collimator*.

Figure 2.9: A picture of the goniometer used for the production of linearly polarized photons. In the center of the goniometer is where the target ladder is located. When used in the hall, this gonimeter is positioned perpendicular to the beamline.

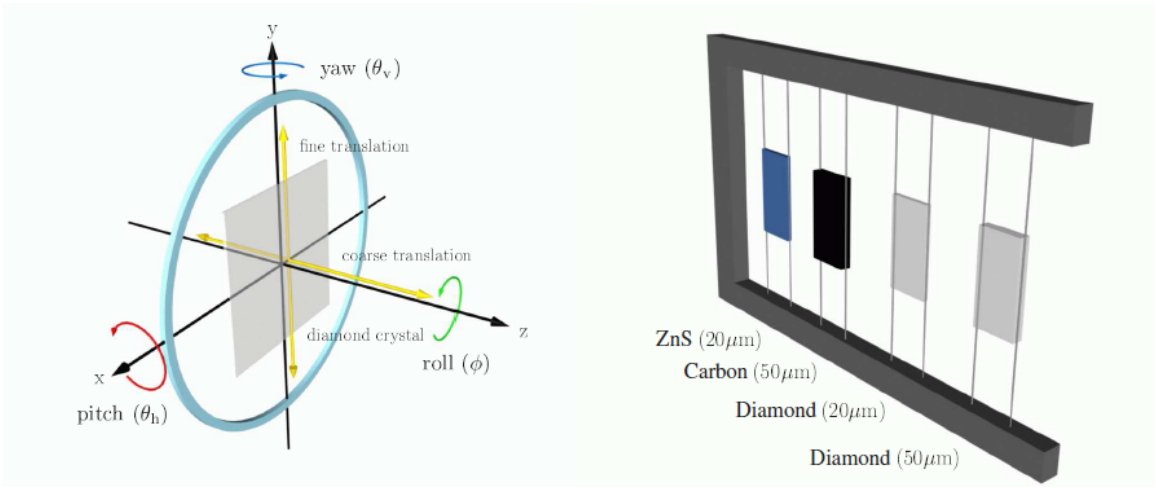

(a) Rotation axes. (b) Target ladder.

Figure 2.10: (a) The available rotational axes of the goniometer as well as translation directions. (b) A diagram of the target ladder used with the GWU goniometer. Here, the different types of radiators are held and moved into position as needed.

2.3.3 Target

The beam of linearly polarized photons continues down the beamline and interacts with the g8b target, located 20 m downstream of the tagger. The target cell itself is a cylinder made mainly of Kapton, is 40 cm long with a 2 cm radius and is placed such that the center of the target cell is 20 cm upstream from the geometric center of the CLAS detector. Inside the target cell resides the target material which for g8b was liquid hydrogen (LH_2) which was kept at a density of 0.071 g/cm^2. A Computer Aided Design (CAD) drawing of the target used can be seen in Figure 2.11.

Figure 2.11: A CAD drawing of the g8b target cell. The photon beam is incident on the target cell from the left-hand side of the figure.

2.4 CEBAF Large Acceptance Spectrometer (CLAS)

The main detector used in both electro- and photo-production experiments in Hall B is the CEBAF Large Acceptance Spectrometer, also known as CLAS. This detector is made up of several layers of sub-detectors providing a solid angle coverage of almost 4π. The CLAS detector can be used to detect both charged and uncharged particles although it is more efficient at the detection of charged particles. The magnetic field used for bending the particles through the detector systems is provided by the Torus Magnet. The detection of final state particles come from the Start Counter, Drift Chambers, Time of Flight Scintillators, Cherenkov Counters, and Electromagnetic Calorimeters. These detectors are used to obtain information on the charge, momentum, timing, mass and velocity of any particle of interest and can be seen in Figure 2.12. The following sections will describe the Torus Magnet and the detectors used in this analysis.

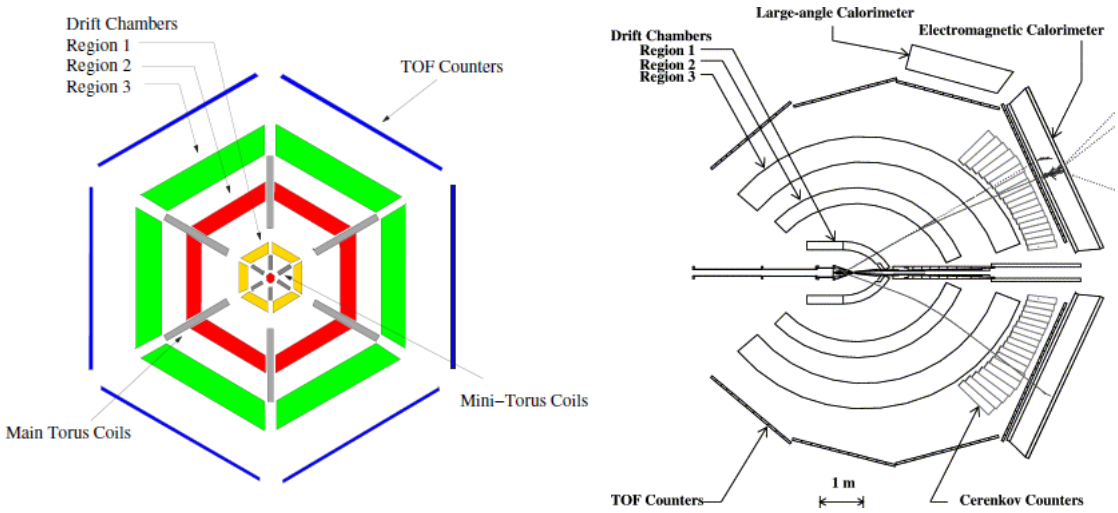

Figure 2.12: Cross sections of the CLAS detector showing the major parts such as the Drift Chambers, Torus Coils, and TOF counters. Figure (a) shows the CLAS detector as viewed from the front. The mini-torus was not used for g8b and in its place was the Start Counter. Figure (b) shows the CLAS detector as viewed from above, sliced at the beamline. The two curved lines going through the detector represent two charged particles as they would behave when transversing the detector.

2.4.1 Torus Magnet

The CLAS detector was designed, geometrically, for use with a toroidal magnetic field. This magnetic field is provided by the CLAS Torus Magnet. This type of magnetic field was chosen as it affords the ability to measure the momentum of charged particles with good resolution while providing a large-angle coverage for the detection of final state particles. A toroidal magnetic field also provides a magnetic field-free region around the target which allows for the use of dynamically polarized targets [43].

The Torus Magnet provides the magnetic field through the use of six superconducting coils arranged in a toroidal fashion around the beamline. This arrangement results in a magnetic field pointing in the ϕ_{lab} direction while also geometrically dividing CLAS into six sectors. A picture of these coils and the magnet outside of CLAS is shown in Figure 2.13 and maps of the produced magnetic field in Figure 2.14. The Torus Magnet as a whole is 5 m in diameter and 5 m long. Each one of the six superconducting coils contains four layers each with 54 turns of aluminum-stabilized NbTi/Cu superconducting wire. These wires are cooled to superconducting temperatures and kept superconducting by forcing supercritical helium through cooling tubes at the edge of the windings. This torus magnet was designed to handle a maximum current of 3860 A (resulting in a 3.5 T magnetic field) but in order to keep the mechanical stresses to a minimum the usual current used is around 3375 A. However, the resulting magnetic field is not perfectly uniform. Close to the coils, there is a deviation from the "pure" ϕ direction (Fig. 2.14). The effect of this deviation on the paths of charged particles moving through the field is minimized by the circular inner shape of the kidney-shaped coils, making any deflection non-significant [43].

The g8b run period had its own requirements for the running of the Torus Magnet. A feature of the magnet is that it can be run in *positive polarity* or *negative polarity* mode. This simply indicates the direction of the current put through the coils and therefore the direction of the resulting magnetic field. Using a positive polarity means that any positively charged particle encountering the magnetic field will be bent away from the beamline and any negatively charged particle will be bent towards the beamline. The g8b run used a positive polarity setting produced from a *half current* of 1930 A. A half current setting was used to produce a lower magnetic field, increasing acceptance for negatively charged particles so less of these will be lost down the beamline hole at forward angles.

Figure 2.13: A picture of the CLAS Torus Magnet outside of CLAS during installation into Hall B. Three of the six superconducting coils of the Torus Magnet can be seen.

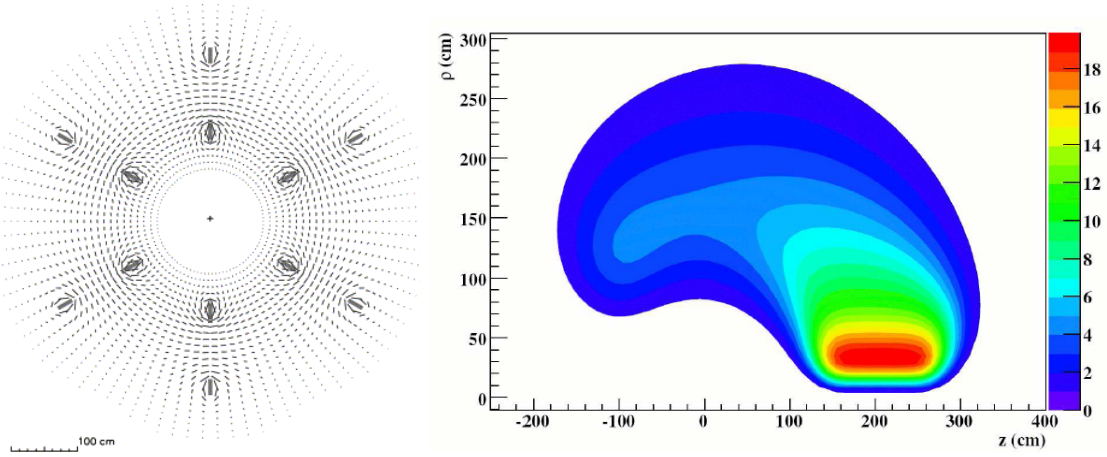

(a) (b)

Figure 2.14: A mapping of the magnetic field produced by the CLAS Torus Magnet. (a) The toroidal magnetic field as seen from a plane centered on the target. The length of the lines indicates field strength at that point. (b) A plot of the absolute magnetic field strength as seen from a vantage point that is between two coils.

2.4.2 Start Counter

When a run period calls for the use of a photon beam instead of an electron beam, the mini-torus (which is used only for runs involving an electron beam as it prevents the electrons in the beam from reaching the drift chambers) is replaced with the Hall B Start Counter. This detector surrounds the 40 cm target cell and is the first detector that the particles coming from the target interact with. A CAD drawing of the Start Counter can be seen in Figure 2.15. Its position immediately surrounding the target means that when used in conjunction with the Time of Flight, it can provide a precise start time for every trigger recorded by CLAS as well as the time at which the photon was at the interaction vertex.

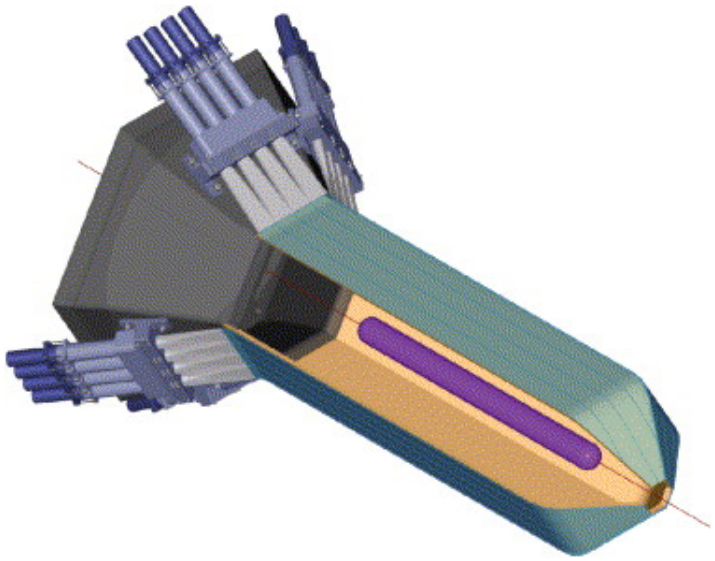

Figure 2.15: A CAD drawing of the Start Counter used for g8b.

The Start Counter provides complete coverage of the target cell. It is divided into six sectors corresponding with the six sectors of CLAS with each sector containing four scintillator paddles. Each paddle has a straight section 502 mm long with a bend at each end. The portions of the scintillators that are located at the downstream end of the Start Counter are tapered to form a "nose" while the upstream end of each scintillator is attached to an acrylic light guide and a photomultiplier tube. Measurements of the timing resolution of the Start Counter have shown that the straight section, or "leg", of the start counter has resolution of ≈ 290 ps while the nose portion has shown a resolution of ≈ 320 ps [50]. Such a sub-nanosecond resolution is needed to determine the timing of an event and the β ($\beta = v/c$ where v = the particle's velocity and c = the speed of light) of the final state particles.

2.4.3 Drift Chambers

The CLAS Drift Chambers are used to track any charged final state particle as it moves through the magnetic field produced by the Torus Magnet and consists of a total of 18 separate drift chambers. This tracking of the trajectory of the final state particles leads to a determination of the momentum and particle type. The Drift Chambers are divided into six sectors as mandated by the geometry of the Torus Magnet and its coils. Each one of these six sectors is then further divided into three regions which are numbered according to their distance from the target cell. These multi-layer regions are located at different radial positions in CLAS termed *Regions*. The drift chambers located in Region 1 are inside the torus coils in an area of very low magnetic field. These drift chambers are mainly used to determine the beginning of the particle's trajectory as it is the first part of the drift chamber system the particle encounters. The next region, *Region 2*, is located between the coils of the Torus in an area of highest magnetic field. This means that this region is located near the area of maximum curvature of the particle's trajectory providing for excellent momentum resolution. The furthest region from the target cell, *Region 3*, lies in an area of low magnetic field. This region provides an end-point of the particle's trajectory as it leaves the Drift Chambers and continues on to the outlying detector systems. This setup of the Drift Chambers leads to a polar angle (θ) coverage of 8° to 142° and an 80% coverage of the azimuthal angle ϕ [51]. Diagrams showing the CLAS Drift Chamber can be found in Figure 2.12.

Each region of the drift chambers contains two superlayers which each contain six layers of wires. The first superlayer is the *axial* layer as it is positioned axial to the magnetic field. The second superlayer, the *stereo* layer, is tilted at a 6° stereo angle around the radius to provide azimuthal information. The individual drift chambers are arranged with the sides of the chambers being parallel to the neighboring Torus coils and therefore tilted at 60° with respect to each other. This means that the wires contained in the superlayers are approximately perpendicular to the particle's trajectory, providing maximum sensitivity to the track's curvature [43]. The six layers of wires contained in each superlayer are arranged in layers of partial circles such that neighboring layers were offset by half a cell width. This pattern of two field-wire layers and one sense-wire layer gives rise to a quasi-hexagonal pattern of six field-wires surrounding one sense-wire (Figure 2.16). The sense-wire is made of gold-plated tungsten and has a diameter of 20 μm while the surrounding six field-wires are made of an gold-plated aluminum alloy with a diameter of 140 μm. This hexagonal pattern was chosen since this type of cell shape is approximately an ideal circular cell. In such a cell, the drift time and drift distance is independent of the particle's entrance angle which is useful as events in CLAS will traverse the chambers at varying angles. The number of sense wires contained in the CLAS Drift Chambers totals 35,148. More detailed information regarding the construction and function of the Drift Chambers can be found in [43] and [51].

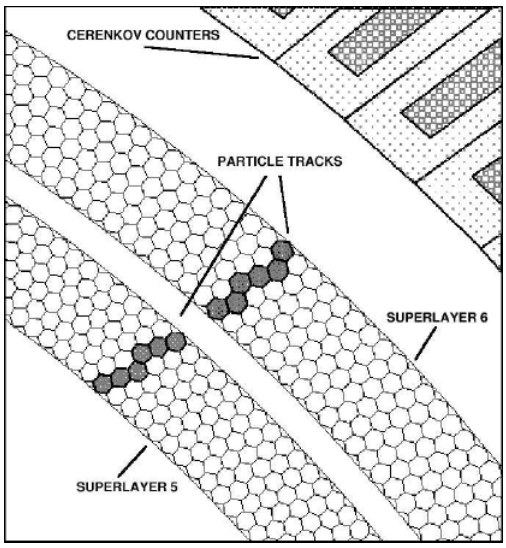

Figure 2.16: A diagram showing the hexagonal cells of the CLAS Drift Chambers. The shaded region represents a particle's track through the cells located in each superlayer of the Region 3 drift chambers.

2.4.4 Time Of Flight Scintillators

Located between the CLAS Cherenkov Counters and the Electromagnetic Calorimeters approximately 4 m from the target cell are the CLAS Time of Flight scintillators (Figure 2.12). This subsystem of CLAS comprises of six panels of scintillators (one panel for each sector of CLAS) that provide coverage in the polar angle from 8° to 142° and completely cover the azimuthal angle ϕ [43]. This system was designed to provide excellent timing resolution to aid in particle identification while possessing good segmentation for flexible triggering and prescaling. Timing requirements for the Time of Flight stated that it have a timing resolution of 120 ps at the smaller angles and 250 ps at angles above 90° [52]. A picture of a Time of Flight panel can be seen in Figure 2.17a.

Each one of the six panels of the Time of Flight contains 57 scintillator paddles each being 5.08 cm thick. Each scintillator paddle is constructed of Bicron BC-408 scintillator with a Photomultiplier Tube (PMT) attached to each end. These paddles are arranged with the last 18 in each sector being coupled into 9 logical pairs, giving a total of 48 logical paddles per sector. These paddles and the panels themselves are positioned such that each scintillator is perpendicular to the average local particle trajectory. The width of the scintillators varies with polar angle (θ). In the forward region (θ less than 45°) the scintillators are 15 cm wide and in the large angle region (θ greater than $\approx 70°$) the width of the scintillators is 22 cm. This is done such that the width of each counter subtends about 1.5° of the scattering angle. The lengths of the scintillators also vary according to their polar angle coverage. The length of the forward angle counters vary from 32 cm to 376 cm and the large angle counters from 371 cm to 445 cm. The timing resolution of these counters degrades with an increase in length but has been shown, using cosmic rays, to be $\approx$ 80 ps for the short counters and $\approx$ 160 ps for the long counters, surpassing the initial requirements. A diagram of a Time of Flight panel is shown in Figure 2.17b.

The g8b run period used the prompt signals from the Time of Flight for the CLAS Level 1 trigger. The Time of Flight was used as the counting rates seen in the Tagger were too high to be incorporated into the trigger. During reconstruction of the g8b data, the Time of Flight was also used to calculate the velocity of particles moving through the CLAS detector. This was done through the use of timing information obtained by the Start Counter and the Time of Flight. By combining this calculated velocity and information regarding the particle's momentum (taken from the Drift Chambers), the particle's mass and therefore also ID, can be determined.

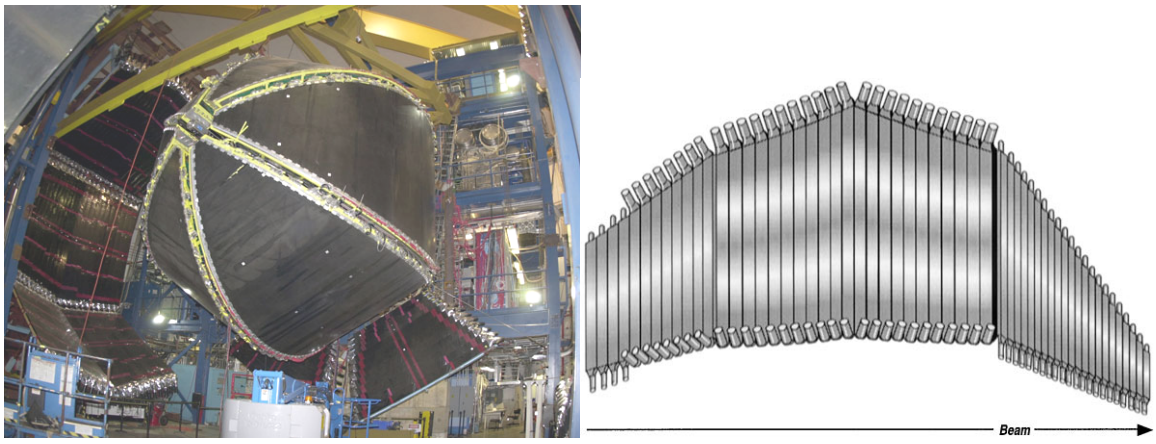

(a) (b)

Figure 2.17: (a) A picture of CLAS when opened revealing the Time Of Flight which can be seen to the far left. (b) A diagram of one panel of the Time Of Flight.

2.5 Beamline Devices

2.5.1 Beam Position Monitors

To determine and monitor the position of the electron beam used for experiments in Hall B, Beam Position Monitors (BPMs) are used. These Beam Position Monitors are located at three different places along the beamline. The 2C21A BPM is positioned just upstream of the Goniometer (36 m upstream of the target), the 2C24A BPM is just upstream of the tagger (24.6 m upstream of the target) and the 2H01A BPM is downstream of the Tagger (8.2 m upstream of the target). For experiments involving a photon beam (such as g8b), the third BPM is not used as it is downstream of the Tagger magnet [43]. The BPMs provide the position of the beam as well as its intensity at each BPM location and insert this information into the data stream every 20 seconds.

2.5.2 Beam Profile Monitors: Harps

The profile of the electron beam and the photon beam can be determined using the Beam Profile Monitors (or Harps). The harps used for determining the profile of the electron beam are located 36.7, 22.1, and 15.5 m upstream of the CLAS target. The electron beam

harps are made of thin, crossed wires oriented along the horizontal and vertical axes. When performing a "Harp Scan", this arrangement of wires moves across the beamline at an angle of 45° from the horizontal axis. As these crossed wires move across the beamline, PMT's are used to detect the Cherenkov light emitted by the scattered electrons. An example of such a Harp Scan can be seen in Figure 2.18. Since this Harp Scan involves interception of the beam before the target, this process occurs when CLAS is not taking data and at startup of the electron beam or after any interruption of the electron beam. The harp used for determining the profile of the photon beam is located 20 m downstream of the CLAS target. This harp is made of crossed scintillator fibers. These scintillator fibers detect the electron-positron pairs produced by the photons in the target, the atmosphere between the target and harp, and the fibers themselves [43].

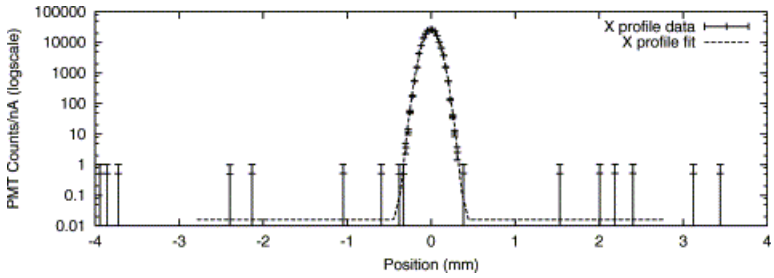

Figure 2.18: Typical electron beam profile in the x-dimension measured by the harp located just upstream of the tagger magnet. The profile should be able to be fit to a Gaussian and a constant background term.

2.5.3 Total Absorption Shower Counter

When using a photon beam, knowing the total photon flux is necessary to determine the efficiency of the Tagger hodoscope. To determine this photon flux, a large lead-glass Total Absorption Shower Counter (TASC) is inserted into the beamline. Each of the four glass-lead blocks has a length of ≈ 17 radiation lengths and is coupled to a phototube. This TASC has an efficiency of essentially 100%, but can only be operated at beam currents up to 100 pA due to counting pile-ups [43]. Due to this restriction on the beam current, special *normalization runs* must be conducted using the TASC and when not in use, it is removed from the beamline.

2.5.4 Pair Spectrometer

Cross-calibrated with the TASC and also able to measure photon flux is the Hall B Pair Spectrometer [43]. This spectrometer consists of a dipole magnet, an aluminum foil (to induce pair production), eight scintillator paddles, and 2 pairs of microstrip detectors which are used to detect the produced e^+e^- pairs. The aluminum foil, 10^{-3} radiation lengths thick, is positioned 5.77 cm upstream of the dipole magnet, within its magnetic field. Arranged symmetrically on either side of the beamline are the scintillators and microstrip detectors, positioned such that photons covering the entire tagging range may be sampled.

The center of the dipole magnet used for the Pair Spectrometer is positioned ≈ 13 m upstream of CLAS, with the spectrometer being just downstream of the active collimator.

Photons produced via coherent bremsstrahlung at the radiator interact with the aluminum foil and produce e^+e^- pairs. These e^+e^- pairs are then swept out of the beamline by the magnetic field and strike the scintillators and microstrip detectors. The energy of the photon that gave rise to the e^+e^- pair can then be reconstructed according to the position of the detected hit. While not having the near-perfect efficiency of the TASC, this spectrometer has the ability to operate at much higher beam currents. For the running of g8b, the Pair Spectrometer was also used to see any shift in beam position. This was done by measuring the rates of e^+e^- pairs seen in the scintillators of the spectrometer. By tuning the Pair Spectrometer to the energy of the coherent edge currently being produced, it could also be used to determine the flux of linearly polarized photons present after the active collimator.

2.6 The g8b Trigger

Each one of the detector sub-systems in CLAS is connected to a series of electronics which read out the information collected by the detector. In order to collect information regarding physics events, criteria called *Triggers* are used. For information regarding an event to be recorded, the criteria cited by the trigger(s) must be met. These triggers help to prevent information about detector hits that arise from other sources such as cosmic rays, electronic noise, etc. and can be restrictive enough to be biased toward a particular final state (or fairly open as it was for g8b). The types of triggers and restrictions used to record data in Hall B are the *Level 1* trigger, the *Level 2* trigger, and the *Trigger Supervisor*. The use of a trigger also aids in the minimization of the dead-time of the Data Acquisition System.

The first of the triggers used with Hall B's Data Acquisition System is the Level 1 Trigger, the fastest of the triggers. This trigger requires that there be a hit in both the Start Counter and the Time of Flight. For g8b, the Level 1 trigger required that the hit in the Start Counter and the TOF be in the same sector: the track of a single charged particle. The second trigger, the Level 2 trigger, involves using tracking information from the Drift Chambers. For an event to pass the requirement of the Level 2 trigger, a particle's path (or trajectory) must be able to be reconstructed in the Drift Chambers. This prevents things such as a cosmic ray event, which could pass a Level 1 trigger but not a Level 2 trigger, from being written into the data stream. Finally, the Trigger Supervisor decides whether or not the event will be recorded. There are two main configurations of the Trigger Supervisor. The first configuration requires that the event only pass a Level 1 trigger. The second configuration (the configuration used for g8b) requires that for an event to be recorded, both the Level 1 and Level 2 conditions be satisfied.

2.7 Data Acquisition System (DAQ)

The data taken during a run period in Hall B is recorded by the Data Acquisition System (DAQ). Data from all of the various detectors is digitized in 24 FASTBUS and VME crates inside of the experimental hall. This data is then collected by the 24 VME Readout Controller located in the crates. This assortment of detector signals is then translated into tables where each data value is associated with the active detector component from which it

arose. These data arrays are then buffered and transferred to the CLAS online acquisition computer (CLON10). Three main processes are then carried out. These are the Event Builder (EB), Event Transport (ET), and Event Recorder (ER). The EB assembles the data stream into events with the tables of information being organized into data *banks* with each event being labeled by run and event number. The ET manages the shared memory of the DAQ and allows access by various event producer and consumer processes. The ER then writes the data in a single stream to an array of local magnetic media called RAID disks. This data is then transferred from these local RAID disks to a remote tape silo where the data is stored for the long-term.

During the g8b run period, the DAQ experienced an event rate of ≈ 4.5 kHz. This led to a live-time of $\approx 87\%$ (dead-time of $\approx 13\%$). Event rates are usually determined by the data acquisition hardware and software, however the event rate during g8b was not determined by the performance of the DAQ but rather by the performance of the Tagger. It was seen that when the number of photons produced in the coherent peak got too high, part of the Tagger Hodoscope would not perform well. In order to reduce the number of photons being produced at the radiator, the number of electrons coming from the accelerator needed to be reduced. For this reason, g8b used a relatively low electron beam current of ≈ 10 nA.

CHAPTER 3

PREPARATION OF THE $p\ \pi^+\pi^-$ FINAL STATE

Data collection for the g8b experiment was carried out by the CLAS Collaboration between July 20^{th} and September 1^{st} of 2005. The data set boasts 11,475 data files, is $\approx$ 30 TB in size and contains 10.7 billion triggers. These data taken during the running of the g8b is stored on large data tapes in a "silo" at Jefferson Lab. This data was initially in its raw format, consisting of only detector signals and information about the various detector elements. Therefore the data must undergo reconstruction, or be *cooked* (transforming the data into information about scattered particle angles, masses, velocities, momenta, etc), in order for it to be ready for a physics analysis. It is also during this cooking phase that the calibration of the detectors is carried out with each detector being calibrated independently.

Quark model calculations suggest that the excited baryon resonances decay back to their ground state through decays involving intermediate states (with the emission of a meson). Some of these intermediate states, for example, are then expected to decay further into $\Delta\pi$ which then decays into a $p\ \pi^+\pi^-$ final state. Therefore the primary final state/channel investigated in this work is:

- $\vec{\gamma}\ p \rightarrow p\ \pi^+\pi^-$,

where all final state particles are detected. Three additional topologies are investigated as well:

- $\vec{\gamma}\ p \rightarrow p\ \pi^+(\pi^-)$ (π^- not detected),
- $\vec{\gamma}\ p \rightarrow p\ \pi^-(\pi^+)$ (π^+ not detected),
- $\vec{\gamma}\ p \rightarrow \pi^+\pi^-(p)$ (proton not detected).

The investigation of these three additional final state topologies serves to provide a way to extract the polarization observables over topology-dependent acceptance holes resulting in a continuous measurement. Several steps and techniques were used to carry forth this analysis and are described in the following sections.

3.1 Pre-Event Selection

After the detectors have been calibrated and the particle tracks have been reconstructed, the cooking of the data is complete and the data is made available for analysis. Each event

in the data has its information organized into data banks. These data banks hold not only the properties of the particles involved in the reaction but information about detector hits. Specific data banks of interest in this analysis are the GPID, TAGR, TBID, TBER, and MVRT banks. How and where these banks were used will be explained during the course of this chapter.

Explanation of data banks:

- GPID: This data bank contains much of the information regarding the event. This information includes the particle IDs, vertex positions (for each detected particle), 4-vectors, charge, beta ($\beta = \frac{v}{c}$) of the particle, the vertex time of the particle's track, particle masses (calculated), the incident photon's energy, photon time, and an index to the TAGR bank for the incident photon. Information from several detectors are used to fill this data bank. These detectors are: the Drift Chambers, Time of Flight Scintillators, Tagger and Start Counter.

- TAGR: Information recorded by the Hall B tagging system (the Tagger) is stored here. Information includes: energy of all recorded photons, reconstructed time of photon as calculated by the Tagger, the corrected time of the photon using information from other detectors as well, the *status* of the photon (whether or not it was properly reconstructed), and the E- and T- counter the scattered electron hit.

- TBER: The tracking resolution errors associated with the tracking measurements of the particles in the event are stored in this bank. Information comes mainly from the Drift Chambers and the Time of Flight. This bank is used to build up the covariance matrix used for kinematic fitting.

- MVRT: This bank uses information from the Drift Chambers and the Time of Flight and contains the vertex information for the event as a whole using individual particle tracks.

3.2 Event Selection

Since the g8b experiment was not designed for this analysis alone, the trigger file (for this run period, a single charged, able-to-be-reconstructed track in a single sector of CLAS) used during data-taking allowed for the recording of a large variety of events. In order to analyze a specific channel, the first step of this analysis is therefore to find events possessing the final states of interest. As stated before, there are 4 different topologies of interest in this analysis. However since the data contains all events which passed the single-sector requirement of the trigger, the data must be *filtered*, keeping only the final states of interest.

This filtering occurs by placing requirements regarding what data to keep based on the particle's identification number, or *PID*, which is determined during the cooking process and is based on the value of the particle's calculated mass. Events that do not meet this requirement are ignored and subsequently omitted from the analysis. The calculation of the detected particle's mass uses two independently measured quantities, its momentum (p) and velocity as a fraction of the speed of light, β. The magnitude of the particle's momentum (p) is determined with an error of $< 1\%$ [43] using the measurements made by the Drift

Chambers. The β of the detected final state particle is determined using a combination of the Start Counter, the Time of Flight, and the particle's detected trajectory through CLAS (with an error of up to 5%). A detected particle's mass can then be calculated according to equation (3.1):

$$m^2_{particleX} = \frac{p^2(1-\beta^2)}{\beta^2}. \tag{3.1}$$

After the particle's mass has been calculated, it is compared to the masses of known particles (hadrons and leptons). If this calculated mass matches that of a known particle (within resolution errors), the PID associated with that mass is assigned to the final state particle. This value can then be used to select certain final state particles for analysis.

Therefore to select events that match one of the four topologies, the first requirement is based on this PID value and requires that the necessary final state particles are detected, no more, no less. Information regarding the properties of these final state particles (their 4-vectors, vertex information for individual particles, etc.) was then extracted from the GPID data bank and used for kinematic fitting, determination and application of cuts and systematic corrections, and the extraction of the polarization observables.

3.3 Photon Selection

The g8b run period used photoproduction on the proton via a beam of tagged photons. As the electrons used to produce this beam of polarized photons arrive in Hall B from the accelerator in 2 ns bunches with each bunch containing many electrons, the photons too arrive at the target in bunches with each bunch containing many photons. Therefore an accurate determination of the correct photon is very important in order to have a full understanding of the initial state of the event. This determination uses data collected by the Drift Chambers (for tracking the particle's path), Time of Flight (for velocity and timing information), and the Tagger (for photon timing information). The timing information collected by the Time of Flight and the Tagger (both independently calibrated) are used to make a time-based determination of the correct photon.

Each event in the g8b data set has an average of 16 *candidate* photons associated with it (Figure 3.1(a)). For a photon to be considered a candidate, it must occur within the timing window set by the trigger and satisfy several consistency checks involving the Tagger. These consistency checks involve the photon having a corresponding hit in the E- and T-counters, depositing a certain amount of energy in the E-counter, and producing a PMT signal at both ends of the scintillator bars that make up the E- and T-plane of the Tagger.

In spite of these requirements, many candidate photons are present in the data stream for one physics event as a result of the 2 ns bunching of the electron beam. To determine the exact photon corresponding to a physics event, vertex information of the physics event along with the timing information regarding the photon(s) are used. The time of the event's vertex is determined by using information from the Time of Flight along with an extrapolation of a particle's track (a particle in the event) through CLAS. The process for determining the correct photon uses the following:

First, the vertex time of the event (t_v) is calculated:

$$t_v = t_{TOF} - \frac{d_{TOF}}{c\beta_c}, \tag{3.2}$$

where t_{TOF} is the time at which the hadron was detected by the TOF, d_{TOF} is the calculated distance from the event vertex to the hit in the TOF scintillator paddle, c is the speed of light, and β_c is the hadron's velocity as a fraction of c. Next, the time of each candidate photon associated with the current event at the event vertex position (t_γ) is calculated:

$$t_\gamma = t_{center} + (\frac{z}{c}), \tag{3.3}$$

where t_{center} is the time at which the photon arrives at the center of the target (calculated by mathematically propagating the electron as it leaves the accelerator to the radiator and then propagating the photon from the radiator to the center of the target cell), z is the distance between the center of the target cell and the event vertex (with both positions being measured along the beam axis), and c is again the speed of light. The small offsets in the x- and y-positions of the event vertex do not appear in the calculations as they are comparable to the resolution of vertex measurements.

The correct incident photon is then found by comparing these two times calculated in equations (3.2) and (3.3) (t_v and t_γ) as in equation (3.4):

$$\Delta t = \mid t_v - t_\gamma \mid. \tag{3.4}$$

A distribution of the time differences between the event vertex time and the times of all candidate photons for the event can be seen in Figure 3.1(b). The 2 ns-wide structures to the right and left of the central peak show the 2 ns beam buckets in which the beam is delivered to the target.

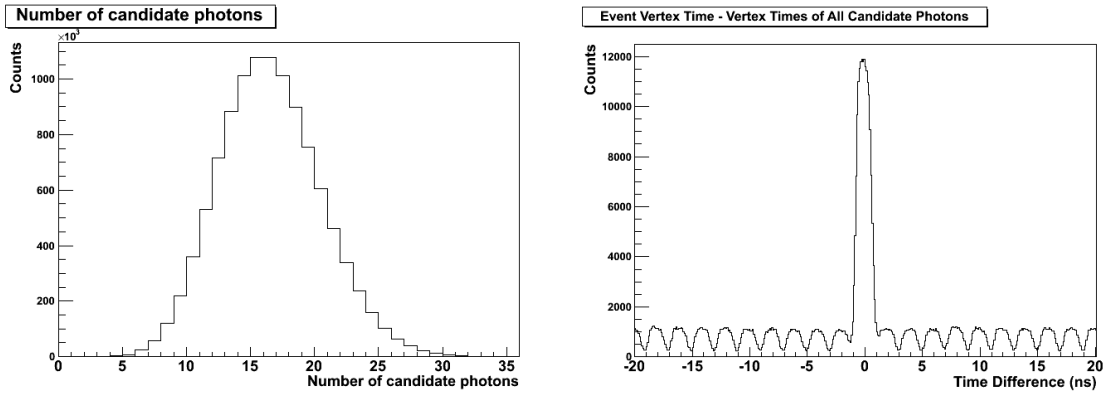

(a) (b)

Figure 3.1: (a) Shows the number of candidate photons per event in the data. There is an average of 16 candidate photons associated with every physics event. (b) Shows a distribution of the time difference (Δt) between the event vertex time (t_v) and the vertex time of all candidate photons. The 2 ns-wide distributions to the right and left of the central peak represent the 2 ns bucket structure in which the electrons (and therefore photons) in the beam arrive. Both histograms were produced using run #048326.

The photon in the list of candidate photons with the smallest time difference between the event vertex time and the time of the photon at the event vertex (smallest value of Δt) is then labeled as the correct incident photon. The distribution seen in Figure 3.2 shows the time difference (in ns) between the event vertex time and photon which was determined to be the correct photon.

Using the above method usually results in the determination of a single photon in the beam bucket which is responsible for the event. However, in the instance that more than one photon is found with a time $\Delta t < 1$ ns, the statement as to which photon was actually responsible for the event cannot be made. In this case, the ambiguity of the photon determination is reflected in the GPID bank and these events are subsequently not analyzed.

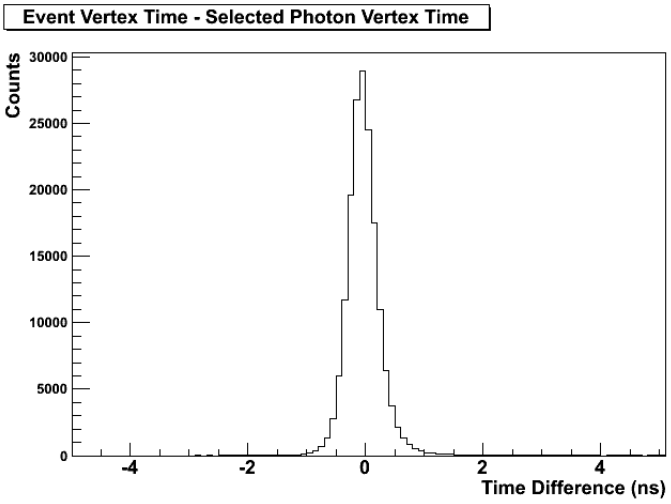

Figure 3.2: The time difference between the event vertex time and the time of the correct photon after photon determination. This distribution shows a large peak around zero, signifying the quality of photon selection. Produced using run #048326.

Once a single photon is found to be the incident photon, the information regarding the incident photon is then stored in the GPID bank for each final state particle. The fact that the incident photon is found per particle track means that a quick cross check of the reconstruction code can be carried out by comparing the photon times for each final state particle. When analyzing an event, the photon's energy and time (as well as other information regarding the photon) are obtained from the GPID and TAGR banks. This information is then used in the reconstruction of the event, the binning of the data, systematic corrections for the photon energy and to perform cuts.

3.4 ELoss

As a charged particle travels from the target cell to the Drift Chambers of CLAS, it loses energy through atomic excitations and ionization when interacting with the target material (liquid hydrogen), target walls, support structures, beam pipe, start counter, and the air gap between the start counter and the Region 1 drift chambers. Therefore the

reconstructed momentum seen in the Drift Chambers is actually less than the momentum of the particle(s) at the production vertex. To account and correct for this, the 4-vectors of the final state particles (as taken from the data) were corrected event-by-event according to the ELoss package developed for charged particles moving through CLAS (using the g8b parameters such as target geometry and target material) [53]. This ELoss package calculates the momentum of the particle in the target cell. To perform this calculation, the particle's 4-momentum as measured by the Region 1 Drift Chambers is used to track the particle back to the reaction vertex in the target cell. As the particle is tracked back to the reaction vertex, the materials and distances it traverses are considered and the energy loss of the detected particle calculated and the 4-vector of the particle appropriately corrected. The energy-loss-corrected 4-vectors are then used in the analysis with the corrections being on the order of a few MeV.

3.5 KinFit

Unique to this g8b analysis is the implementation of the COBRA kinematic fitter developed at Carnegie Melon University for CLAS experiments [54]. The use of this kinematic fitter further refines the data through the enforcement of energy-momentum conservation and missing mass cuts (should the fit hypothesis contain a missing particle). The kinematic fitter is also very useful for the precise determination of systematic errors such as momentum corrections (needed to account for variations of the magnetic field of CLAS as well as any inconsistencies in the Drift Chambers) and photon energy corrections (needed to account for mismeasurements of the photon's energy) to be applied to the data. The following briefly describes the fitter and its implementation.

When an event is kinematically fitted, it is forced to obey energy-momentum conservation. The 4-vectors of the final state particles as determined by the reconstruction code are fed to the fitter as well as the incident photon energy. The components of these 4-vectors and the photon energy are then altered until the event satisfies energy-momentum conservation. These alterations occur within the limits (measurement errors) contained in the *full covariance matrix* which uses the *tracking covariance matrix*, built event-by-event from the data, and the scaling parameters associated with the tracking covariance matrix. After the tracking covariance matrix has been constructed for an event, the scaling parameters are then applied to it to form the full covariance matrix. These scaling parameters are unique to and must be determined for every run period and run condition. The resolution errors contained in the full covariance matrix represent the actual resolution of the detectors while the tracking covariance matrix is the resolution reported (calculated) by the reconstruction code. Once an event has been kinematically fitted, the quality of that fit can be quantified via a confidence level value of the fit as well as a pull value for every measurement parameter.

3.5.1 Confidence Level and Pulls

When using a kinematic fitter, the *goodness of fit* (the agreement between the data and the fit hypothesis) can be determined by examining the confidence level and pull distributions (Fig. 3.3). The confidence level is defined as:

$$CL = \int_{\chi^2}^{\infty} f(z;n)dz, \tag{3.5}$$

where *f(z;n)* is the χ^2 probability density function possessing n degrees of freedom. It is a determination of the probability that a χ^2 from the theoretical distribution is greater than the χ^2 obtained from the fit.

An ideal data set containing only events which satisfy the fit hypothesis and with normally distributed errors would result in a confidence level distribution that is flat from (0,1]. However, a real-life data set run through the fitter (assuming the resolution errors have been properly determined) would produce a confidence level distribution that has a peak at zero. This distribution should then possess a negative slope as you move to higher confidence level values with this slope becoming level (flat) from [0.5,1] (representing confidence levels of 50% - 100%). The large number of events with a low confidence level represent the events which did not match the particular fit hypothesis used. These events include, but are not relegated to only being from: background events, poorly reconstructed events, or events with misidentified particles. This makes the confidence level a good parameter to cut on as doing so will remove a large number background and "bad" events while only losing a small portion good events.

Pull distributions are generated for every fit parameter for every (detected) final state particle involved in the fit. A pull is a measure of how much (and in what direction) the kinematic fitter had to alter, or pull, the value of that parameter in order to enforce energy-momentum conservation normalized to the error of that measurement. A pull value for the i^{th} fit parameter (z_i) is given by:

$$z_i = - \frac{\epsilon_i}{\sigma(\epsilon_i)}, \tag{3.6}$$

where $\epsilon_i = \eta_i - y_i$ is the difference between the value of the i^{th} parameter from the final iteration of the fitting routine, y_i and the measured value of the i^{th} parameter, η_i. The quantity σ represents the standard deviation, or error, of the parameter. Therefore, the i^{th} pull can be written as:

$$z_i = - \frac{\eta_i - y_i}{\sqrt{\sigma^2(\eta_i) - \sigma^2(y_i)}}. \tag{3.7}$$

Assuming that the errors of the parameters used for kinematic fitting are properly determined and all systematic errors have been corrected, the distribution of pull values (z_i values) will be Gaussian in shape with a width of one ($\sigma = 1$) and a mean value of zero ($\mu = 0$). Any systematic error in the quantity η_i will be seen as an overall shift away from zero. An overestimation or underestimation of the error of the quantity η_i will cause the pull distribution to be too narrow or broad, respectively [54].

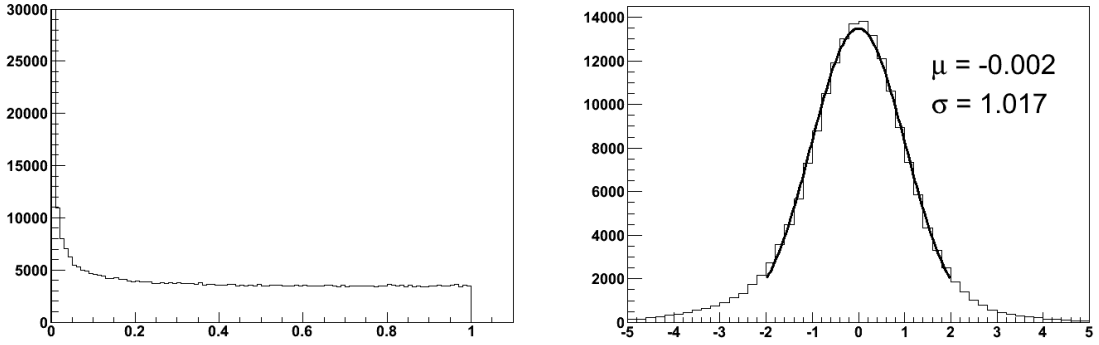

(a) Confidence Level Distribution

(b) Pull Distribution

Figure 3.3: Example of fit results coming from a fit to a $p\ \pi^+\pi^-$ final state. (a) Shows an example of a confidence level distribution. A confidence level distribution (working with real data) peaks toward zero but flattens out toward one. (b) Shows an example of a pull distribution (the photon energy pull). Ideally, a pull distribution is Gaussian in shape around the origin with a mean (μ) of zero and a sigma (σ) of one.

The above describes ideal confidence level and pull distributions. When one begins using the kinematic fitter with their data, this is not the case. The scaling parameters applied to the covariance matrix (the covariance matrix will be discussed in the following subsection) are related to the tracking measurements made for each track, target and magnetic field and are therefore unique to every run period and must be determined as such.

This determination of the proper covariance matrix errors is an iterative process. As a starting point, one may use the scaling parameters from another run period (this analysis started with the g11a scaling parameters). These parameters can then be adjusted/modified, keeping track of all changes to the confidence levels and the pull widths. As these scaling parameters exist as arrays read in by the kinematic fitter, a simple script may be used in order to alter these parameters to be specific to one's data set.

When iterating through this process, one needs to keep track of the pull sigmas and the slope of the confidence level plots, specifically the *normalized slope*. This normalized slope is the slope of a linear fit to the confidence level distribution from [0.5,1] (50% - 100%) which has been normalized to the number of entries at the point 0.5 (the number of events possessing a confidence level of 50%). The choice of the fit range used to calculate the normalized slope was determined with the expectation that the negative slope arising from the large number of events which resulted in poor fits flattens out at 50%. This normalized slope is then defined as seen in Eq. (3.8) where a is the slope of a linear fit from [0.5,1] and b is the y-intercept.

$$\bar{a} = \frac{a}{(a/2) + b} \tag{3.8}$$

Checking the widths (σ's) of the pull distributions is as simple as fitting them to a Gaussian with a 2σ ([$-$2,2]) fit range.

The quality of the covariance matrix errors for a particular data set can be determined

thusly: Errors which are too large will result in a confidence level distribution having a positive slope between 0.5 and 1 and pull distributions with widths less than 1 ($\sigma < 1$). The positive slope of the confidence level distribution signifies that one is artificially increasing the number of events that fit, or pass, the fit hypothesis. In other words, the fitter is being given too much freedom to alter the measured values of the particle's 4-vectors. If the determined and applied errors are too small, the confidence level plot will have a negative slope between 0.5 and 1 signifying that one is excluding possible good events (by not allowing the fitter enough "wiggle room"). The resulting pull distributions will then possess widths greater than 1 ($\sigma < 1$). If the determined and applied errors are appropriate (not too small, not too large), then the confidence level plot will be flat from 0.5 to 1 (resulting in a normalized slope of zero) and the pull distributions will have a sigma of 1 ($\sigma = 1$).

Systematic errors in the data can be seen and corrected by examining the mean values of the pull distributions. For example, the effects of the ELoss package as well as momentum corrections (described in Section 3.6) can be easily seen by monitoring the momentum pull distributions. An examination of the momentum pulls generated by the kinematic fitter shows off the fitter's sensitivity to small changes in the fit parameters. Pull distributions showing this sensitivity can be seen in Figure 3.4. These proton momentum pulls were generated using no momentum alterations for the proton (Fig. 3.4(a)) and a small alteration in momentum equivalent to a 2 MeV shift (Fig. 3.4(b)). This correction corresponds to a change that is smaller than the resolution of CLAS yet still results in a noticeable shift in the pull distribution. Therefore the sensitivity of the kinematic fitter surpasses the resolution of the detector systems. This was one of the reasons the kinematic fitter was used to generate momentum corrections. This process was also an iterative one involving a binning of the pull distributions (in p_p, θ_{lab}, and ϕ_{lab}) that matched the binning of the corrections and a script to alter the momentum correction factors. Corrections were refined by generating correction factors, running over the data using these factors, fitting all of the binned pulls, extracting the mean values, generating new corrections based on the results of the previous iteration and repeating.

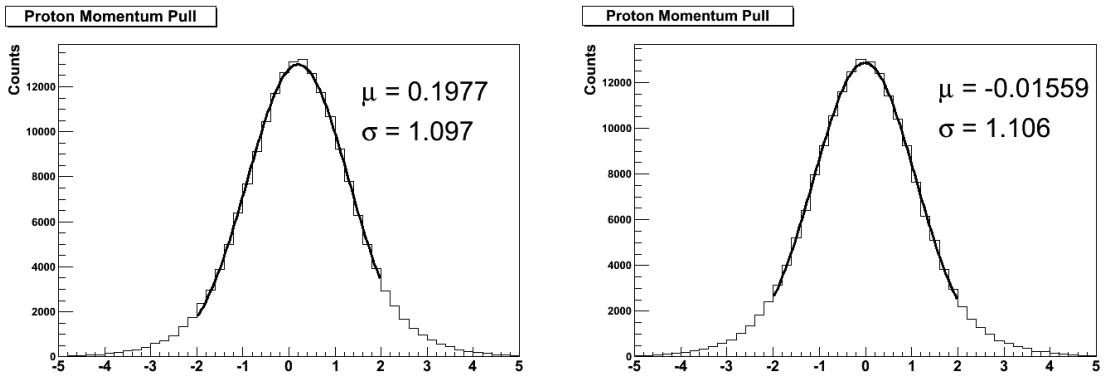

Figure 3.4: Pull distributions for the proton momentum for a $\gamma\ p \rightarrow p\ \pi^+\pi^-$ final state showing the sensitivity of the kinematic fitter to systematic effects. The distribution on the left, (a), was generated using one run (#048326) with alterations of the proton momentum. The distribution to the right was generated using the same run but after an alteration to the proton's 3-vector. This alteration was small (a 0.4% increase) and is equivalent to a 2 MeV increase in the proton's momentum. The high degree of sensitivity of the kinematic fitter to systematic effects is clearly seen as this very small correction shifted the mean (μ) value from 0.1977 to -0.01559.

3.5.2 Use

Kinematically fitting an event requires a process involving several steps. The 4-vectors of the final state particles as well as the incident photon energy must first be extracted from the data. The resolution errors of the tracking measurements used for determining these 4-vectors are then used to build the tracking covariance matrix. Scaling parameters which serve to refine these resolution errors are then applied to the tracking covariance matrix to create a second matrix, the full covariance matrix. The event is then ready for a kinematic fit.

Covariance Matrix. The covariance matrix used for kinematic fitting is built for every event using information from the TBER and GPID data banks and has the form seen below [54]. The TBER bank is used as it contains the errors pertaining to the measured values of the detected particle's momentum and the drift-chamber-specific angles lambda (λ) and phi (ϕ) which are sector dependent and describe the particle's track as it moves through the Drift Chambers. To obtain the magnitude of the 3-momentum of the final state particle, the GPID bank is used. The dimensions of the covariance matrix depend on the number of detected final state particles being used for the fit hypothesis. It is a square matrix of dimensions $(3n+1) \times (3n+1)$ where n is the number of detected final state particles. The extra row and column (the '+1') is reserved for containing the error in the measurement of the photon energy. The tracking resolutions regarding the detected final state particles are used to build 3×3 matrices along the diagonal of the covariance matrix, one for each detected final state particle. In these mini-matrices, the diagonal terms hold the "pure" (non correlated terms) measurements of momentum, lambda, or phi while the off-diagonal terms represent the correlation (mixing) of these measurements. The C's present in the generalized covariance matrix seen below represent the elements of the covariance matrix and are polynomials with values extracted or calculated from the data.

$$C = \begin{pmatrix} \sigma^2_{E_\gamma} & 0 & 0 & 0 & \cdots & 0 & 0 & 0 \\ 0 & C_1^{pp} & C_1^{p\lambda} & C_1^{p\phi} & \cdots & 0 & 0 & 0 \\ 0 & C_1^{p\lambda} & C_1^{\lambda\lambda} & C_1^{\lambda\phi} & \cdots & 0 & 0 & 0 \\ 0 & C_1^{p\phi} & C_1^{\lambda\phi} & C_1^{\phi\phi} & \cdots & 0 & 0 & 0 \\ \vdots & \vdots & \vdots & \vdots & \ddots & \vdots & \vdots & \vdots \\ 0 & 0 & 0 & 0 & \cdots & C_k^{pp} & C_k^{p\lambda} & C_k^{p\phi} \\ 0 & 0 & 0 & 0 & \cdots & C_k^{p\lambda} & C_k^{\lambda\lambda} & C_k^{\lambda\phi} \\ 0 & 0 & 0 & 0 & \cdots & C_k^{p\phi} & C_k^{\lambda\phi} & C_k^{\phi\phi} \end{pmatrix}$$

Photon Error. The energy of the photons are determined by using the 384 E-counter scintillator paddles contained in the E-plane of the Tagger. These scintillator paddles are arranged in an overlapping fashion such that each counter optically overlaps its adjacent neighbors by one-third of their respective widths, leading to a total of 767 bins in photon energy (767 E-bins). This configuration leads to an energy resolution of $r = 0.001 E_{beam}$

[46]. Due to the fact that the information regarding the incident photon's energy comes from a measurement made by a detector, there is an error that must be associated with the photon energy. If one assumes that this error is the same for all paddles then the error can be given by equation (3.9):

$$\sigma^2_{E_\gamma} = \frac{1}{2r}\int_{-r}^{r} E^2 dE = \frac{r^2}{3}, \tag{3.9}$$

where again, $r = 0.001E_{beam}$. Therefore for the g8b run period, which used an electron beam with energy $E_{beam} = 4.559$ GeV, the associated error in photon energy is $\sigma^2_{E_\gamma} = 6.928$ MeV.

Momentum and Tracking Angle Error. The measurements made regarding the momentum and tracking angles (λ and ϕ) describe the path of the detected final state particles as they moved through the Drift Chambers of CLAS. These measurements, like all other measurements, carry with them an error. This error comes from several sources. Tracking errors which lead to inaccurate momentum (and angle) measurements, multiple scattering leading to differences between the measured angles and the angles at the interaction vertex, and the performance of the reconstruction code (the fitting of the tracks) being the main culprits. When an event is reconstructed, the reconstruction code includes the calculated errors but this calculation assumes a complete knowledge of the resolution of detector components which vary in a small amount from one run period to the other. Therefore it is necessary that the resolution of the detector components for the run period under analysis be completely determined. This true resolution comes in the form of scaling parameters. These scaling parameters are binned in sector number and θ_{lab} and are applied to the momentum, and tracking angle components of the tracking covariance matrix.

Once a fit is performed, the user has access to several fit results. These are: the fitted 4-vectors of the final state particles (except the missing particle if the fit hypothesis involved a missing particle), the fitted photon energy, the confidence level of the fit, and the pull value for each pure element of the covariance matrix (elements along the diagonal of the covariance matrix). The information returned by the fitter can then be used to check the quality of the performed fit as well as provide quantities on which cuts may be imposed during the course of the analysis.

3.6 Momentum Corrections

Since the CLAS detector is not a perfect detector, corrections for momentum must be determined for every run period. This mainly is a result of unknown variations in the magnetic field provided by the Torus Magnet as well as inefficiencies and misalignments of the Drift Chambers. As mentioned before, the momentum corrections were determined using the kinematic fitter, specifically looking at the momentum pull distributions for the topology $\vec{\gamma}\ p \rightarrow p\ \pi^+\pi^-$ and have been incorporated into the various analyses which use the g8b data set.

To properly determine the momentum corrections for the g8b data set, these pulls (and corresponding correction factors) must be binned in momentum (p) and the lab angles θ and ϕ of the particle to be corrected (in this case, the proton). The binning used to determine these correction factors was determined based upon the observed distribution

of momentum, θ_{lab} and ϕ_{lab} for the proton seen in Figure 3.5. The momentum binning utilized 6 momentum bins covering a range of 0.2 GeV to 1.7 GeV with the angle binning utilizing 7 bins in θ_{lab} (10° - 70°) and 18 bins in ϕ_{lab} (covering the full range of ϕ_{lab}). First, the proton momentum pulls and correction factors were binned in the above manner with the correction factors existing in an array (each possessing a default value of 1). The pull distributions were then individually fitted to a Gaussian and the resulting mean value (μ) and width (σ) recorded into another array. Then through the examination of the mean values resulting from the (Gaussian) fits of the pulls and determining the direction and magnitude in which these mean values should be moved, the correction factors were altered to either a value above or below 1 with these new correction factors being read into a new array. These new correction factors were then applied to the data, the pulls regenerated and then fit again to determine whether further corrections were needed. For example: if the proton momentum pull has a mean value that is above zero, then for the majority of the fits, the kinematic fitter is increasing the proton's momentum in order to satisfy energy-momentum conservation. In this case, the correction factor should be greater than one such that the fitter *pulls* the momentum of the proton equally in both directions. The same course of logic may be applied to a pull distribution with a (fitted) mean value that is negative. This mean value indicates that the fitter is decreasing the proton momentum the majority of the time. Therefore the appropriate correction factor would decrease the proton's momentum before it is kinematically fitted. Once these correction factors have been determined, they are applied to the 3-momentum of the final state particles thereby correcting its momentum. The effect of the momentum corrections on the momentum pull of the proton can be seen in Figure 3.6.

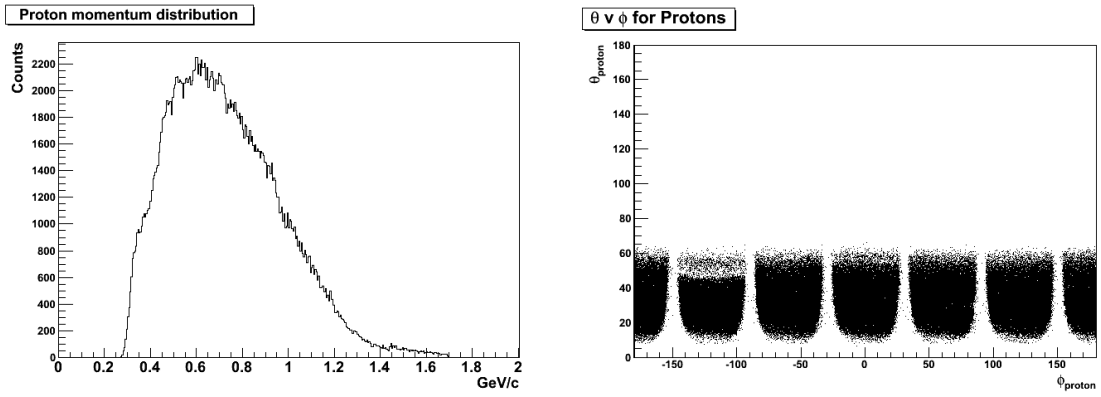

(a) (b)

Figure 3.5: The observed distributions of momentum (a), θ_{lab} and ϕ_{lab} (b) for the proton used to determine the binning for momentum corrections. Distributions were produced for $p\ \pi^+\pi^-$ events contained in run #048326 (a) and #048229 (b) which pass a confidence level cut of 1%. The region seen in (b) showing low statistics for $-150° < \phi_{proton} < -110°$ is seen in several runs and can be attributed to dead wires in the Drift Chambers.

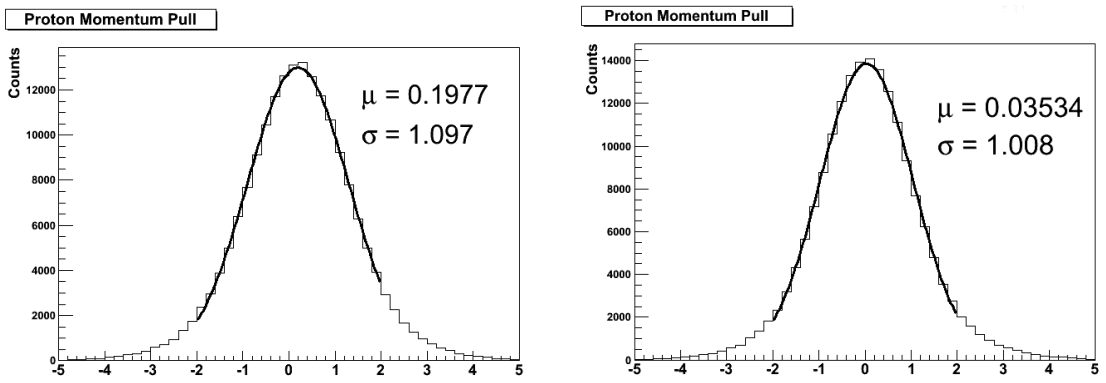

(a) Without momentum corrections

(b) With momentum corrections

Figure 3.6: Proton momentum pulls without momentum corrections (a) and with momentum corrections (b) as extracted from the fitter for a fit to a $\vec{\gamma}p \rightarrow p\ \pi^+\pi^-$ final state. After application of the final momentum corrections, the pull becomes symmetric and has a mean value close to zero. Produced using a full run (#048326).

3.7 Tagger Sag

The Hall B tagging system is an invaluable tool for determining the energy of the photons that are incident on the target. This detection system, however, is not beyond the need for corrections. It has been seen in the g8b data set (as well as in past experiments) that there is a physical sagging of the support structures used to support the E-counter scintillator bars in the Tagger hodoscope which has been attributed to gravitational forces [55]. The consequence of this sagging is a misalignment of the scintillator bars which leads to a mis-measurement of the scattered electron's energy. This mis-measurement must then be compensated for via an energy-dependent photon energy correction.

The sagging of the hodoscope's support structures can be seen by comparing the calculated photon energy, E_{true} (which for this study was the photon energy returned by the kinematic fitter) and the measured photon energy, $E_{measured}$, as a function of photon energy ($E_{measured}$) as seen in Figure 3.7. This sagging is demonstrated by the "humps" of the ($E_{true} - E_{measured}$) values with the vertical support structures (which support the sagging beams on which the E-counter scintillators rest) of the detector plane evidenced by the sharp dips. The iterative routine used to correct the photon energies was developed at Arizona State University (ASU) and verified using the Kinematic Fitter at FSU [56]. Corrections applied to the photon energies typically are on the order of a few MeV and greatly improve the quality of the data. The before and after effects of these corrections can be seen in Figure 3.8 with the effects on the photon energy pull distributions being shown in Figure 3.9. These two histograms were generated using the kinematic fitter and therefore are very sensitive to systematics. The plot seen in Figure 3.8 is a distribution of the mean values of the photon energy pulls generated from fitting to a $p\ \pi^+\pi^-$ final state versus the measured photon energy. The effects of the sagging can be seen in this plot as deviations from zero. Seen in Figure 3.9 is the y-projection of the photon pull distributions used in Figure 3.8.

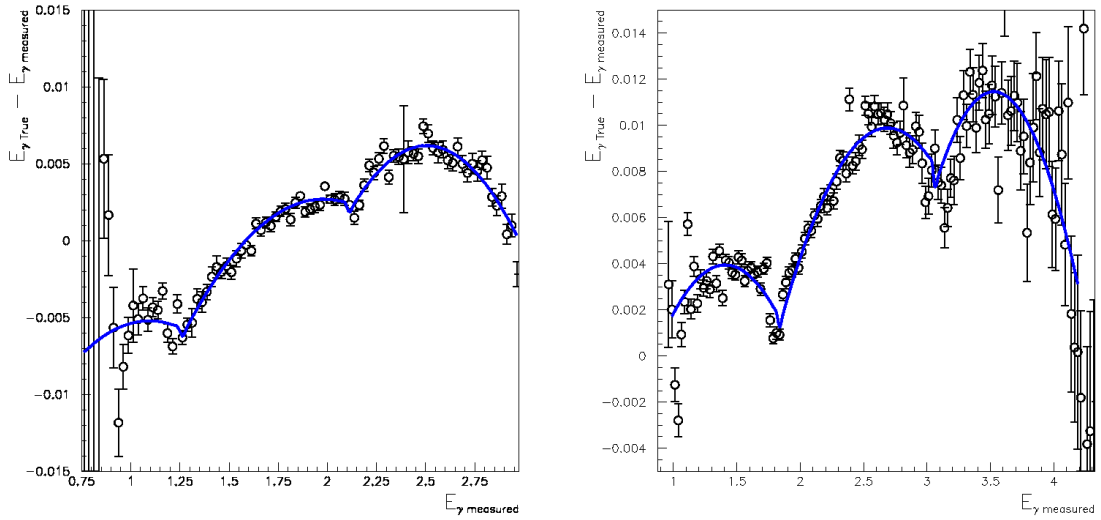

(a) g1c (b) g8b

Figure 3.7: A plot of the difference between the calculated photon energy and the measured photon energy as a function of incident photon energy using the g1c data set (a) and the g8b data set (b). The effects of the sagging of the E-counter scintillator support structures can be seen in the "humps".

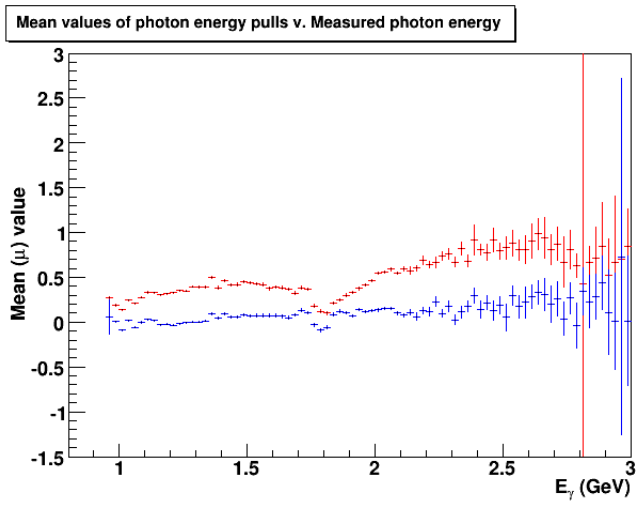

Figure 3.8: Superimposed on one another are the mean values of the photon energy pulls as extracted from the kinematic fitter versus the measured photon energy. The red points represent the mean values of the photon energy pulls before the correction and the blue points represent the mean values after the application of the photon energy corrections. These pull distributions were generated using one run for each coherent edge energy for a $p\,\pi^+\pi^-$ final state. The "humps" after this correction is applied are suppressed and the mean values shift toward zero. The sharp dip seen near $E_\gamma = 1.8$ GeV represents an effect which could not be overcome using these corrections.

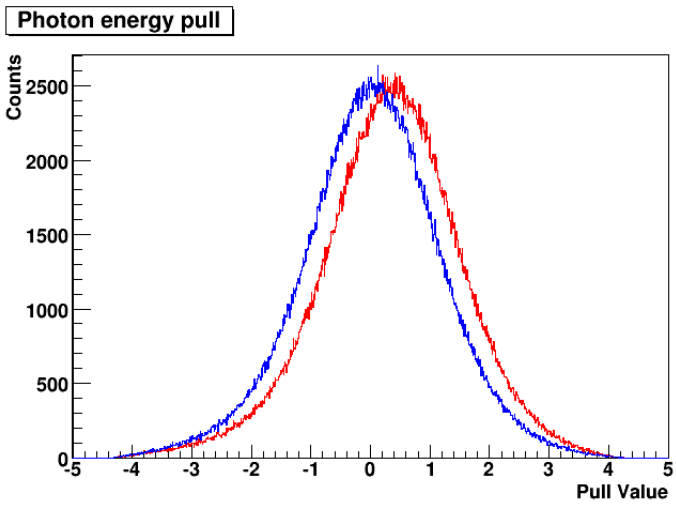

Figure 3.9: Superimposed on one another are the y-axis projections of the photon energy pulls used make Figure 3.8. These photon energy pulls were extracted from the kinematic fitter with (blue) and without (red) the energy-dependent photon corrections for $p\ \pi^+\pi^-$ final states. After the application of the photon energy corrections, the σ of the Gaussian fit changed from 1.087 to 1.069 and the μ improved from 0.374 to 0.042.

3.8 Cuts

Once the events that match one of the four topologies have been obtained and kinematically fitted, it is necessary to impose a series of cuts before extracting polarization observables. These cuts will serve to further refine the data sample and help remove accidental particles/events and other things that corrupt the data set. In the histograms contained in this section, the blue region represents the data which passes the imposed cuts.

3.8.1 Photon Energy Cut

The first cut that is applied is a cut on the photon energy. While photons are produced with a wide range of energies, the highly polarized photons occur in a 200 MeV wide window (the upper limit of which is the coherent edge energy) with this window occupying five different positions (the five different coherent edge energies). A cut on the upper and lower limits of this window ensures that the events passing this cut came from a highly polarized photon in the coherent peak (Fig. 3.10 shows an example of such a cut). This leads to a total of 5 photon energy cuts (one for each coherent edge energy):

- 1.1 GeV $\leq E_\gamma <$ 1.3 GeV
- 1.3 GeV $\leq E_\gamma <$ 1.5 GeV
- 1.5 GeV $\leq E_\gamma <$ 1.7 GeV
- 1.7 GeV $\leq E_\gamma <$ 1.9 GeV
- 1.9 GeV $\leq E_\gamma \leq$ 2.1 GeV

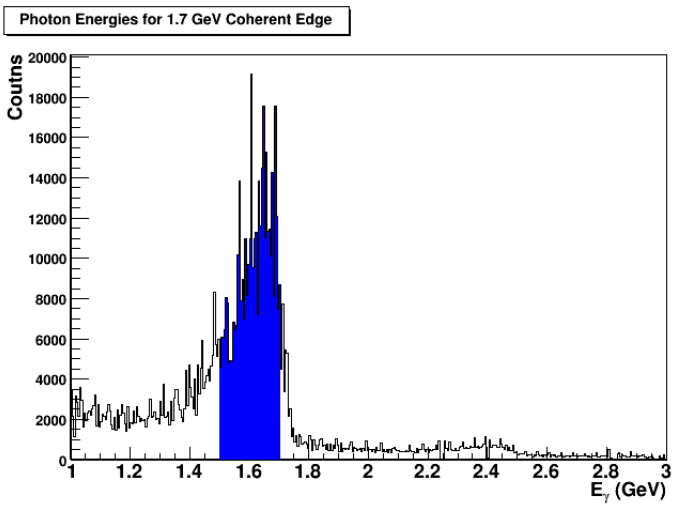

Figure 3.10: Photon energies taken from data (run #048544) produced with a coherent edge energy of 1.7 GeV using events passing a 5% confidence level cut for all final state topologies. The highly polarized photons in this coherent edge energy reside in the region between 1.5 and 1.7 GeV and therefore cuts are applied to use only these photons.

3.8.2 Final State Momentum Cut

A low momentum particle moving through CLAS presents a problem to the reconstruction of the event. These particles' possession of low momentum can affect the accuracy of the ELoss corrections applied to them. More importantly however is the fact that particles with this characteristic have a low-acceptance for detection. Using these acceptance limitations, cuts in the proton momentum and the momentum of the pions were determined and applied. This cut requires all protons have a minimum momentum of 320 MeV/c ($p_{proton} > 320$ MeV/c) and all pions have a momentum of at least 125 MeV/c ($p_{\pi^\pm} > 125$ MeV/c). These cuts may be seen in Figure 3.11.

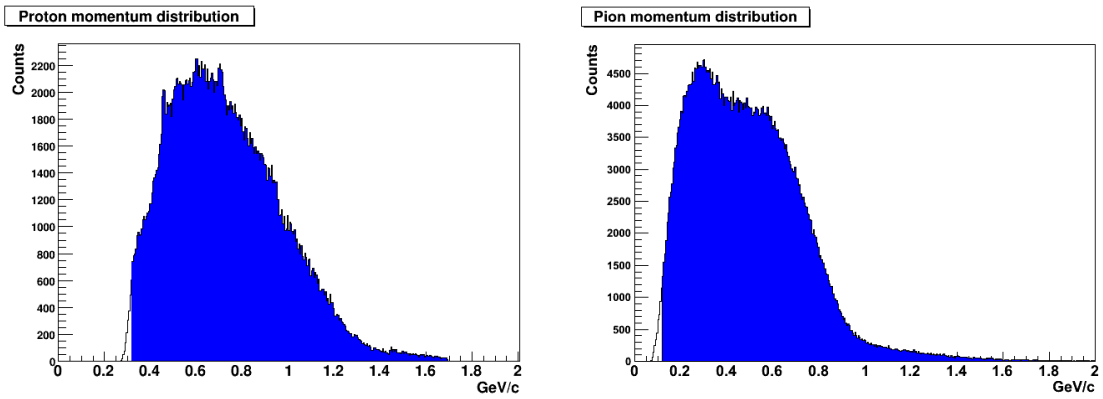

(a) All protons

(b) All pions

Figure 3.11: Momentum distributions showing the range of momentums for all (a) protons and (b) pions. Generated for $p\ \pi^+\pi^-$ events passing a confidence level cut of 1% using one full run: #048326.

3.8.3 Vertex Cut

The next set of cuts imposed in this analysis involves the vertex information for each final state particle and event. This set of cuts then ensures that the physics event originated in the target cell and all particles are from the same event.

Position. The dimensions of the target cell are well defined quantities. Therefore cuts on the vertex positions of all the final state particles which mimic these dimensions ensure that the event originated in the target cell. The first of these cuts is on the z-component of the vertex position for all final state particles. The g8b target was a 40 cm long target with its center located at z = −20 cm (Figure 3.12(a)). This vertex cut therefore requires that $-40 < z_{AllParticles} < 0$. The next cut that is applied involves comparing the vertex z-positions of all final state particles. This cut requires that the z-component of the vertex positions all final state particles be within 4 cm of each other ($| z_{particleX} - z_{particleY} | < 4$ cm) (Figure 3.12(b)). The third cut on the vertex position(s) involves the x- and y-components of the event itself. This cut makes sure that the event originated no more than 2 cm from the axis of the beamline (the z-axis). A distribution of event vertices in x, y, and x-y can be seen in Figure 3.13.

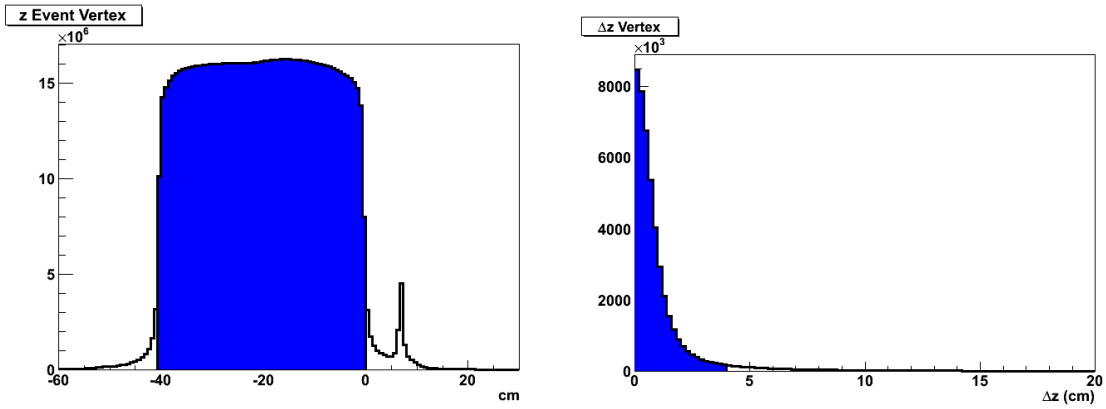

(a) (b)

Figure 3.12: (a) The vertex z-position (axis along the beam line) of all reconstructed particles showing the length and position of the target cell. The peak at ≈ 7 cm shows the exit window of the scattering chamber (the vacuum tight chamber in which the target cell resides). Events must have a z-vertex occurring between 0 and −40 cm. (b) A distribution showing the differences between the vertex z-position of the π^+ and π^- for a $\pi^+\pi^-(p)$ final state. The cut applied to this difference requires that it be no more than 4 cm.

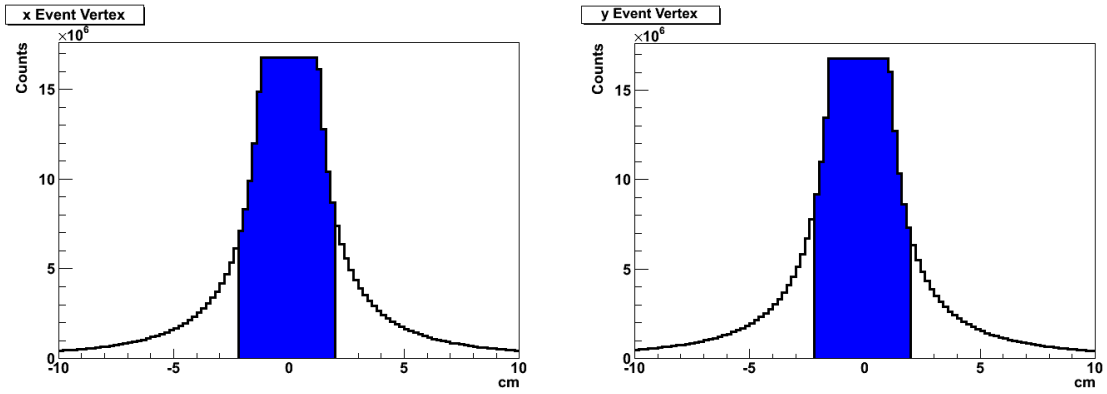

(a) x-Vertex

(b) y-Vertex

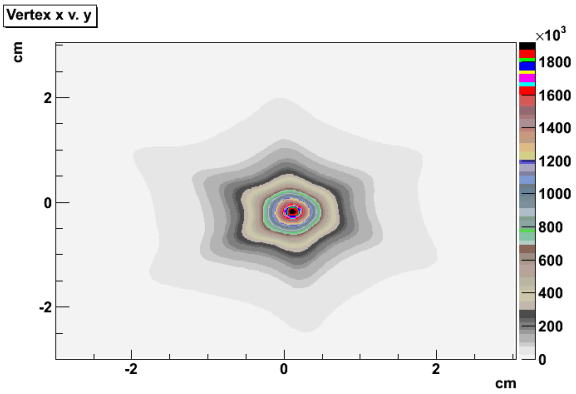

(c) x v. y Vertex

Figure 3.13: Plots showing the x- and y- vertices of all final state particles. (a) Shows the x-vertices, (b) shows the y-vertices. Histogram (c) is a plot of the x v. y vertices of the reconstructed final state particles. The vertex cut applied requires that the x- and y-components of the event to be no more than 2 cm from the beamline.

Timing. Timing information regarding the vertex time for all final state particles is used once again, but this time is used to make a cut on the time stamp of the particles' vertex. This cut is the same for all final state particles and further aids in removal of accidentals by requiring that the vertex time (for all final state particles) be between -10 ns and 20 ns (Figure 3.14).

3.8.4 Angular Cuts

The CLAS detector, while having a large acceptance, does not possess a *completely* 4π solid angle coverage. The existence of the forward-angle hole in CLAS means that it lacks acceptance from $0^\circ < \theta < 8^\circ$ and in the backward region lacks acceptance at angles greater than $\theta = 142^\circ$. These limitations combined with the observed distributions of the θ values for all final state particles (Figures 3.15 and 3.16) determine the angular cuts used. The applied cut requires that the lower limit (in θ) for all final state particles be $\theta > 10^\circ$ and the upper limit for pions be $\theta < 120^\circ$.

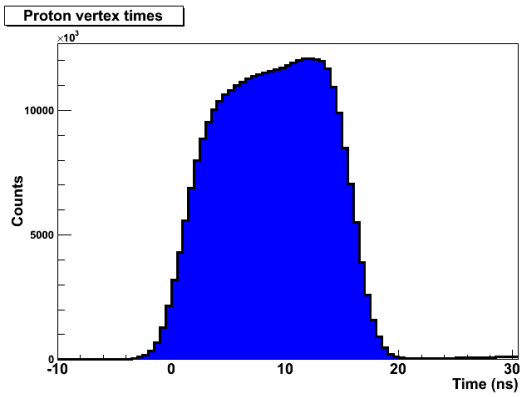

(a) Proton Vertex Time

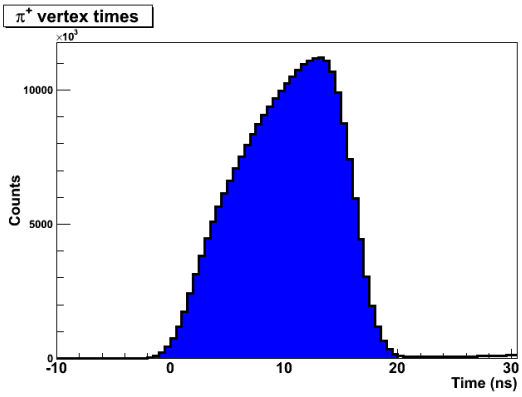

(b) π^+ Vertex Time

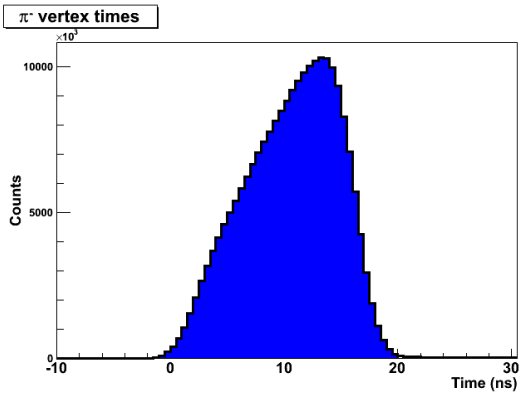

(c) π^- Vertex Time

Figure 3.14: Vertex times of final state particles. A loose cut of (−10,20) ns is enforced to help remove accidentals from the data set.

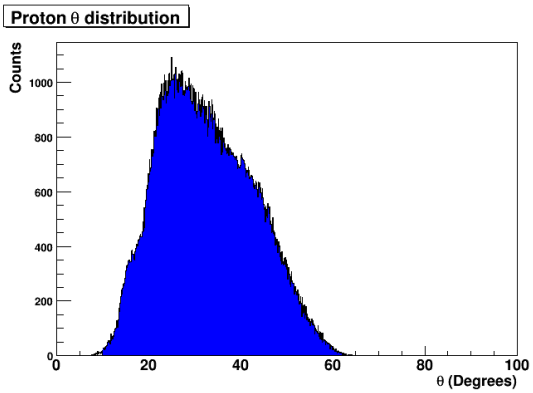

(a) Proton θ range.

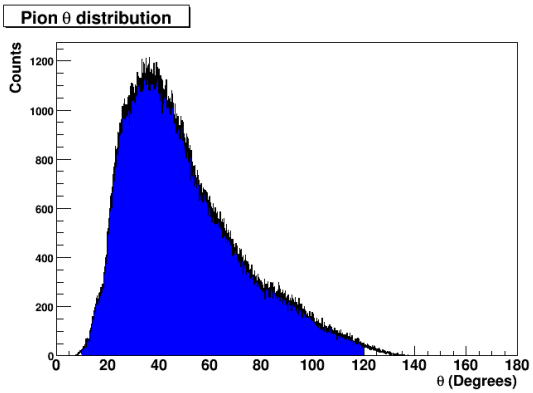

(b) Pion θ range.

Figure 3.15: Distributions showing the values of θ for all (a) protons and (b) pions. Generated for $p\,\pi^+\pi^-$ events passing a confidence level cut of 1% using one full run #048326.

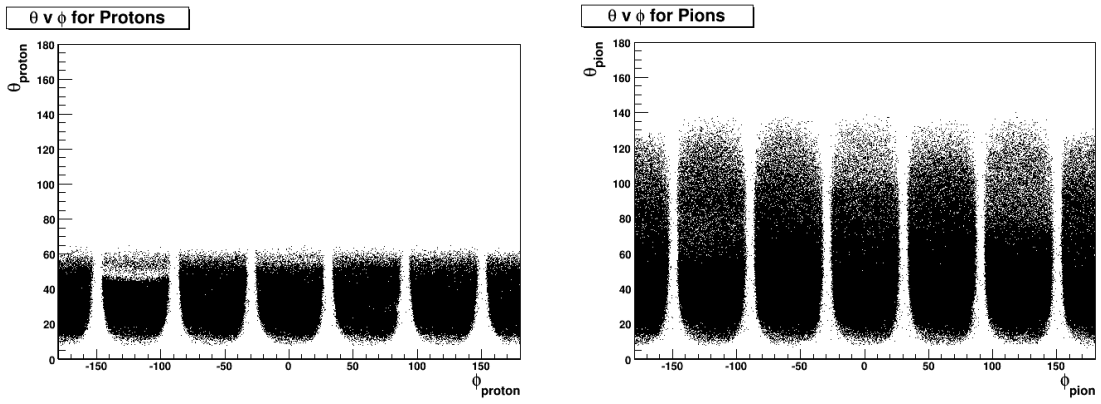

(a) θ v ϕ for Protons

(b) θ v ϕ for Pions

Figure 3.16: Distributions showing θ v ϕ for protons ((a)) and pions ((b)). The six structures apparent in the histograms represent the six sectors of CLAS. Generated for $p\,\pi^+\pi^-$ events passing a confidence level cut of 5% using one full run: #048326. The region seen in (b) showing low statistics for $-150^\circ < \phi_{proton} < -110^\circ$ is seen in several runs and can be attributed to dead wires in the Drift Chambers.

3.8.5 Other Cuts

'ngrf' and 'tagrid' Cuts. Another cut imposed on the g8b data set during this analysis is one that uses specific bank variables. These variables can be found in the GPID bank with the names 'ngrf' and 'tagrid' with both being in reference to the incident photon. The 'ngrf' variable indicates how many of the candidate photons the reconstruction code found which passed the reconstruction timing cut for finding the incident photon (using the process outlined in Section 3.3). The 'tagrid' provides an index to the location of that photon in the TAGR bank (therefore pointing to the correct photon). The cut on the 'ngrf' value imposed on all final state particles requires that they all have a value of one (ngrf=1). This means that for every final state particle, there was only one photon that was found to pass the timing requirements (occasionally the reconstruction code will find two photons that are close enough in time for a time-based selection to be inconclusive). For the 'tagrid' variable, the requirement that the value of this variable be the same for all final state particles guarantees that the reconstruction code found the same photon for all final state particles (as the photon determination occurs for every detected final state particle). These cuts ensure that the events being analyzed include a successful determination of the incident photon and that this photon is the same for all final state particles thus leading to a well-defined initial state.

Confidence Level Cut. By performing a cut on the confidence level, one can easily remove many of the background events, poorly reconstructed events as well as events with misidentified particles. A confidence level cut of 5% was imposed in this analysis (shown in Fig 3.17). This cut removes much of the background events while only cutting out 5% of the good events.

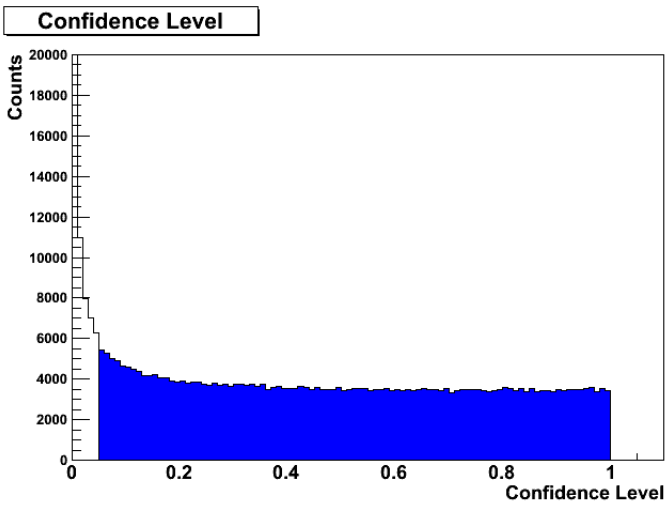

Figure 3.17: A confidence level distribution generated from run #048326 for a $p\,\pi^+(\pi^-)$ final state showing the imposed confidence level cut of 5%.

3.9 Results of Corrections and Cuts

The process of developing and applying energy and momentum corrections during the course of an analysis serves the purpose of correcting for the effects of the experimental setup, therefore resulting in a data set that is as nature intended it. Additionally, determining and enforcing cuts in an analysis serves not only to remove the remaining effects of the experimental setup but also to remove the contribution to the data set from physics events not of interest to the analysis (the background). This background may be comprised of accidental events (where a detected particle was attributed to an event to which it does not belong), events with an incorrect initial state (misidentification of a photon) and/or events originating from interactions with matter other than the target material. A typical method of observing the background is to choose a final state topology and construct the missing mass of that topology. A single cut on the confidence level greatly reduces this background but does not entirely remove it. Through the application of vertex position, vertex timing, photon identification variables, angular and momentum cuts, this background may be reduced even further or, as in the case of this analysis, almost entirely removed (the background is negligible after all cuts are imposed). The missing mass distribution seen in Figure 3.18 was generated for all $p\,\pi^+(\pi^-)$ events in run #048326 which passed the imposed cuts (with the exclusion of the confidence level cut).

The confidence level and pull distributions reveal the quality of systematic corrections as well as how well the covariance matrix errors were determined. Therefore to determine the quality of the fits, these two quantities are examined. The confidence level distributions produced in this analysis can be found in Figure 3.19. These confidence level distributions show the typical peak at zero (corresponding to poor fits, these are cut from the analysis via the confidence level cut) and a flat behavior from [0.5,1]. Distributions seen in Fig. 3.20 show the normalized slopes (given by Eq. (3.8)) of the confidence level distributions for each final state topology. Each plot shows a distribution centered around zero. This is a strong indication that the covariance matrix errors are correct.

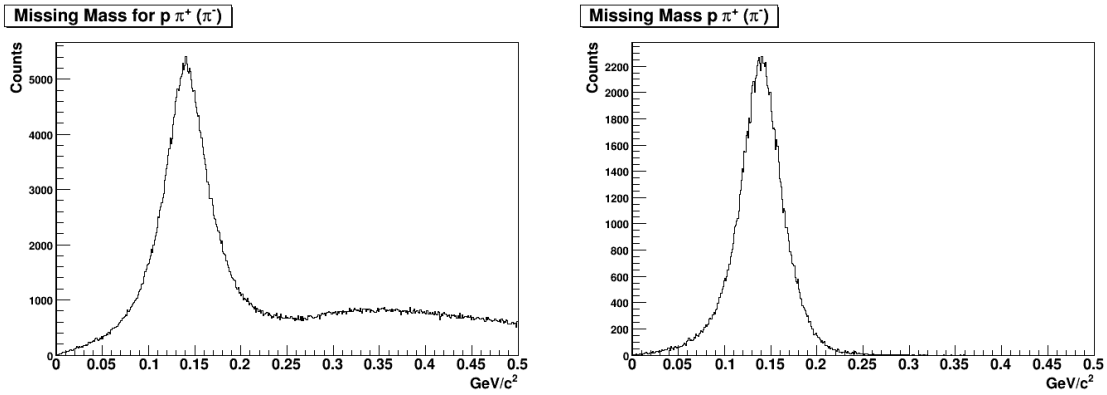

(a) Before Cuts (b) After Cuts

Figure 3.18: A missing mass plot for the final state topology $p\ \pi^+(\pi^-)$ generated from run #048326 for events passing all cuts (confidence level cut not imposed). The background events are reduced to a negligible contribution via the application of cuts imposed on the final state measurements.

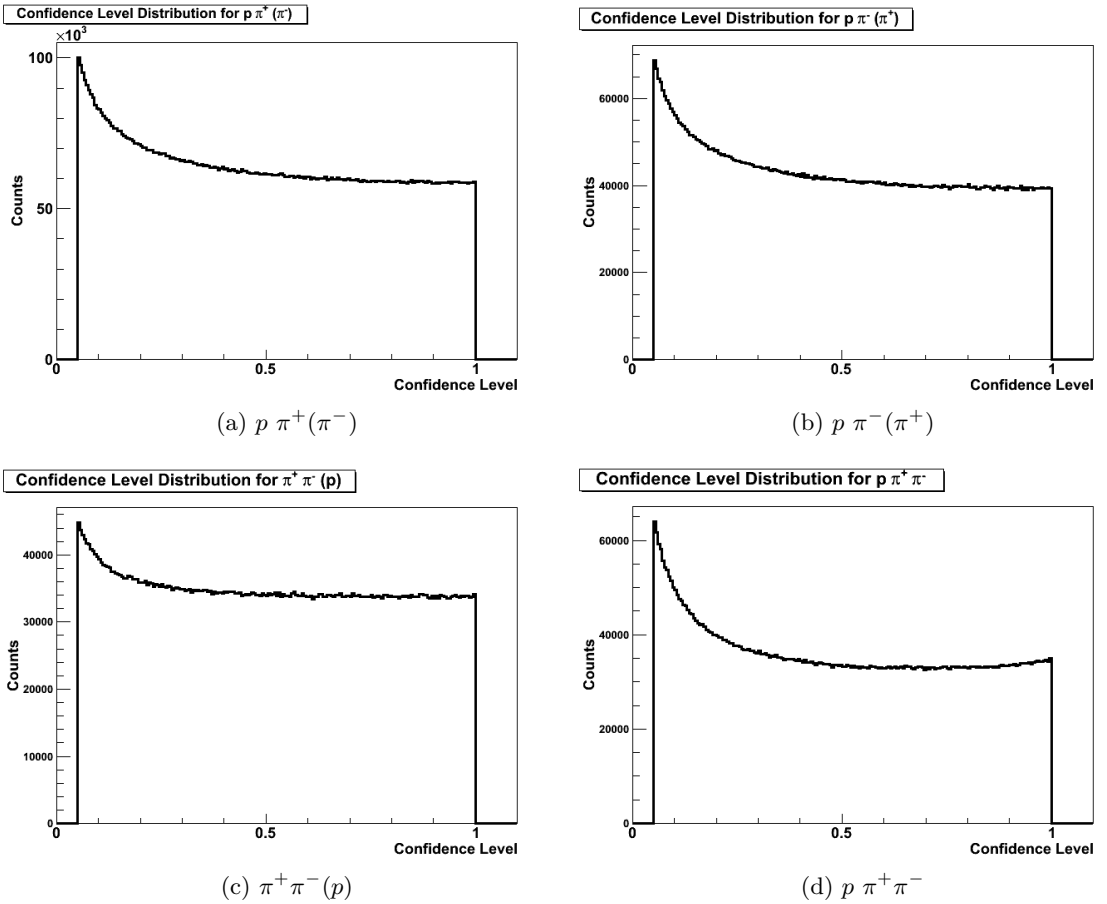

(a) $p\ \pi^+(\pi^-)$ (b) $p\ \pi^-(\pi^+)$

(c) $\pi^+\pi^-(p)$ (d) $p\ \pi^+\pi^-$

Figure 3.19: A set of confidence level distributions for all final state topologies after the application of all corrections and cuts. Generated using one run (#048326).

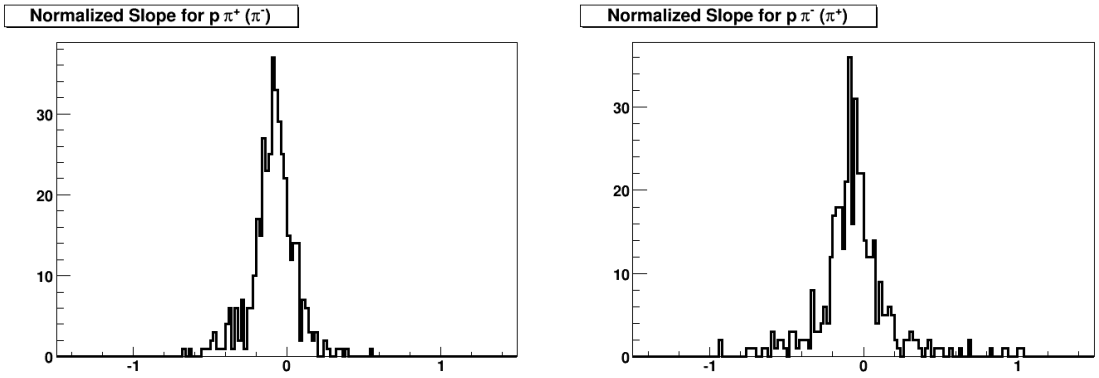

(a) $p\ \pi^+(\pi^-)$ (b) $p\ \pi^-(\pi^+)$

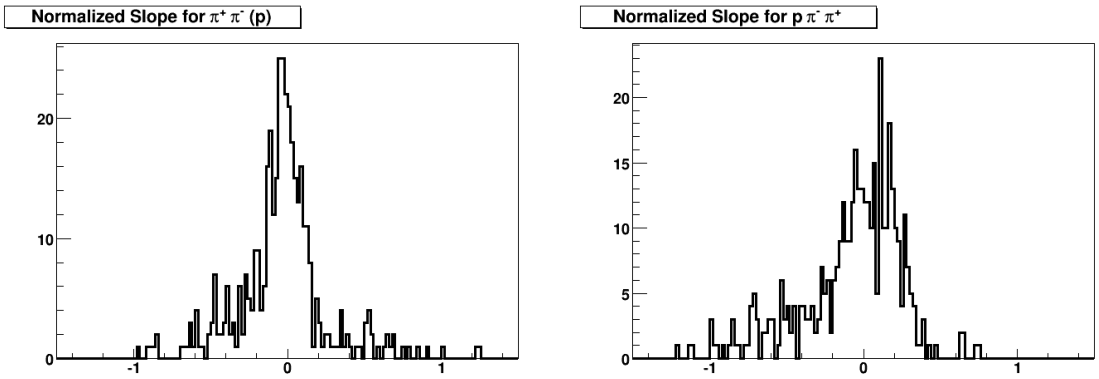

(c) $\pi^+\pi^-(p)$ (d) $p\ \pi^+\pi^-$

Figure 3.20: The normalized slope distributions for each final state topology. Each confidence level distribution was fitted to a linear equation from [0.5,1] and the normalized slope determined using Equation (3.8). The behavior of the distributions (centered around zero) indicated the flatness of the confidence level histograms. Entries that stray away from zero can be attributed to kinematical regions containing low statistics.

To provide a second check to verify if the covariance matrix errors have been properly determined, the pull distributions are examined. The following figure (Figure 3.21) shows all pull distributions resulting from a fit to a $p\ \pi^+\pi^-$ final state for events in run #048326. These pulls have been fitted with a Gaussian distribution from [−2,2]. The resulting fits show a σ close to one, indicative of the covariance matrix errors being properly determined. Also seen in Figure 3.21 are the mean values of the Gaussian fits of the pull distributions. The proximity of these mean values to zero affirms that the systematic corrections (energy loss corrections, momentum corrections and photon energy corrections) were properly determined and applied. A table containing the mean and sigma values of all of the fits seen in Figure 3.21 can be found in Table 3.1.

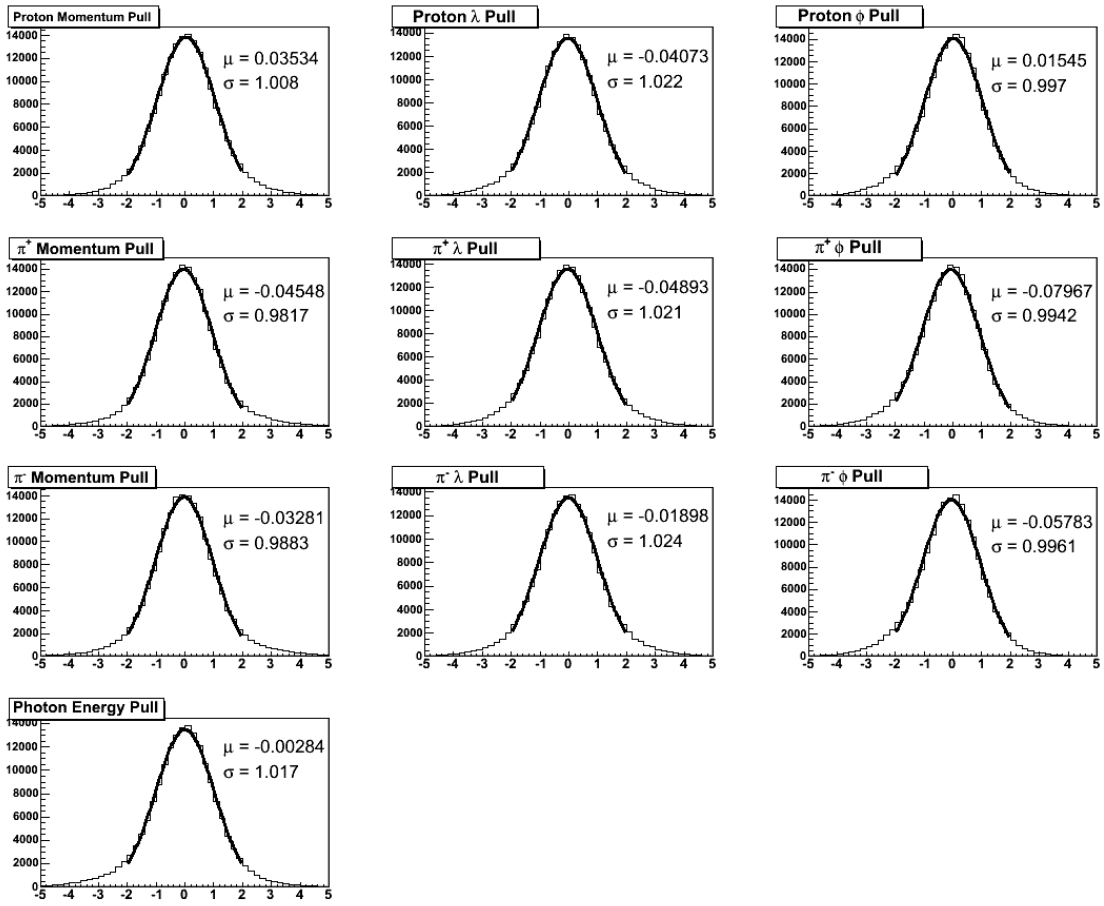

Figure 3.21: Pull distributions generated from a kinematic fit to a $p\ \pi^+\pi^-$ final state for events in run #048326. Distributions are fitted with a Gaussian from [−2,2].

Table 3.1: The Gaussian mean (μ) and sigma (σ) values for all fits to the pull distributions seen in Figure 3.21.

Parameter	Mean (μ)	Sigma (σ)
p_p	0.035	1.008
λ_p	−0.041	1.022
ϕ_p	0.015	0.997
$\mathrm{p}_{\pi+}$	−0.045	0.982
$\lambda_{\pi+}$	−0.049	1.021
$\phi_{\pi+}$	−0.080	0.994
$\mathrm{p}_{\pi-}$	−0.033	0.988
$\lambda_{\pi-}$	−0.019	1.024
$\phi_{\pi-}$	−0.058	0.996
E_γ	−0.003	1.017

CHAPTER 4

DATA ANALYSIS

Once the final state topologies of interest have been selected from the data, the corrections and cuts applied and kinematic fitting performed, the process of extracting the polarization observables I^s and I^c may begin. This chapter will focus on the methods used to extract these two polarization observables.

4.1 Binning and Angles

In order for any analysis to be carried out, the kinematics involved in the reaction of interest must be understood. The description of the kinematics involved in the reaction $\vec{\gamma}\ p \rightarrow p\ \pi^+\pi^-$ requires a choice of five independent kinematic variables. The kinematic variables chosen for this analysis are $\cos\theta^p_{CM}$, a mass ($m_{p\pi^+}$, $m_{p\pi^-}$, or $m_{\pi+\pi^-}$), the incident photon energy (k), $\theta^*_{\pi^+}$, and $\phi^*_{\pi^+}$. A diagram showing the kinematics involved in the analysis of this $p\ \pi^+\pi^-$ final state can be seen in Figure 4.1. This diagram illustrates the kinematics in not only the center-of-mass frame (the blue plane in the figure) but also the decay frame in which the two final state pions occur back-to-back (the gold plane). The vectors describing the final state particles in the center-of-mass frame are shown by the vectors drawn with a solid line while the vectors with a dashed line represent the final state particles in the decay frame.

The angle ϕ^* is a kinematical variable unique to a final state containing two mesons. It describes the orientation of the decay plane containing the two pions (defined by the z′-axis and the π' 4-vector) with respect to the production plane (defined by the incident photon and recoiling proton) and is measured with respect to one final state pion. This angle (ϕ^*) is calculated via two boosts, the first being a boost along the beamline (the z-axis) into the center-of-mass frame. The second boost occurs along the axis that is antiparallel to the recoiling proton and results in a boosting into the decay frame where the two final state pions occur back-to-back. Describing the angle between one of the final state pions and the axis defined as being anti-parallel to the recoiling proton in the center-of-mass frame (the z′-axis) is the angle θ^*_π. This angle is also calculated via boosting into the pion frame. For this analysis, the pion from which both angles are measured was chosen to be the π^+. The coordinate system formed to calculate these angles is put together thusly (see also Figure 4.1):

1. The z′-axis is formed by adding the 4-vectors of the two final state mesons:

$$\vec{z}\,' \;=\; (\vec{\pi}^{+}_{CM} \;+\; \vec{\pi}^{-}_{CM}). \tag{4.1}$$

2. The y′-axis (pointing "up" perpendicular to the production plane) is formed by taking the cross product of the target proton and the recoiling proton in the center-of-mass frame:

$$\vec{y}\,' \;=\; (\vec{p} \;\times\; \vec{p}\,'). \tag{4.2}$$

3. Finally, the x′-axis is formed by taking the cross product of the y′- and the z′-axes:

$$\vec{x}\,' \;=\; (\vec{y}\,' \;\times\; \vec{z}\,'). \tag{4.3}$$

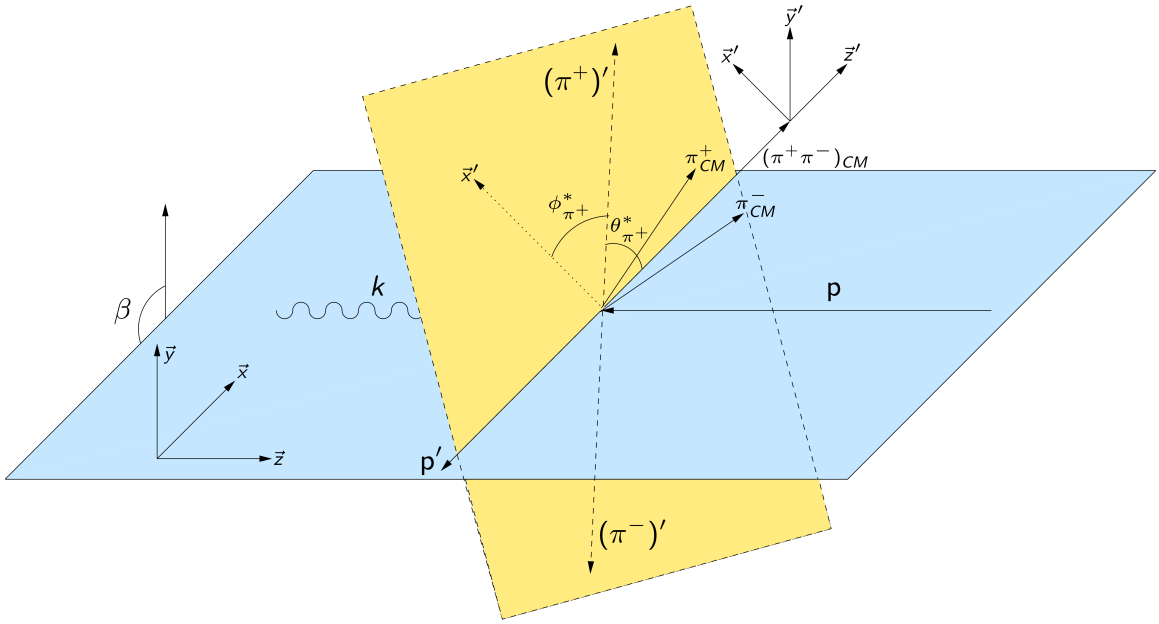

Figure 4.1: A diagram describing (one possible configuration of) the kinematics of $\vec{\gamma}p \to p\,\pi^+\pi^-$ reactions. The blue plane represents the center-of-mass (CM) production plane while the gold plane represents the decay plane (where the two pions are produced back-to-back). Vector drawn with a solid line represent final state particles in the CM frame while the vectors drawn with a dashed line represent the final state particles in the decay frame. The pion 4-vectors in the CM frame ($\vec{\pi}^{+}_{CM} \;+\; \vec{\pi}^{-}_{CM}$) are used to form the $\vec{z}\,'$-axis. The $\vec{y}\,'$-axis is formed by determining the cross product of the target and recoil proton's 4-vector ($\vec{p} \;\times\; \vec{p}\,'$). The $\vec{x}\,'$-axis is then determined by forming the cross product of the $\vec{y}\,'$ and $\vec{z}\,'$ axes ($\vec{y}\,' \;\times\; \vec{z}\,'$). The angle $\phi^*_{\pi^+}$ is shown here and is the angle between the $(\pi^+)'$ (the 4-vector of π^+ after a boost into the decay frame) and the $\vec{x}\,'$-axis (which lies in the production plane). The angle $\theta^*_{\pi^+}$, also shown here, is the angle between the $(\pi^+)'$ and the $\vec{z}\,'$-axis.

The data is then binned in three out of these five independent kinematical variables. These binning variables are: incident photon energy (k), $\theta^*_{\pi^+}$ and $\phi^*_{\pi^+}$. The decision to bin in the incident photon energy (E_γ) was a matter of convention while the decision to bin in the angles θ^* and ϕ^* came from the fact that they are unique to a three-body final

state. A diagram of the reaction of interest and the angles used for binning can be seen in Figure 4.1. In terms of photon energy, k, each 200 MeV-wide window of highly polarized photons is divided into four bins each being 50 MeV wide. With there being 5 different coherent edge energies, this leads to a total of 20 bins in incident photon energy, covering a range from 1.1 GeV to 2.1 GeV. For the other two binning variables ($\theta^*_{\pi^+}$ and $\phi^*_{\pi^+}$), 20 bins in $\cos\theta^*_{\pi^+}$ (covering a range from $-1 \leq \cos\theta^*_{\pi^+} \leq 1$) and 20 bins in $\phi^*_{\pi^+}$ (covering a range from $-\pi \leq \phi^*_{\pi^+} \leq \pi$) are used. This choice of binning therefore results in a total of 8000 bin combinations per final state topology.

4.2 Phi Distributions

When using unpolarized photons, the production of the final state particles is independent of the azimuthal lab angle ϕ. This analysis, however, involves the use of linearly polarized photons which breaks this symmetry. Therefore a plot of the distribution of events over the full range of the lab angle ϕ (with respect to a particular final state particle) can be made, revealing this asymmetry.

The two orthogonal linear polarization settings used during g8b, termed PARA and PERP, denote the relationship between the $\vec{E}$ field of the polarized photon and the axis where $\phi_{lab} = 0$. Therefore a PARA setting indicates that the photon was polarized such that its $\vec{E}$ field (electric field) oscillates in a plane parallel to $\phi_{lab} = 0$ (the floor of the experimental hall) and the PERP setting indicates that the oscillation of the photon's $\vec{E}$ field is perpendicular to $\phi_{lab} = 0$. The cartoon seen in Figure 4.2 demonstrates these two settings. To produce unpolarized photons, an amorphous radiator was used in place of the diamond radiator. This setting is termed the amorphous (AMO) setting.

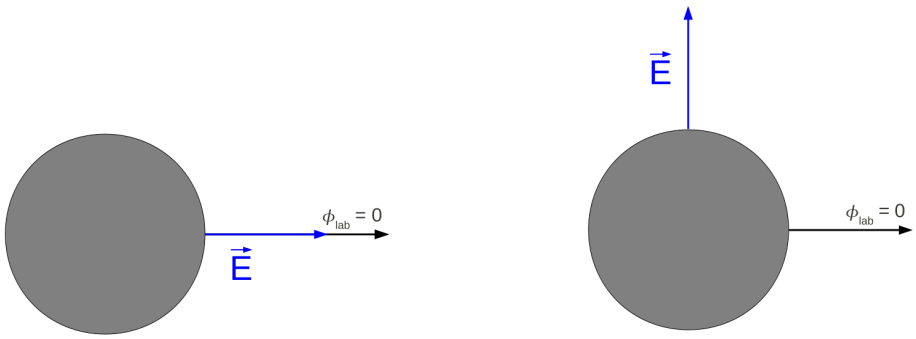

(a) PARA (b) PERP

Figure 4.2: A cartoon describing the two linear polarization settings of the photon. For the PARA setting (a), the $\vec{E}$ field oscillates in a plane parallel to the floor ($\phi = 0$) of the experimental hall while for the PERP setting (b), the oscillation of the $\vec{E}$ field is perpendicular to the floor of the experimental hall.

During the course of this analysis there were two methods developed to extract the polarization observables. The common trait between these two methods is that they both begin with the production of histograms containing the ϕ_{lab} distributions (hereby referred

to as ϕ-*distributions*) containing the ϕ_{lab} value of a final state particle (in this case, the π^+) for all events which pass the imposed cuts. Exploiting the fact that the use of polarized photons breaks the ϕ symmetry, events are plotted as a function of the lab angle ϕ_{π^+} for each polarization setting (Figure 4.3).

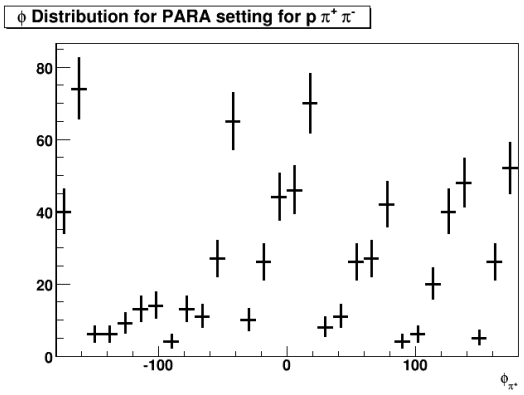

(a) PARA ϕ-distribution

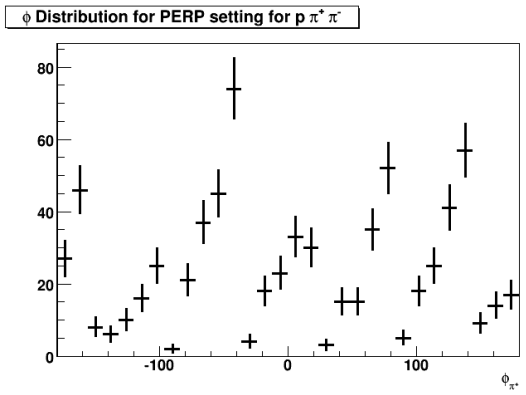

(b) PERP ϕ-distribution

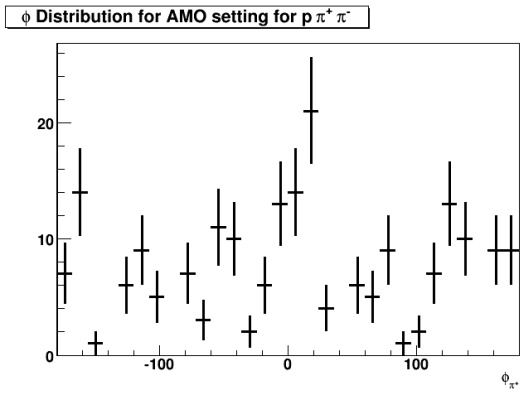

(c) AMO ϕ-distribution

Figure 4.3: ϕ-distributions for each polarization setting for a $p\,\pi^+\pi^-$ final state using data from the 1.3 GeV coherent edge setting. All three histograms belong to the same bin combination (1.25 GeV $< E_\gamma <$ 1.3 GeV, $-1 < \cos\theta^*_{\pi^+} < -0.9$, $180^\circ < \phi^*_{\pi^+} < 198^\circ$). Acceptance effects (such as the support structures of the Drift Chambers) can be seen in all figures and demonstrate the need for a method which would remove these acceptance effects. Furthermore, as the error bars for the measurements are an indication of available statistics, the low-statistics problem for the AMO setting is clearly evident. This low amount of statistics for the AMO setting leads to observable measurements which also possess large error bars.

Systematic effects which drown out the ϕ asymmetry can easily be seen in these distributions. An example of such an effect are the support structures of the Drift Chambers which, as one might expect, affect the distributions as no particle will be detected where the support structure is. The effects of these support structures can be seen at $\phi_{pi^+} = -150^\circ$, -90°, -30°, 30°, 90° and 150° in all three histograms. For this reason, two methods are carried out which remove these systematic effects, leading to a measurement of the polarization

observables.

4.2.1 Method 1: Using unpolarized (AMO) data

The first method for extracting the polarization observables involves using the unpolarized (AMO) data. Even though corrections and cuts have been imposed on the events that are plotted in the ϕ-distributions, systematics such as the support structure of the the Drift Chambers are still present in the distributions. In order to remove these effects, the ϕ-distributions for each of the linear polarization settings is divided by the AMO ϕ-distribution (for matching bin combinations) (Figure 4.4). The resulting distribution is then fitted to the double-meson final state equation with the g8b run conditions applied [4]:

$$I = I_0 \{ 1 + \delta_l [\mathbf{I^s} \sin(2\beta) + \mathbf{I^c} \cos(2\beta)] \}, \tag{4.4}$$

which when written as a fit equation, becomes:

$$f(\beta) = \mathrm{y_0} + \delta_\mathrm{l} [\mathbf{I^s} \sin(2\beta) + \mathbf{I^c} \cos(2\beta)], \tag{4.5}$$

where the quantity $\mathrm{y_0}$ represents the possible vertical offset of the ϕ-distribution and the corresponding fit.

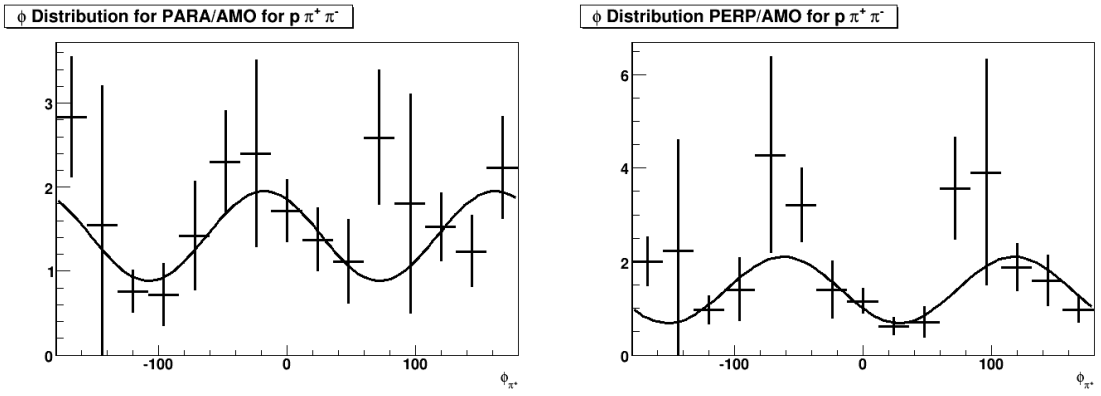

(a) PARA/AMO (b) PERP/AMO

Figure 4.4: ϕ-distributions generated by dividing the PARA and PERP ϕ-distributions by the AMO ϕ-distribution (using the histograms seen in Figure 4.3). The solid line on both (a) and (b) represents the fitting of the distributions with Equation (4.5). Once this fit is performed, the observables $\mathrm{I^s}$ and $\mathrm{I^c}$ can be extracted. The large error bars and low number of data points seen in both histograms demonstrate the limitation of extracting the polarization observables in this manner. This limitation arises from the low amount of statistics contained in the amorphous (AMO) data.

The polarization observables $\mathrm{I^s}$ and $\mathrm{I^c}$ can then be readily extracted from the fitted ϕ-distributions. The downside of producing observable measurements in this way is that the statistics of the ϕ-distribution to be fit is limited by the number of events in the AMO distribution. This AMO setting possesses the lowest amount of statistics in the g8b data set. This reduction of events in the PARA/AMO or PERP/AMO distributions directly

affects the fits and the fit qualities therefore affecting the final polarization observable measurements. This difference in statistics can be seen in Figure 4.3. Both the PARA and PERP phi distributions contain roughly five times the statistics of the AMO ϕ-distribution for the same bin combination. In order to produce observable measurements with minimal statistical errors, another method is needed which does not depend on the statistics of the AMO polarization setting.

4.2.2 Method 2: Asymmetry between the two linear polarization settings, PARA and PERP

The second method for extracting polarization observables from the data is independent of the (statistic-poor) AMO data and therefore leads to observable measurements with much smaller statistical errors. This method possesses the characteristic that it uses the asymmetry between the PARA and PERP polarization settings. Just like the previously discussed method, the starting point is the generation of ϕ-distributions for both the PARA and PERP settings. The asymmetry between these ϕ-distributions is then formed. Finally, this asymmetry is fit to the asymmetry equation involving PARA and PERP (substituting in the final state equation for two mesons for each setting):

$$A(E_\gamma, \theta^*_{\pi^+}, \phi^*_{\pi^+}, \theta^{cm}_p, m_{p\pi} or m_{\pi\pi}) \;=\; \frac{I^{PARA} \;-\; I^{PERP}}{I^{PARA} \;+\; I^{PERP}}, \tag{4.6}$$

with m standing for an invariant mass ($m_{\pi\pi}$ or $m_{p\pi}$) and I having the form seen in Equation (4.4) with I^{PARA} and I^{PERP} being defined as:

$$I^{PARA} \;=\; I_0 \;\{\; 1 \;+\; \delta_l \;[\mathbf{I^s} \sin(2\beta) \;+\; \mathbf{I^c} \cos(2\beta) \;]\;\} \tag{4.7}$$

and

$$I^{PERP} \;=\; I_0 \;\{\; 1 \;+\; (-)\delta_l \;[\mathbf{I^s} \sin(2\beta) \;+\; \mathbf{I^c} \cos(2\beta) \;]\;\}, \tag{4.8}$$

where δ_l represents the degree of linear polarization. The orthogonality of the two polarization settings, PARA and PERP, gives rise to the minus sign seen in Equation (4.8). The angle β denotes the azimuthal angle being a combination of ϕ_{lab} and the orientation of linear polarization ($\beta = \phi_{lab} + \phi_{polarization}$) where $\phi_{polarization}$ equals 0° or 90° (0 or $\frac{\pi}{2}$ radians). Placing equations (4.7) and (4.8) in equation (4.6) then gives (after simplification):

$$A(E_\gamma, \theta^*_{\pi^+}, \phi^*_{\pi^+}) \;=\; y_0 + B(E_\gamma, \theta^*_{\pi^+}, \phi^*_{\pi^+}) \tag{4.9}$$

where y_0 is the vertical offset of the distribution and

$$B(E_\gamma, \theta^*_{\pi^+}, \phi^*_{\pi^+}) \;=\; \frac{(\delta_l^{\parallel} \;+\; \delta_l^{\perp})\; \mathbf{I^s} \sin(2\beta) \;+\; (\delta_l^{\parallel} \;+\; \delta_l^{\perp})\; \mathbf{I^c} \cos(2\beta)}{2 \;+\; (\delta_l^{\parallel} \;-\; \delta_l^{\perp})\; \mathbf{I^s} \sin(2\beta) \;+\; (\delta_l^{\parallel} \;-\; \delta_l^{\perp})\; \mathbf{I^c} \cos(2\beta)} \tag{4.10}$$

(here $\parallel$ represents the PARA setting and $\perp$ represents the PERP setting).

The resulting ϕ-distribution can then be fit to this asymmetry equation (4.9). Provided as an example, the fits of two ϕ-distributions to this equation for a $p\ \pi^+\pi^-$ final state can be seen in Figure 4.5. Once the fit is performed, the polarization observables (being simply the constants in front of the cosine and sine terms) can be extracted.

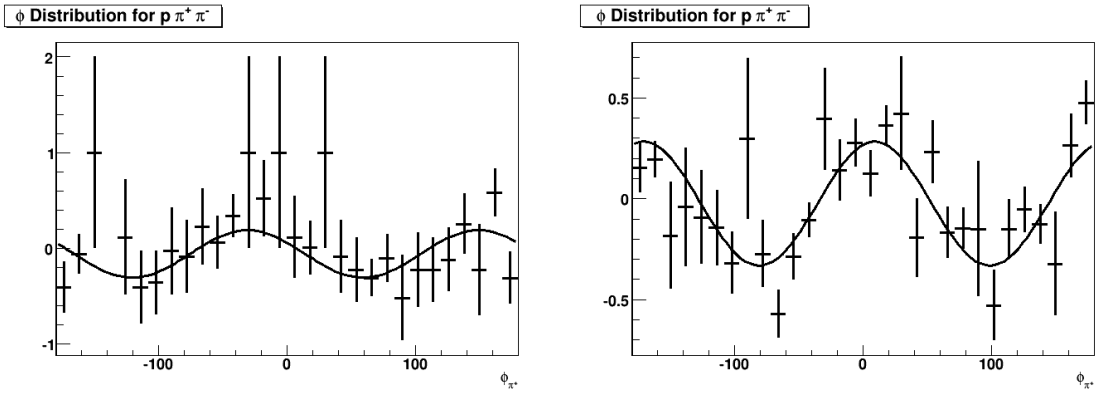

Figure 4.5: Examples of ϕ-distributions generated using the asymmetry between PARA and PERP which have been fitted with the final state equation (Equation (4.9)). The distribution seen in (a) corresponds to 1.1 GeV $< E_\gamma <$ 1.15 GeV, $-0.9 < \cos\theta^*_{\pi^+} < -0.8$, $108^\circ < \phi^*_{\pi^+} < 126^\circ$ and the distribution seen in (b) corresponds to 1.25 GeV $< E_\gamma <$ 1.3 GeV, $-1 < \cos\theta^*_{\pi^+} < -0.9$, $180^\circ < \phi^*_{\pi^+} < 198^\circ$). Both distributions were generated for a $p\ \pi^+\pi^-$ final state. By using the asymmetry between the PARA and the PERP settings to generate the ϕ-distributions, the number of data points is greater and the error bars for these points smaller leading to a much better fit.

4.3 χ^2 of ϕ-distributions

The high amount of statistics available in the g8b data set results in the ability to bin in three or more of the independent kinematical variables (although the statistics contained in each bin combination decreases as the number of binning variables used increases). The cost of this however (whether binning in all or three of the kinematic variables), is the large number of possible bin combinations and therefore a large number of ϕ-distributions to be fit. For example, binning in only three of the five kinematic variables for each final state topology leads to 32000 individual fits of the generated ϕ-distributions. When considering the methods used to produce the fitted histograms (PARA/AMO, PERP/AMO, and the asymmetry between PARA and PERP), this total increases to 96000. This makes it such that there are too many individual fits to be checked by eye. Due to this large number of individual fits, the most efficient method for judging the quality of the fits is to examine the distribution of the χ^2 values for the fits. Such a distribution can be seen in Figure 4.6 for a $p\ \pi^+(\pi^-)$ final state for all bin combinations. The ϕ-distributions which are fitted to extract the observables have 30 bins each in ϕ_{lab} leading to 30 degrees of freedom in the fit. With the freezing of three of these degrees of freedom to use as fit parameters, the final total degrees of freedom is then 27. As the values of the χ^2s coming from each fit should (ideally) reflect the number of degrees of freedom possessed by the fit, a plotting of the χ^2 values from the fits of the ϕ-distributions is expected to be a distribution centered around a value of 27. The distribution seen in Figure 4.6 shows such a behavior, indicating quality fitting of the ϕ-distributions generated from the data.

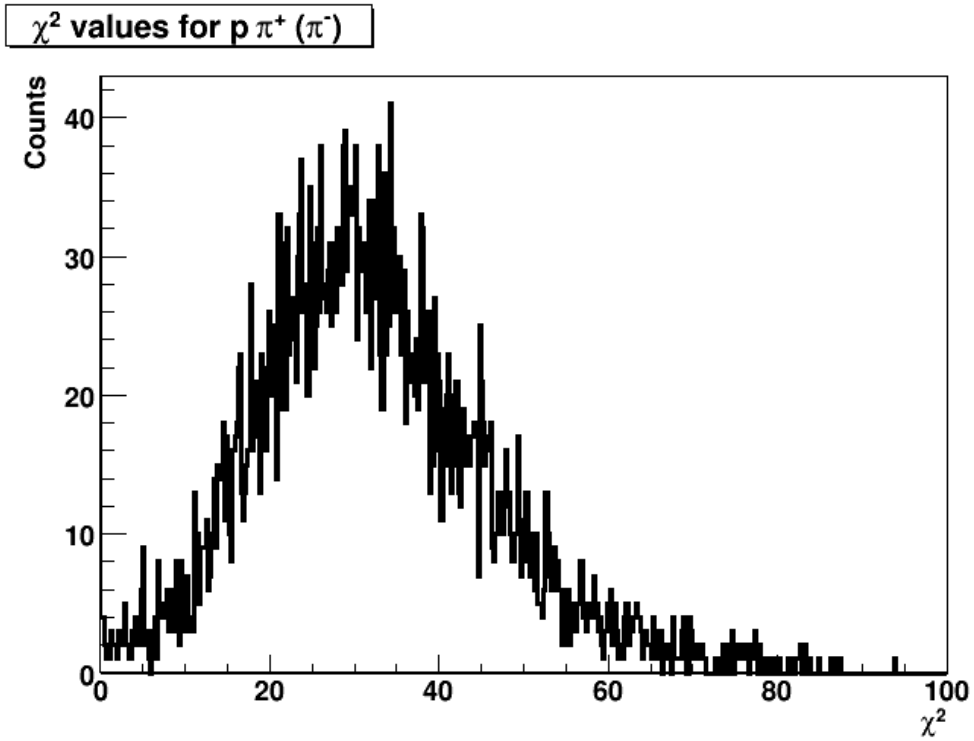

Figure 4.6: A distribution of χ^2 values reflecting the fit quality of the fits of the ϕ-distributions for all events with a $p\ \pi^+(\pi^-)$ final state. Each ϕ-distribution has 30 total degrees of freedom involved in the fit. With three degrees of freedom being reserved for fit parameters, the total degrees of freedom total 27. Therefore a χ^2 distribution around 27 is an indication that the fits of the ϕ-distributions are of good quality and trustworthy.

4.4 Vertical offset of ϕ-distribution fits

The main fit parameters of interest concerning the fits of the ϕ-distributions are of course the polarization observables. However, the vertical offsets of the fitted ϕ-distributions are indicative of and hold weight in the discussion of the quality of the measurements of these observables. Resulting from the method used to produce the observable measurements (forming the asymmetry between PARA and PERP), this offset is expected to have a value of zero. To verify this, histograms containing the offsets for each final state topology for all bin combinations were generated (Figure 4.7). The resulting histograms show a distribution centered around zero. A fit of the histograms to a Gaussian from [−0.1,0.1] and the results are shown in the figure. These fit results indicate that the fits of the ϕ-distributions (and of course, the ϕ-distributions themselves) have the appropriate vertical offset consistent with zero.

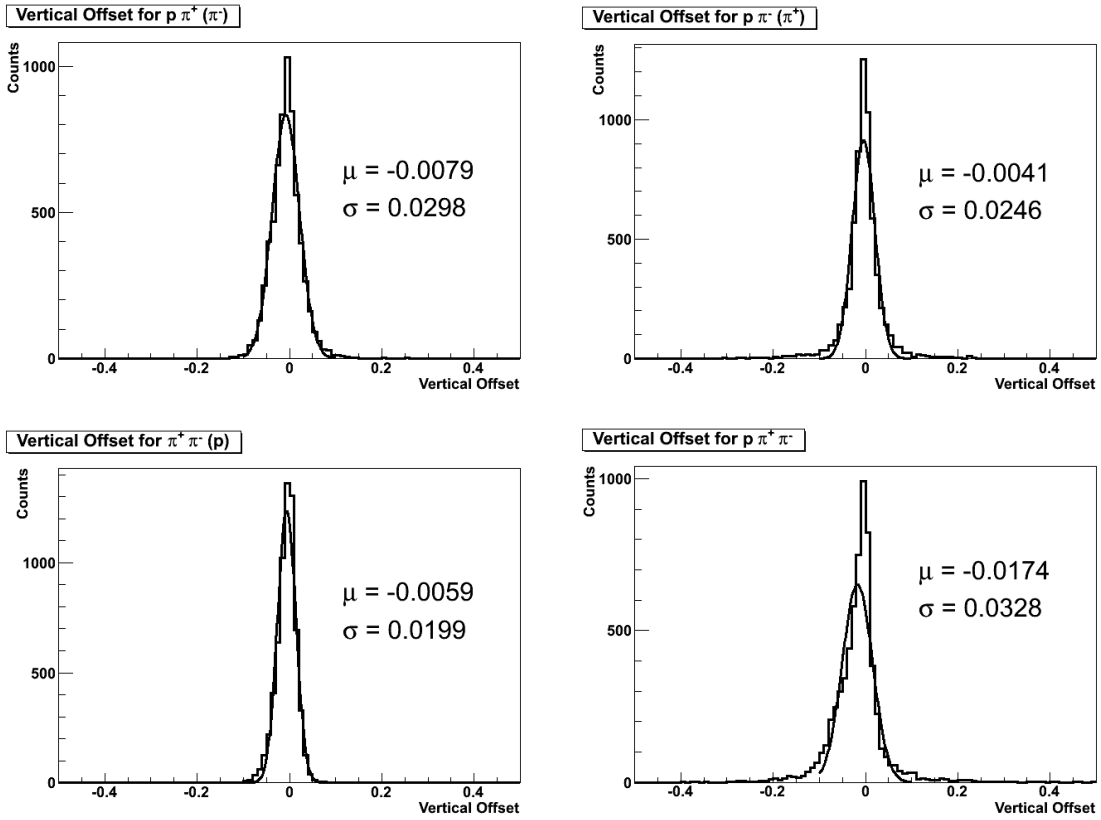

Figure 4.7: Histograms containing the offsets for each final state topology for all bin combinations. A fit of these histograms to a Gaussian from [−0.1,0.1] show the distributions as being centered around zero. These fit results indicate that the fits of the ϕ-distributions (and the ϕ-distributions themselves) have the appropriate vertical offset.

4.5 Accounting for detector acceptance

The acceptance of the events occurring in the CLAS detector is not uniform for all kinematical regions. This kinematically-dependent acceptance must then be considered in the analysis of the data and presentation of results. The traditional method for accounting for such acceptance effects is done via Monte Carlo simulations of the data. In these simulations, events are generated and the detector response to said events simulated. The results of this simulation can then be analyzed, the acceptance determined and the data corrected for acceptance.

However, this acceptance can also be accounted for through the use of analysis techniques using the data alone. In this work, the analysis techniques used to produce observable measurements account for this kinematically-dependent acceptance rendering a Monte Carlo simulation of the data unnecessary. First of all, both methods used to extract I^s and I^c use only ϕ-distributions with matching bin combinations to produce the observable measurements for each final state topology. Additionally, each kinematic variable that is used for binning the data (E_γ, $\theta^*_{\pi^+}$, $\phi^*_{\pi^+}$) is divided into 20 bins. This leads to bin widths that

are small enough for the kinematic acceptance to not vary within a particular bin combination. Therefore the combination of (sufficiently) small bins and the two methods used to extract the observables leads to this kinematically-dependent acceptance being accounted for (divided out) by comparing the same region of phase space.

4.6 Systematic Uncertainty

4.6.1 Degree of photon polarization (δ_l)

One source of systematic uncertainty in this analysis comes from the determination of the degree of polarization of the photons (δ_l). In order to carry out this calculation, the position of the coherent edge, defined as the part the photon energy spectrum with the highest negative gradient, must be determined. This is done by producing a photon enhancement plot (such as those seen in Figure 2.8) then fitting this enhancement plot over the range of the coherent peak. This peak position (determined from the enhancement plot) is then compared to the ANB analytic bremsstrahlung calculation [57]. This calculation models the production of linearly polarized photons produced via an electron beam and a diamond radiator. This modeling allows for the consideration of (and adjustment of) the electron beam divergence as well as the size of the beam spot, both affecting the coherent edge position. This calculation is run many times, varying parameters which affect the degree of polarization such as the electron beam energy, radiator thickness and the geometry of collimator. A more detailed description of these parameters may be found in [58]. This is carried out until the ANB calculations show good agreement with the enhancement plot produced from the data (Figure 4.8). This process is carried out for the entire range of coherent edge positions. The calculated mean polarization as a function of photon energy (E-counter) is then read into a look-up table per coherent edge position which is accessed during the analysis.

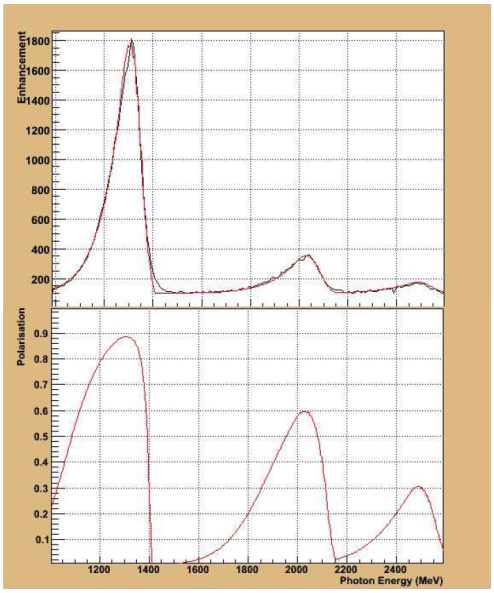

Figure 4.8: The top plot of this figure shows the collimated photon energy spectra compared with the result from the ANB calculation for the 1.3 GeV coherent edge. The bottom plot here shows the degree of photon polarization versus photon energy.

The systematic uncertainty involved in the calculation of the photon's degree of linear polarization can be attributed to four sources. The first of these sources arises from the dependence of the degree of polarization on the energy measurement of the photon coming from the Tagger E-plane. In the Tagger hodoscope, up to six of the E-counter bins can be associated with a single T-counter bin. This leads to an uncertainty in the true position of the coherent peak, affecting the calculated degree of polarization. The second source comes from the set of parameters used in the ANB calculations. This uncertainty can be attributed to the fact that there exists a range of values these parameters may possess which would lead to a satisfactory comparison with the data. Thirdly, instabilities in the position of the electron beam lead to instabilities in the position of the coherent edge. This variation in edge position leads to a fluctuation in the degree of polarization of the photons contained in the peak. This fluctuation is not handled in the ANB calculations which leads to an uncertainty in the calculated value of δ_l. Lastly, the normalization procedure can be affected by the "spikiness" of the photon energy spectra which may cause errors when producing the enhancement plots. These effects were studied in reference [57] with the total systematic uncertainty in the degree of photon polarization being found to be $\pm 4.3\%$.

4.6.2 Fit offsets (y_0)

Another possible source of systematic error can be attributed to the technique used to extract the observable measurements: forming and fitting the asymmetry, $A(E_\gamma, \theta^*_{\pi^+}, \phi^*_{\pi^+}, \theta^{cm}_p, (m_{p\pi}, m_{\pi\pi}))$, between the PARA and PERP settings. Forming and fitting the ϕ-distributions in this manner (see Eq. (4.6)) results in a vertical offset of zero. As seen in Figure 4.7, a plotting of the vertical offsets for each final state topology (y_0) coming from the fits of the ϕ-distributions shows (for all kinematic bin combinations) shows a distribution around zero. However, while the distribution indicates a quality fitting of the data, not all offsets are equal to zero. The results of a fitting of each of the histograms contained in Figure 4.7 to a Gaussian from $[-0.1,0.1]$ demonstrates this point. While these (Gaussian) fit results show only small divergences from zero, the inclusion of the fits corresponding to offset values above or below zero may introduce a systematic error. It is not clearly known however, exactly how these vertical offsets affect the final observable measurements let alone the effect of small vertical offsets. Nevertheless, as the variation around zero is small, the potential systematic error associated with the observable measurements coming from the fits leading to these (non-zero) offsets is also expected to be very small.

4.6.3 Effects from averaging

Forming the average value for the polarization observables I^s and I^c provides a way of extending the observable measurements across topology-dependent acceptance holes. These average values are determined by first extracting the polarization observables per kinematic bin combination per final state topology. Once all of the observable measurement have been made, this average value is determined.

However, the averaging of these observable measurements to span these acceptance holes may introduce a systematic error. The origins of this error lies in the integration over two of the kinematic variables: invariant mass ($m_{p\pi}$ or $m_{\pi\pi}$) and $\cos(\theta^{CM}_p)$. As these variables were not used for binning the data (in the main part of the analysis), the observable

values as a function of these two variables is not presently known. More importantly, how the polarization observables behave in the acceptance holes is not known. These acceptance holes are regions of phase space (as a function of these two integrated-over kinematic variables) where the final state of interest was not produced. By averaging the observables across all studied final state topologies, the assumption is made that the topology-dependent acceptance holes in these two variables are the same for all final state topologies. This, however, is known to not be reality. Therefore a study into the error introduced from this averaging is needed to determine how the integration over these two kinematic variables affects the final measurements.

CHAPTER 5

MEASUREMENT RESULTS AND DISCUSSION

5.1 Measurements of I^s and I^c

The extraction of the polarization observables I^s and I^c comes from the extraction of fit parameters. These parameters are contained in the fit function applied to the ϕ-distributions produced using the asymmetry between the PARA and PERP ϕ-distributions (Method 2). This extraction is a relatively straight forward one.

As previously stated, using the asymmetry for PARA and PERP for the same kinematic bin combinations (and therefore the same kinematic regions) removes acceptance effects which are dependent in the three binning variables used (two of the kinematic variables, m and $\cos\theta_p^{CM}$, are integrated over). Building on this concept and practice, the polarization observables are also independently measured for each final state topology ($p\ \pi^+(\pi^-)$, $p\ \pi^-(\pi^+)$, $\pi^+\pi^-(p)$, $p\ \pi^+\pi^-$). Therefore, each set of polarization observable measurements (one set of measurements per topology) carries with it the acceptance "holes" specific to that final state. These acceptance holes are kinematic regions in which the final state particles of interest were not produced and is dependent upon the final state topology. This lack of statistics means that for a particular topology, the polarization observables cannot be measured for certain kinematic regions. The effect of these holes on the observable measurement can be seen in Figure 5.1 as a breaking in the distribution of the observable measurement. A good example of such breaking can be seen in Figure 5.1 in the eleventh block (corresponding to $0.0 < \cos\theta^*_{\pi^+} < 0.1$) where the blue points (representing the observable measurement for a specific final state topology) are absent in the middle of the plot.

However, since the extraction of the observables I^s and I^c was carried out per kinematic bin combination per final state topology, the topology- and kinematic-dependent acceptance effects have been appropriately accounted for (again, in terms of the three binning variables used). These individual measurements can then be combined to form a continuous distribution for all kinematical regions in which the data was binned. This is done by averaging the observable measurements for all topologies. This averaging can first be seen in Figure 5.1 as the set of red points which extend over the holes in the observable measurement for a single final state (blue points). Returning to the example of the $0.0 < \cos\theta^*_{\pi^+} < 0.1$ block of Figure 5.1, the red dots (the average across topologies) span much better the topology-dependent acceptance hole previously discussed.

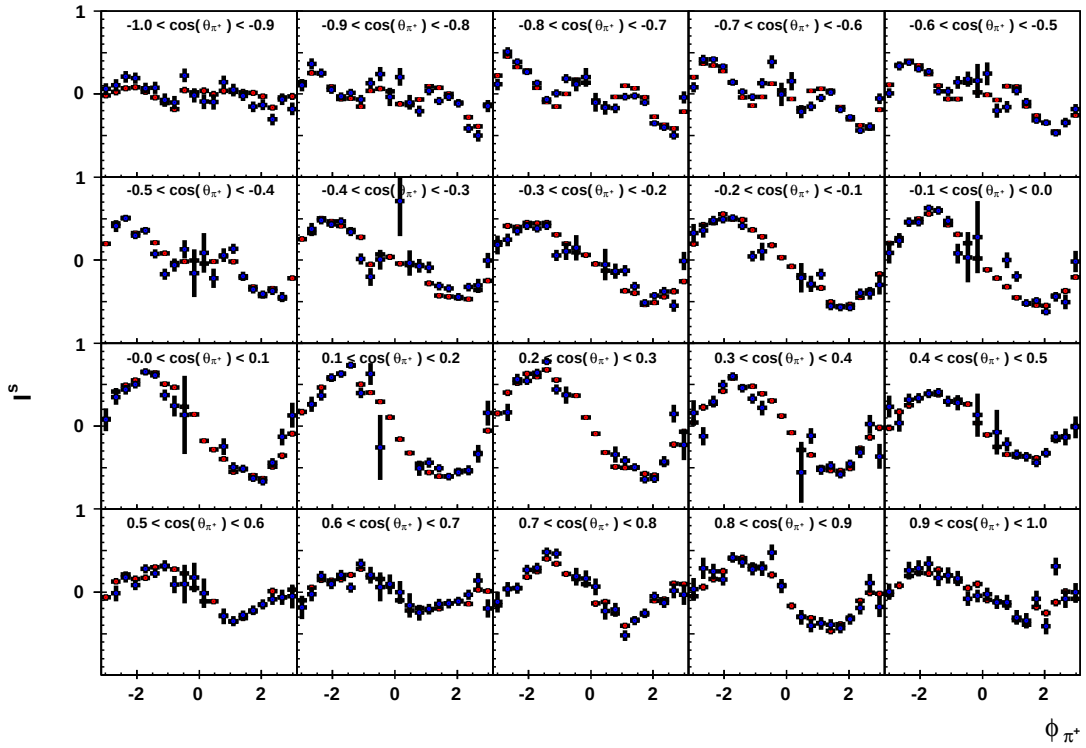

Figure 5.1: Measurement of the polarization observable I^s for a $p\ \pi^+\pi^-$ final state for $1.50 < E_\gamma < 1.55$ GeV. The observable measurements (blue points), being quite continuous across bins, are broken up by the effects of the topology-dependent acceptance. The averaging of the observable measurement across all topologies is represented by the red points. This averaging is conducted per final state topology per kinematic bin combination.

5.1.1 Observable Measurement: I^c (also known as Σ)

The quantity Σ is a fairly well-known polarization observable which exists in the final state equation for both a single- and double-meson final state. This observable has been measured by several analyses involving a single-meson final state and more recently, for final states containing two mesons (such as the measurements coming from CB-ELSA for a $p\pi^0\eta$ final state [42]). For a final state containing two neutral pions, measurements of this observable have recently been carried out at GRAAL for $N\pi^0\pi^0$ final states [40, 41]. However, previous to this analysis, this observable has not been measured for a final state containing two charged pions. For this analysis of double charged-meson final states, this observable is termed I^c [4]. This observable exists as the coefficient of the cosine term in the final state equation (equation (1.5)) as well as the fit equation (equation (4.9)) and is expected to be symmetric around zero ($\phi^*_{\pi^+} = 0$). This is in fact the observed symmetry seen in the distribution of I^c measurements. A further discussion regarding the observed behavior of I^c can be found in Sections 5.2.1 and 5.2.2.

The following set of figures show a sample of the measurements made for I^c (Figures 5.2 through 5.5). The measurements presented in these histograms represent the averaged

value of the polarization observable (averaged across final state topologies). To produce these measurements, the ϕ-distributions were binned in photon energy (k), $\cos\theta^*_{\pi^+}$, and $\phi^*_{\pi^+}$. The manner in which the results are presented reflects such a binning although a binning in any combination of the five kinematic variables is possible. In each of these figures (Figures 5.2 through 5.5), the y-axis represents the extracted value of the polarization observable and the x-axis represents the ϕ^* values measured with respect to the π^+ (20 bins in ϕ^* were used, hence there are 20 points on the x-axis). Each entire figure corresponds to a single bin in k (E_γ) thereby providing a glimpse into the measurement results for four of the five coherent edge settings (1.3 GeV, 1.5 GeV, 1.7 GeV and 2.1 GeV) with each square representing a bin in $\cos\theta^*_{\pi^+}$. Measurements of I^c using the data from the 1.9 GeV coherent edge position are not presented as the data from this coherent edge position was unusable.

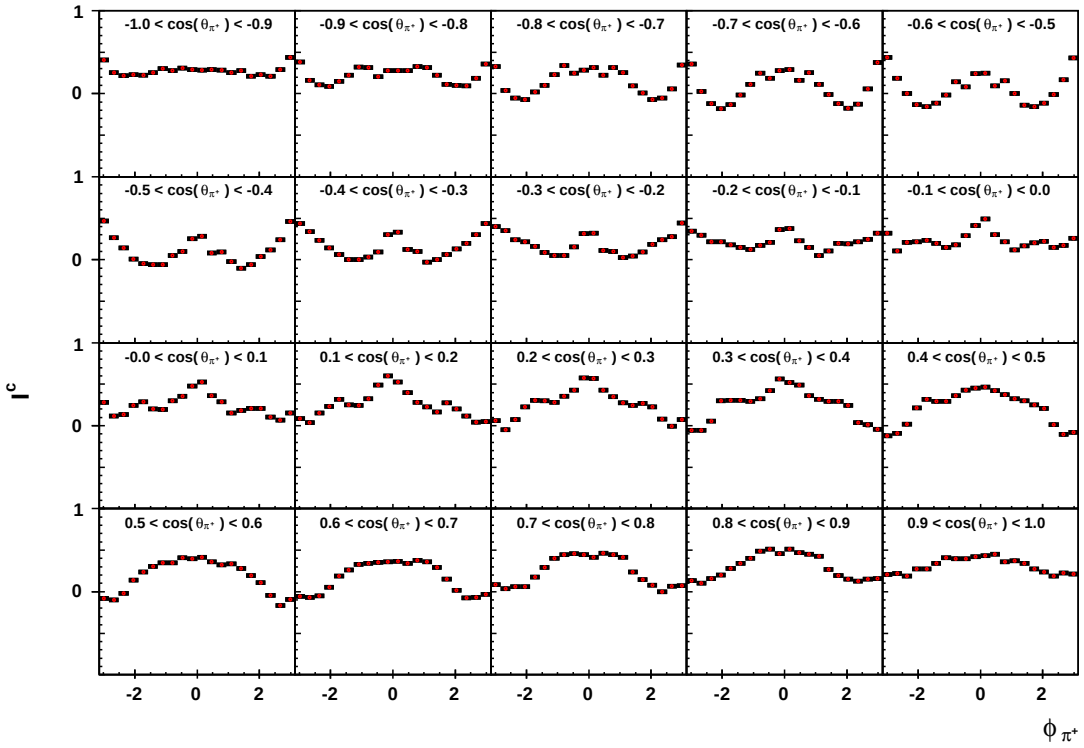

Figure 5.2: Measurement of the polarization observable I^c for $1.20 < E_\gamma < 1.25$ GeV. The red points seen in the figure represent the average value of the observable across all final topologies for the shown kinematic bin combination. The errors bars for each data point represent the statistical error for the measurement. For almost all of the data points, this error is smaller than the symbol size representing the measurement.

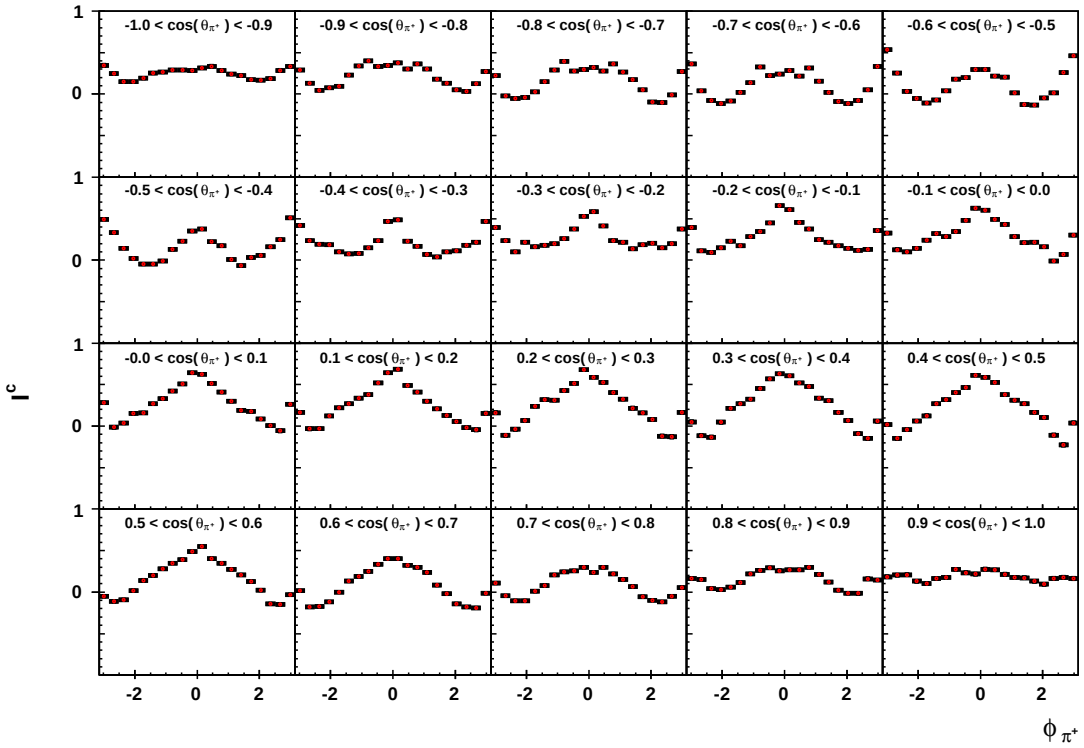

Figure 5.3: Measurement of the polarization observable I^c for $1.40 < E_\gamma < 1.45$ GeV. The red points seen in the figure represent the average value of the observable across all final topologies for the shown kinematic bin combination. The errors bars for each data point represent the statistical error for the measurement. For almost all of the data points, this error is smaller than the symbol size representing the measurement.

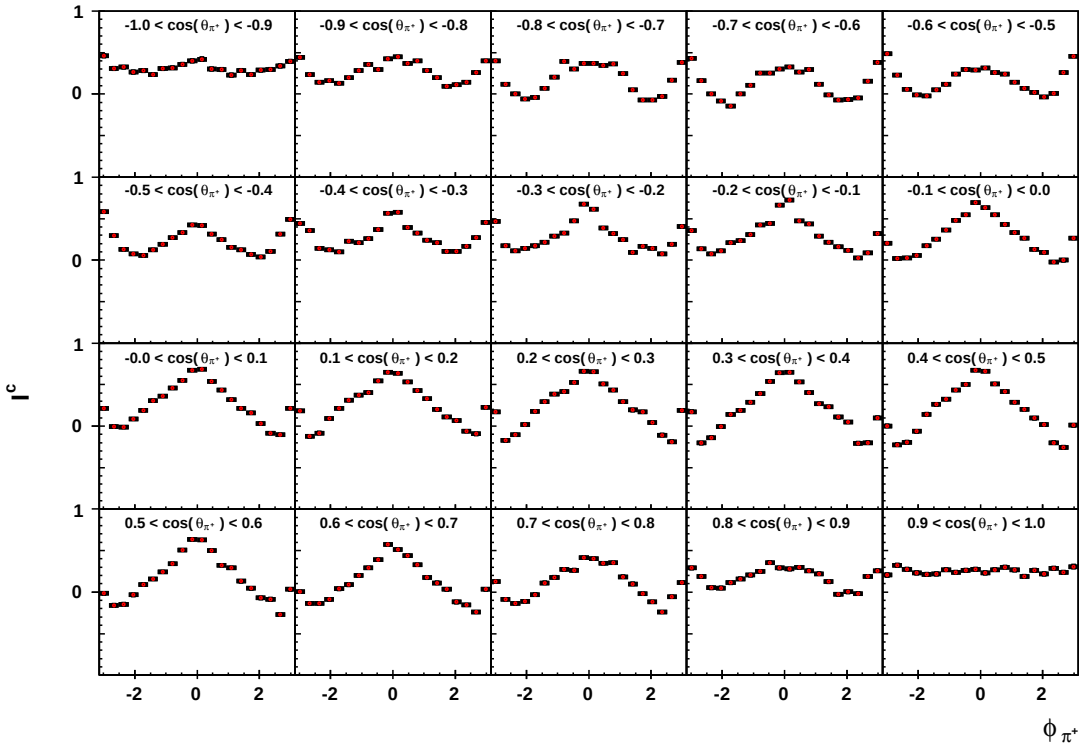

Figure 5.4: Measurement of the polarization observable I^c for $1.60 < E_\gamma < 1.65$ GeV. The red points seen in the figure represent the average value of the observable across all final topologies for the shown kinematic bin combination. The errors bars for each data point represent the statistical error for the measurement. For almost all of the data points, this error is smaller than the symbol size representing the measurement.

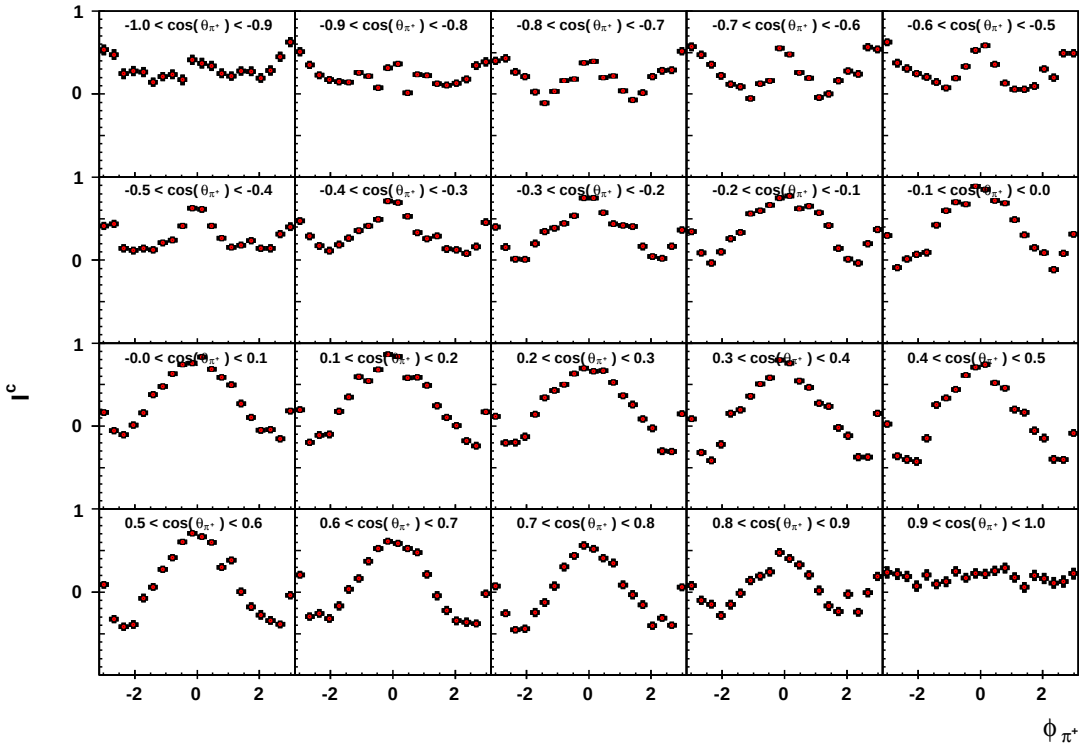

Figure 5.5: Measurement of the polarization observable I^c for $2.00 < E_\gamma < 2.05$ GeV. The red points seen in the figure represent the average value of the observable across all final topologies for the shown kinematic bin combination. The errors bars for each data point represent the statistical error for the measurement. The error bars here are more noticeable due the lower amount of statistics for the 2.1 GeV coherent edge (when compared to the other coherent edge settings).

When comparing the topology-specific extractions for I^c to the averaged values of I^c, a few discrepancies may be noted. As seen in Figure 5.6, for a few bins in $\cos(\theta^*_{\pi^+})$ the topology-specific and averaged values do not agree. This disagreement occurs mainly in the $-1 < \cos(\theta^*_{\pi^+}) < -0.9$ bin and again in the last three $\cos(\theta^*_{\pi^+})$ bins ($0.7 < \cos(\theta^*_{\pi^+}) < -1$). The exact cause of this discrepancy and why it only shows itself in measurements of I^c is currently not completely understood. Acceptance effects due to the integration over two of the kinematic variables, $m_{p\pi}$ (or $m_{\pi^+\pi^-}$) and $\cos(\theta^{CM}_p)$, may be the root of this discrepancy. Further studies into the effects of this integration as well as symmetry effects are needed in order to settle this issue.

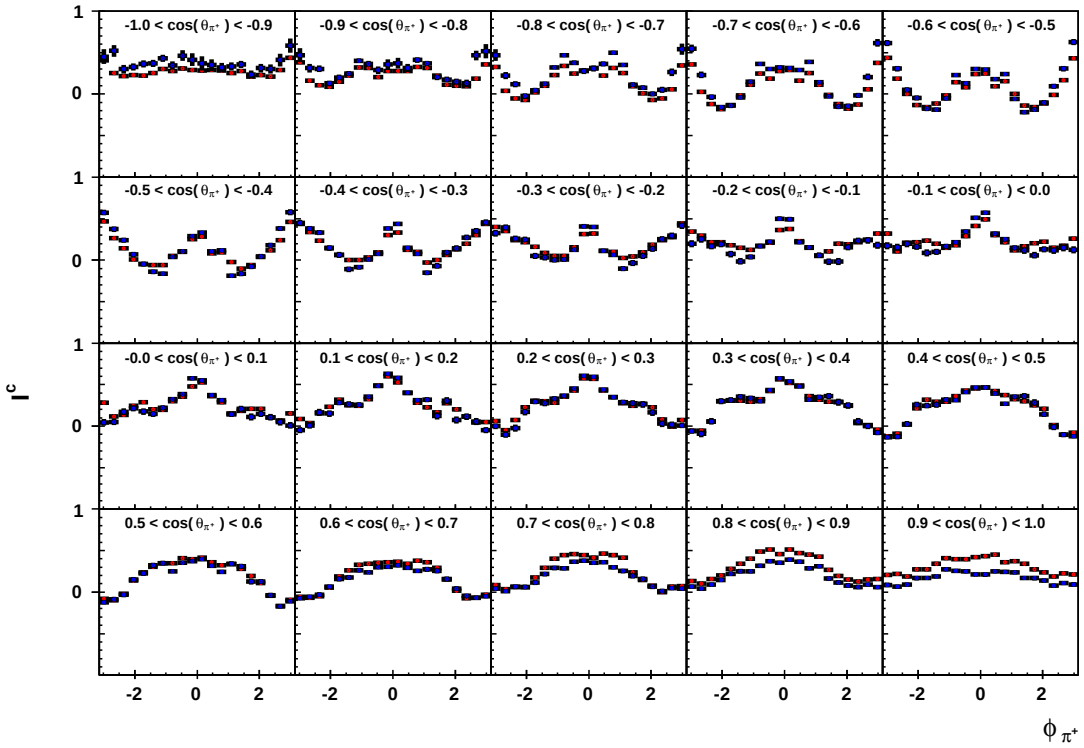

Figure 5.6: Measurement of the polarization observable I^c for a $p\ \pi^+(\pi^-)$ final state for $1.20 < E_\gamma < 1.25$ GeV. The observable measurements for the $p\ \pi^+(\pi^-)$ final state are represented by the blue points while the red points represent the average value of the observable across all final topologies for the shown kinematic bin combination. The errors bars for each data point represent the statistical error for the measurement. For almost all of the data points, this error is smaller than the symbol size representing the measurement.

5.1.2 Observable Measurement: I^s

The second measured observable, I^s, is one that is unique to multi-meson final states and appears in the double-meson final state equation (equation (1.5)). This observable is a quantity for which no previous measurement has been made for a final state containing two pions, let alone the specialized case of two non-neutral pions. For $\vec{\gamma}p \to p\pi^0\eta$ reactions however, this observable has been measured for the first time at CB-ELSA [42]. This observable is extracted from the ϕ-distributions as the coefficient of the sine term in the fitting equation (equation (4.9)) and is expected to be anti-symmetric around $\phi^* = 0$. A further discussion of this expected behavior may be found in the Sections 5.2.1 and 5.2.2.

The following set of figures show a sample of the measurements made for I^s (Figure 5.7 through 5.10). The measurements presented in these histograms represent the averaged value of the polarization observable (averaged across final state topologies). These measurements were extracted using the same method as was used for I^c and thusly presented in the same manner. The y-axis is again the value of the polarization observable and the x-axis the ϕ^* of the π^+. Each figure represents a single bin in photon energy (k) for the

1.3 GeV, 1.5 GeV, 1.7 GeV and 2.1 GeV coherent edge settings. Each individual box again represents a single bin in $\cos\theta^*_{\pi^+}$. As mentioned in the description of the measurements of I^c, extractions of the polarization observable I^s are not shown for the 1.9 GeV coherent edge setting due to the lack of usable data.

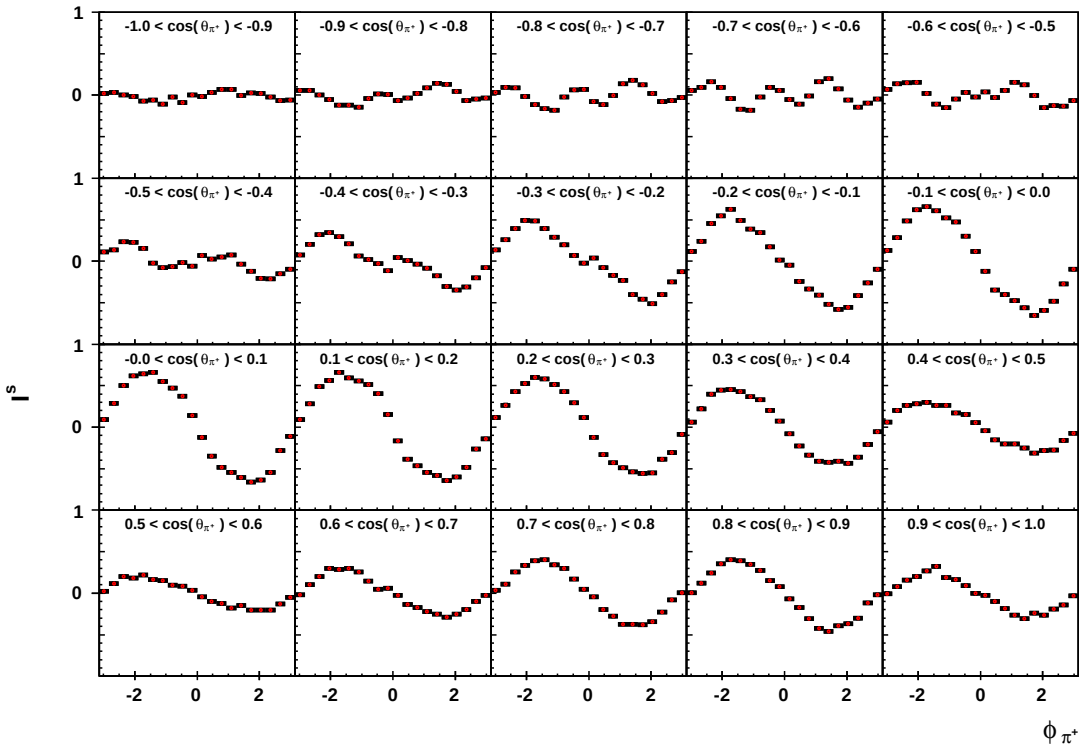

Figure 5.7: Measurement of the polarization observable I^s for $1.20 < E_\gamma < 1.25$ GeV. The red points seen in the figure represent the average value of the observable across all final topologies for the shown kinematic bin combination. The errors bars for each data point represent the statistical error for the measurement. For almost all of the data points, this error is smaller than the symbol size representing the measurement.

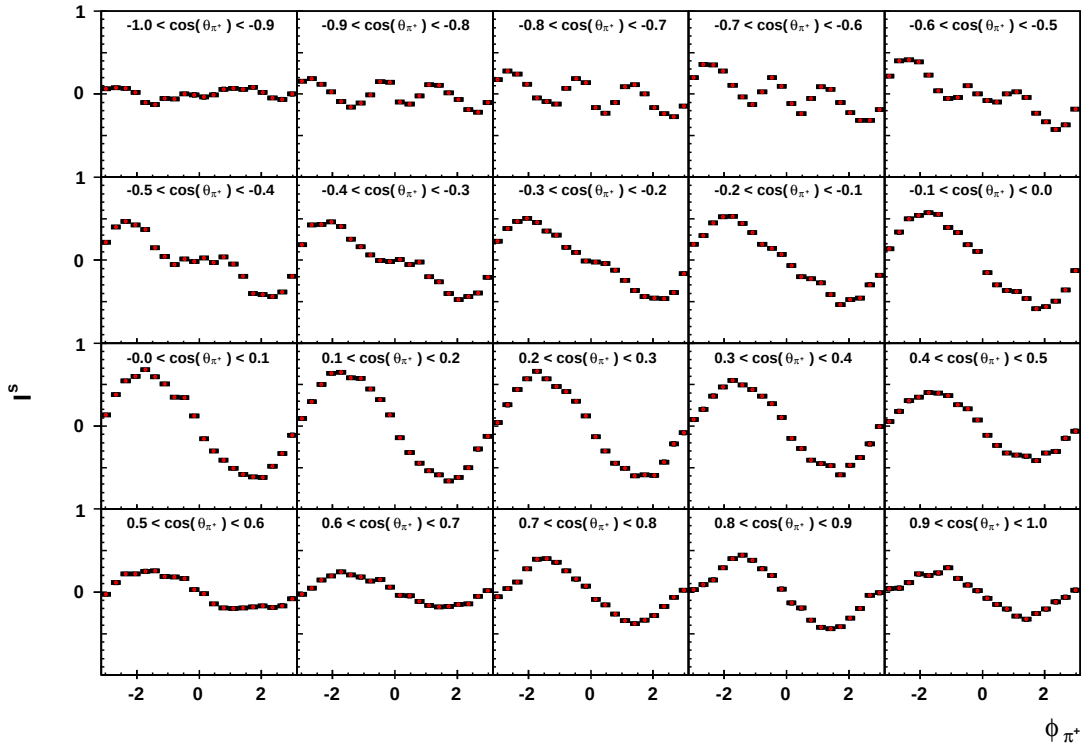

Figure 5.8: Measurement of the polarization observable I^s for $1.40 < E_\gamma < 1.45$ GeV. The red points seen in the figure represent the average value of the observable across all final topologies for the shown kinematic bin combination. The errors bars for each data point represent the statistical error for the measurement. For almost all of the data points, this error is smaller than the symbol size representing the measurement.

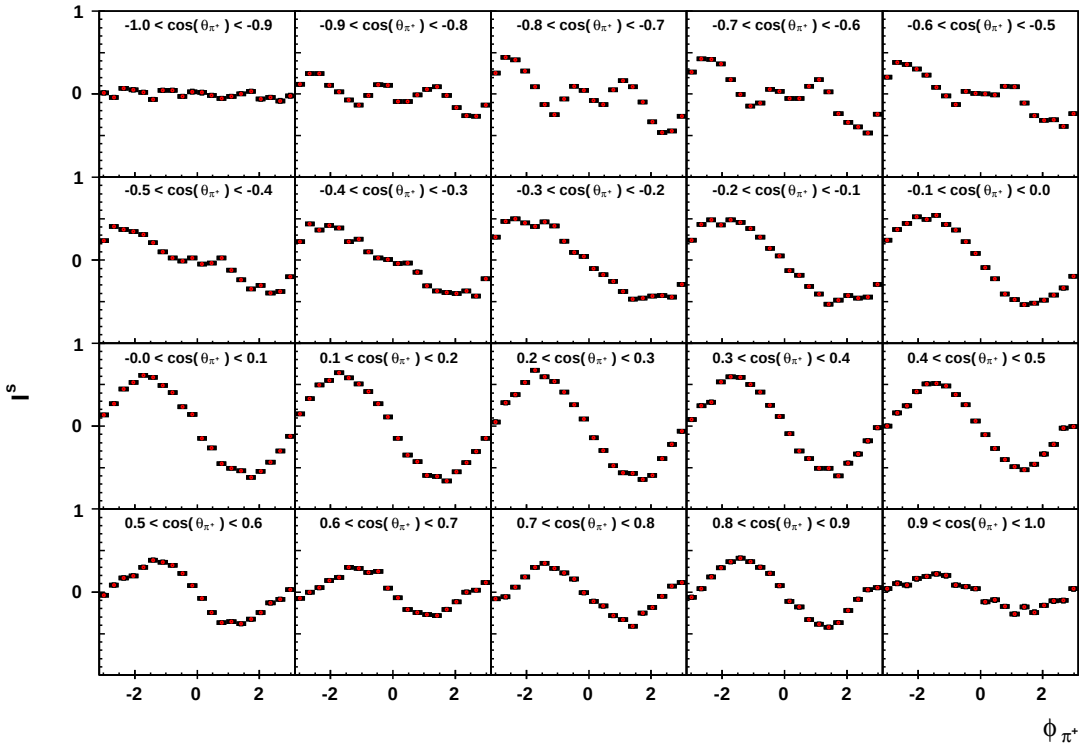

Figure 5.9: Measurement of the polarization observable I^s for $1.60 < E_\gamma < 1.65$ GeV. The red points seen in the figure represent the average value of the observable across all final topologies for the shown kinematic bin combination. The errors bars for each data point represent the statistical error for the measurement. For almost all of the data points, this error is smaller than the symbol size representing the measurement.

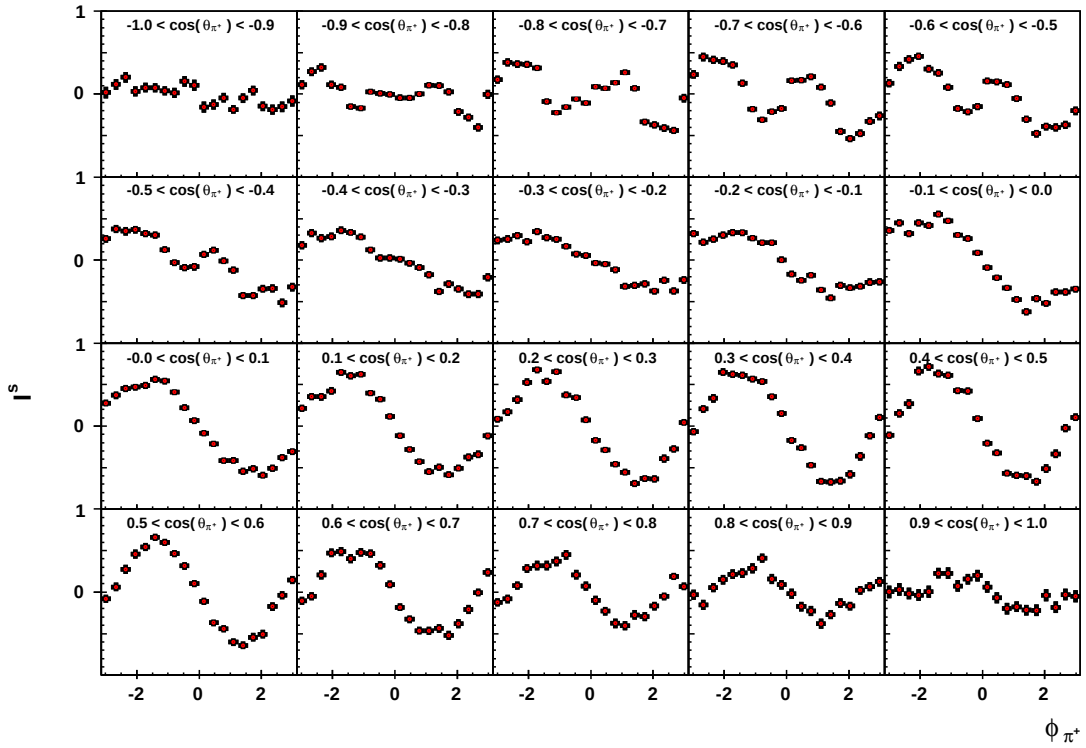

Figure 5.10: Measurement of the polarization observable I^s for $2.00 < E_\gamma < 2.05$ GeV. The red points seen in the figure represent the average value of the observable across all final topologies for the shown kinematic bin combination. The errors bars for each data point represent the statistical error for the measurement. The error bars here are more noticeable due the lower amount of statistics for the 2.1 GeV coherent edge (when compared to the other coherent edge settings).

The following figure (Figure 5.11) demonstrates the high level of agreement seen between the topology-dependent measurements of I^s and the averaged value of I^s. In this figure, the measurement of I^s for a $p\ \pi^+(\pi^-)$ final state is shown by the blue points and the measurement of I^s averaged across all final state topologies is shown by the red points. These measurements were both produced for $1.40 < E_\gamma < 1.45$ GeV. Unlike the observable I^c, the topology-dependent measurements of I^s agree very well with the averaged values of I^s. This high level of agreement is even observed in the early $\cos(\theta^*_{\pi^+})$ bins where the observable exhibits a more complicated behavior. While only one figure is shown here demonstrating this agreement, the topology-dependent measurement of I^s and the averaged value exhibit this behavior for all kinematic bin combinations.

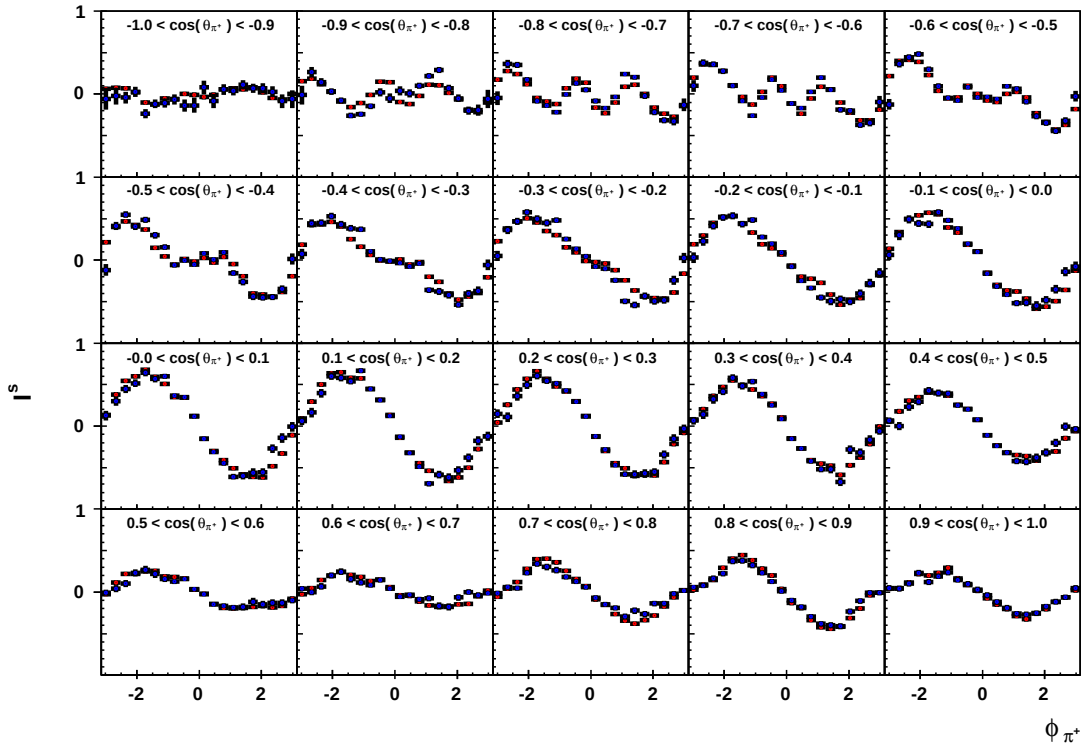

Figure 5.11: Measurement of the polarization observable I^s for a $p\ \pi^+(\pi^-)$ final state for $1.40 < E_\gamma < 1.45$ GeV. The observable measurements for the $p\ \pi^+(\pi^-)$ final state are represented by the blue points while the red points represent the average value of the observable across all final topologies for the shown kinematic bin combination. The errors bars for each data point represent the statistical error for the measurement. A comparison between the blue and the red points here demonstrates the high level of agreement between the topology-dependent observable extraction and the averaged value of the polarization observable.

The extracted values of both polarization observables show a clear dependence on $\cos\theta^*_{\pi^+}$ with measurements being continuous across $\cos\theta^*_{\pi^+}$ bins. For small values of $\cos(\theta^*_{\pi^+})$, the observables are rather small in magnitude with most measurements showing a value of I^s and I^c smaller than ≈ 0.5. This behavior however changes as the value of $\cos(\theta^*_{\pi^+})$ increases. Measurements of I^s and I^c show that both observables become larger as $\cos(\theta^*_{\pi^+})$ approaches zero with some values approaching the maximum value of one. The magnitude of the observables then begins to decrease as the value of $\cos(\theta^*)$ moves towards $+1$.

5.2 Discussion of the Measurements of I^s and I^c

5.2.1 Expected Behavior of I^s and I^c

The polarization observables I^s and I^c are predicted to have a certain behavior according to theory. This expected behavior states that, as a function of ϕ^*, the observable I^s should be seen to be odd and I^c should be seen as even. The source of this behavior can be traced

back to the kinematics of the reaction under investigation and how they relate to helicity amplitudes (M) [59, 60]. When considering helicity amplitudes for a 2-body final state, a comparison of these amplitudes before and after a parity transformation of the reaction kinematics shows that they are equivalent in magnitude. This relation can be written as:

$$M^{-\lambda_\gamma}_{-\lambda_N-\lambda_{N'}} = \pm M^{\lambda_\gamma}_{\lambda_N\lambda_{N'}}, \tag{5.1}$$

where λ_γ is the helicity of the photon, λ_N is the helicity of the target nucleon and $\lambda_{N'}$ is the helicity of the recoil nucleon.

For a 3-body final state however, this is not the case. When the parity transformation is performed for this type of reaction, the magnitude of the helicity amplitudes are not equivalent and require a rotation of π in ϕ^* in order to be made equivalent (see Figure 5.12). This means that the helicity amplitudes are related by:

$$M^{-\lambda_\gamma}_{-\lambda_N-\lambda_{N'}}(\phi^*) = \pm M^{\lambda_\gamma}_{\lambda_N\lambda_{N'}}(2\pi \ - \ \phi^*) \tag{5.2}$$

A consequence of this rotation in kinematic space is that some of the polarization observables will show themselves to be odd and the others even under the transformation of $\phi^* \rightarrow 2\pi$ - ϕ^*. Furthermore, any observables that show/are-predicted-to-show an odd behavior in 3-body final states are zero for 2-body final states as a result of their "oddness".

5.2.2 Analysis of the Behavior of I^s and I^c

As the observables are expected to exhibit certain behaviors, the behavior of the extracted values can be examined in order to verify this behavior. To demonstrate and carry out this examination, the averaged observable measurements seen in Figures 5.2 and 5.7 (chosen just to provide an example) were fit with a Fourier expansion of sine (for I^s) and cosine (for I^c). In addition to this expansion, an additional term was added to the fit equation: cosϕ^* for the equation used to fit I^s and sinϕ^* for the equation used to fit I^c. Therefore the two fit equations used are:

$$\begin{aligned} I^s(\phi^*) \ = \ f(\phi^*) \ &= A_0 \ + \ A_1 sin(\phi^*) \ + \ A_2 sin(2\phi^*) \ + \ A_3 sin(3\phi^*) \ + \ A_4 sin(4\phi^*) \\ &+ \ A_5 sin(5\phi^*) \ + \ A_6 sin(6\phi^*) \ + \ A_7 sin(7\phi^*) \ + \ A_8 cos(\phi^*) \end{aligned} \tag{5.3}$$

and

$$\begin{aligned} I^c(\phi^*) \ = \ f(\phi^*) \ &= A_0 \ + \ A_1 cos(\phi^*) \ + \ A_2 cos(2\phi^*) \ + \ A_3 cos(3\phi^*) \ + \ A_4 cos(4\phi^*) \\ &+ \ A_5 cos(5\phi^*) \ + \ A_6 cos(6\phi^*) \ + \ A_7 cos(7\phi^*) \ + \ A_8 sin(\phi^*) \end{aligned} \tag{5.4}$$

with the "0^{th}" term of equation (5.4) being A_0cos(0*ϕ^*).

For the observable I^s, it is expected that the contribution to the fit of the extraction be dominated by the A_1sin(ϕ^*) term with some contribution from the A_2sin($2\phi^*$), a small contribution from the A_3sin($3\phi^*$) term and no contribution from the A_0, A_4cos(ϕ^*) and the higher-order terms [60]. The fit results seen Figure 5.13 show this type of behavior. The contribution from the A_1sin(ϕ^*) term is clearly shown to be dominant for almost all cos(θ^*) bins. The A_2sin($2\phi^*$) term shows it contributes in the region of $-0.6 < \cos\theta^* < -0.1$ with its

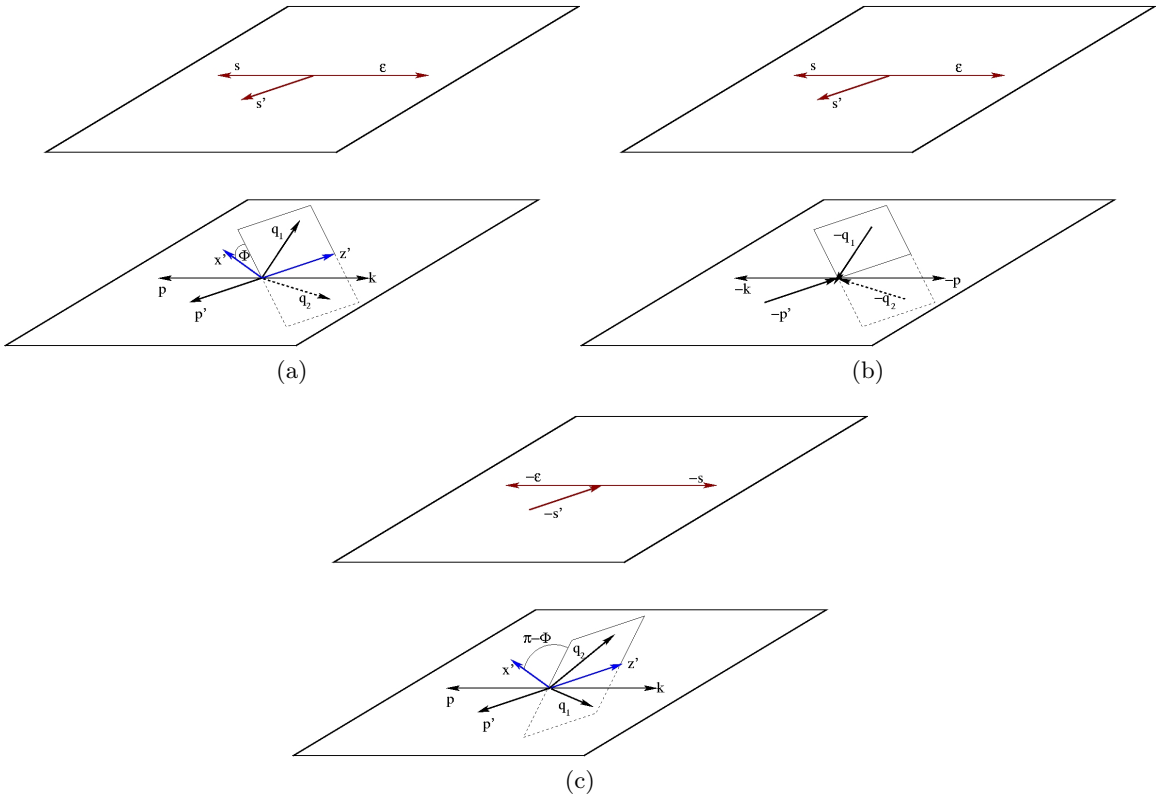

Figure 5.12: Three diagrams showing the parity transformation leading to even and odd polarization observable for a 3-body final state. In (a), a choice of axes is shown for spin orientations (top) and momentum (bottom). The image seen in (b) shows the same system after a parity transformation ($x_i \rightarrow -x_i$). Finally, (c) shows the rotation of axes by the angle π around the y-axis. This rotation in ϕ^* results in the momenta of the final state particles being what they were before parity transformation. Image source: [59].

contribution being smaller than the $A_1\sin(\phi^*)$ term for $\cos\theta^* > -0.1$. A small contribution from the $A_3\sin(3\phi^*)$ is seen in the early $\cos\theta^*$ bins with little to no contribution seen for the A_0, $A_4\cos(\phi^*)$ and higher order terms.

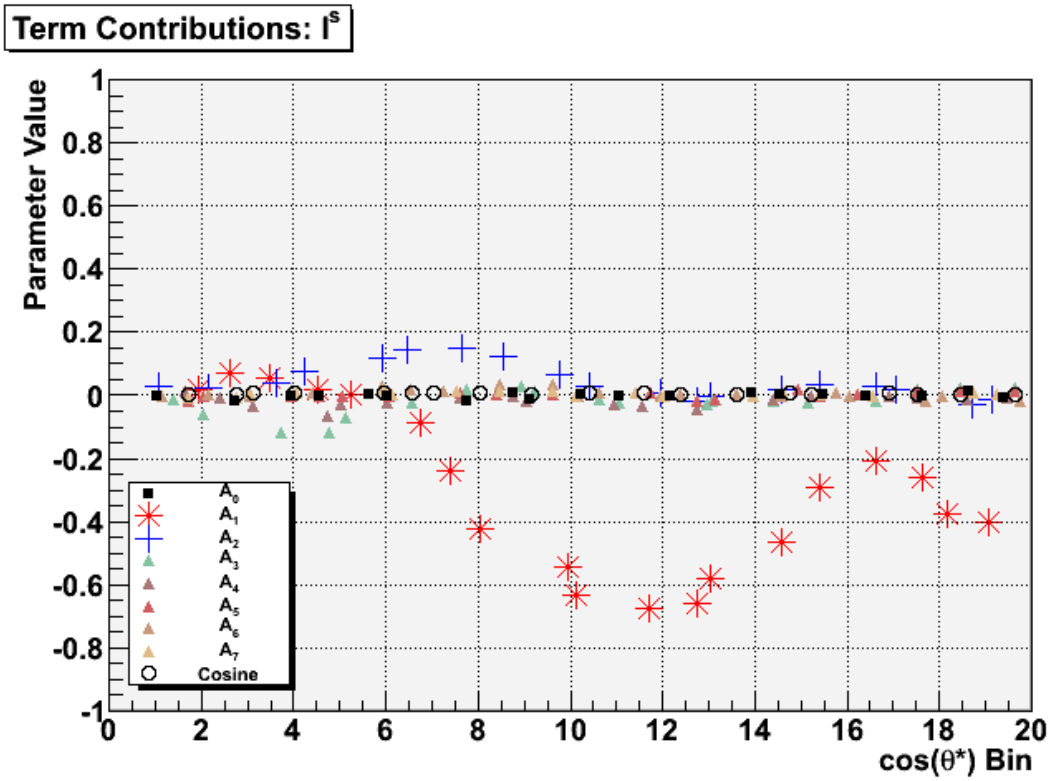

Figure 5.13: The results of the fitting of the averaged observable measurements with equation (5.3) showing the contributions of the different terms to the fit as a function of $\cos(\theta^*_{\pi^+})$. The contribution from the A_0 term is shown as the black squares, the $A_1\sin(\phi^*)$ contribution is shown by the red stars, the $A_2\sin(2\phi^*)$ contribution is shown by the blue +'s, the contributions from the $A_3\sin(3\phi^*)$ through $A_7\sin(7\phi^*)$ terms are shown by the triangles. Lastly, the $A_8\cos(\phi^*)$ contribution is shown by the black $\circ$'s.

The observable I^c (as a function of $\cos\theta^*$) is expected to show a dominant contribution from the A_0 and $A_1\cos(\phi^*)$ terms with an additional contribution from the $A_2\cos(2\phi^*)$ term. The contributions from the $A_3\cos(3\phi^*)$ through $A_7\cos(7\phi^*)$ terms and $A_8\sin(\phi^*)$ are expected to be very small, almost zero [60]. This behavior is verified in Figure 5.14. Although fluctuating and trading off who is more dominant, the A_0, $A_1\cos(\phi^*)$ and $A_2\cos(2\phi^*)$ terms show themselves to be the main contributors to the fit for all $\cos\theta^*$ bins. The contribution from the $A_3\cos(3\phi^*)$ term shows itself mainly in the early $\cos\theta^*$ bins in the region of $-0.9 < \cos\theta^* < -0.5$ while in the other bins, it is on par with the higher order terms. These higher order terms, as expected, show themselves to not contribute much to the fitting of the extraction and the sine term shows itself to possess no influence.

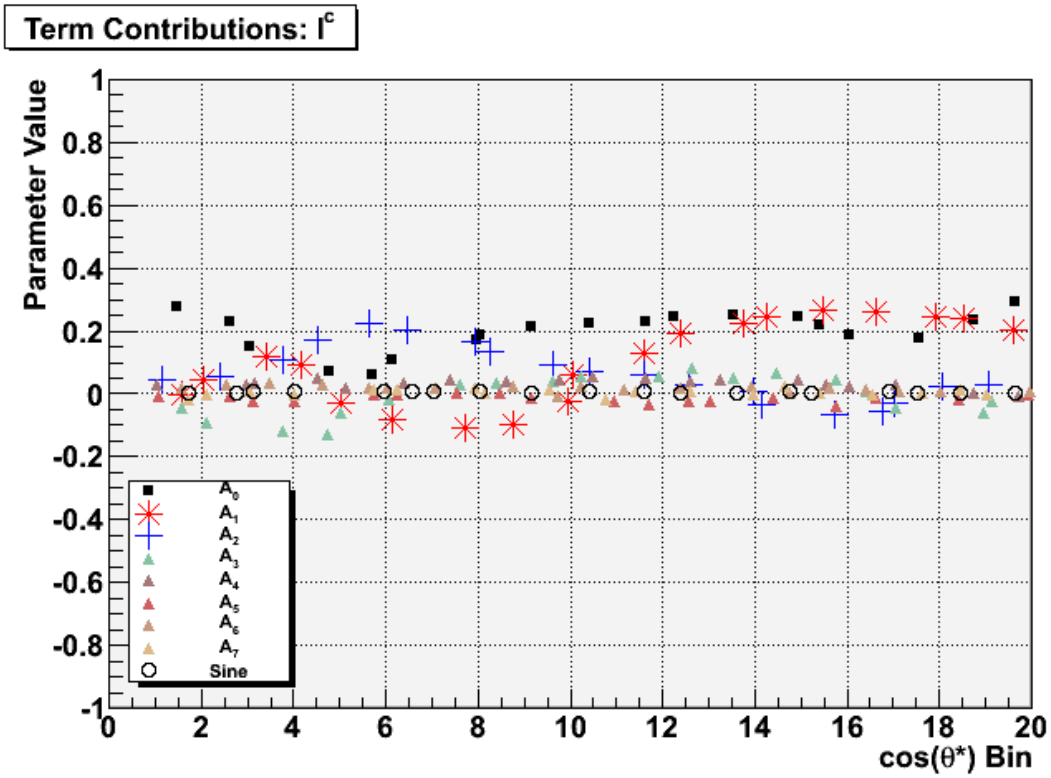

Figure 5.14: The results of the fitting of the averaged observable measurements with equation (5.4) showing the contributions of the different terms to the fit as a function of $\cos(\theta^*_{\pi^+})$. The contribution from the A_0 term is shown as the black squares, the $A_1\cos(\phi^*)$ contribution is shown by the red stars, the $A_2\cos(2\phi^*)$ contribution is shown by the blue +'s, the contributions from the $A_3\sin(3\phi^*)$ through $A_7\sin(7\phi^*)$ terms are shown by the triangles. Lastly, the $A_8\cos(\phi^*)$ contribution is shown by the black $\circ$'s.

The measurement results for (I^s) and (I^c) can be checked via a fit of the measurement values as a function of $\cos\theta^*$. This check was carried out by fitting the observable measurements averaged across all final state topologies with an expansion of cosine (I^c) and sine (I^s). This fitting shows that overall, both observables exhibit their respective expected behavior. For I^s, the small modulations (or flatness) seen in the early $\cos\theta^*$ bins is reflected in the fitting of the I^s extraction. In these bins, all of the fit terms are close to zero. As the observable begins to exhibit modulations however, the expected contributions coming from the terms in the fit equation become very apparent. When considering I^c, it is observed that for $\cos\theta^* < 0$, the observable extractions show a more complicated behavior than for later $\cos\theta^*$ bins. This shows itself in the fit results as a brief contribution from the $A_3\sin(3\phi^*)$ term as well as a shifting in which one of the first three terms is dominant. For $\cos\theta^* > 0$, the observable measurements (as a function of ϕ^*) smooth out. This behavior is also reflected in the fit results as a consistent contribution from the A_0 and $A_1\cos(\phi^*)$ terms. For both polarization observables, the higher order terms do not contribute much to the overall fit.

5.2.3 I^s and I^c vs Invariant Mass: Comparison to Predictions

The absence of a complete set of Constituent Quark Model calculations to which the measurements of I^s and I^c can be compared makes an interpretation of the results a difficult task. However, there does exist a few predictions to which these observables may be compared as provided by Winston Roberts [60]. Two sets of these predictions may be found in Figure 5.15 with the predicted value of the observables I^s and I^c being plotted as a function of the $p\pi^+$ invariant mass ($m_{p\pi^+}$).

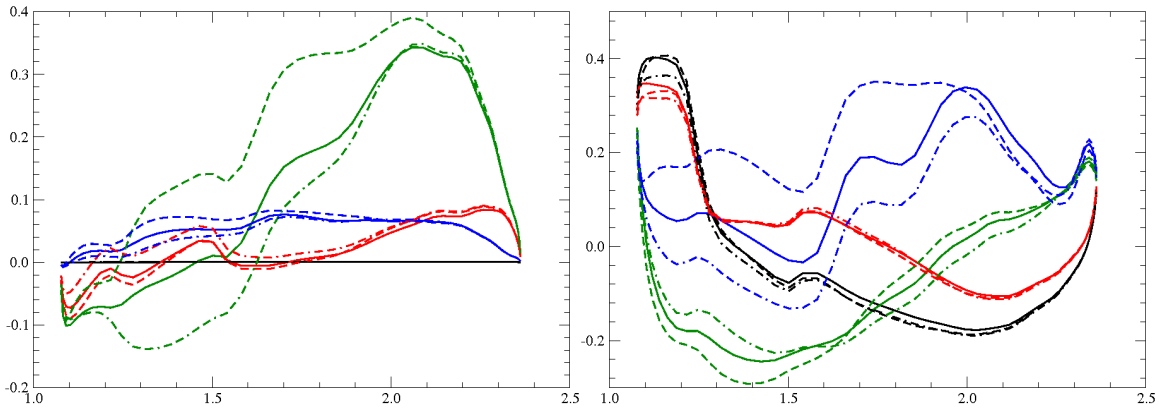

(a) I^s v. $m_{p\pi^+}$ (b) I^c v. $m_{p\pi^+}$

Figure 5.15: Model calculations provided by Winston Roberts [4, 60] which show the predicted values of the polarization observables I^s (a) and I^c (b) for $\gamma p \to p\ \pi^+\pi^-$ reactions as a function of $m_{p\pi^+}$. These predictions are shown for various values of ϕ^* with the inclusion or exclusion of certain resonances. The black curve represents $\phi^* \approx 0$, red represents $\phi^* \approx \frac{\pi}{6}$, green represents $\phi^* \approx \frac{2\pi}{3}$, and blue represents $\phi^* \approx \pi$. For each color, the solid line represents a full model calculation including all resonances (the baryons considered here have a spin of 3/2 or less), the dashed lines represent model calculations with the omission of the $S_{31}(1900)$ Δ^* resonance and the dot-dashed lines represent the omission of the $P_{31}(1910)$ Δ^* resonance. Here, the angle ϕ^* (for a $p\ \pi^+\pi^-$ final state) is defined as the angle between the plane formed by the two pions and the reaction plane (measured with respect to one of the final state pions) (see Fig. 4.1).

In order to extract the polarization observables in the manner in which they are displayed in Figure 5.15, new measurements were made with the data being re-binned in E_γ, $\phi^*_{\pi^+}$ and $m_{p\pi^+}$. The extracted values of the observables I^s and I^c now as a function of invariant mass can be seen in Figures 5.16 and 5.17. Here the average values of the observables (averaged across all topologies post-extraction) are shown. The y-axis is once more the value of the polarization observable while the x-axis represents the invariant mass of the $p\pi^+$ system ($m_{p\pi^+}$). Each individual box seen in the figures represents a single bin in $\phi^*_{\pi^+}$.

While the predicted values of the observables are presented in a manner different than the extractions, a general comparison may still be discussed. It should be noted however, that the extractions seen in Figures 5.16 and 5.17 cover an invariant mass range with a maximum of $\approx$ 1.85 GeV while the predictions seen in Figure 5.15 covers and invariant mass range up to $\approx$ 2.45 GeV. This difference therefore makes a discussion regarding the comparison for $m_{p\pi^+} > 1.85$ GeV not feasible. In addition to this, the predicted values of the observables seen in Figure 5.15 are for specific, singular values of $\phi^*_{\pi^+}$ while the

measurements are binned in $\phi^*_{\pi^+}$ with each bin covering 0.314 radians. Therefore it should not be expected that the predictions and the extractions as presented match exactly as the extractions include contributions from the range of $\phi^*_{\pi^+}$ contained in each bin.

The comparison between the magnitudes of the model predictions and the extractions shows them to be rather similar. In general, the predictions show a magnitude that is smaller than the observed magnitude of the observables. More importantly though, the prediction that the observables will show themselves to be "large" (meaning that they are not flat and in fact show an undeniable variation in magnitude) for some values of ϕ^* and small for others has been shown to be true. For instance, a comparison between the prediction for I^s for $\phi^* \approx 0$ seen in Figure 5.15(a) (the black line) to the measurement seen in Figure 5.16 for $\phi \approx 0$ (the tenth and eleventh ϕ^* bin) shows both observables to be rather flat. Furthermore, a comparison between the prediction for I^c for $\phi^* \approx 0$ (again denoted by the black line) seen in Figure 5.15(b) and the extracted value as shown in Figure 5.17 for $\phi \approx 0$ (the tenth and eleventh ϕ^* bin) both show the observable peaking at a large value. The referred to prediction for I^c seen in Figure 5.15(b) peaks at a value of 0.4 while the corresponding observable measurement peaks at a value of 0.7. While the observable measurement in this example is larger than the predicted value, the point remains that they both exhibit these large, non-zero values for the chosen value (or range) of ϕ^*. This comparison may be carried out again, this time comparing the predictions for I^s and I^c seen in Figure 5.15 for $\phi^* \approx \pi$ (the blue curves) to the extracted values of I^s and I^c seen in the last ϕ^* bin of Figures 5.16 and 5.17. The prediction for I^s for this value of ϕ^* says that the observable should exhibit a small yet non-zero value in the invariant mass range in which the observable is presented. The measurement seen in Figure 5.16 shows this small yet non-zero magnitude. The differences in the shape of the observable in this example have some root in the fact that a prediction for a fixed value of ϕ^* is being compared to a measurement for a range of ϕ^*. When comparing the prediction for I^c for $\phi^* \approx \pi$ to the extracted value of I^c it can be seen that both observables exhibit a maximum magnitude of ≈ 0.4 (although for different $p\pi$ invariant mass values). The early predictions for the polarization observables I^s and I^c, while generally possessing a smaller magnitude than the extracted values, do show a level of agreement with the observable measurements presented in this section.

The behavior of the extracted observables as a function of invariant mass may also be compared to the theoretical predictions. Immediately one may notice that the flat, zero value for I^s for $\phi^* \approx 0$ (seen as the black line in Figure 5.15(a)) is apparent in the data (Figure 5.16). The shapes and behavior of the red, green, and blue curves (corresponding to predictions for different fixed values of $\phi^*_{\pi^+}$ seen in Figure 5.15(a)) can also be recognized in the data (with these three values of $\phi^*_{\pi^+}$ corresponding to bin numbers 12, 17 and 20 in Figure 5.16). A comparison of the predictions seen in Figure 5.15(b) to the measurements seen in Figure 5.17 shows a lesser amount of agreement. Firstly, there appears to be a minus sign difference (inversion) between the predicted values and the measured quantities for several values of $\phi^*_{\pi^+}$ with the blue, red and black curves seen in Figure 5.15(b) being examples of this (corresponding to $\phi^*_{\pi^+}$ bin numbers 12, 17 and 20 in Figure 5.17). The prediction for I^c for $\phi^*_{\pi^+} = 2.0876$ radians (the green curve) however does not seem to match the data. Presently an explanation of this is not available but should be fleshed out once a complete set of model calculations is made available.

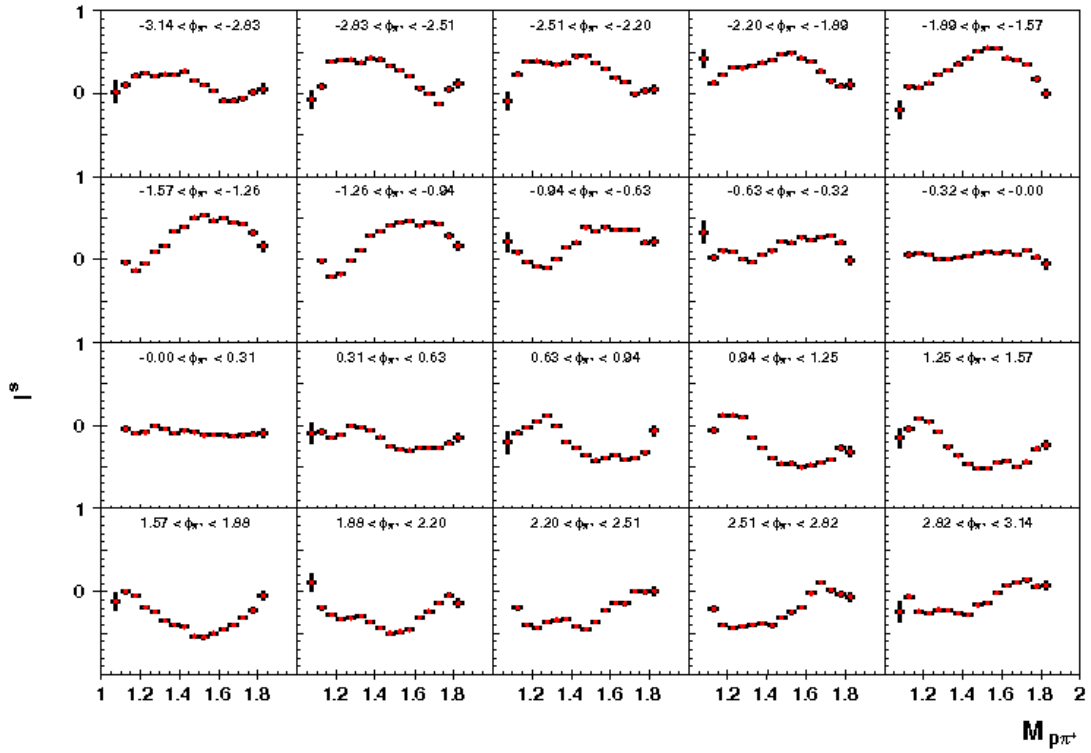

Figure 5.16: Measurement of the polarization observable I^s averaged across all final state topologies for $1.60 < E_\gamma < 1.65$ GeV. The errors bars for each data point represent the statistical error for the measurement. For almost all of the data points, this error is smaller than the symbol size representing the measurement.

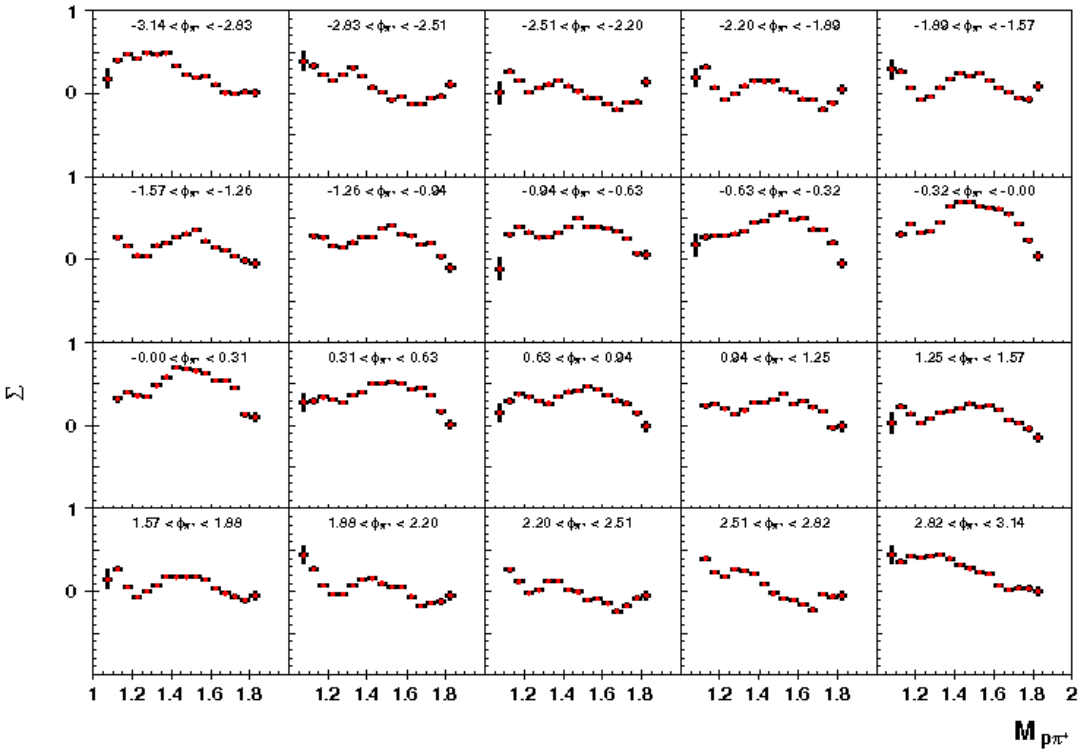

Figure 5.17: Measurement of the polarization observable I^c averaged across all final state topologies for $1.60 < E_\gamma < 1.65$ GeV. The errors bars for each data point represent the statistical error for the measurement. For almost all of the data points, this error is smaller than the symbol size representing the measurement.

A further comparison between the theoretical predictions of the polarization observables and the extracted measurements can be made through the examination of the behavior of the observable versus invariant mass (or invariant mass squared). In this comparison, the influence of certain intermediate states on the polarization observable may be seen when inspecting the observable's value at the mass (or mass squared) of the intermediate state. As an example, Figure 5.18 shows a prediction of the polarization observable I^c plotted versus the $p\pi^+$ invariant mass ($m_{p\pi^+}$) [4, 60]. Here it can be seen that at the mass of the $\Delta^{++}(1232)$ ($\Delta^{++} \rightarrow p\pi^+$), a feature in the value of the polarization observable for all fixed values of ϕ^*. This feature presents itself as a bump in the observable value or a highly negative slope. The set of plots seen in Figure 5.19 are measurements of the polarization observable I^c produced by binning in photon energy (E_γ), $\phi^*_{\pi^+}$ and $m^2_{p\pi^+}$. Here at the mass squared of the $\Delta^{++}(1232)$, features are also observed in the measurement of the polarization observable. If this process is repeated again with the predicted value of the observable I^c plotted as a function of the $\pi^+\pi^-$ invariant mass ($m_{\pi^+\pi^-}$), the influence of the $\rho^0(770)$ ($\rho^0 \rightarrow \pi^+\pi^-$) can also be seen (Figure 5.20). A comparison between this prediction and the measurements produced by binning in E_γ), $\phi^*_{\pi^+}$ and $m^2_{\pi^+\pi^-}$ shows the presence of this intermediate state (the $\rho^0(770)$ through its effect on the polarization observable (Figure 5.21). These effects are clear evidence of the presence of these intermediate states in the $\gamma p \rightarrow p\ \pi^+\pi^-$ reactions.

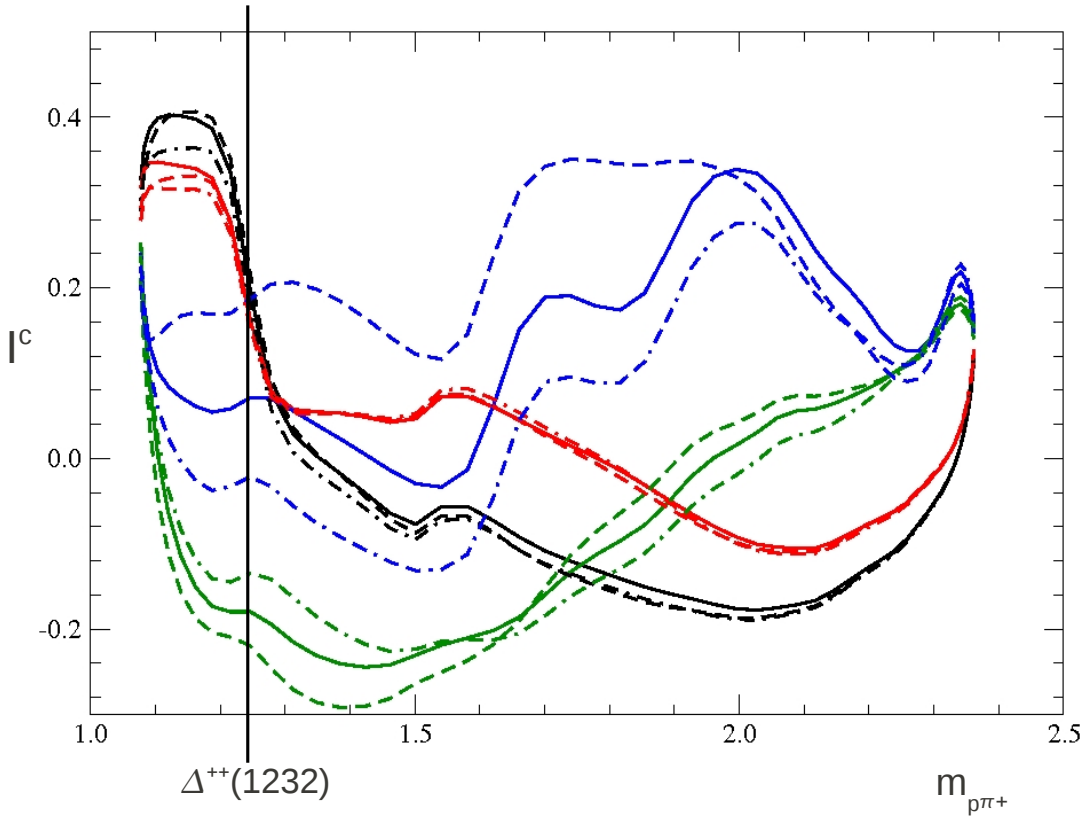

Figure 5.18: Model calculations provided by Winston Roberts [4, 60] which show the predicted values of the polarization observable I^c for $\gamma p \to p\ \pi^+\pi^-$ reactions as a function of $m_{p\pi^+}$. On the mass axis, at the mass of the $\Delta^{++}(1232)$, a feature is observed in the predicted value of I^c for all fixed values of ϕ^* (represented by the different colors). This feature presents itself as a bump in the distribution or a highly negative slope.

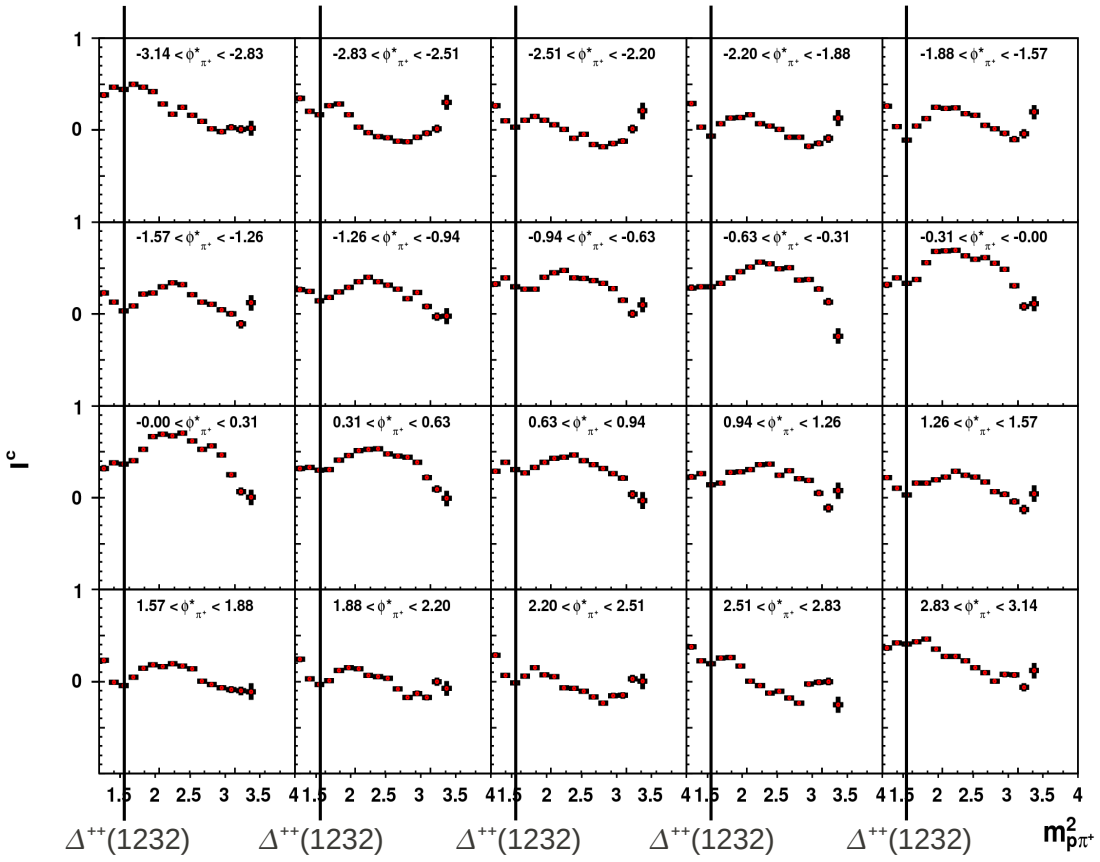

Figure 5.19: Measurements of I^c produced using a binning in E_γ), $\phi^*_{\pi^+}$ and $m^2_{p\pi^+}$. Here 1.60 GeV $< E_\gamma <$ 1.65 GeV. Each square represents a bin in $\phi^*_{\pi^+}$ while the x-axis represents the binning in $m^2_{p\pi^+}$ and the y-axis represents the extracted value of the polarization observable. At the point on the x-axis corresponding to the square of the Δ^{++} mass, a feature is seen in the observable measurement. This indicates the presence of this intermediate state.

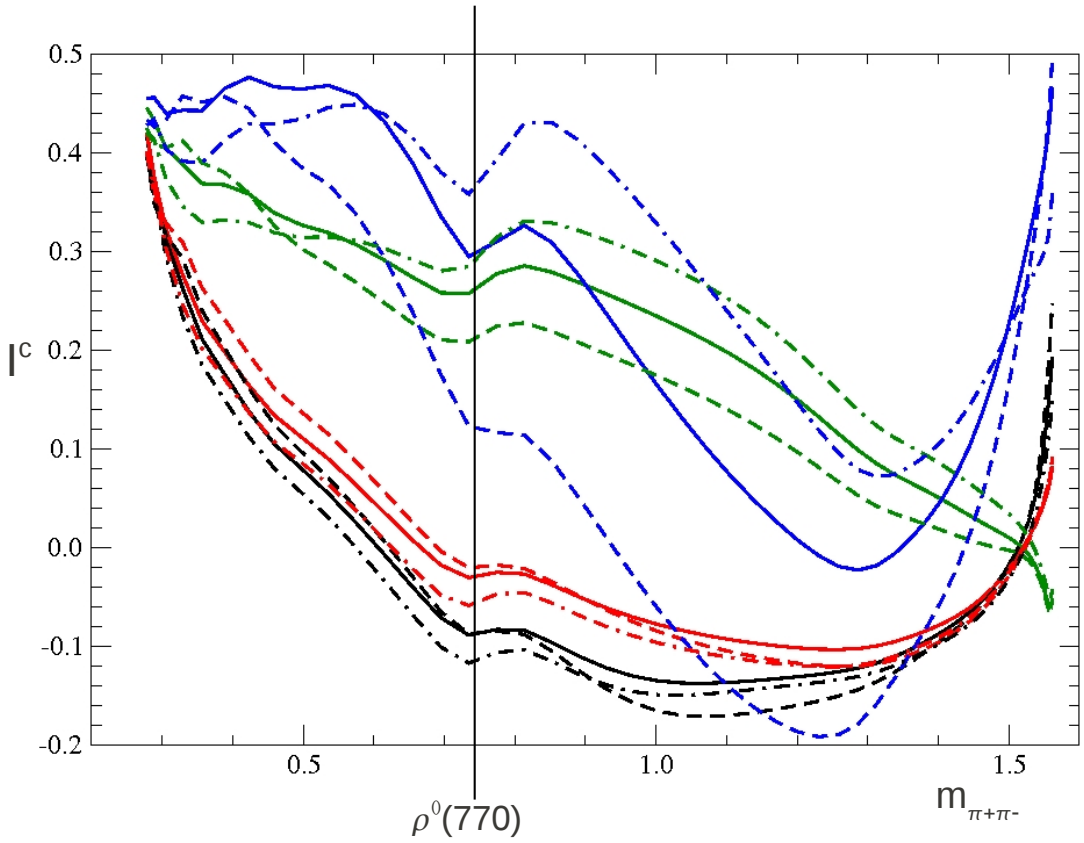

Figure 5.20: Model calculations provided by Winston Roberts [4, 60] which show the predicted values of the polarization observable I^c for $\gamma p \to p\,\pi^+\pi^-$ reactions as a function of $m_{\pi^+\pi^-}$. On the mass axis, at the mass of the $\rho^0(770)$, a feature is observed in the predicted value of I^c for all fixed values of ϕ^* (represented by the different colors). This feature present itself as a rapid change in slope in the distribution.

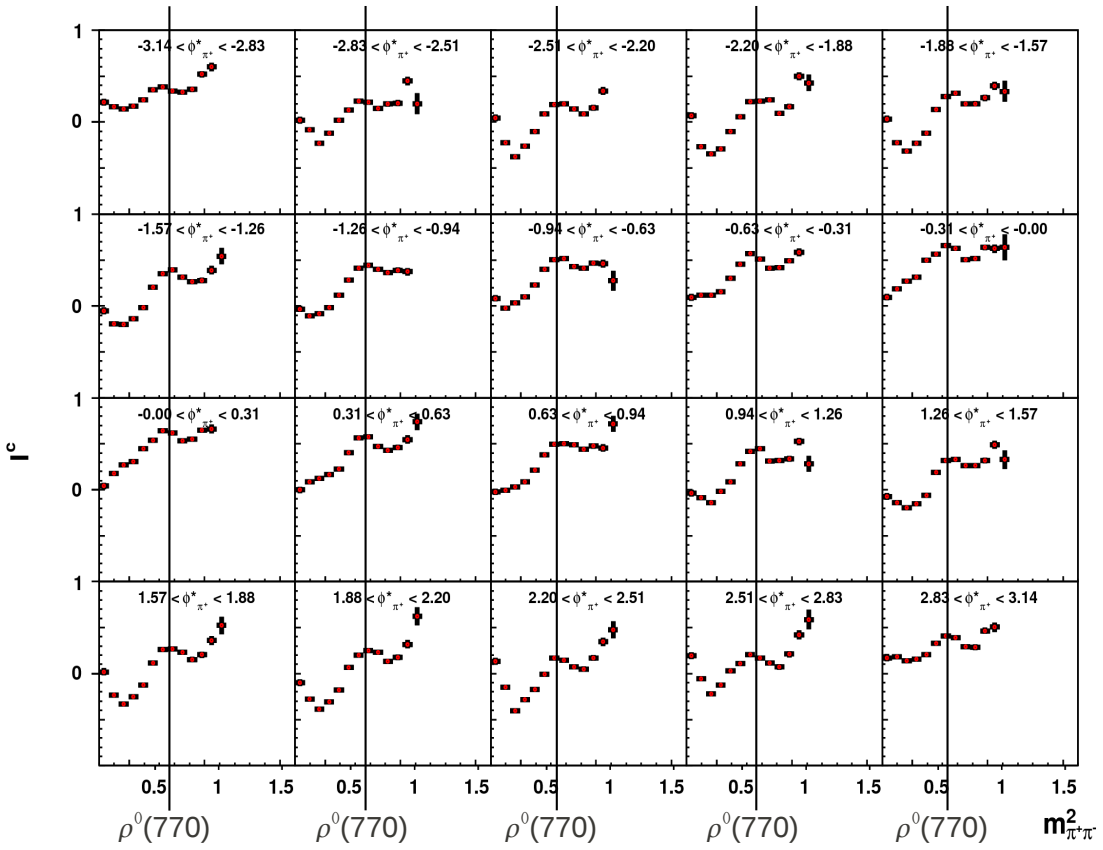

Figure 5.21: Measurements of I^c produced using a binning in E_γ), $\phi^*_{\pi^+}$ and $m^2_{\pi^+\pi^-}$. Here 1.60 GeV $< E_\gamma <$ 1.65 GeV. Each square represents a bin in $\phi^*_{\pi^+}$ while the x-axis represents the binning in $m^2_{\pi^+\pi^-}$ and the y-axis represents the extracted value of the polarization observable. At the point on the x-axis corresponding to the square of the ρ^0 mass, a feature is seen in the observable measurement. This indicates the presence of this intermediate state.

CHAPTER 6

SUMMARY

The major focus of modern nuclear physics (and really, all of physics) is gaining an understanding of the nature of the world around us. In Hadronic Nuclear Physics, the focus is gaining an understanding of the two most fundamental systems found in nature: the baryon and the meson. These two particle types are considered as bound states of quarks with the baryon containing three quarks (qqq) and the mesons containing a quark, anti-quark pair ($q\bar{q}$). As these particles are systems, a study of their behaviors when excited can and does reveal the underlying dynamics otherwise hidden from science. Presently, theoretical predictions from a fundamental theory are not available to predict the behavior of these systems (specifically, the baryon). However, calculations coming from model predictions (Constituent Quarks Models) are possible and provide a "best estimate" in regards to describing the excited spectrum of baryons.

A pressing issue in Hadronic Nuclear Physics has it origins in the comparison of model predictions coming from the various Constituent Quark Models (CQMs) and experimental findings ("various" because the different model calculations differ in how they treat the short-range interactions between the quarks in the baryons). This discrepancy comes from the fact that many more resonances are predicted to exist than have been experimentally measured. This is the infamous *missing resonance* problem. This discrepancy is currently one of the most driving motivations in Hadronic Nuclear Physics and the focus of many experimental queries, starting with πN scattering and more recently, γN experiments.

This missing resonance problem is further compounded by the extremely short lifetimes of the excited baryons. These short lifetimes lead to these resonances possessing mass peaks which are both broad and overlapping. This causes a major issue in separating and identifying specific resonances via a mass scale. Therefore measurable quantities that arise when polarization is introduced (as in $\vec{\gamma}$N experiments), called polarization observables, are sought after. These polarization observables are highly sensitive to which resonances are produced/contained in the excited spectrum of the baryon. The measurement of two such polarization observables which exist for $\vec{\gamma}\, p \rightarrow p\, \pi^+\pi^-$ reactions called I^s and I^c was the focus of this work.

Measurements of I^s and I^c were made using data gathered during the g8b run period using the CLAS detector for incident polarized-photon energies of 1.1 GeV $< E_\gamma <$ 2.3 GeV for $\vec{\gamma}\, p \rightarrow p\, \pi^+\pi^-$ reactions. The statistics available in the g8b data set for the reaction under investigation allowed for a binning in incident photon energy of 50 MeV and twenty bins in

both $\cos(\theta^*_{\pi^+})$ and $\phi^*_{\pi^+}$. Using this binning, measurements of I^c and I^s were conducted via a fitting of event distributions as a function of ϕ_{lab} using the asymmetry between the two polarization settings, PARA and PERP. This work therefore presents the first measurements of I^c for a double-charged pion final state and the first measurements of I^s for a double-pion final state (let alone a final state with two charged pions).

The extractions of I^s and I^c obtained for $\vec{\gamma}\, p \rightarrow p\, \pi^+\pi^-$ reactions show these observables to be fairly large with values approaching one (the maximum value possible). These two observables also show a dependence on the kinematic variables in which they are binned and presented. With the measurements presented in the manner seen in this work, both observables show an increase in magnitude as $\cos(\theta^*)$ increases (starting from $\cos(\theta^*) = -1$). The magnitude of the observables is seen to peak as $\cos(\theta^*)$ approaches zero before it begins to decrease again as the value of $\cos(\theta^*)$ moves towards $+1$.

To carry out a check of the extracted values of I^s and I^c, a fit of the extractions to a function representing their respective predicted symmetries was conducted. The antisymmetry of I^s was checked by fitting the extracted values (as a function of $\phi^*_{\pi^+}$) with a Fourier expansion of $\sin(\phi^*_{\pi^+})$ (up to seven terms) as well as a $\cos(\phi^*_{\pi^+})$ function. The results of this fit show that the behavior of this observable indeed does show a $\sin(\phi^*_{\pi^+})$ and $\sin(2\phi^*_{\pi^+})$ behavior with a temporary and small contribution from the $\sin(3\phi^*_{\pi^+})$ term. No contributions from higher order sine terms as well as the cosine term were observed. The measured values of I^c were also checked in the same manner but with a function containing an expansion of $\cos(\phi^*_{\pi^+})$. This function contained a total of seven terms in the expansion of cosine and an additional $\sin(\phi^*_{\pi^+})$ term. The fit results show that the dominant contribution of this fitting comes mainly from the first three terms, a small contribution from the fourth therm and no contribution from the higher-order terms or the $\sin(\phi^*_{\pi^+})$ term.

The measurement of these two polarization observables will serve to shed light on the issue of the missing resonance problem encountered in Hadronic Nuclear Physics. The high level of sensitivity of these quantities to resonance contributions will allow the theoretical community working on this problem to include or exclude certain resonances in their respective Constituent Quark Model calculations. These model-based calculations of the polarization observables can then be compared to experimental findings allowing for a possible refinement of the models. Subsequent PWA analyses may also take advantage of these measurements and what they say regarding specific resonance states.

In addition to these polarization observables providing hints as to which resonances are actually contained in the excited baryon spectrum, knowledge regarding the states already known to the physics community may be refined through subsequent Partial Wave Analyses (PWAs) using the measurements made in this work. In the low-energy regime ($W \leq 1.7$ GeV), the difference between the theoretical and experimental masses of the well-known $P_{11}(1440)$ Roper resonance may be investigated. In the same energy region, the contribution of the $D_{13}(1520)$ to the $\gamma\, p \rightarrow p\, \pi^+\pi^-$ cross section may be explored as different model calculations result in differing magnitudes of contribution. The properties of the $P_{33}(1600)$ resonance may also be further determined as this "Roper of the Δ's" is not well understood although its coupling to 2π appears to be small. In the medium-energy region (1.7 GeV $\leq W \leq 1.9$ GeV), several states which have been seen in unpolarized photoproduction data may be further investigated due to the information provided by the polarization observables. These resonances are the: $F_{15}(1680)$, $D_{13}(1700)$, $D_{33}(1700)$, and

$P_{13}(1720)$. Finally in the high-energy region (W $\geq$ 1.9 GeV), the question regarding the quark-diquark structure of the baryon may be addressed as several of the high lying states cannot be generated using a quark-diquark structure of the baryon. The confirmation or exclusion of these resonances will serve to refine how physics considers the baryon.

The questions which confront modern physics are numerous to say the least. A world-wide effort is (and has been) in play with the ultimate goal of understanding the most basic and numerous of natural systems. This work, while not answering all the questions regarding these building blocks of the universe, will serve to move humanity toward this ultimate goal.

APPENDIX A

THE FROST EXPERIMENT

A.1 The FROST Experiment

In 2003, an ambitious project for Hall B called the FROST experiment began at Jefferson Lab. The goal of this project as well as subsequent analyses was to provide the hadronic physics community with a plethora of new information which would reveal much about the excited baryon spectrum. The potential importance of the data collected from this experiment comes from its polarization capabilities. As with several other photoproduction experiments carried out in Hall B, the photon beam used to produce the final state particles is polarized. The defining characteristic of this experiment however is the FROST target itself. This new target has the capability of not only polarizing the target material, Butanol (C_4H_9OH), in four orthogonal directions but also to "freeze" this polarization (as FROST stands for "Frozen Spin Target") via a cooling of the target material and the use of a small yet powerful magnet [61].

In order for the polarization setting to be "frozen" in place, very cold temperatures are needed in the target cell, colder than the normal methods used to cool target materials can reach. In order for the (spin) polarization of the target material to be frozen in place, temperatures of 50 mK are needed (the use of LHe_4 alone results in temperatures of $\approx$ 4 mK). Therefore a process called "dilution refrigeration" is needed to reach these incredibly low temperatures. Dilution refrigeration works on the principle that when a mixture of LHe_4 and LHe_3 (a fairly rare isotope of Helium) is cooled below 0.87 mK, these two isotopes undergo a phase separation. This divides the mixture into a LHe_3-rich region and a LHe_3-poor region. The LHe_3 atoms then move from the LHe_3-rich region to the LHe_3-poor region of the mixture. In doing this, as with evaporative cooling, heat energy is used. This process occurs in the "mixing chamber" of the FROST target where the target cell itself resides therefore meaning that when this "evaporation" of LHe_3 into the LHe_4 occurs, heat is taken from the target material (the target material is cooled). The LHe_3 which had moved to the LHe_3-poor region of the mixing chamber then moves to a part of the dilution refrigerator called the "still". Here the LHe_3 evaporates out of the mixture at a rate 1000 times that of the LHe_4 and is removed, cleaned and recondensed via a system of pumps before being returned to the dilution refrigerator. This process of evaporation along with the moving of gas and liquid of different temperatures is made more complicated due to the orientation of this target. The majority of dilution refrigerators operate in a vertical manner, taking

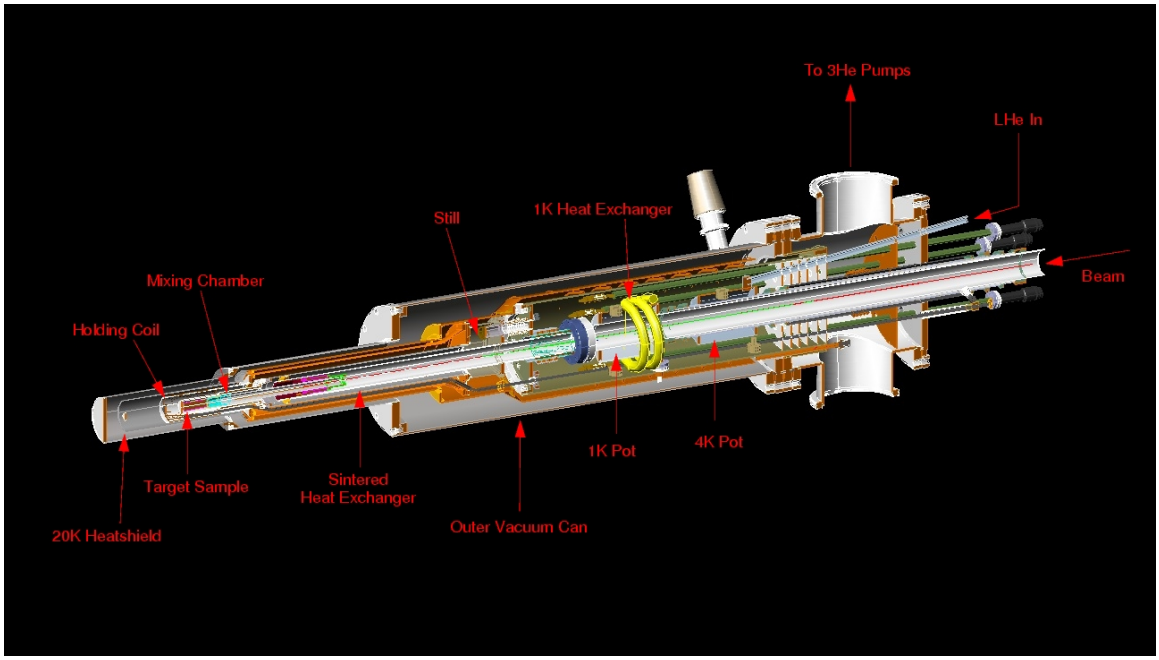

Figure A.1: A cut-away diagram of the FROST target showing the major parts of the target [62].

advantage of the natural movement of "hot" and "cold". The FROST target, however, is oriented horizontally as required for its use with the CLAS detector. The consequence of this was a complication in the manner in which the gases and liquid are transported and the manner and methods used to construct the dilution refrigerator (and the rest of the target) which were eventually overcome. A diagram of the FROST target can be seen in Figure A.1.

In order to preserve the polarization of the target material contained in the FROST target, extremely low temperatures are used in conjunction with relatively low-field "holding magnets" (having a field strength of around 0.5 T). The holding magnets of FROST come in two types, a solenoid which will produce a magnetic field either parallel (or anti-parallel) to the beamline and second magnet with racetrack shaped coils which produces a magnetic field perpendicular to the beamline (leading to four possible polarization orientation of the target material). The purpose of using both low temperatures and a holding magnet is minimize the amount of material between the target cell and the detectors of CLAS. Typically, experiments using a polarized target material use a relatively large electromagnet to maintain a large magnetic field in which the target material resides. The consequence of this is the fact that the large magnet prevents the majority of the particles created in the target cell from ever reaching the detectors, severely limiting the detection of final state particles and any subsequent analyses. As this is never desirable and definitely not acceptable for an experiment with ambitions such as those of FROST, the perpetual use of such a magnet is not included in the FROST plans. When polarizing the target material, the target cell is inserted into a large "polarizing magnet" which polarizes the free electrons in a 5 T field (which the Butanol has been impregnated with) via brute force (at this

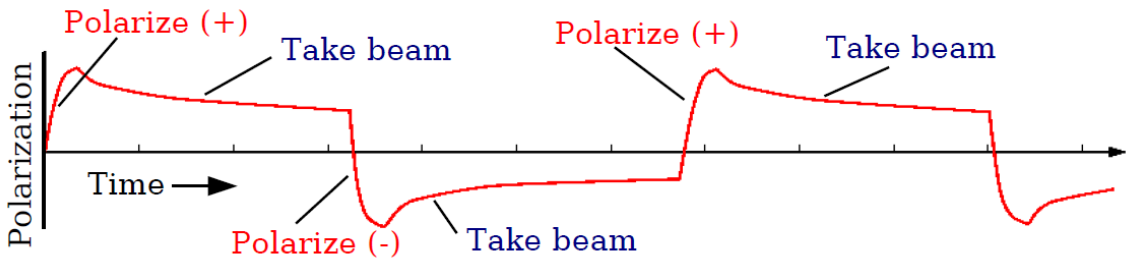

Figure A.2: A cartoon describing the polarization scedule for FROST. The time axis (the x-axis) represents time as measured in days. The original goal was to only repolarize the FROST target every 3.25 days. However, due to the supererb performance of the target, repolarization was needed only every 4-5 days.

point, dilution refrigeration and therefore LHe_3 is not used and the target material is at $\approx$ 1 K). This magnet can be seen in the lower right-hand side of Figure A.6. Once this process is complete and the polarization transferred from the free electrons to the protons via microwaves, the target is set to "dilution mode" (LHe_3 is pumped into the mixing chamber). Simultaneously, the polarizing magnet is slowly ramped down while the holding magnet (which is inside the target assembly, surrounding the target cell) is ramped up. Once this process is complete, the spins of the protons in the target cell are all aligned in one direction and held in place using a combination of the extremely low temperature and the magnetic field of the holding magnet (the low temperatures reached while the target is in dilution mode reduce the strength of the magnetic field needed to preserve polarization). By polarizing the target material and preserving the polarization in this manner, the amount of particles created in the target cell which reach the detectors is maximized along with the relaxation time of the target material. Repolarization of the target material using this method is only needed every 4-5 days meaning that much more time can be spent collecting data instead of repolarizing the target material. A cartoon describing the repolarization schedule may be seen in Figure A.2.

As the direction and type of polarization of the photon beam used for the FROST experiment can be controlled as well as the direction of polarization of the target material, there are several polarization combinations (of beam + target) possible. This capability allows for an analysis of the data to have access to many polarization observables, the measurements of which were made impossible by the lack of polarization in many past experiments. This unprecedented access is the goal of the FROST program and the aim of those involved and will serve to reveal a great deal about the excited baryon spectrum and aide in the quest for a understanding of the physics of the baryon.

A.2 Hardware Contribution to FROST

In the summer of 2005, I began my work on the hardware components of the FROST experiment, working with Youri Sharabian. My introduction into the program (and thusly my first contribution to the FROST program) involved the transverse holding coil to be used for run periods involving a transversely polarized target (polarization of the target material

vertically, perpendicular to the beamline). The responsibility I undertook was to develop two prototypes and a final version of the transverse holding coil as a superconducting magnet of this type had not yet been fabricated. This entailed not only developing the methods to be used for the fabrication of the magnet but also determining which materials would be best for its construction. The support structure on which the superconducting (Formvar-coated) Niobium wire was placed was a cylinder onto which grooves were cut. These grooves were necessary to provide a secure place on which a subset of the wire coils could reside as the design of the magnet was not a solenoid but rather a cylinder on which two racetrack-shaped coils sat (one on top and the other on the bottom). The racetrack coils each comprised of three layers of superconducting wire with the first layer being made of 186 turns, the second having 166 turns, and the third 144 turns. Two pieces of thick paper cut into semi-circles provided a template for forming the "180° turns" at each end of the racetrack shape. The two coils, rather than being made from one continuous piece of wire, were constructed using two separate pieces of superconducting wire. This was done in case one coil failed, the whole apparatus would not have to be made again. When energized, these two sets of racetrack-shaped coils would then produce individual magnetic fields adding to each other to produce a larger magnetic field perpendicular to the axis of the cylinder. When used during running, it is this magnetic field which preserves the polarization of the target material, Butanol (C_4H_9OH). A close-up picture of part of the first prototype produced can be seen in Figure A.3.

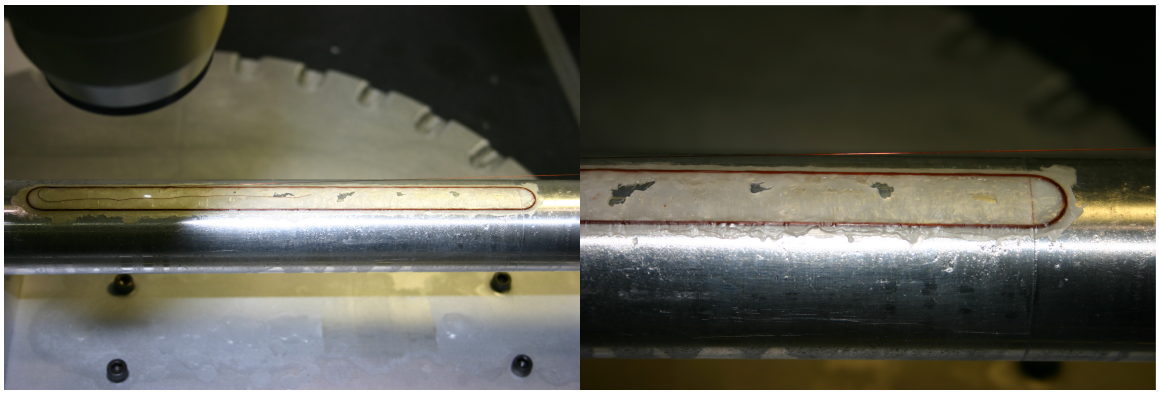

Figure A.3: A picture of the first prototype magnet showing the beginnings of one racetrack coil (a) and approximately half of one coil with two full windings (b). The white substance is purified paraffin which the wire is melted into thereby securing it in place. Visible in the right-hand side of (b) the picture is one of the semi-circles used as a template for forming the 180° turns.

The construction of the magnet, while requiring a skilled hand, was a fairly straightforward process. The main components used were a system of pulleys, a manually rotating table, a jig on which the cylinder was mounted, purified paraffin, a soldering iron, and a microscope (Figure A.4). The superconducting wire used to make the coils needed to be precisely guided to the cylinder while not having much tension placed upon it as it was a fragile wire with a 0.0055 inch (0.1397 mm) diameter. To accomplish this, wire coming off of the spool would go through a system of pulleys which placed just a small amount

of tension on the wire. This system of pulleys also guided the wire to the cylinder which sat on a manually rotating table. The wire was put into the proper position with the aid of a microscope along the straight portions of the cylinder. To secure the position of this wire, a soldering iron was used to gently melt the wire into a layer of purified paraffin. In order to construct the 180° turns seen at each end of the racetrack coil, the semi-circles made of thick paper were used as templates for constructing a smooth curve with the wire being secured to the cylinder in the same manner. As previously described, each coil was comprised of three layers of wire with each coil being made from a single length of wire. The first layer of these coils sits in the shallow grooves cut into the cylinder forming a steady base. Each subsequent layer of wire then sat in the groove formed by two neighboring wires in the previous layer. Transitions between layers were made by "bending" the wire up to start the next layer. When beginning with a new layer, however, the placement of the coil windings alternated. The first layer was constructed from the inside of the racetrack coil to the outside, the second layer from the outside to the inside, and the third layer from the inside to the outside. This arrangement was also carried out for the turns at each end (although no grooves were cut for the 180° turns). For a single layer, each turn was placed on the outside of the arc made by the previous turn (Fig A.4(b)). The arrangement of the layers at each 180° turn was the same as the layers for the straight portions.

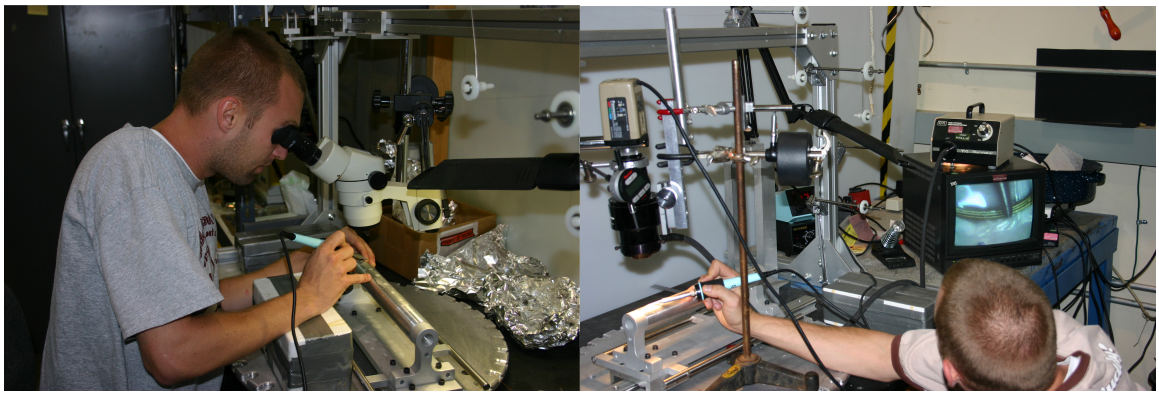

Figure A.4: A picture of the prototype magnet during its fabrication (a) as well as a magnification of one of the 180° turns. Viewable in (a) is the majority of the setup used for fabrication. The bottom portion of the spool of superconducting wire can be seen in the top, center of the photograph. Three of the pulleys used to guide and place a small amount of tension on the wire can be seen in the right-hand side. In the bottom of the photograph is the manually rotating table on which the cylinder-holding jig sat. This table was rotated when making every 180° turn. This setup is again partially seen in (b). Several of the pulleys used to provide the small amount of tension on the wire can be seen towards the center of the picture. The small display right-center of the picture shows a magnification of one of the 180° turns with the camera used to produce the image on the display being on the left-hand side of the picture. This magnification of one of the 180° turns was done to show the small diameter of the superconducting wire as well as how these turns are fabricated.

This design was ultimately put aside due to an overall modification of the design of the FROST target. The technique developments and design developments that arose during my time spent working on this magnet did not. The new transverse holding magnet used

for FROST resides on a cylinder with a slightly larger diameter. The process has also been changed from a manual one to a semi-automated one in which the coils are formed on a rotating table using epoxy instead of purified paraffin. The resulting magnet using this procedure can be seen in Figure A.5.

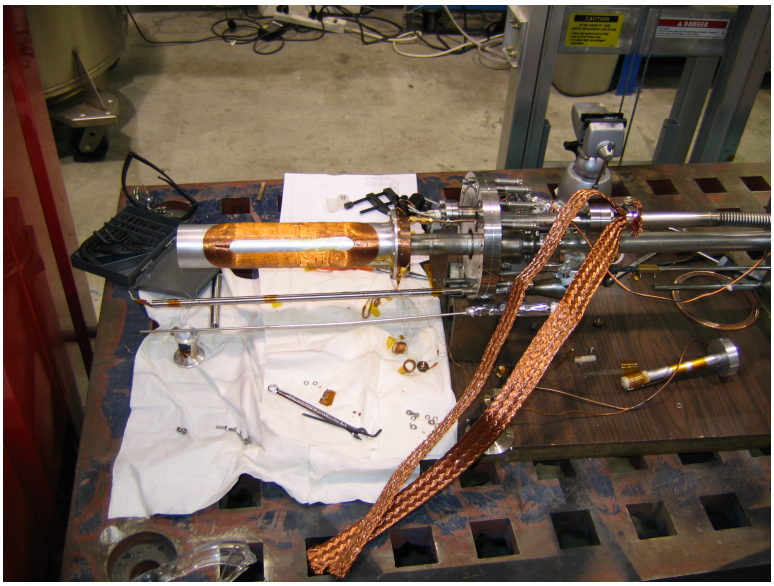

Figure A.5: A picture of the transverse holding coil produced using the semi-automated procedure. One of the two racetrack-shaped coils is visible.

In the summer of 2006, I was offered the opportunity to work with the JLab Target Group on the construction of the FROST dilution refrigerator. This opportunity was highly beneficial as I was able to work on the FROST target from when it was just a few parts on a table, to the testing of the target, all the way to its final installation in Hall B and doing so under the tutelage of a great and skilled group of people. I learned many aspects of hardware development during this time. My roles in the construction of FROST included (but were not limited to):

- Fabrication of parts to be used for the construction of FROST.
- Machining parts and support structures for the gas handling system (Pump Cart).
- Machining valves, heat exchangers, tubing, supports, and flanges on the metal lathe and mill.
- Leak checking all parts of FROST.
- Assembly of parts.
- Testing of assembly.
- Installation in Hall B.

- Testing of the target in Hall B.

Due to the conditions under which the target and all of it parts must operate, all parts as well as the completed assembly must be deemed leak-tight. Due to this highly important requirement, each part of FROST was immediately leak-checked after any welds or joints were made. These leak checks were performed using a a high-vacuum system and a helium spectrometer. The piece under investigation was attached to the high-vacuum system and pumped upon until the internal pressure reached about 10^{-5} Torr. Once this pressure was reached, the helium spectrometer could be used. A canister of Helium gas was then tapped and a very weak stream of helium gas was sprayed via a small tube and sprayer on weld joints or any other type of interfaces. The highly sensitive helium spectrometer was used to detect any helium that may have been sucked into the vacuum. Detection of helium by the spectrometer would indicate that the tested piece is not leak tight and therefore must be fixed. If no helium was detected, the piece was deemed leak-tight and became a part of the FROST target.

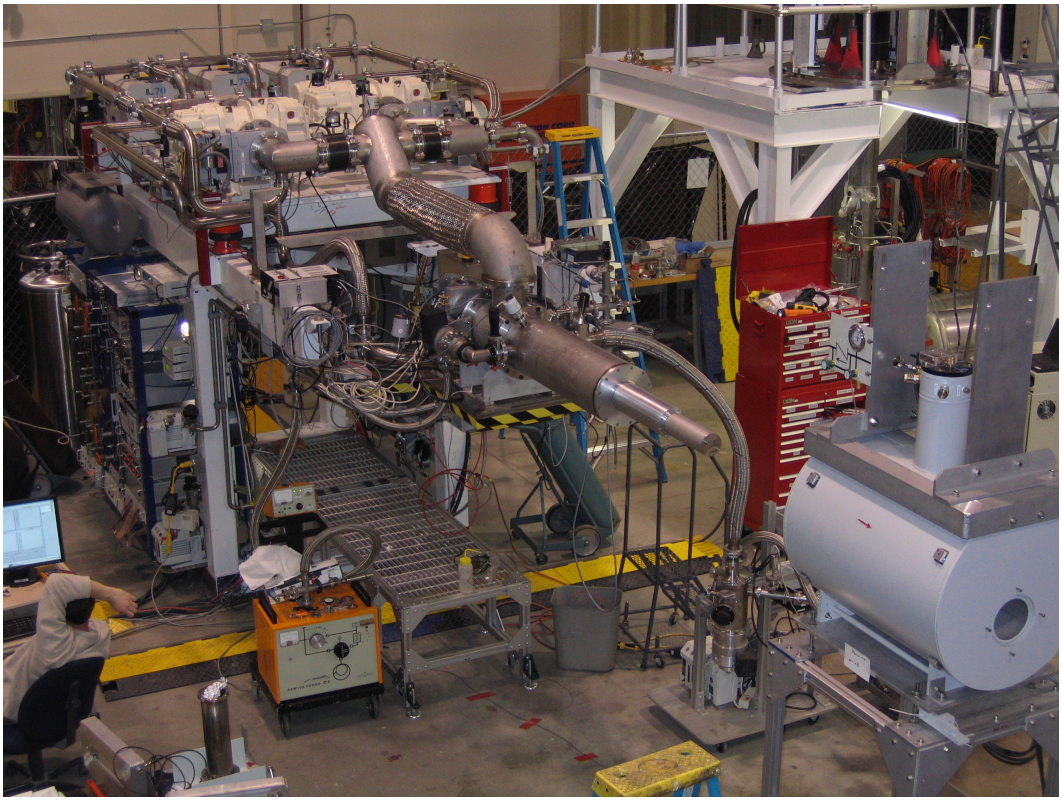

Figure A.6: The final FROST assembly being tested in the Test Lab at JLab. The FROST dilution refrigerator can be seen in the middle-right of the picture (the three cylinders decreasing in size from left to right). The large platform on the left is the "Pump Cart" used to maintain a vacuum on the system and to capture, recondense, and recirculate the helium (its purpose in terms of helium is to capture, recondense, and recirculate the He_3). Pictured in the bottom, right-hand corner is the polarizing magnet.

My work with the FROST target continued with the final testing of the entire assembly in the Test Lab at JLab (Fig A.6). Once the target repeatedly proved itself to work in all stages of its operation, it was disassembled and taken to the experimental hall (Hall B). Here the Pump Cart was reassembled and the dilution refrigerator very carefully placed into position using the crane in Hall B. In-hall testing of the FROST target then began. It was during this testing that problems related to the transportation of such a sensitive device were discovered. Once these problems were discovered, the dilution refrigerator was removed to the hall, taken back to the Test Lab and disassembled for investigation. This process occurred twice, once because of an electrical connection made faulty during transport and once due to an misaligned flange. After the target's third trip to the hall, it showed itself to be in perfect working order. The dilution refrigerator was repeatedly tested and the process of repolarization practiced. This repolarization process involves moving the entire assembly (the refrigerator and Pump Cart) one to two meters (back and forth) via wenches and a metal track as well as a one to two meter sideways movement of the polarizing magnet. This routine was practiced several times as to familiarize those responsible for repolarizing the target material with the process in the interest of speed and safety (Figure A.7 shows the insertion of the target into the polarizing magnet in Hall B). Once all of the pre-run requirements were satisfied, the target was ready for the experiment.

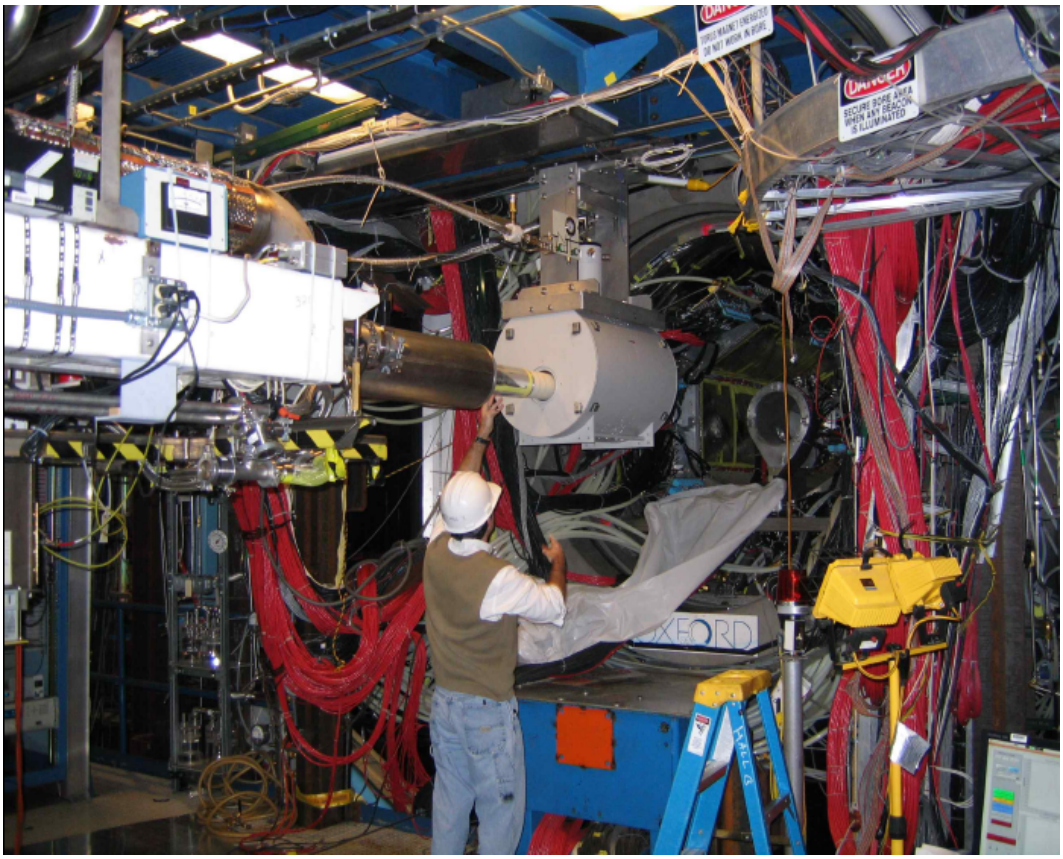

Figure A.7: A picture of the FROST target after installation in Hall B. Here the entire assembly is slowly being moved forward, toward the center of CLAS and into the polarizing magnet to begin the polarization of the target material.

A.3 Performance of the FROST target

The performance of the FROST target during both run periods (deemed "g9a" which ran from 03 November 2007 to 12 Febuary 2008 and "g9b" which ran from 25 March 2010 to 01 April 2010) and the experiment as a whole was quite excellent. The temperature of the target material during run conditions surpassed the goal of 50 mK, reaching a temperature of 30 mK (28 mK when no beam was striking the target) in the target cell. This better-than-expected performance meant that the relaxation time of the target material was extended to 3-5 times the expected amount, leading to fewer repolarizations (the expected polarization degradation was 5% per day but under operation, this number was 1-1.5% per day) and more data-taking. The target also was very stable during the FROST run with no major problems being reported.

The two parts of the FROST experiment (deemed g9a and g9b) were both testaments to the quality of skill brought to the table by those who contributed to the effort. The first half of this experiment (g9a) boasts a data set that is 35 TB in size and contains 10.5 billion events using a polarized photon beam incident on a longitudinally polarized target. The second part of the FROST experiment, g9b (using a polarized photon beam incident on a transversely polarized target), has recently finished thus bringing a close to the data gathering portion of the FROST program. Considering the wonderful performance of the target, the quality of the polarized photon beam and the performance of CLAS, the FROST experiment was a great success. Now the attention turns to the analyses from the FROST group as there are several analyses presently underway which hold the potential for adding much knowledge to the field of Hadronic Physics and answering many questions regarding the missing resonances of the baryon spectrum.

APPENDIX B

ϕ-DISTRIBUTIONS

The following figures are a sampling of the ϕ-distributions used to produce the (averaged) observable measurements shown in Chapter 5 (Figures 5.2 through 5.10). These figures show the asymmetry between the PARA and PERP ϕ-distributions versus ϕ_{lab} of the π^+. Each set of ϕ-distributions (each figure) represents a single bin in k (E_γ) and a single bin in $\phi^*_{\pi^+}$ with each square representing a bin in $\cos\theta^*_{\pi^+}$.

B.1 ϕ-distributions for $p\ \pi^+\pi^-$ events

B.1.1 $1.20 < E_\gamma < 1.25$ GeV

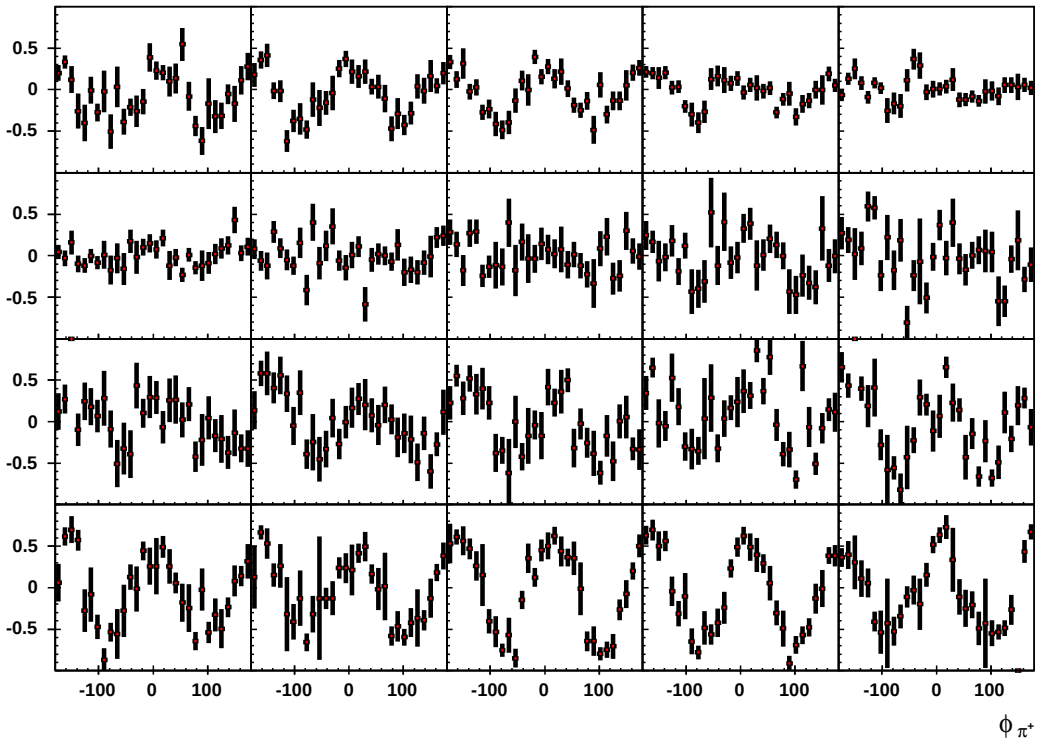

Figure B.1: A sampling of the ϕ-distributions used to extract I^s and I^c for a $p\ \pi^+\pi^-$ final state. Here, $-18^\circ < \phi^*_{\pi^+} < -36^\circ$.

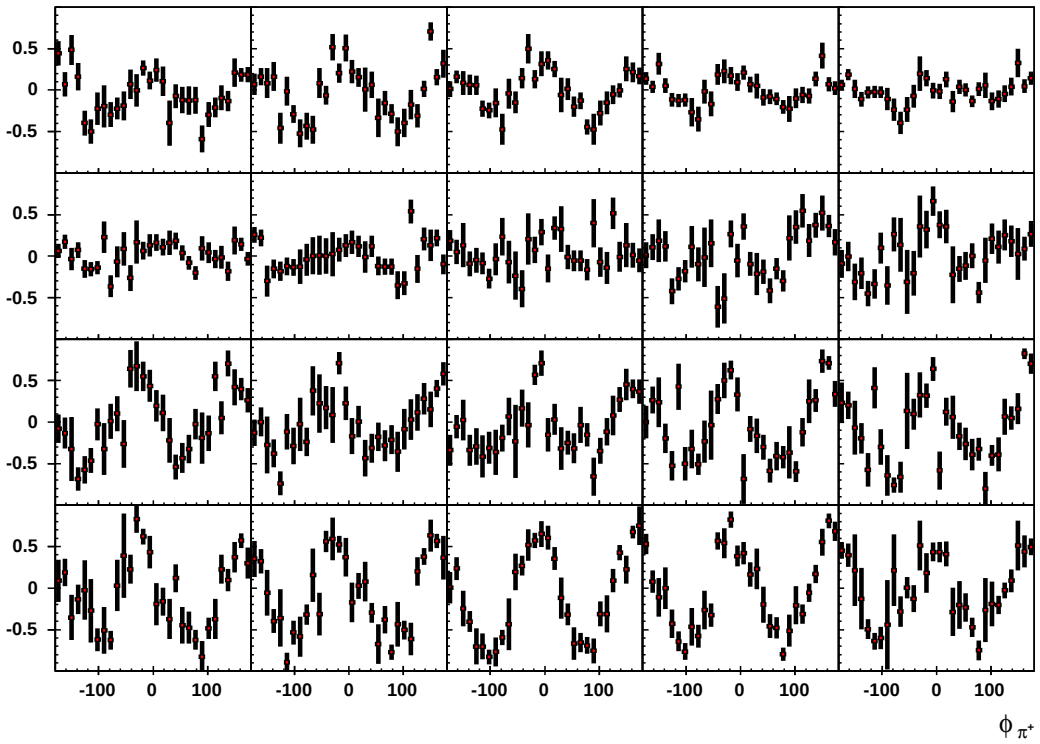

Figure B.2: A sampling of the ϕ-distributions used to extract I^s and I^c for a $p\ \pi^+\pi^-$ final state. Here, $36^\circ < \phi^*_{\pi^+} < 54^\circ$.

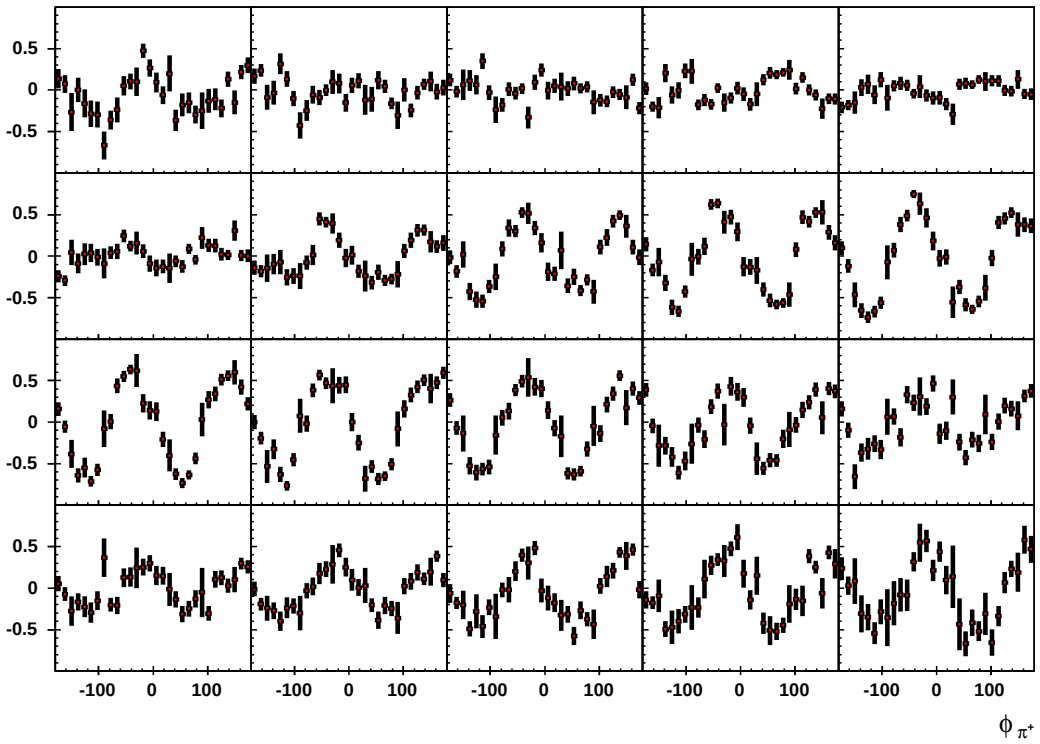

Figure B.3: A sampling of the ϕ-distributions used to extract I^s and I^c for a $p\ \pi^+\pi^-$ final state. Here, $90^\circ < \phi^*_{\pi^+} < 108^\circ$.

B.1.2 $1.40 < E_\gamma < 1.45$ GeV

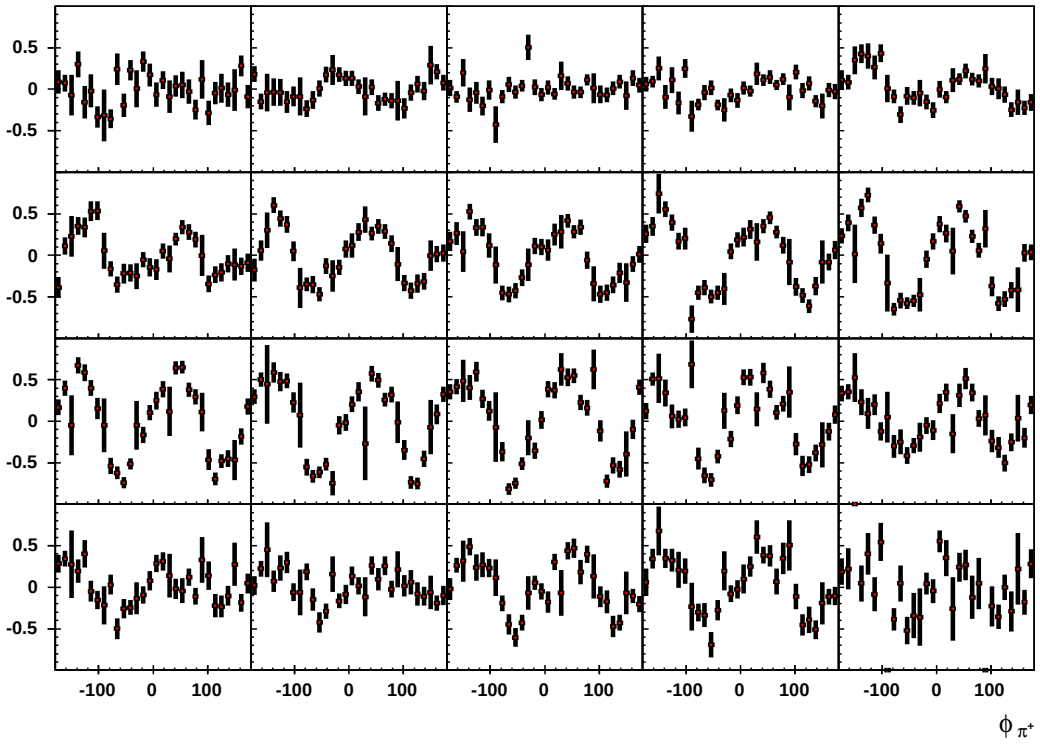

Figure B.4: A sampling of the ϕ-distributions used to extract I^s and I^c for a $p\ \pi^+\pi^-$ final state. Here, $-108^\circ < \phi^*_{\pi^+} < -90^\circ$.

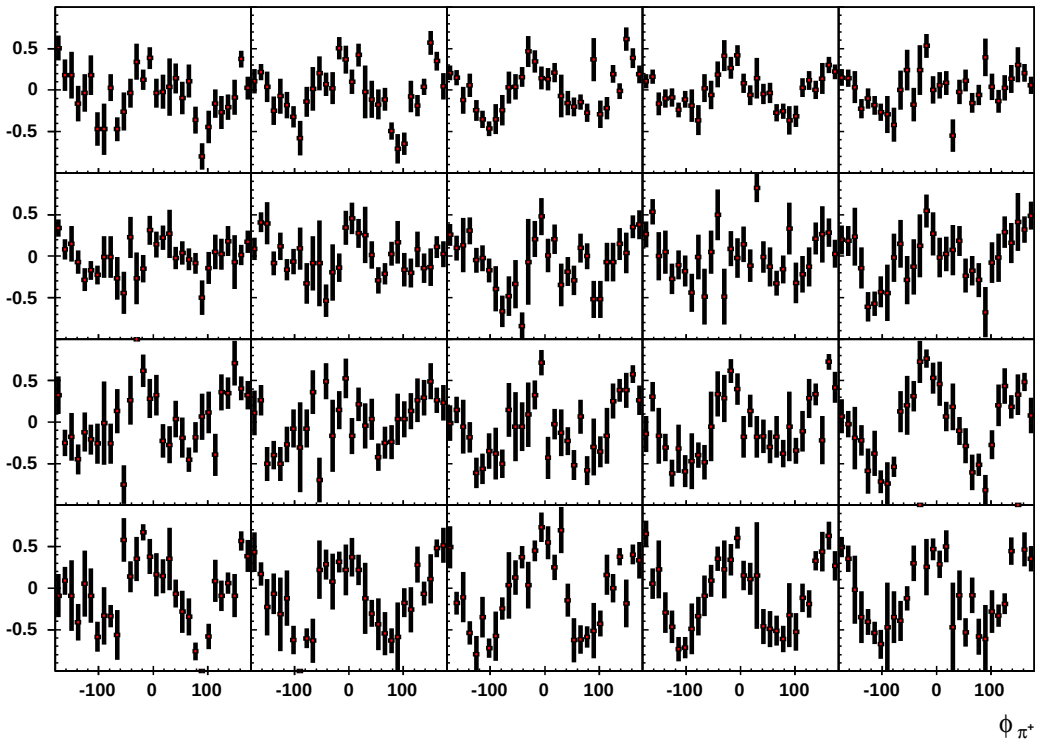

Figure B.5: A sampling of the ϕ-distributions used to extract I^s and I^c for a $p\ \pi^+\pi^-$ final state. Here, $36^\circ < \phi^*_{\pi^+} < 54^\circ$.

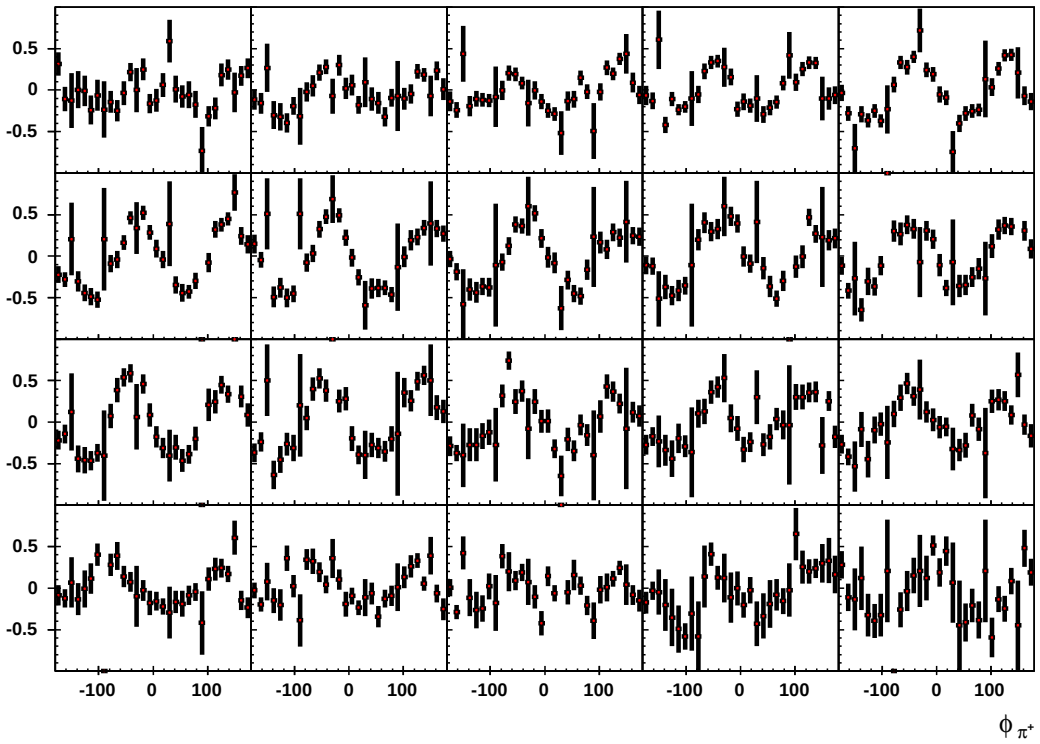

Figure B.6: A sampling of the ϕ-distributions used to extract I^s and I^c for a $p\ \pi^+\pi^-$ final state. Here, $126^\circ < \phi^*_{\pi^+} < 144^\circ$.

B.1.3 $1.60 < E_\gamma < 1.65$ GeV

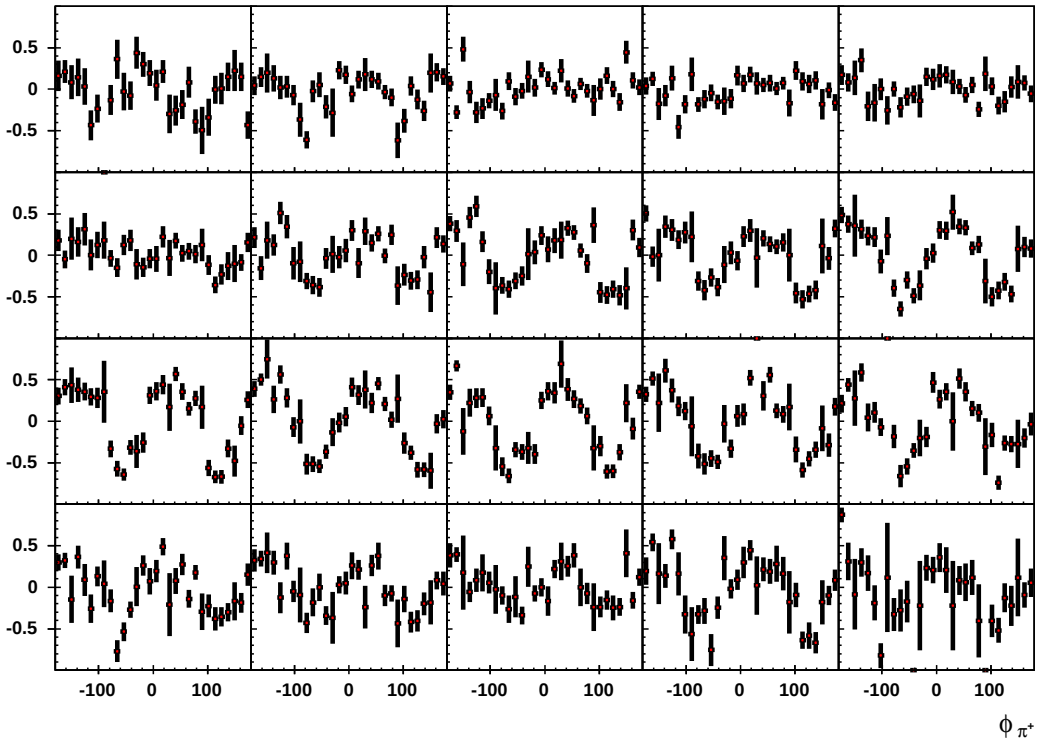

Figure B.7: A sampling of the ϕ-distributions used to extract I^s and I^c for a $p\ \pi^+\pi^-$ final state. Here, $-90^\circ < \phi^*_{\pi^+} < -72^\circ$.

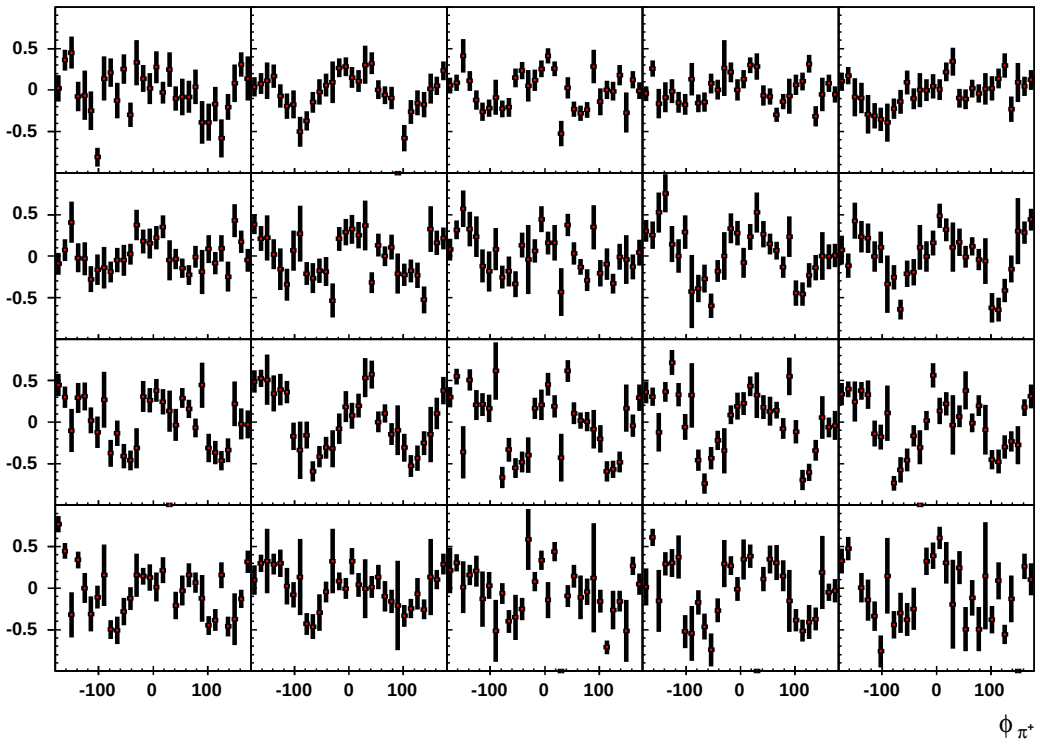

Figure B.8: A sampling of the ϕ-distributions used to extract I^s and I^c for a $p\ \pi^+\pi^-$ final state. Here, $-72^\circ < \phi^*_{\pi^+} < -54^\circ$.

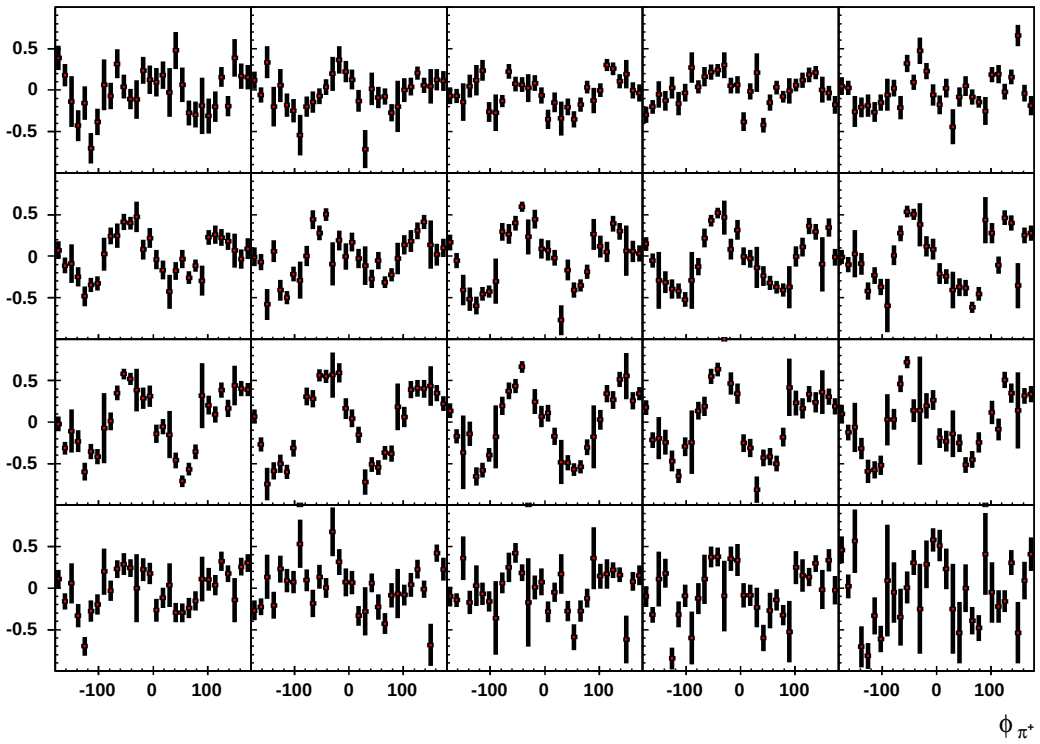

Figure B.9: A sampling of the ϕ-distributions used to extract I^s and I^c for a $p\ \pi^+\pi^-$ final state. Here, $90^\circ < \phi^*_{\pi^+} < 108^\circ$.

B.1.4 $2.00 < E_\gamma < 2.05$ GeV

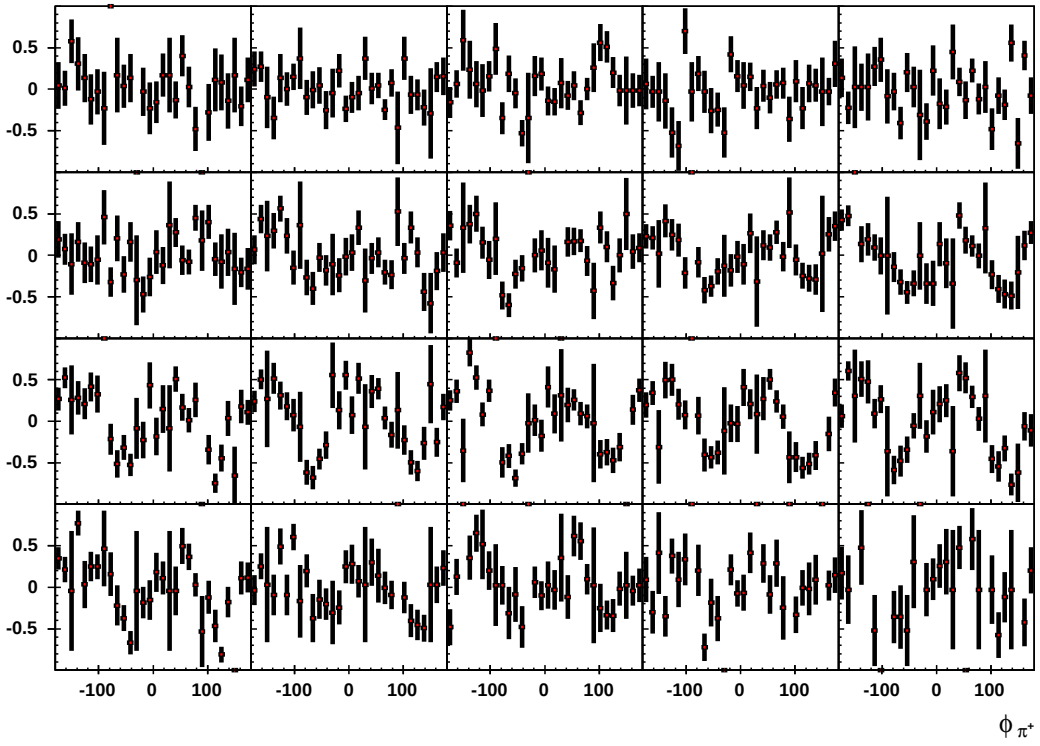

Figure B.10: A sampling of the ϕ-distributions used to extract I^s and I^c for a $p\ \pi^+\pi^-$ final state. Here, $-90^\circ < \phi^*_{\pi^+} < -72^\circ$.

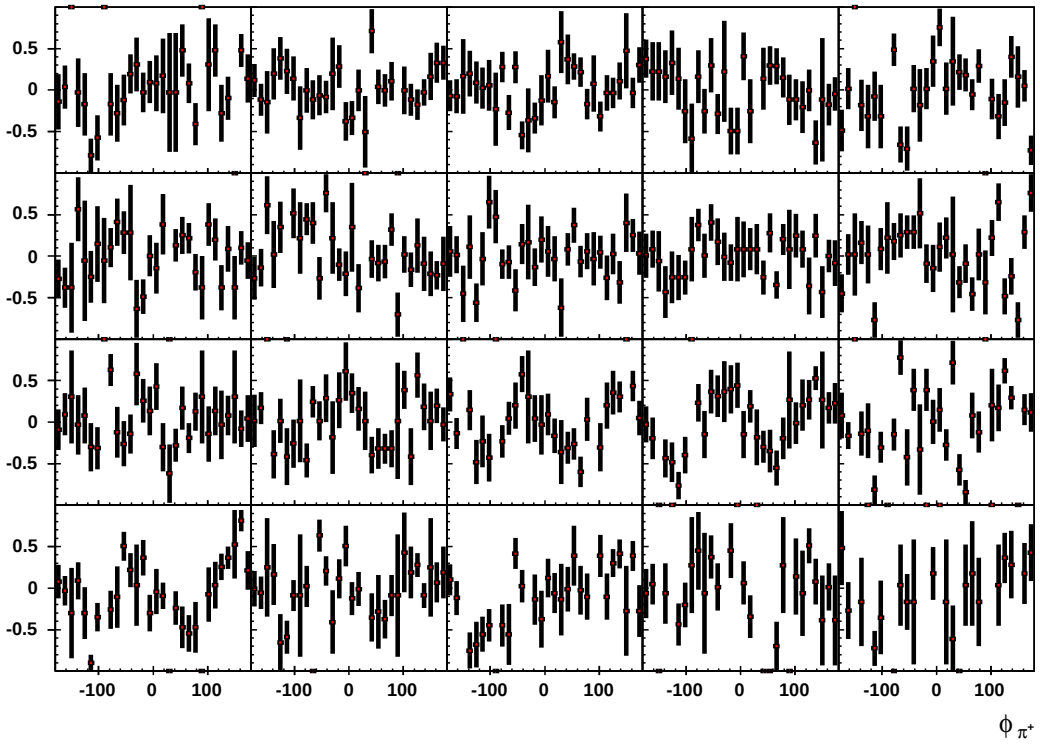

Figure B.11: A sampling of the ϕ-distributions used to extract I^s and I^c for a $p\ \pi^+\pi^-$ final state. Here, $54^\circ < \phi^*_{\pi^+} < 72^\circ$.

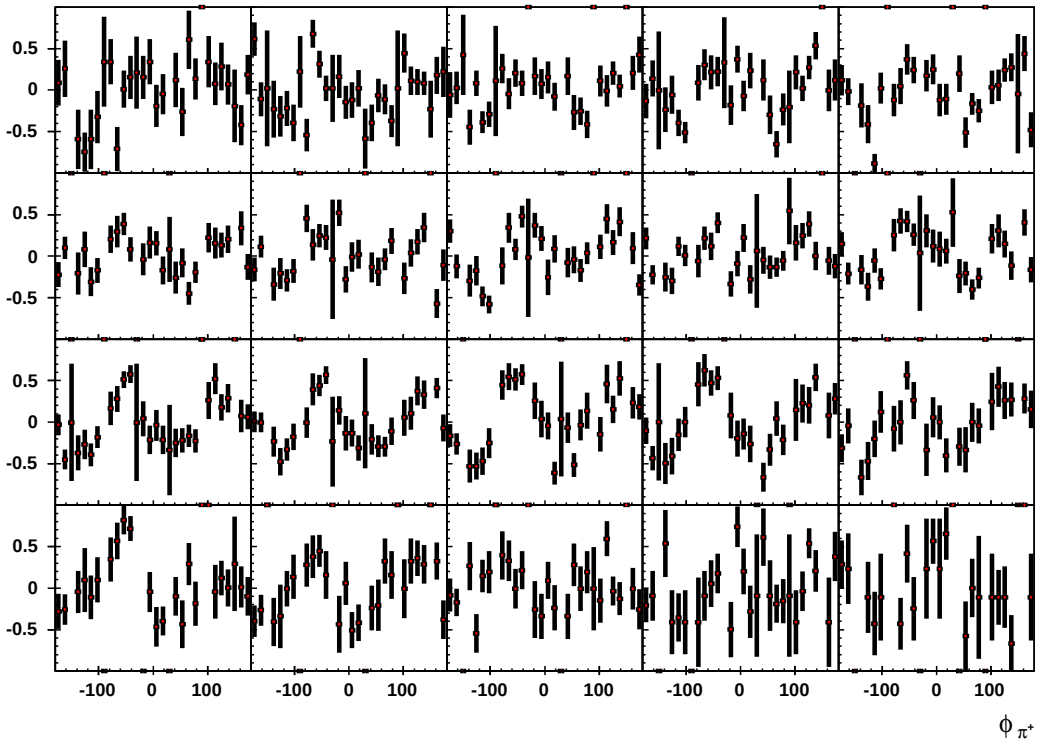

Figure B.12: A sampling of the ϕ-distributions used to extract I^s and I^c for a $p\ \pi^+\pi^-$ final state. Here, $108^\circ < \phi^*_{\pi^+} < 126^\circ$.

B.2 ϕ-distributions for $p\ \pi^+(\pi^-)$ events

B.2.1 $1.20 < E_\gamma < 1.25$ GeV

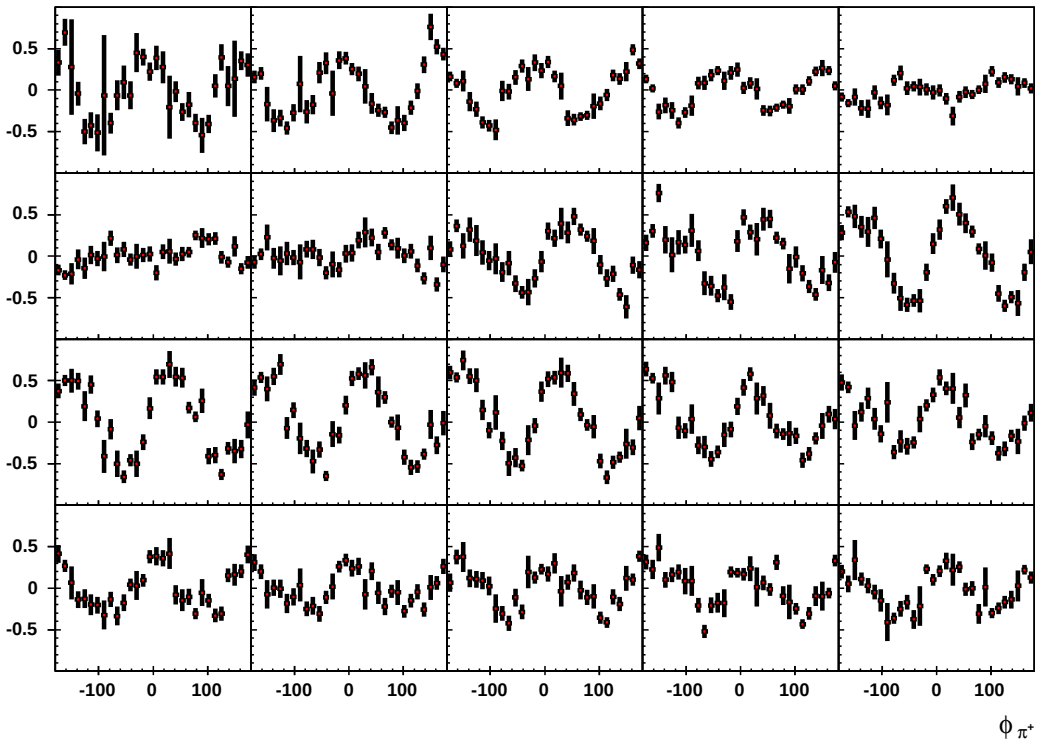

Figure B.13: A sampling of the ϕ-distributions used to extract I^s and I^c for a $p\ \pi^+(\pi^-)$ final state. Here, $-72^\circ < \phi^*_{\pi^+} < -54^\circ$.

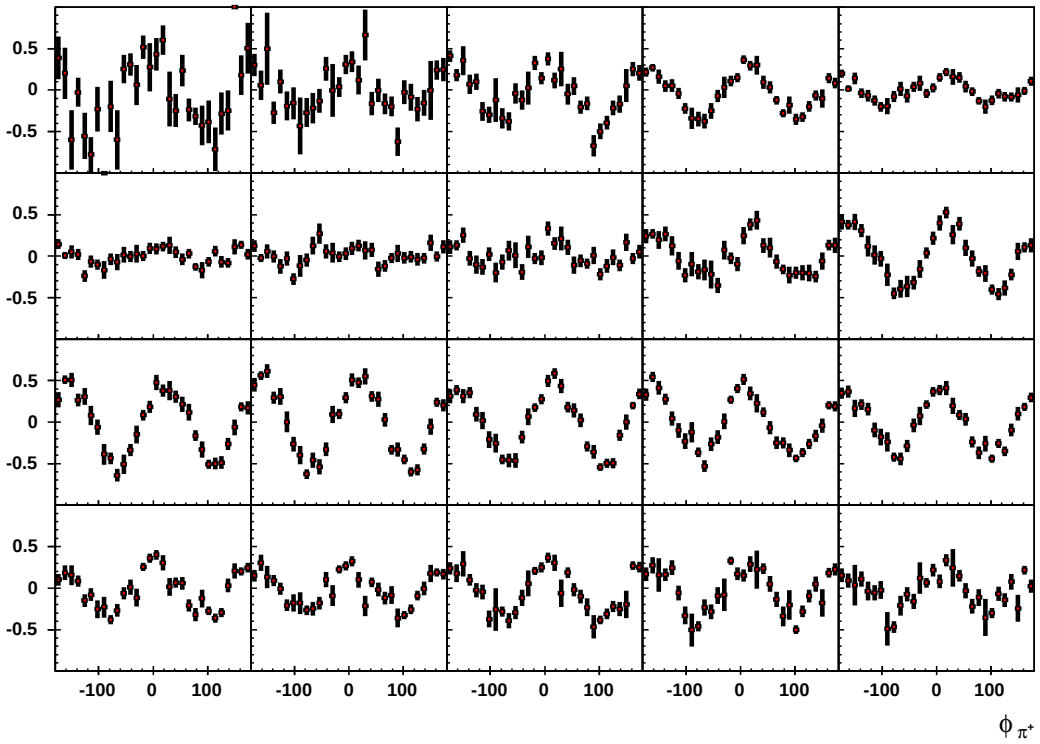

Figure B.14: A sampling of the ϕ-distributions used to extract I^s and I^c for a $p\ \pi^+(\pi^-)$ final state. Here, $-36^\circ < \phi^*_{\pi^+} < -18^\circ$.

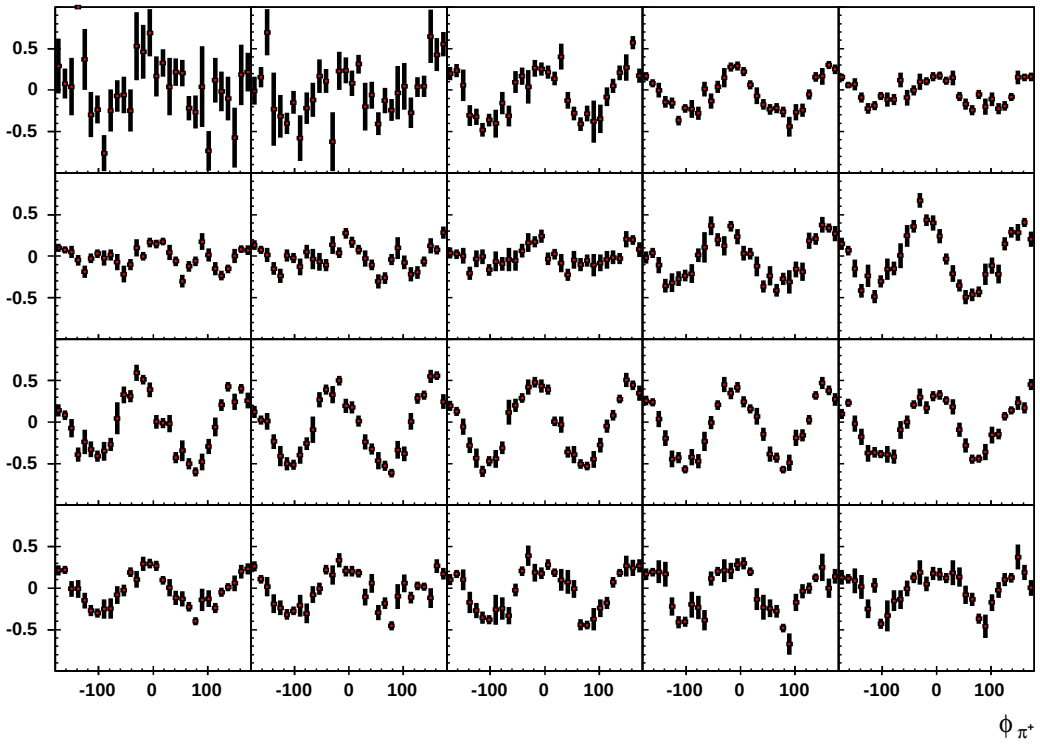

Figure B.15: A sampling of the ϕ-distributions used to extract I^s and I^c for a $p\ \pi^+(\pi^-)$ final state. Here, $18^\circ < \phi^*_{\pi^+} < 36^\circ$.

B.2.2 $1.40 < E_\gamma < 1.45$ GeV

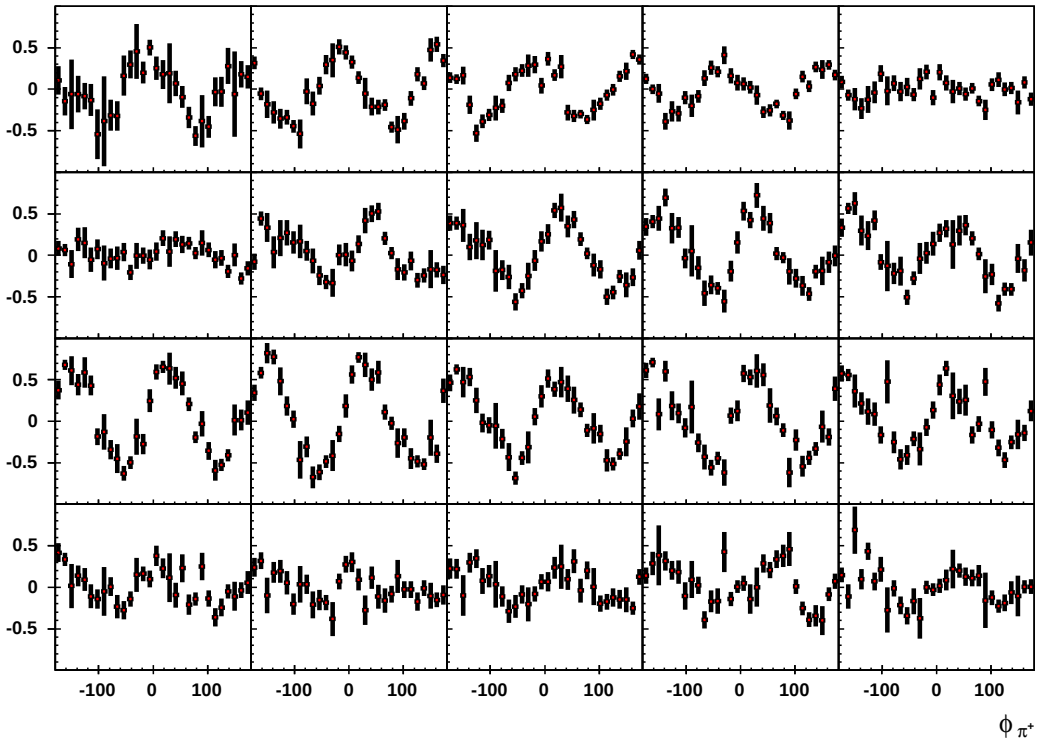

Figure B.16: A sampling of the ϕ-distributions used to extract I^s and I^c for a $p\,\pi^+(\pi^-)$ final state. Here, $-72^\circ < \phi^*_{\pi^+} < -54^\circ$.

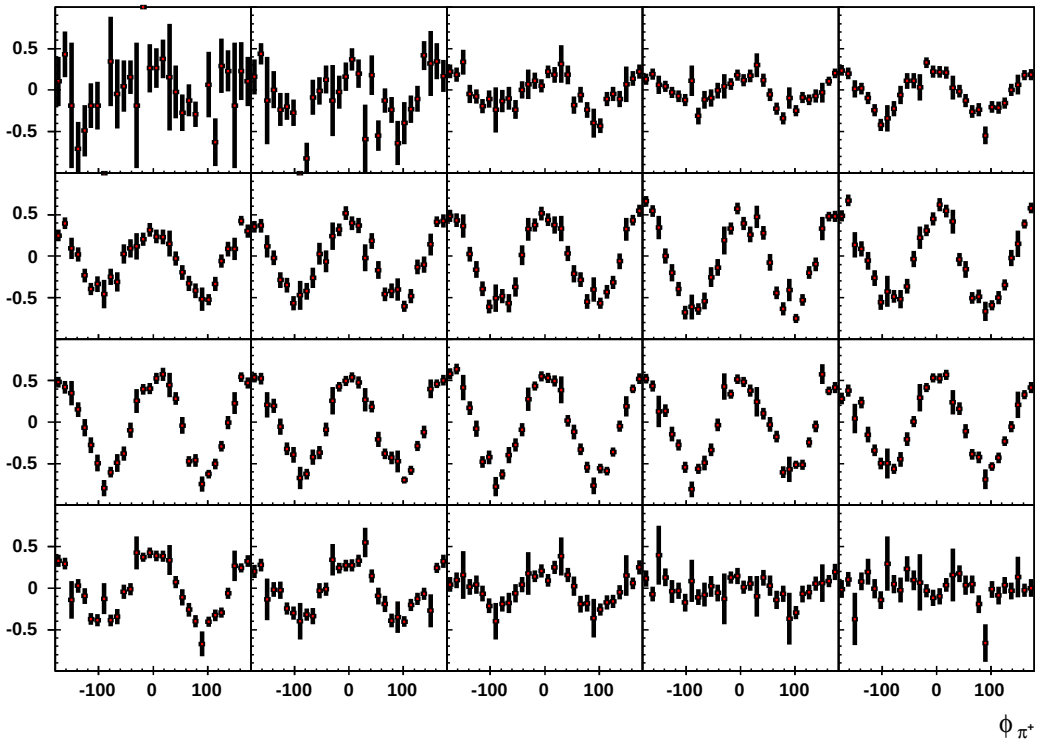

Figure B.17: A sampling of the ϕ-distributions used to extract I^s and I^c for a $p\ \pi^+(\pi^-)$ final state. Here, $-18^\circ < \phi^*_{\pi^+} < 0^\circ$.

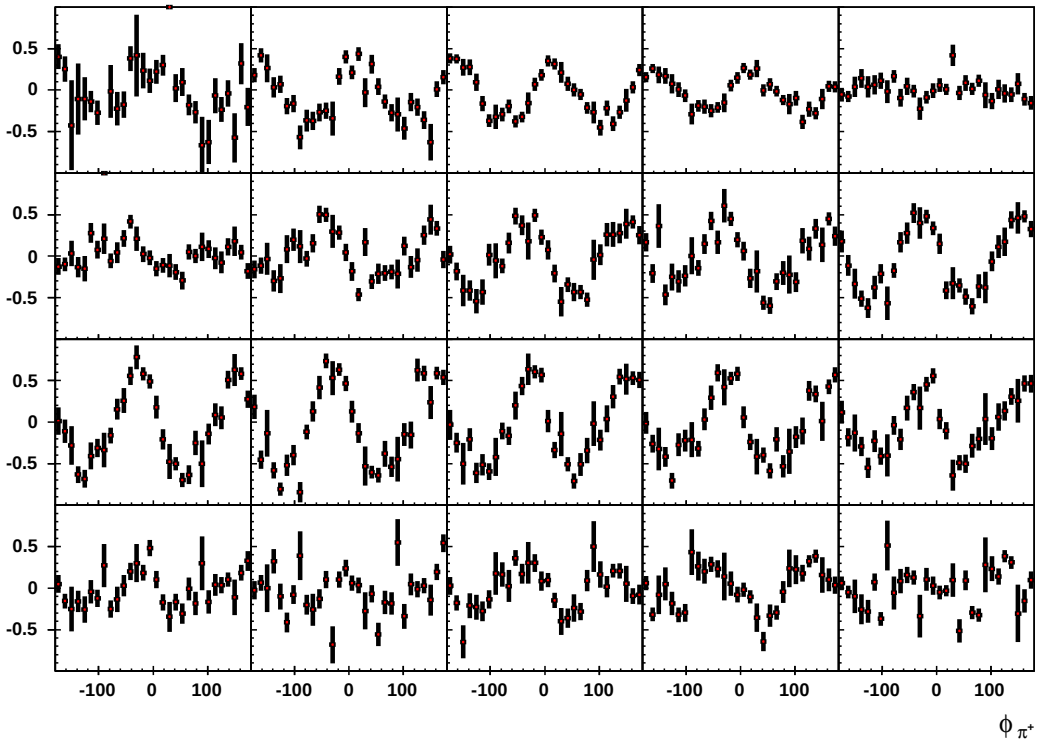

Figure B.18: A sampling of the ϕ-distributions used to extract I^s and I^c for a $p\ \pi^+(\pi^-)$ final state. Here, $54^\circ < \phi^*_{\pi^+} < 72^\circ$.

B.2.3 $1.60 < E_\gamma < 1.65$ GeV

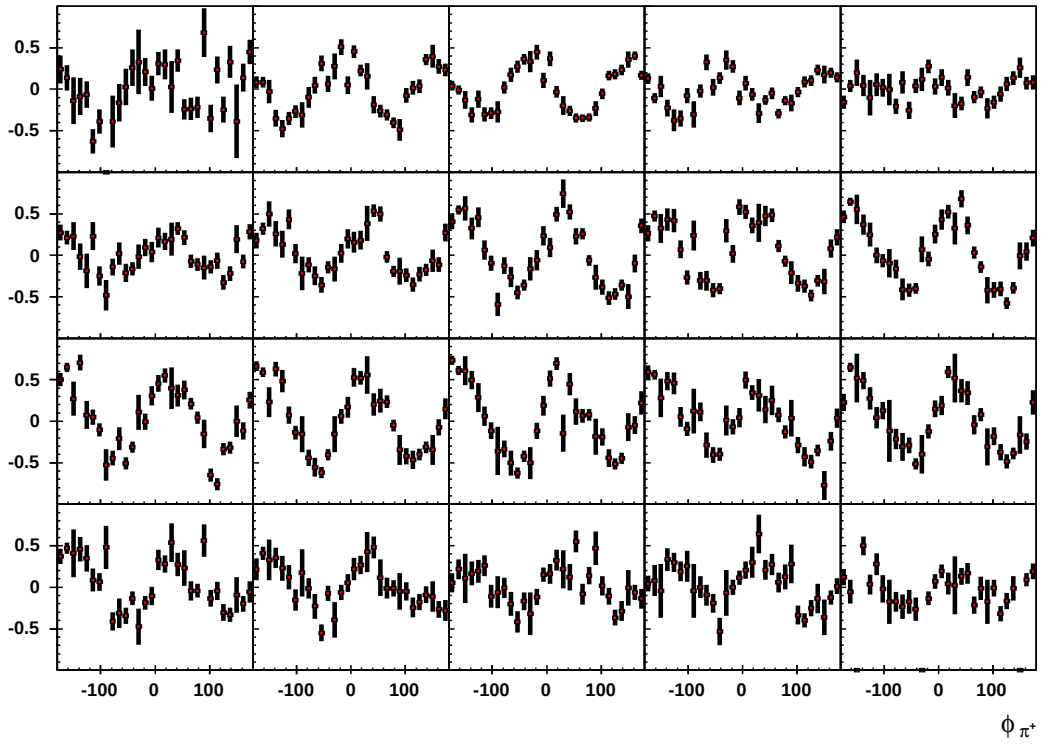

Figure B.19: A sampling of the ϕ-distributions used to extract I^s and I^c for a $p\,\pi^+(\pi^-)$ final state. Here, $288^\circ < \phi^*_{\pi^+} < 306^\circ$.

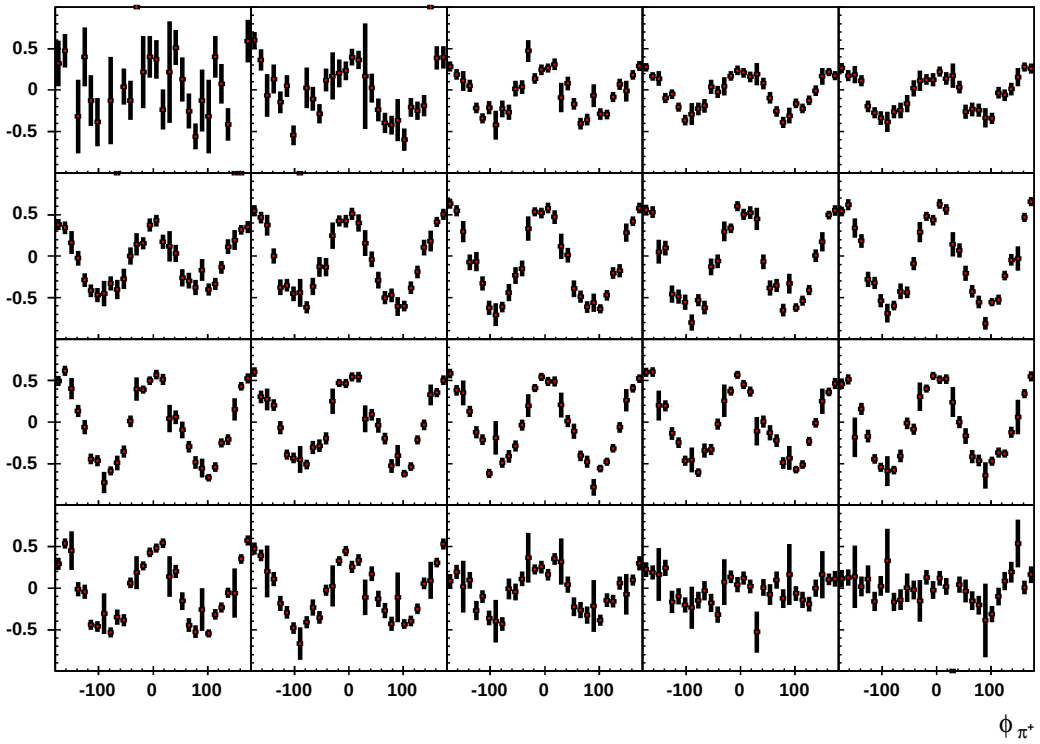

Figure B.20: A sampling of the ϕ-distributions used to extract I^s and I^c for a $p\ \pi^+(\pi^-)$ final state. Here, $-18^\circ < \phi^*_{\pi^+} < 0^\circ$.

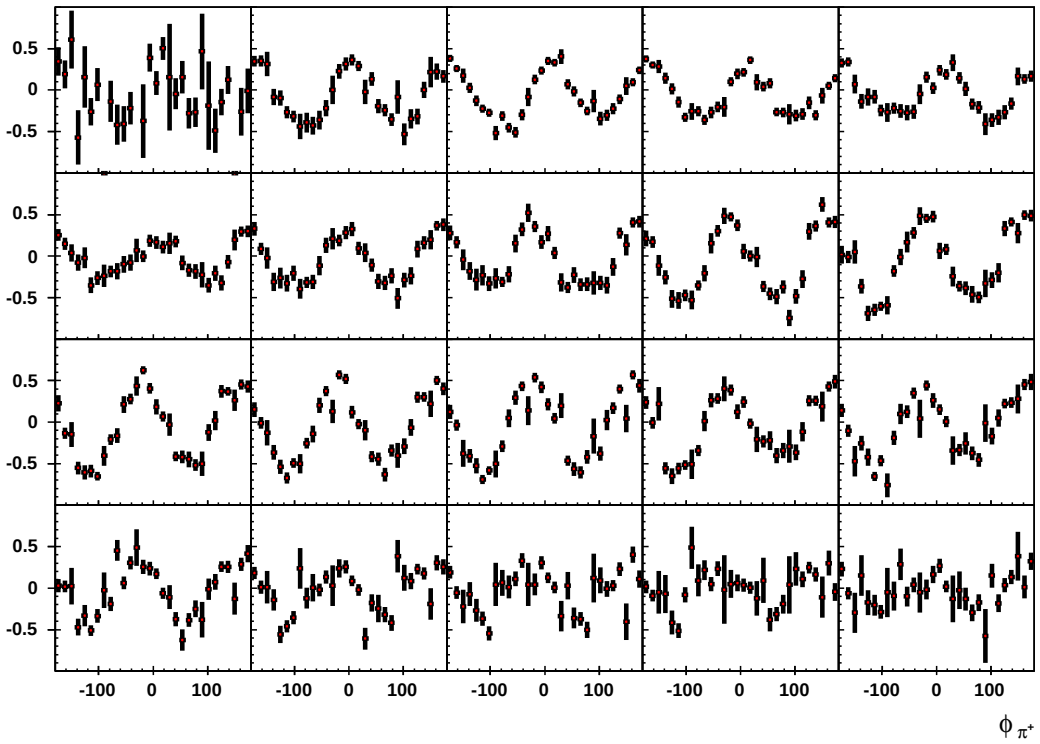

Figure B.21: A sampling of the ϕ-distributions used to extract I^s and I^c for a $p\ \pi^+(\pi^-)$ final state. Here, $36^\circ < \phi^*_{\pi^+} < 54^\circ$.

B.2.4 $2.00 < E_\gamma < 2.05$ GeV

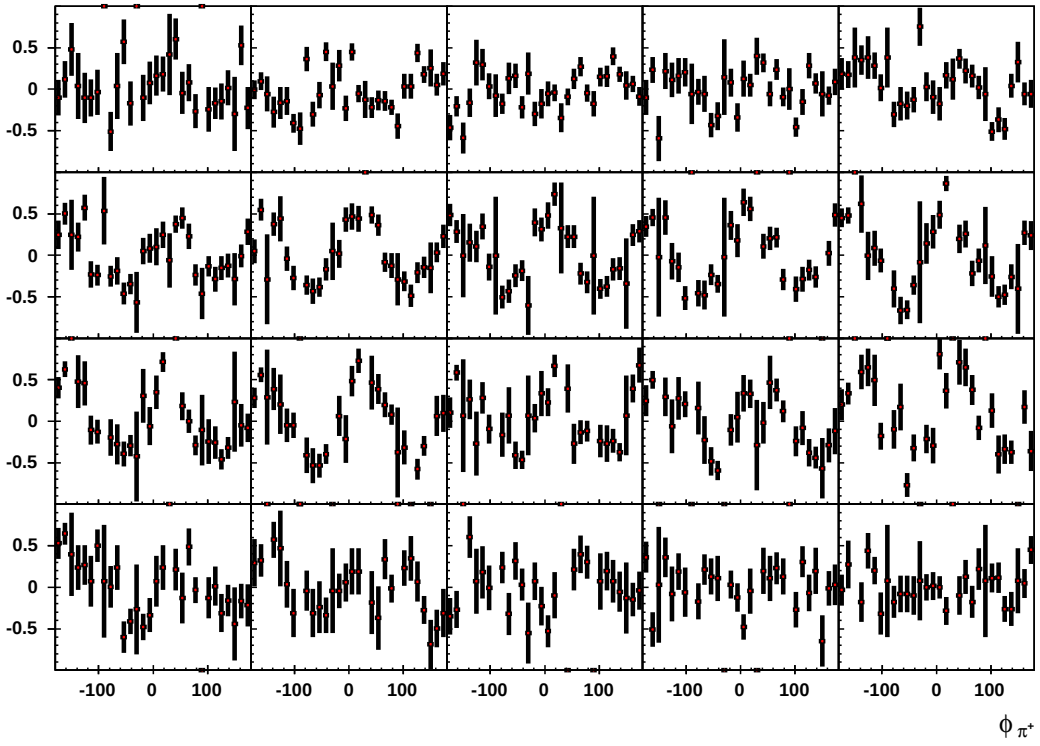

Figure B.22: A sampling of the ϕ-distributions used to extract I^s and I^c for a $p\,\pi^+(\pi^-)$ final state. Here, $-90^\circ < \phi^*_{\pi^+} < -72^\circ$.

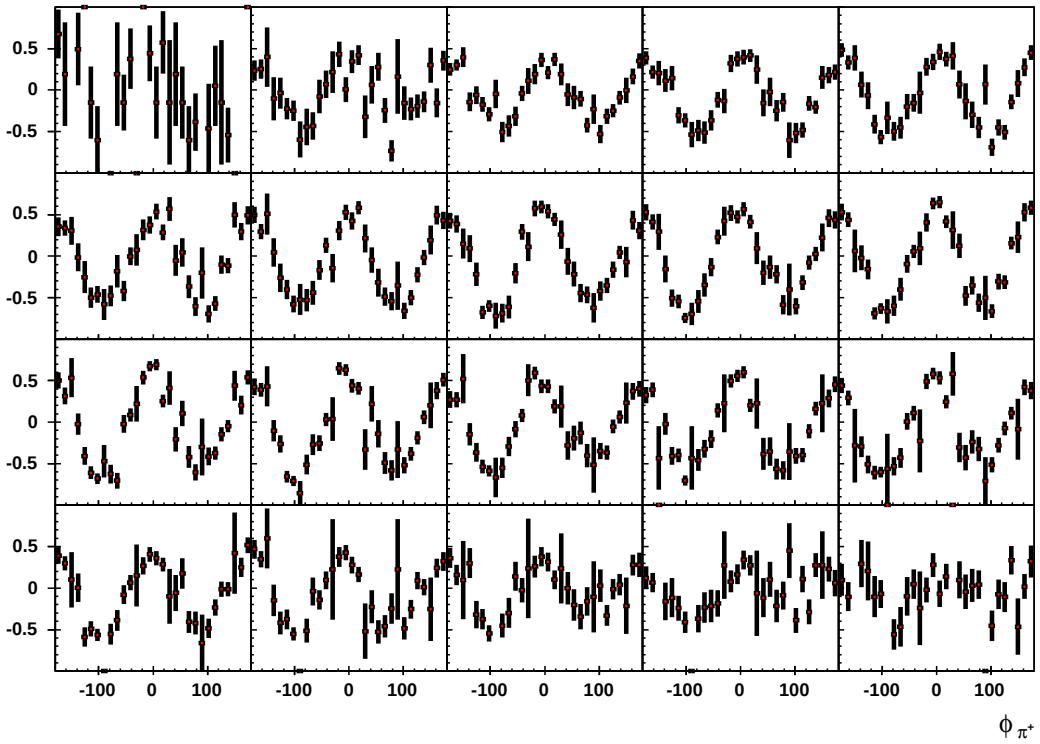

Figure B.23: A sampling of the ϕ-distributions used to extract I^s and I^c for a $p\ \pi^+(\pi^-)$ final state. Here, $0^\circ < \phi^*_{\pi^+} < 18^\circ$.

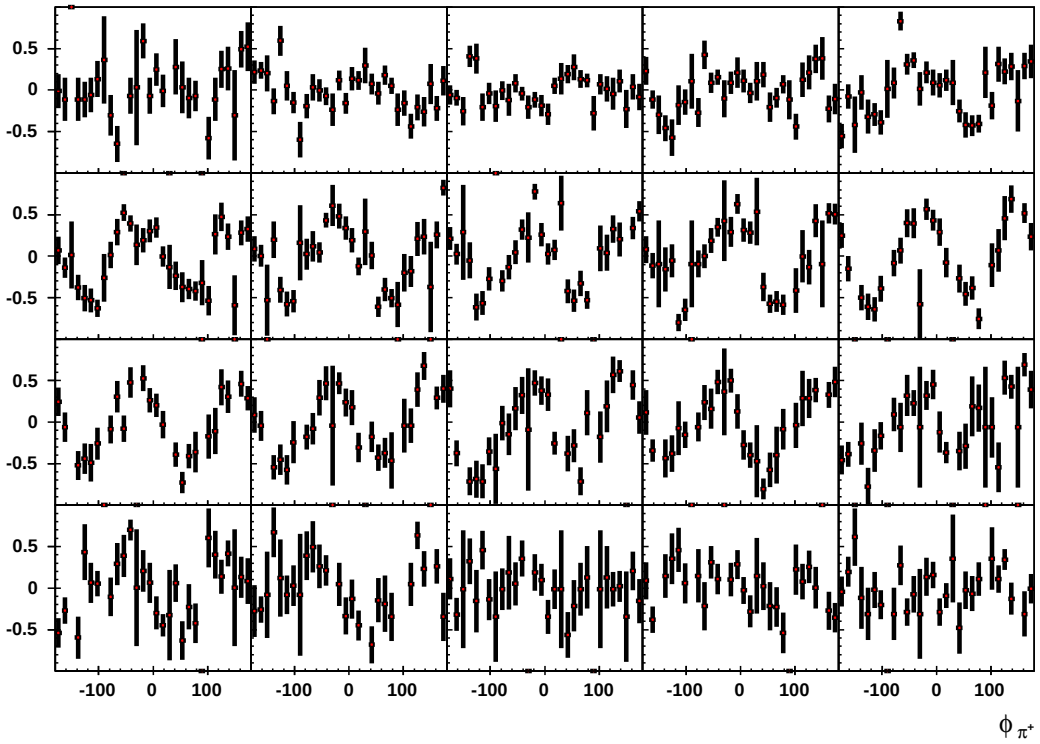

Figure B.24: A sampling of the ϕ-distributions used to extract I^s and I^c for a $p\ \pi^+(\pi^-)$ final state. Here, $72^\circ < \phi^*_{\pi^+} < 90^\circ$.

BIBLIOGRAPHY

[1] U. Loring, K. Kretzschmar, B. Metsch, and H. Petry, "*Relativistic quark models of baryons with instantaneous forces*", Eur. Phys. J. **A10**, 309 (2001), hep-ph/0103287.

[2] S. Capstick and N. Isgur, "*Baryons in a Relativized Quark Model with Chromodynamics*", Phys. Rev. **D34**, 2809 (1986).

[3] S. Capstick and W. Roberts. Phys. Rev. D, 58:074011, 1998.

[4] W. Roberts and T. Oed, "*Polarization Observables for Two-Pion Production off the Nucleon*", (2004), nucl-th/0410012.

[5] E. Rutherford, Phil. Mag. **21** (1911) 669.

[6] N. Bohr, Phil. Mag. **26** (1913) 476.

[7] E. Rutherford, Phil. Mag. **37** (1919) 581.

[8] http://www.particlephysics.ac.uk/news/picture-of-the-week/picture-archive/the-pion-muon-death-cycle–a-double-anniversary.html

[9] J.E. Augustin *et al.* (1974). "*Discovery of a Narrow Resonance in e+e Annihilation*". Physical Review Letters **33**: 1406.

[10] J.J. Aubert *et al.* (1974). "*Experimental Observation of a Heavy Particle J*". Physical Review Letters **33**: 1404.

[11] Fermilab (7 August 1977). "*Discoveries at Fermilab - Discovery of the Bottom Quark*". Press release.
http://www.fnal.gov/pub/inquiring/physics/discoveries/bottom_quark_pr.html.

[12] F. Abe *et al.* (CDF Collaboration) (1995). "*Observation of Top Quark Production in pp Collisions with the Collider Detector at Fermilab*". Physical Review Letters **74**: 26262631.

[13] http://www.physics.fsu.edu/users/roberts/roberts_color_tech.html

[14] S. Bethke, Prog. Part. Nucl. Phys. **58**, 351 (2007).

[15] F. X. Lee *et al.* "*Excited baryons from Bayesian priors and overlap fermions*", hep-lat/0208070, 2002.

[16] J. Bulava *et al.* "Nucleon, Δ, and Ω excited state spectra in N_f=2+1 lattice QCD" Phys. Rev. D **82**, 014507 (2010).

[17] http://cerncourier.com/cws/article/cern/29524

[18] http://en.wikipedia.org/wiki/Cubical_atom.

[19] http://en.wikipedia.org/wiki/Plum_pudding_model.

[20] http://en.wikipedia.org/wiki/Hantaro_Nagaoka.

[21] A. de Rujula *et al.* "*Hadron masses in a gauge theory*", Phys. Rev. D 12, 147 (1975).

[22] L. Glozman and D. Riska, "*The Spectrum of the nucleons and the strange hyperons and chiral dynamics*", Phys. Rept. **268**, 263 (1996), hep-ph/9505422.

[23] K. Nakamura *et al.* (Particle Data Group), J. Phys. G 37, 075021 (2010).

[24] D.B. Lichtenberg *et al.* "*Quark-Diquark Model of Baryons and SU(6)*", Phys. Rev. 167, 1535, 1968.

[25] http://adsabs.harvard.edu/abs/1983PhDT.....98H

[26] E. Klempt "Baryon Spectroscopy and the Origin of Mass", Hadron 2009, arXiv:1001.3290v1.

[27] K. Glander *et al.*, [SAPHIR Collaboration], "*Measurement of* $\gamma p \to K^+\Lambda$ *and* $\gamma\ p \to K^+\Sigma^0$ *at photon energies up to 2.6 GeV*", Eur. Phys. J. A19, 251 (2004), nuclex/0308025.

[28] J. W. C. McNabb *et al.*, [CLAS Collaboration], "*Hyperon Photoproduction in the Nucleon Resonance Region*", Phys. Rev. C69, 042201 (2004), nucl-ex/0305028.

[29] N. Sparks, [CBELSA-TAPS Collaboration], "*Beam asymmetries in pi0 photoproduction on the proton*", AIP Conf. Proc. **1257**, 591 (2010).

[30] W. Roberts and A. Rakatovao, "*A model for two-pion photoproduction amplitudes*", (1997), hep-ph/9708236.

[31] M. Bellis *et al.*, "*Measurement of* $\pi^+\pi^-$ *Photoproduction in Double-Polarization Experiments using CLAS*". CLAS Analysis Proposal E-06-013.

[32] O. Krehl, C. Hanhart, S. Krewald, and J. Speth, "*What is the structure of the Roper resonance?*", Phys. Rev. **C62**, 025207 (2000), nucl-th/9911080.

[33] Z.-p. Li, V. Burkert, and Z.-j. Li, "*Electroproduction of the Roper resonance as a hybrid state*", Phys. Rev. **D46**, 70 (1992).

[34] Volker D. Burkert, Inna Aznauryan1, and the CLAS Collaboration, "*New Results on Nucleon Resonance Transition Form Factors*", arXiv:0908.3507v1 [nucl-ex] 24 Aug 2009.

[35] J. Gomez Tejedor and E. Oset, "*Double pion photoproduction on the nucleon: Study of the isospin channels*", Nucl. Phys. **A600**, 413 (1996), hep-ph/9506209.

[36] L. Murphy and J. Laget, 1996, "DAPHNIA/SPhN 96-10".

[37] V. Mokeev, *et al.*, "*Electroexcitation of nucleon resonances at Q^2=0.65(GeV/c^2 from a combined analysis of single- and double-pion electroproduction data*", Phys. Rev. C 72, 045201 (2005).

[38] V.A. Nikonov, *et al.*, "*Further evidence for N(1900)P_{13} from photoproduction of hyperons*", Phy. Lett. B Volume 662, Issue 3, 24 April 2008, Pages 245-251.

[39] S. Strauch, "*Beam-Helicity Asymmetries in Double-Charged-Pion Photoproduction on the Proton*", Phys. Rev. Lett. 95, 162003 (2005).

[40] Y. Assafiri *et al.* "*Double π^0 Photoproduction on the Proton at GRAAL*". Phys. Rev. Lett. 90 (2003), p. 222001.

[41] J. Ajaka *et al.* "*Double π^0 photoproduction on the neutron at GRAAL*". Phys Lett B, Volume 651, Issues 2-3, 26 July 2007, Pages 108-113.

[42] E. Gutz. *et al.* "*Photoproduction of meson pairs: First measurement of the polarization observable I^s*". Phys. Lett. B687:11-15, 2010.

[43] B. Mecking. "*The CEBAF large acceptance spectrometer (CLAS)*". Nucl. Instr. and Meth. A503/03, 513, 2003.

[44] http://www.jlab.org/visitors/science/unique.html.

[45] M. Crofford *et al.* "*The RF System for the CEBAF Polarized Photoinjector*". Technical Report, Thomas Jefferson National Accelerator Facility, 1993.

[46] D.I. Sober *et al.* "*The bremsstrahlung tagged photon beam in Hall B at JLab*". Nucl Instr. Meth. A440, 263 (2000).

[47] U. Timm. "*Coherent bremsstrahlung of electrons in crystals*". Fortschritte der Physik, 1969.

[48] L. Montanet *et al.* Phys. Rev. **D50** 1173, 1994.

[49] W.J Briscoe *et al.* NSF Major Research Instrumentation, NSF Award 9724489. Technical report.

[50] Y.G. Sharabian *et al.* "*A new highly segmented start counter for the CLAS detector*". Nucl. Phys. A 556, 246 (2006).

[51] M.D. Mestayer. "*The CLAS Drift Chamber System*". Nucl. Instr. and Meth. A449, 81, 200.

[52] E.S. Smith *et al.* "*The time-of-fight system for CLAS*". Nucl Inst Meth A 432, 265-298, 1999.

[53] E. Pasyuk. "*Energy loss corrections for charged particles in CLAS*". CLAS-Note 2007-016.

[54] M. Williams. "*Measurement of Differential Cross Sections and Spin Density Matrix Elements along with a Partial Wave Analysis for $\gamma p \to p\omega$ using CLAS at Jefferson Lab*". Doctoral Thesis, Carnegie Mellon University.

[55] S. Stepanyan *et al.* "*Energy calibration of the JLab bremsstrahlung tagging system*". Nucl Inst Meth A **572**, 654 (2007).

[56] M. Dugger, C. Hanretty. "*Correction to the incident photon energy for g8b data*". CLAS-Note 2009-030.

[57] A. Natter. Analytic bremsstrahlung code. http://www.pit.physik.uni.tuebingen.de/bremsanalytic.html.

[58] C.I.O. Gordon. "*Rho photoproduction using linearly polarized photons with the CLAS detector*". PhD thesis, Glasgow University, 2004.

[59] http://www.physics.fsu.edu/users/roberts/roberts_polarization.html.

[60] W. Roberts, *Private Communication* (2010).

[61] C. Keith. "*The JLab Frozen Spin Target*". S&T Review, July 2, 2008. http://www.jlab.org/~ckeith/Frozen/SciTech.pdf

[62] http://clasweb.jlab.org/rungroups/g9/wiki/index.php/Main_Page

BIOGRAPHICAL SKETCH

Charles Hanretty was born on April 16th, 1982 in Camp Lejeune, North Carolina to Charles Patrick Hanretty and Angela Gaye Hanretty (Davis). In the Spring of 2000 he graduated from Hampton High School in Hampton, Virginia and began his undergraduate education in Physics the following fall at Florida A&M University. In the Spring of 2004, he graduated *Magna cum Laude* from Florida A&M University with a bachelor's degree in Physics. In the Fall of 2004, he began his Graduate School education at The Florida State University (FSU). In 2005 he joined the Experimental Hadronic Physics group at FSU and began work with his advisor, Dr. Volker Credè. He obtained his Master's degree in Experimental Nuclear Physics in 2007 from FSU and continued to work toward his Ph.D. He met this goal on 7 December 2010.